



The  
University  
Of  
Sheffield.

# **Parent Material Surface Deposits Origin in Finish Turning Operations of the Powder Processed Nickel Based Superalloy RR1000**

**Ioannis P. Lambrou**

**Department of Materials Science and Engineering**

**The University of Sheffield**

A thesis submitted in partial fulfilment of the requirements for the degree of  
Engineering Doctorate

September 2017



**Rolls-Royce**

**EPSRC**

Engineering and Physical Sciences  
Research Council

 **idc** Machining  
Science.

## ABSTRACT

The origin of material surface deposits, often denoted as pick-up, on finish turned advanced nickel based superalloy RR1000 has been investigated. Three types of pick-up were defined: streaks of chip residue producing relatively low surface roughness changes, minor pick-up deposits ranging in length from 10-100  $\mu\text{m}$ , and major pick-up deposits ranging in length from 200-500  $\mu\text{m}$  leading to significant protrusions. The corresponding chips were in the form of continuous ribbon with primary hook shaped serrations, with some hooks containing smaller secondary serrations, both forming at the thin trailing edge of the chip. The sizes of the minor and major pick-ups corresponded directly with the size of the secondary and primary serrations, respectively, with the smearing residue streaks formed by serration entrapment between the tool and the workpiece. Maximum pick-up surface coverage occurred at high cutting speed and high depth of cut combined with a fine grain RR1000 and dry machining conditions. This corresponded to maximum serration detachment, i.e. serration break-off, at the chip's trailing edge, where the stress state is most triaxial and the strain is at its maximum within the chip. It was found that the selection of machining parameters and the workpiece ductility performance were key factors for influencing pick-up severity. Low cutting speed, low tool radius, higher feed rate and sharper tools limited the serrations size and their tendency for failure, by reducing total strain and temperature within the chip. In turn, lower chip formation heat loads due to the application of coolant or the use of uncoated tools reduced chip temperatures, enhancing chip's plasticity tolerance, led to less severe chip serration and reduced pick-up. Hence, for low ductility powder processed alloys like RR1000 with strict requirements for finished low surface roughness values, which dictates the use of low feed rates, the key to minimising pick-up is to reduce chip temperatures and strains. This can be achieved by the application of coolant and optimised chip geometry to maximise the chip's trailing edge thickness to minimise the amount of material that exceeds the ductility limit of the material.

## ACKNOWLEDGMENTS

First of all, I would like to thank my supervisors Professor Bradley Wynne, Dr Adrian Sharman and Dr Gregor Kappmeyer for their support and guidance during this project. I would like to express my appreciation to Professor Bradley Wynne for the numerous discussions we had over the last few years, in which he tirelessly motivated me to progress both academically and personally, shaping me into the researcher I am today. I am grateful to Dr Adrian Sharman for sharing his machining science experience and for his limitless support during my machining experiments. I am also grateful to Dr Gregor Kappmeyer for the enlightening discussions concerning my project and for introducing me to the stimulating environment of Rolls-Royce plc.

I also thank Tim Sowa, who I consider my mentor in RR1000 manufacturing process and a good friend. I am also particularly grateful to Holger Krain, Dr Pete Crawforth and Dr Chris Taylor from the AMRC for their technical support. Furthermore, I would like to thank Rolls-Royce plc. and the Engineering and Physical Science Research Council (UK), through the IDC in Machining Science (EP/I01800X/1), for the financial support.

Finally, I reserve my deepest thanks and appreciation to my parents Pavlos and Chriso, my two brothers and my fiancée for their continued selfless support and patience, making this thesis possible. For that, I dedicate this thesis to them.

# CONTENTS

ABSTRACT .....	i
ACKNOWLEDGMENTS .....	ii
LIST OF FIGURES .....	vii
LIST OF TABLES .....	xxi
NOMENCLATURE .....	xxiii
1 PREFACE .....	1
1.1 PROJECT BACKGROUND.....	1
1.2 PROJECT SCOPE AND HYPOTHESIS .....	3
1.3 THESIS OUTLINE.....	4
2 LITERATURE REVIEW .....	5
2.1 INTRODUCTION.....	5
2.2 NICKEL BASED SUPERALLOYS .....	9
2.2.1 Introduction .....	9
2.2.2 Microstructure and Mechanical Properties of Polycrystalline Superalloys.....	10
2.2.3 Effect of Mechanical Properties and Microstructure in Machining .....	17
2.3 METAL CUTTING.....	20
2.3.1 Introduction .....	20

2.3.2 Chip Formation in Turning Operations .....	21
2.3.2.1 Orthogonal Cuts .....	21
2.3.2.2 Oblique Turning.....	32
2.3.3 Surface Integrity .....	39
2.3.3.1 Sub-surface Integrity.....	39
2.3.3.2 Surface Finish .....	45
2.3.4 Cutting Mechanics and Temperatures .....	54
2.3.4.1 Cutting Forces .....	54
2.3.4.2 Cutting Temperatures.....	57
2.3.4.3 Effect on Tool Performance.....	60
2.3.5 Cooling Strategy .....	64
2.4 SUMMARY .....	68
3 EXPERIMENTAL WORK.....	72
3.1 INTRODUCTION.....	72
3.2 EXPERIMENTAL PROCESS .....	73
3.2.1 Pick-up Investigation Trials (Phases 1-2).....	73
3.2.1.1 Dry Trials (Phase 1).....	77
3.2.1.2 Minimum Cooling Trials (Phase 2a).....	77
3.2.1.3 Low Pressure Cooling Trials (Phase 2b) .....	78
3.2.2 Cooling Performance Investigation Trials (Phase 3).....	80
3.2.3 Chip Formation Trials (Phase 4) .....	82

3.3 DATA ANALYSIS METHODS AND EQUIPMENT .....	84
4 RESULTS AND DISCUSSION .....	90
4.1 INTRODUCTION.....	90
4.2 PICK-UP INVESTIGATION TRIALS .....	91
4.2.1 Dry Trials (Phase 1).....	91
4.2.1.1 Surface Integrity.....	91
4.2.1.2 Chip Formation and Geometry .....	99
4.2.1.3 Cutting Forces .....	114
4.2.1.4 Discussion - Dry Trials (Phase 1) .....	119
4.2.2 Minimum Cooling Trials (Phase 2a) .....	128
4.2.2.1 Surface Integrity.....	128
4.2.2.2 Chip Geometry.....	132
4.2.2.3 Cutting Forces .....	136
4.2.3 Low Pressure Cooling Trials (Phase 2b) .....	138
4.2.3.1 Surface Integrity.....	138
4.2.3.2 Chip Geometry.....	141
4.2.3.3 Cutting Forces .....	148
4.2.3.4 Effect of Cooling Failure .....	151
4.2.3.5 Discussion - Cooled Trials (Phase 2).....	153
4.3 COOLING PERFORMANCE INVESTIGATION TRIALS .....	159
4.3.1 Cooling Strategy Performance Assessment Trials (Phase 3) .....	159

4.3.1.1	Surface Integrity.....	159
4.3.1.2	Chip Geometry.....	160
4.3.1.3	Low pressure rake and flank cooling case study .....	166
4.3.1.4	Cutting Forces.....	167
4.3.1.5	Discussion - Cooling Strategy Performance Assessment Trials (Phase 3)...	168
4.4	CHIP FORMATION TRIALS .....	172
4.4.1	Chip Formation - Dry Trials (Phase 4).....	172
4.4.1.1	Surface Integrity.....	172
4.4.1.2	Chip Geometry.....	173
4.4.1.3	Cutting Forces.....	183
4.4.1.4	Discussion – Chip Formations Trials (Phase 4).....	185
5	SUMMARY DISCUSSION .....	190
6	CONCLUSIONS.....	195
7	RECOMMENDED FURTHER WORK.....	198
	REFERENCES .....	202
	APPENDICES .....	220
	APPENDIX 1 .....	220
	APPENDIX 2 .....	222
	APPENDIX 3 .....	223

# LIST OF FIGURES

Figure 1-1: High pressure compressor assembly; (a) Seal fins, (b) Circum groove, (c) Cone profile, (d) Internal spigot profile, (e-f) Typical pick-up examples as detected during binocular inspection.....	2
Figure 2-1: Rolls-Royce Trent family high bypass turbofan assembly illustration; (a) Compressor, (b) Combustion chamber, (c) Turbine. {Courtesy of Rolls-Royce plc}.....	5
Figure 2-2: Factors affecting the jet engine thermodynamic efficiency, National Academy of Sciences (2006).....	6
Figure 2-3: Superalloys used by Rolls-Royce in the manufacturing of high pressure rotative components, Kappmeyer et al. (2012). .....	7
Figure 2-4: High pressure turbine disc; (a) Forged preform, (b) Finished component, Kappmeyer et al. (2012). .....	8
Figure 2-5: Advanced high strength materials, National Academy of Sciences (2006).....	9
Figure 2-6: Face centred cubic crystal structure (FCC), Reed (2006).....	10
Figure 2-7: Gamma prime precipitation illustration of Udimet 720Li microstructure, Jackson and Reed (1999).....	12
Figure 2-8: Effect of tertiary gamma prime precipitate size on dislocation movement; (a) Weak coupling, (b) Strong coupling, Jackson and Reed (1999).....	12
Figure 2-9: Fine grain RR1000 microstructure uniformity; (a) Primary gamma prime and (b) Secondary and tertiary gamma prime, Mitchell et al. (2004). .....	14
Figure 2-10: Creep performance comparison between RR1000 and Udimet 720Li, Hardy et al. (2004).....	14

Figure 2-11: RR1000 dual microstructure turbine disc; (a) FG RR1000, (b) CG RR1000, (c) Fatigue crack growth performance assessment at 700°C and (d) Creep performance assessment, Mitchell et al. (2008).....	15
Figure 2-12: Cutting speeds used for machining different material categories, Schulz and Moriwaki (1992). ....	17
Figure 2-13: Effect of mechanical properties and cutting speed on 100Cr6 steel chip morphology, Poulachon and Moisan (2000).....	18
Figure 2-14: Turning operation configurations; (a) 2D orthogonal cut and (b) 3D oblique cut, Denguir et al. (2014). ....	22
Figure 2-15: Merchant` s cutting force prediction model, Merchant (1945).....	22
Figure 2-16: Chip formation physics in orthogonal cutting ; (a) Machining speed vector diagram and (b) Shear-strain model, Trent and Wright (2000). ....	23
Figure 2-17: Effect of rake angle on chip formation; (a) $\alpha = 80^\circ$ , (b) $\alpha = 50^\circ$ , (c) $\alpha = -10^\circ$ , Bitans and Brown (1965). ....	25
Figure 2-18: Effect of tool edge rounding radius on chip formation; (a) $r_e = 0.8$ mm, (b) $r_e = 3.2$ mm, Bitans and Brown (1965).....	25
Figure 2-19: Effect of high negative rake angles; (a) No chip formation and (b) Chip formation minimum conditions, Komanduri (1971).....	26
Figure 2-20: Typical examples of chip types formed in orthogonal cutting; (a) Continuous chip, (b) Continuous chip formed with built-up edge, (c) Semi-continuous segmented chip, (d) Discontinuous chip, Childs et al. (2000). ....	27
Figure 2-21: Effect of uncut chip thickness on steel chip segmentation; (a) Thick chip at high $a_p$ , (b) Thin chip at low $a_p$ , König et al. (1993). ....	28

Figure 2-22: Shear band formation in segmented chips; (a) Adiabatic shear mechanism, (b) Fracturing mechanism, Vyas and Shaw (1999). ....	29
Figure 2-23: Discontinuous chip formation; (a) Brittle fracture, Okushima and Hitomi (1961), (b) FEM simulation, Guo and Yen (2004).....	30
Figure 2-24: Chip formation mechanism transformation when machining Inconel 718; Continuous ribbon shaped chips (a) $V_C = 15$ m/min, (b) $V_C = 90$ m/min, Discontinuous chips (c) $V_C = 122$ m/min (d) $V_C = 213$ m/min, Komanduri and Schroeder (1986).....	31
Figure 2-25: Predicted chip flow data at varying $V_C$ when machining Ti6Al4V; (a) Effect on chip thickness, (b) Effect on chip shear angle, Daymi et al. (2009). .....	31
Figure 2-26: Illustrations of oblique turning with round tools; (a) Chip formation process, Kishawy et al. (2006), (b) Machining force configuration, Denguir et al. (2014).....	33
Figure 2-27: Effect of tool geometry on uncut chip cross-section in oblique turning; (a) Sharp tool, (b) Nose-radiusied tool, (c) Round tool, Bushlya et al. (2015). .....	33
Figure 2-28: Round tool uncut chip geometry in oblique turning, Bushlya et al. (2015).....	34
Figure 2-29: Effect of uncut chip thickness on chip segmentation and edge serration when turning hard steel AISI 1550; (a) $r_n = 3.6$ mm, (b) $r_n = 1.2$ mm, Kishawy (1998). .....	36
Figure 2-30: Chip lateral flow when turning of hard steel at $V_C = 160$ m/min, $f = 0.05$ mm and $a_p = 4$ mm, El-Wardany et al. (2000b). .....	36
Figure 2-31: Chip edge serrations when turning Inconel 718 at $f = 0.08$ mm/rev, $a_p = 0.5$ mm and $r_n = 0.8$ mm; (a) $V_C = 40$ m/min, (b) $V_C = 50$ m/min, (c) $V_C = 60$ m/min, Thakur et al. (2009).....	37
Figure 2-32: Chip edge serrations when milling hard steel ASSAB 718 at $V_C = 150$ m/min, $f = 0.05$ mm/tooth and $a_p = 0.35$ mm; Uncoated tool (a) Dry cut, Coated tool (b) Dry cut, (c) Conventional cooling , (d) High pressure cooling, Kumar et al. (2002). .....	38

Figure 2-33: Acceptable sub-surface damage when machining RR1000; (a) Fine grain material, (b) Coarse grain material, Hardy et al. (2014).....	40
Figure 2-34: Sub-surface distortion when finish turning Inconel 718; (a) New tool, (b) Worn tool, Sharman et al. (2006).....	41
Figure 2-35: Chip cross-section profiles for varying tool radius at fixed maximum uncut chip thickness $h_{max\_u} = 0.145$ mm; (a) Thick chip, (b) Thin chip, Sharman et al. (2015). .....	42
Figure 2-36: Effect of tool radius on residual stresses in the cutting direction when finish turning Inconel 718 at fixed maximum uncut chip thickness $h_{max\_u} = 0.145$ mm, $V_C = 40$ m/min and worn tools; Sharman et al. (2015).....	43
Figure 2-37: White layer formation when turning Inconel 718 with worn tool at $V_C = 300$ m/min, $a_p = 0.3$ mm and $f = 0.2$ mm/rev; (a) Cutting direction, (b) Feed direction, Bushlya et al. (2011).....	44
Figure 2-38: 3D reconstruction of Udimet 720 finish turned surface topography, (a) Low feed rate, (b) High feed rate, Ardi et al. (2014). .....	46
Figure 2-39: 2D surface finish profile illustration, Thomas (1981).....	46
Figure 2-40: Effect of machining parameters on finish turned Inconel 718 surface roughness Ra values, Ezugwu et al. (1999). .....	47
Figure 2-41: Parent material surface deposits on dry turned Inconel 718 at $V_C = 80$ m/min and $f = 0.1$ mm/rev , Arunachalam and Mannan (2003).....	48
Figure 2-42: Surface defects in high speed machining of Inconel 718 at $f = 0.05$ mm/rev; (a) $V_C = 125$ m/min, (b) $V_C = 300$ m/min, (c) $V_C = 425$ m/min, Pawade et al. (2007). .....	49
Figure 2-43: Surface defects in hard turning steel AISI 4615 with ceramic tools at $V_C = 107$ m/min, $r_n = 4.7$ mm, $a_p = 0.125$ mm and $f = 0.075$ mm/rev; (a) Grooves, (b) Sideflow, (c) Material deposits, (d) Cavities, Bresseler et al. (1997).....	50

Figure 2-44: Material side flow in hard turning; (a) Surface defects, (b) Defect formation mechanism, Kishawy and Elbestawi (1999).....	50
Figure 2-45: Effect of cooling conditions on surface defects when turning Inconel 718 at $V_C = 200$ m/min, $a_p = 0.3$ mm and $f = 0.1$ mm/rev; Dry cuts (a) Worn tool, (b) New tool, Cooled cuts (c) Worn tool, (d) New tool, Zhou et al. (2012). .....	51
Figure 2-46: RR1000 finish turned surface integrity; (a) Pick-up 3D morphology, Pick-up deposits (b) $Q = 30$ $\text{mm}^3/\text{sec}$ , (c) $Q = 37$ $\text{mm}^3/\text{sec}$ , (d) Sub-surface damage at $Q = 37$ $\text{mm}^3/\text{sec}$ , Axinte et al. (2006). .....	52
Figure 2-47: Parent material deposits in hole making operations; (a) Drilling RR1000, Soo et al. (2011), (b) Milling Inconel 718, Sharman et al. (2008).....	53
Figure 2-48: Effect of cutting parameters and tool wear on Inconel 718 turning forces; Sharman et al. (2006).....	55
Figure 2-49: Effect of the tool's CBN content on AISI H13 steel machining conditions; (a) Cutting forces, (b) Predicted cutting temperature; Huang and Liang (2003). .....	57
Figure 2-50: Temperature and cutting force relationship in segmented chip formation, Li et al. (2014). .....	57
Figure 2-51: Thermodynamics in material removal operations; (a) Heat generation and dissipation areas, Abukhshim et al. (2006), (b) Cutting temperatures in turning Inconel 718, Kitagawa et al. (1997).....	59
Figure 2-52: Cutting speed effect on Inconel 718 cutting temperatures; $V_C = 30$ mm/min (a) Chip and (b) Tool, $V_C = 70$ mm/min (c) Chip and (d) Tool, Ozel et al. (2011). .....	60
Figure 2-53: Tool wear mechanisms of coated tools; (a) Flank wear, (b) Crater Wear, (c) Notch wear - Leading edge, (d) Notch wear - Trailing edge, Dearnley and Trent (1982). ....	61

Figure 2-54: Tool wear mechanisms when turning GH4169 at $f = 0.13 \text{ mm/rev}$ and $a_p = 1.2 \text{ mm}$ ; (a-b) $V_C = 82 \text{ m/min}$ , (c-d) $V_C = 115 \text{ m/min}$ , Xue and Chen (2011) .....	62
Figure 2-55: Cooling strategy effect on tool temperatures when turning Inconel 718 at $a_p = 1 \text{ mm}$ and $f = 0.2 \text{ mm/rev}$ , Klocke et al. (2011) .....	65
Figure 2-56: Cooling strategy effect on tool temperatures when turning Ti6Al4V at $a_p = 1 \text{ mm}$ and $f = 0.2 \text{ mm/rev}$ , Klocke et al. (2011) .....	65
Figure 2-57: Effect of cooling strategy performance and coolant supply jet configuration on chip morphology when turning steel SAE EV-8; (a) Conventional flood cooling, (b) Focused rake cooling, (c) Focused flank cooling, (d) Focused multi-face cooling, Sanchez et al. (2012) .....	66
Figure 2-58: Effect of cooling strategy on tool temperatures when turning nickel at $V_C = 46 \text{ m/min}$ , $a_p = 1.25 \text{ mm}$ and $f = 0.25 \text{ mm/rev}$ ; (a) Dry machining – Tool cross-section, (b) Flank face cooling, (c) Rake face cooling, Smart and Trent (1975a) .....	67
Figure 3-1: Trials Phases 1-2; (a) Machining setup, (b) Experimental configuration .....	73
Figure 3-2: Cutting tools used in the experimental trials; (a) Tool geometry, (b) Cutting edge cross-section, (c) S05F coating grade. {Courtesy of Sandvik} .....	74
Figure 3-3: Microstructure of machined superalloys; (a) FG RR1000-Kalling's N°2, (b) FG RR1000-10% Phosphoric acid, (c) CG RR1000-Kalling's N°2 and (d) Alloy718-Kalling's N°2 .....	75
Figure 3-4: Average Vickers hardness of the machined workpieces measured at 1kgf load and 15 seconds dwell time .....	76
Figure 3-5: Minimum cooling conditions; (a) Coolant supply, (b) Cooling setup .....	78
Figure 3-6: Illustration of uncut chip cross-section geometry; (a) $f = 0.12 \text{ mm/rev}$ and $a_p = 0.25 \text{ mm}$ and (b) $f = 0.25 \text{ mm/rev}$ and $a_p = 0.12 \text{ mm}$ .....	79

Figure 3-7: Phase 2 trials; (a) Experimental configuration and (b) Machining diagram.....	80
Figure 3-8: Cooling process configurations; (a) Rake face cooling only and (b) Rake and flank cooling. ....	81
Figure 3-9: Phase 4 quick study machining experimental configuration. ....	83
Figure 3-10: Chip cross-section geometry; (a) Uncut, (b) Cut. ....	85
Figure 3-11: Examples of the chip 3D scans; (a) Length AC, (b) Angle $\hat{A}$ , (c) Serration spacing $d_s$ , (d) Maximum serration thickness $h_s$ . ....	87
Figure 4-1: Typical examples of pick-up deposits in RR1000 dry machining; (a) Surface finish, (b) Type 1 pick-up cross-section, (c) Type 2 pick-up cross-section, (d-e) Type 3 pick-up cross-sections. ....	92
Figure 4-2: Further observations; (a) Pick-up deposit characteristics, (b) Tool state - end of the cut, FG RR1000 pick-up severity (c) Start of the cut and (d) End of the cut. ....	93
Figure 4-3: FG RR1000 dry turning surface damage; $a_p = 0.13$ mm (a) $V_C = 30$ m/min and (b) $V_C = 50$ m/min, $a_p = 0.25$ mm (c) $V_C = 30$ m/min and (d) $V_C = 50$ m/min. ....	96
Figure 4-4: FG RR1000 dry turning subsurface deformation; $a_p = 0.13$ mm (a) $V_C = 30$ m/min and (b) $V_C = 50$ m/min, $a_p = 0.25$ mm (c) $V_C = 30$ m/min and (d) $V_C = 50$ m/min. ....	96
Figure 4-5: CG RR1000 dry turning surface damage; $a_p = 0.13$ mm (a) $V_C = 30$ m/min and (b) $V_C = 50$ m/min, $a_p = 0.25$ mm (c) $V_C = 30$ m/min and (d) $V_C = 50$ m/min. ....	97
Figure 4-6: CG RR1000 dry turning subsurface deformation; $a_p = 0.13$ mm (a) $V_C = 30$ m/min and (b) $V_C = 50$ m/min, $a_p = 0.25$ mm (c) $V_C = 30$ m/min and (d) $V_C = 50$ m/min. ....	97
Figure 4-7: Alloy 718 dry turning surface damage; $a_p = 0.13$ mm (a) $V_C = 30$ m/min and (b) $V_C = 50$ m/min, $a_p = 0.25$ mm (c) $V_C = 30$ m/min and (d) $V_C = 50$ m/min. ....	98
Figure 4-8: Alloy 718 dry turning subsurface deformation; $a_p = 0.13$ mm (a) $V_C = 30$ m/min and (b) $V_C = 50$ m/min, $a_p = 0.25$ mm (c) $V_C = 30$ m/min and (d) $V_C = 50$ m/min. ....	98

Figure 4-9: Chip serration geometry in dry turning of RR1000 at $V_C = 50$ m/min and $a_p = 0.25$ mm; (a) FG chip geometry, (b) CG chip geometry, (c) FG primary serrations, (d) CG primary serrations, (e) FG secondary serrations and (f) CG secondary serrations.....	101
Figure 4-10: Chip formation mechanism during the unsteady state of the cut; (a) Uncut chip geometry, (b) Machining forces, (c) Chip morphology at $x+2f$ , (d) Chip morphology at $x+3f$ , (e) Chip morphology at $x+4f$ , (f) Continues chip morphology.....	102
Figure 4-11: FG RR1000 chip serration failure at $V_C = 50$ m/min and $a_p = 0.25$ mm; (a,b) Chip serrations, (c,e) Crack nucleation at trailing edge, (d,f) Fractured surfaces. ....	103
Figure 4-12: Effect of cutting speed on FG RR1000 chips machined at $a_p = 0.13$ mm; Chip geometry (a) $V_C = 30$ m/min and (b) $V_C = 50$ m/min, Chip cross-section (c) $V_C = 30$ m/min and (d) $V_C = 50$ m/min, Secondary chip serrations (e) $V_C = 30$ m/min and (f) $V_C = 50$ m/min. ....	105
Figure 4-13: Effect of the depth of cut on CG RR1000 chip serrations formed at $V_C = 30$ m/min; (a,b) Primary serrations at $a_p = 0.13$ mm and $a_p = 0.25$ mm respectively, (c) Lack of secondary serrations at $a_p = 0.13$ mm, (d) Secondary serrations at $a_p = 0.25$ mm, (e) Crack nucleation at $a_p = 0.13$ mm, (f) Serration fracture surface at $a_p = 0.25$ mm. ....	107
Figure 4-14: Alloy 718 chips machined at $V_C = 30$ m/min and $a_p = 0.13$ mm; (a,b) Chip morphology, (c,d) Primary serraion formation, (e,f) Chip fractured surface. ....	109
Figure 4-15: Effect of cutting speed and depth of cut when machining Alloy 718; Chip morphology (a) $V_C = 50$ m/min and $a_p = 0.13$ mm, (b) $V_C = 30$ m/min and $a_p = 0.25$ mm, Serrations (c) $V_C = 50$ m/min and $a_p = 0.13$ mm, (d) $V_C = 30$ m/min and $a_p = 0.25$ mm.....	110
Figure 4-16: Alloy 718 serrations formed at $V_C = 50$ m/min and $a_p = 0.25$ mm; (a) Serraion morphology, (b) Crack formation. ....	111
Figure 4-17: Tool rake face wear mechanisms for dry machined superalloys. ....	113

Figure 4-18: Examples of FG RR1000 surface indentations; (a) $V_C = 30$ m/min and $a_p = 0.13$ mm, (b) $V_C = 30$ m/min and $a_p = 0.25$ mm. ....	114
Figure 4-19: Machining forces for dry conditions; (a) FG RR1000, (b) CG RR1000, (c) Alloy 718. (Error bars show the standard deviation) .....	117
Figure 4-20: Effect of machining parameters and microstructure on specific cutting load when dry turning superalloys; (a) Traditional calculation methodology, (b) Proposed calculation methodology.....	118
Figure 4-21: Illustration of the depth of cut effect on FG and CG RR1000 chip deformation at $V_C = 30$ m/min compared to the non-deformed chip thicknesses at corresponding conditions. ....	122
Figure 4-22: Illustration of the depth of cut effect on CG RR1000 and Alloy 718 chip deformation at $V_C = 30$ m/min compared to the non-deformed chip thicknesses at corresponding conditions. ....	125
Figure 4-23: Surface defects for minimum cooling at $a_p = 0.25$ mm; (a) $V_C = 30$ m/min, (b) $V_C = 50$ m/min, (c-f) $V_C = 70$ m/min.....	129
Figure 4-24: Pick-up deposition and cut progression effect on surface finish; (a) Surface damage and (b) Tool rake wear at $V_C = 70$ m/min and $a_p = 0.25$ mm.....	130
Figure 4-25: Surface finish at $V_C = 70$ m/min and $a_p = 0.13$ mm; (a) Beginning of the cut, (b) End of the cut and (c-d) Minor surface defects.....	130
Figure 4-26: 3D scan of Type 3 pick-up detected in FG RR1000 machining at $V_C = 70$ m/min and $a_p = 0.25$ mm; (a) 2D profile, (b) Surface roughness Ra estimation.....	131
Figure 4-27: FG RR1000 subsurface deformation at minimum cooling conditions; $V_C = 30$ m/min (a) $a_p = 0.13$ mm and (b) $a_p = 0.25$ mm, $V_C = 70$ m/min (c) $a_p = 0.13$ mm and (d) $a_p = 0.25$ mm. ....	132

Figure 4-28: Chip formation at minimum cooling conditions; $V_C = 30 \text{ m/min}$ (a) $a_p = 0.13 \text{ mm}$ and (b) $a_p = 0.25 \text{ mm}$ , $V_C = 50 \text{ m/min}$ (c) $a_p = 0.13 \text{ mm}$ and (d) $a_p = 0.25 \text{ mm}$ , $V_C = 70 \text{ m/min}$ (e) $a_p = 0.13 \text{ mm}$ and (f) $a_p = 0.25 \text{ mm}$ .....	133
Figure 4-29: Further observations at $V_C = 70 \text{ m/min}$ and minimum cooling conditions; $a_p = 0.25 \text{ mm}$ (a) Serration geometry and (b) Serration partial fracture, $a_p = 0.13 \text{ mm}$ (c) Secondary serration geometry and (d) Secondary serration adherence on the tool.....	135
Figure 4-30: Rake tool wear for minimum cooling conditions; $V_C = 30 \text{ m/min}$ (a) $a_p = 0.13 \text{ mm}$ and (b) $a_p = 0.25 \text{ mm}$ , $V_C = 50 \text{ m/min}$ (c) $a_p = 0.13 \text{ mm}$ and (d) $a_p = 0.25 \text{ mm}$ .....	136
Figure 4-31: FG RR1000 machining forces for minimum cooling conditions. (Error bars show the standard deviation) .....	137
Figure 4-32: Effect of machining parameters on specific cutting load at $f = 0.12 \text{ mm}$ and minimum cooling conditions. ....	137
Figure 4-33: Surface finish at $V_C = 30 \text{ m/min}$ and LP cooling conditions; (a) $f = 0.12 \text{ mm/rev}$ and $a_p = 0.25 \text{ mm}$ , (b) $f = 0.25 \text{ mm/rev}$ and $a_p = 0.12 \text{ mm}$ . ....	138
Figure 4-34: Pick-up when machining FG RR1000 at $f = 0.12 \text{ mm/rev}$ ; (a) $V_C = 50 \text{ m/min}$ and (b) $V_C = 70 \text{ m/min}$ .....	139
Figure 4-35: FG RR1000 subsurface deformation under LP cooling conditions; $V_C = 70 \text{ m/min}$ (a) $f = 0.12 \text{ mm/rev}$ and $a_p = 0.25 \text{ mm}$ , (b) $f = 0.25 \text{ mm/rev}$ and $a_p = 0.12 \text{ mm}$ . ....	139
Figure 4-36: Pick-up deposits at $f = 0.12 \text{ mm/rev}$ ; CG RR1000 (a) $V_C = 30 \text{ m/min}$ and (b) $V_C = 70 \text{ m/min}$ , Alloy 718 (c) $V_C = 30 \text{ m/min}$ and (d) $V_C = 70 \text{ m/min}$ . ....	140
Figure 4-37: Subsurface deformation at $f = 0.12 \text{ mm/rev}$ ; CG RR1000 (a) $V_C = 30 \text{ m/min}$ and (b) $V_C = 70 \text{ m/min}$ , Alloy 718 (c) $V_C = 30 \text{ m/min}$ and (d) $V_C = 70 \text{ m/min}$ .....	141

Figure 4-38: Effect of feed rate and depth of cut on FG RR1000 chip and serration morphology at $V_C = 30$ m/min; $f = 0.12$ mm/rev and $a_p = 0.25$ mm (a) Chip geometry, (c) Serrations, $f = 0.25$ mm/rev $a_p = 0.12$ mm (b) Chip geometry, (d) Serrations. ....	142
Figure 4-39: Chip formation at $V_C = 50$ m/min under LP cooling conditions; $f = 0.12$ mm/rev and $a_p = 0.25$ mm (a) Chip morphology and (b) Chip cross-section, $f = 0.25$ mm/rev and $a_p = 0.12$ mm (c) Chip morphology and (d) Chip cross-section. ....	143
Figure 4-40: Serration morphology at $V_C = 70$ m/min under LP cooling conditions; $f = 0.12$ mm/rev and $a_p = 0.25$ mm (a) Primary serrations and (c) Secondary serrations, $f = 0.25$ mm/rev and $a_p = 0.12$ mm (b) Primary serrations and (d) Secondary serrations. ....	145
Figure 4-41: Tool rake face wear mechanisms when machining FG RR1000 under LP cooling conditions; $f = 0.12$ mm/rev and $a_p = 0.25$ mm (a) $V_C = 30$ m/min, (b) $V_C = 50$ m/min, (c) $V_C = 70$ m/min, $f = 0.25$ mm/rev and $a_p = 0.12$ mm (d) $V_C = 30$ m/min, (e) $V_C = 50$ m/min, (f) $V_C = 70$ m/min. ....	146
Figure 4-42: Serration morphology when machining CG RR1000 and Alloy 718 under LP cooling conditions; $V_C = 30$ m/min (a) CG RR1000 and (b) Alloy 718, $V_C = 50$ m/min (c) CG RR1000 and (d) Alloy 718, $V_C = 70$ m/min (e) CG RR1000 and (f) Alloy 718. ....	147
Figure 4-43: Effect of uncut chip geometry on FG RR1000 machining forces under LP cooling conditions. (Error bars show the standard deviation) ....	149
Figure 4-44: FG RR1000 specific cutting load at LP cooling conditions. ....	150
Figure 4-45: CG RR1000 and Alloy 718 machining forces at $a_p = 0.25$ mm and $f = 0.12$ mm/rev under LP cooling conditions. (Error bars show the standard deviation) ....	150
Figure 4-46: CG RR1000 and Alloy 718 specific cutting load at $a_p = 0.25$ mm and $f = 0.12$ mm/rev under LP cooling conditions. ....	151

Figure 4-47: Effect of chip entrapment during machining; (a) Chip nesting, (b) Surface finish, (c-d) Chip formation and serration failure. ....	152
Figure 4-48: FG RR1000 pick-up severity relationship to serration formation mechanism at corresponding machining and cooling conditions. ....	155
Figure 4-49: Effect of cooling strategy and cutting speed on FG RR1000 chip deformation at $f = 0.12 \text{ mm/rev}$ and $a_p = 0.25 \text{ mm}$ . ....	157
Figure 4-50: FG RR1000 surface finish and subsurface deformation at $V_C = 70 \text{ m/min}$ ; Pick-up (a) Rake face cooling at $P = 12 \text{ bar}$ and $\lambda = 6.5 \text{ l/min}$ , (b) Rake face cooling at $P = 70 \text{ bar}$ and $\lambda = 6.5 \text{ l/min}$ , Subsurface deformation (c) Rake face cooling at $P = 12 \text{ bar}$ and $\lambda = 6.5 \text{ l/min}$ , (d) Rake and flank cooling at $P = 70 \text{ bar}$ and $\lambda = 9.1 \text{ l/min}$ . ....	159
Figure 4-51: FG RR1000 chip formation for low and high pressure rake cooling at $\lambda = 6.5 \text{ l/min}$ ; $V_C = 30 \text{ m/min}$ (a) $P = 12 \text{ bar}$ and (b) $P = 70 \text{ bar}$ , $V_C = 50 \text{ m/min}$ (c,e) $P = 12 \text{ bar}$ and (d,f) $P = 70 \text{ bar}$ , $V_C = 70 \text{ m/min}$ (g) $P = 12 \text{ bar}$ and (h) $P = 70 \text{ bar}$ . ....	161
Figure 4-52: FG RR1000 chip and serration formation under high pressure rake and flank cooling; (a-d) $V_C = 30 \text{ m/min}$ . (e-f) $V_C = 50 \text{ m/min}$ , (g-h) $V_C = 70 \text{ m/min}$ . ....	162
Figure 4-53: Effect of cooling strategy performance on tool rake face wear mechanisms when machining FG RR1000. ....	165
Figure 4-54: Spectroscopy analysis in weight% of worn tool used when machining FG RR1000 at $V_C = 70 \text{ m/min}$ under low pressure rake cooling conditions. ....	165
Figure 4-55: Observations when machining under rake and flank cooling at $V_C = 30 \text{ m/min}$ ; Worn tool (a-b) $P = 12 \text{ bar}$ and (c) $P = 70 \text{ bar}$ , (d) Chip formation at $P = 12 \text{ bar}$ . ....	166
Figure 4-56: Effect of feed rate on surface finish and pick-up deposition when dry machining FG RR1000 at $V_C = 50 \text{ m/min}$ , $a_p = 0.24 \text{ mm}$ and $r_n = 1.5 \text{ mm}$ ; (a) Full cutting length, Pick-up (b) $f = 0.12 \text{ mm/rev}$ , (c) $f = 0.18 \text{ mm/rev}$ and (d) $f = 0.24 \text{ mm/rev}$ . ....	173

Figure 4-57: Effect of tool radius and tool edge rounding on chip and serration formation when dry turning FG RR1000 at $V_C = 50$ m/min, $a_p = 0.24$ mm and $f = 0.12$ mm/rev; (a,c) $r_n = 1.5$ mm and $r_e = 35 \mu\text{m}$ , (b,d) $r_n = 3.0$ mm and $r_e = 35 \mu\text{m}$ , (e-h) $r_n = 3.0$ mm and $r_e = 15 \mu\text{m}$ .....	174
Figure 4-58: Effect of feed rate on chip formation when dry turning FG RR1000 at $V_C = 50$ m/min, $a_p = 0.24$ mm, $r_n = 1.5$ mm and $r_e = 35 \mu\text{m}$ ; $f = 0.24$ mm/rev (a) Chip morphology, (c) Chip cross-section and (e) Serrations, $f = 0.36$ mm/rev (b) Chip morphology, (d) Chip cross-section and (f) Serrations.....	175
Figure 4-59: Effect of feed rate and tool edge rounding on chip formation when dry turning FG RR1000 at $V_C = 50$ m/min, $a_p = 0.24$ mm and $r_n = 3.0$ mm; $f = 0.24$ mm/rev (a) $r_e = 35 \mu\text{m}$ and (b) $r_e = 15 \mu\text{m}$ , $f = 0.36$ mm/rev (c) $r_e = 35 \mu\text{m}$ and (d) $r_e = 15 \mu\text{m}$ .....	176
Figure 4-60: Chip and serration morphology when machining FG RR1000 at $V_C = 50$ m/min, $f = 0.12$ mm/rev, $r_n = 3.0$ mm and $r_e = 15 \mu\text{m}$ with 1105 coating grade; (a) $a_p = 0.24$ mm, (b) $a_p = 0.12$ mm.....	178
Figure 4-61: Chip and serration morphology when machining FG RR1000 at $a_p = 0.12$ mm, $f = 0.12$ mm/rev, $r_n = 3.0$ mm and $r_e = 15 \mu\text{m}$ with uncoated tool; $V_C = 50$ m/min (a) Chip morphology, (c) Serrations and (e) Chip cross-section, $V_C = 30$ m/min (b) Chip morphology, (d) Serrations and (f) Chip cross-section.....	179
Figure 4-62: Effect of depth of cut on FG RR1000 chips machined dry with S05F coated tools at $V_C = 30$ m/min, $f = 0.12$ mm/rev, $r_n = 3.0$ mm and $r_e = 15 \mu\text{m}$ ; (a) $a_p = 0.12$ mm, (b) $a_p = 0.24$ mm.....	181
Figure 4-63: Effect of depth of cut and feed rate on FG RR1000 chips machined dry with S05F coated tools at $V_C = 30$ m/min, $r_n = 3.0$ mm and $r_e = 15 \mu\text{m}$ ; $f = 0.24$ mm/rev (a,c) $a_p = 0.12$ mm and (b,d) $a_p = 0.24$ mm, $f = 0.36$ mm/rev (e) $a_p = 0.12$ mm and (f) $a_p = 0.24$ mm.	182

Figure 5-1: (a) Chip formation in orthogonal turning, Salem et al. (2012); (b) Cold rolled material strips, Dodd and Boddington (1980).....191

Figure 5-2: Effect of cooling strategy and cutting speed on FG RR1000 chip serrations produced at  $a_p = 0.25$  mm,  $f = 0.12$  mm/rev,  $r_n = 1.5$  mm and  $r_e = 35$   $\mu\text{m}$ . ....193

# LIST OF TABLES

Table 2-1: Composition of wrought superalloys balanced with Ni % weight, Reed (2006)....	11
Table 2-2: RR1000 mechanical properties, Qiu (2010).....	16
Table 2-3: Summary of surface material deposit observations in literature. ....	70
Table 2-4: Summary of chip edge serration observations in literature. ....	71
Table 3-1: Machined superalloys mechanical properties; FG and CG RR1000, Qiu (2010), Alloy 718, Donachie and Donachie (2002). .....	76
Table 3-2: List of machining parameters used in the dry turning trials.....	77
Table 3-3: Material removal rates ( $Q \text{ mm}^3/\text{sec}$ ) used in the minimum cooling trials.....	78
Table 3-4: List of machining parameters used in the LP cooling trials. ....	79
Table 3-5: List of machining parameters used in Phase 3 trials. ....	81
Table 3-6: List of machining parameters used in the Phase 4 trials. ....	83
Table 4-1: Average subsurface deformation depth of dry machined superalloys. ....	95
Table 4-2: Chip formation geometry data for dry machined FG RR1000.....	104
Table 4-3: Chip formation geometry data for dry machined CG RR1000. ....	106
Table 4-4: Chip formation geometry data for dry machined Alloy 718. ....	111
Table 4-5: FG RR1000 chip formation geometry data for minimum cooling trials.....	134
Table 4-6: FG RR1000 chip formation data for LP cooling conditions. ....	145
Table 4-7: CG RR1000 chip formation data for LP cooling conditions.....	148
Table 4-8: Alloy 718 chip formation data for LP cooling conditions.....	148
Table 4-9: Effect of cooling performance on FG RR1000 chip formation data. ....	164
Table 4-10: Effect of cooling performance on FG RR1000 machining loads.....	167

Table 4-11: FG RR1000 chip formation data at variable feed rate, tool radius and tool edge rounding for fixed $V_C = 50$ m/min and $a_p = 0.24$ mm. ....	177
Table 4-12: FG RR1000 chip formation data when using different tool grades. ....	180
Table 4-13: FG RR1000 chip formation data at variable feed rate and depth of cut for fixed $V_C = 30$ m/min, $r_n = 3.0$ mm and $r_e = 15 \mu\text{m}$ . ....	183
Table 4-14: Effect of feed rate, tool radius and tool edge rounding on FG RR1000 machining loads at fixed $V_C = 50$ m/min and $a_p = 0.24$ mm. ....	184
Table 4-15: Effect of feed rate and depth of cut on FG RR1000 machining loads at fixed $V_C = 30$ m/min, $r_n = 3.0$ mm and $r_e = 15 \mu\text{m}$ . ....	184
Table 5-1: Recommended machining parameters for pick-up free surfaces and surface roughness $R_a \leq 0.8 \mu\text{m}$ . ....	194
Table 5-2: Recommended machining parameters for pick-up free surfaces and surface roughness $R_a \leq 1.2 \mu\text{m}$ . ....	194

# NOMENCLATURE

$a_p$	depth of cut (mm)	$\alpha$	tool rake angle ( $^{\circ}$ )
CCR	ratio of cut and uncut chip thickness	$\gamma$	shear strain
CG	coarse grain microstructure	$\dot{\gamma}$	shear strain rate
$d_s$	primary serration spacing ( $\mu\text{m}$ )	$\Delta y$	shearing zone thickness
EL	elongation to failure (%)	$\varepsilon$	measurement margin of error
$f$	feed rate (mm/rev)	$\lambda$	coolant flow rate (l/min)
$F$	resultant machining force (N)	$\varphi$	machining shear angle ( $^{\circ}$ )
$F_C$	cutting force (N)	$\sigma_{0.2}$	tensile strength (MPa)
$F_F$	feed force (N)		
FG	fine grain microstructure		
$F_P$	push-off force (N)		
$h_s$	maximum serration thickness ( $\mu\text{m}$ )		
$h_{\max\_c}$	maximum cut chip thickness ( $\mu\text{m}$ )		
$h_{\max\_u}$	maximum uncut chip thickness ( $\mu\text{m}$ )		
P	coolant pressure (bar)		
Q	material removal rate ( $\text{mm}^3/\text{sec}$ )		
$r_e$	tool edge rounding radius (mm)		
$r_n$	tool radius (mm)		
S	cut chip cross-section area ( $\text{mm}^2$ )		
t	orthogonal uncut chip thickness ( $\mu\text{m}$ )		
$t_c$	orthogonal cut chip thickness ( $\mu\text{m}$ )		
UTS	ultimate tensile strength (MPa)		
V	chip speed (m/min)		
$V_C$	cutting speed (m/min)		
$V_S$	shearing speed (m/min)		
w	uncut chip width (mm)		

# 1 PREFACE

## 1.1 PROJECT BACKGROUND

Rolls-Royce plc's most innovative jet engine high pressure critical rotative components are manufactured using the material RR1000, currently considered the most advanced in-service polycrystalline powder metallurgy nickel based superalloy. RR1000 was engineered to maintain its enhanced mechanical properties at high heat environments, allowing the compressor and turbine discs to operate at least 25 °C higher than its predecessor in Rolls-Royce plc production, Udimet 720Li. These capabilities have improved the overall in-service system efficiency in terms of power output, fuel consumption and emission reduction, but at a cost of reduced manufacturing productivity as the alloy has poor machining performance.

The potential for future RR1000 machining optimisation is limited as poor tool life performance and strict production quality standards, set for powder metallurgy alloys, dictate the use of specific machining parameter combinations for finishing the component's low tolerance detail features, Figure 1-1(a-d). Adding to these production complexities, the specific machining operation window validated during the final preproduction Manufacturing Capability Readiness Level (i.e. MCRL6) favours the occurrence of parent material deposits on the finish turned surfaces, Figure 1-1(e-f). Rolls-Royce plc uses the term "pick-up" to describe this defect, which is believed to increase the risk of probable compromise in fatigue life and until recently was the major concern of non-conformance to the production standards for more than 30% of RR1000 finished components.

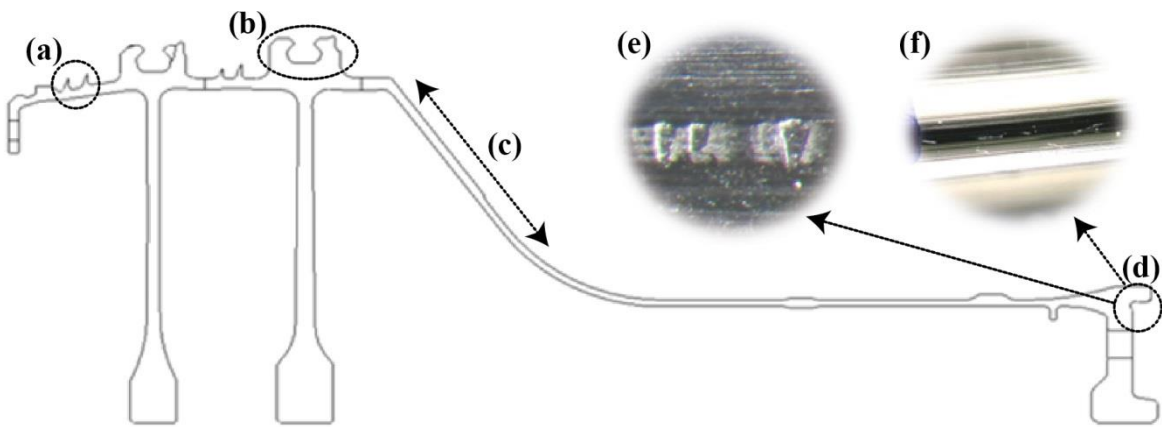


**Figure 1-1: High pressure compressor assembly; (a) Seal fins, (b) Circum groove, (c) Cone profile, (d) Internal spigot profile, (e-f) Typical pick-up examples as detected during binocular inspection.**

The sensitivity of RR1000 to pick-up puts significant pressure on production with high non-quality cost and extended lead delivery times, due to added operations including further inspection and correction of non-conformant components, increasing the risk of low production efficiency compared to other superalloys. This project focused on pick-up investigation under the general scope of MCRL7 to MCRL9, concerned with the RR1000 machining optimisation, accommodating activities that assessed and implemented a series of machining solutions targeting the optimisation of production strategy and pick-up reduction. The experiments and analysis described in this thesis aim to capture the essences of the step-by-step process followed in order to understand the formation and deposition mechanism of pick-up; and investigate possible machining solutions that may reduce or eliminate the defect, while fulfilling the minimum production requirements for these critical rotative components. The knowledge was also captured in Rolls-Royce plc minimum machining standards in order to apply the improvements when machining future new high strength alloy systems.

## 1.2 PROJECT SCOPE AND HYPOTHESIS

This project aims to identify the origin of pick-up and investigate the mechanisms favouring its deposition based on the research hypothesis that “the defect is related to the chip formation mechanism controlled by the adopted machining strategy and cutting conditions”. The main argument states that if parent material was to be found deposited on the finished surface after being machined-off, then it must have been originated from the chip. This indicates that the uncommon phenomenon of serration formation at the chip’s trailing edge detected in RR1000 finish turning operations is of great interest and serves as prime suspect mechanism in this investigation.

The experiments were designed to investigate the effect of machining parameters and material properties on pick-up occurrence, both in and out of the RR1000 production line validated conditions, aiming to link the defect severity to factors affecting chip deformation and chip serration formation. A methodology is also developed to quantify and assess the effect of machining on RR1000 chip geometry, aiming to enhance the knowledge of the chip formation physics favouring the deposition of pick-up. Finally, understanding the conditions at the chip-tool-surface interaction zone should lead to the assessment and validation of machining strategies that would reduce pick-up and optimise the RR1000 production line.

### 1.3 THESIS OUTLINE

Chapter 2 presents the literature review relevant to this machining project, covering briefly the microstructure of polycrystalline superalloys, specifically referring to the characteristics of RR1000 variants. Furthermore, it focuses on outlining the principles of chip formation and the challenges in high strength material machining, whilst identifying possible leads related to the phenomenon of pick-up.

Chapter 3 covers in detail the experimental investigation process, including the selection basis of the assessed parameters and conditions. This section also reports both the equipment and methodologies used for analysing the collected data.

Chapter 4 documents the experimental results extracted by using a range of microscopy techniques (i.e. SEM, 3D scanning etc.) to investigate chip formation and surface integrity. The discussion sections link the chip formation data and optical observations to findings identified in literature, in order to highlight trends in pick-up occurrence and RR1000 chip formation mechanics.

Chapters 5 and 6 summarise the major discussion points and extract conclusions based on the experimental outcomes, whilst suggesting improved machining strategies aiming to reduce pick-up and optimise RR1000 production.

Chapter 7 recommends possible future work that would enhance the learning, based on knowledge gaps identified in the duration of the project.

## 2 LITERATURE REVIEW

### 2.1 INTRODUCTION

Jet engines are designed based on Brayton's thermodynamic cycle principle, Mair and Birdsall (1998), which defines the possible maximum output energy extracted from an ideal three stage heat system consisting of a compressor in series with a combustor and turbine. Based on this principle, in a jet engine pressurised air leaving the compressor mixes up with fuel and ignites in the combustion chamber producing high energy gases, which then expand in the turbine releasing the system's energy and thus propelling the aircraft, Figure 2-1.

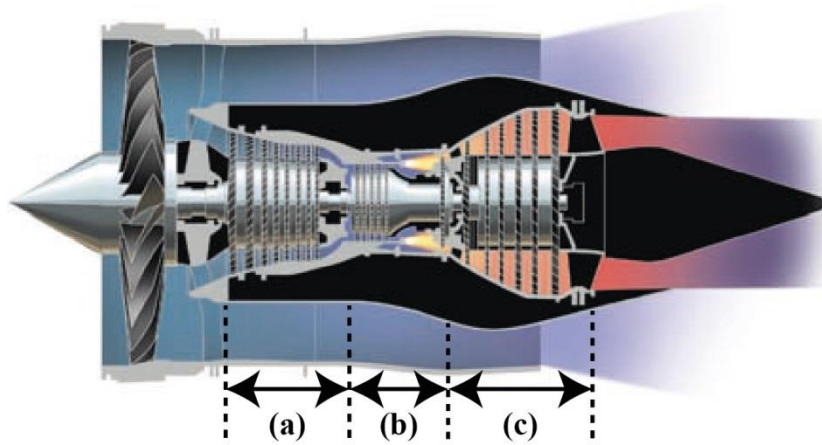


**Figure 2-1: Rolls-Royce Trent family high bypass turbofan assembly illustration; (a)**

**Compressor, (b) Combustion chamber, (c) Turbine. {Courtesy of Rolls-Royce plc}**

Modern jet engines utilise both sophisticated design features (i.e. multi-stage compressor and turbine assemblies, Rolls-Royce three shaft engine configuration etc.) and cutting edge engineering solutions (i.e. integrated turbine blade cooling etc.) to harvest maximum power at

higher efficiency. Figure 2-2 shows that greater performance is ultimately driven by the turbine system operating temperature, though due to the current jet engine configuration reaching its full design potential, further improvement depends on the capabilities of materials available for maintaining structural integrity within these high pressure and high heat systems, National Academy of Sciences (2006).

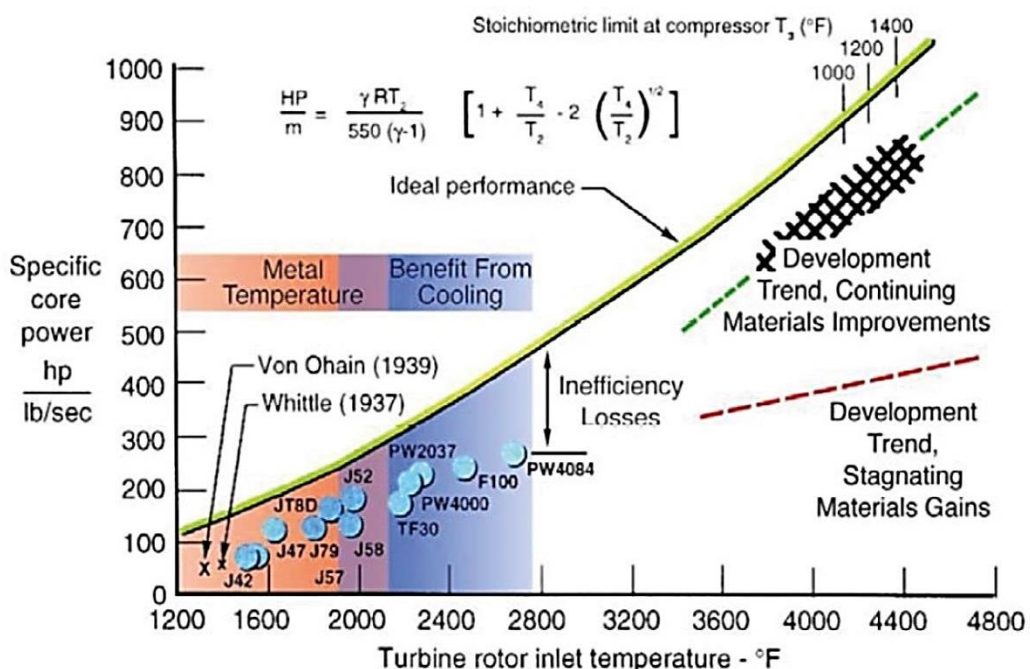


**Figure 2-2: Factors affecting the jet engine thermodynamic efficiency, National Academy of Sciences (2006).**

In practice, the properties of materials selected in jet engine manufacturing are a key restriction for even hotter in-service operation conditions (i.e. currently temperature peaking around  $2000^{\circ}\text{C}$  in the combustion chamber); whilst the cost of developing/selecting more advanced alloys often proves unviable. Figure 2-3 shows the range of nickel based superalloys Rolls-Royce plc introduced in the production of critical rotative jet engine components over the years; highlighting the relationship between their temperature operation capabilities and production cost. RR1000 owes its superiority to the use of exotic alloying elements and more advanced production techniques (i.e. powder metallurgy processing),

raising the pre-machining cost of these components to 320% higher compared to those made of the conventional superalloy Inconel 718, Kappmeyer et al. (2012). Therefore, significant effort has been put into developing advanced production processes to reduce overall cost, including forging RR1000 to a rough component pre-form shape in order to limit wastage and machining time, Figure 2-4, however further manufacturing advances are essential to optimise the RR1000 component production line.

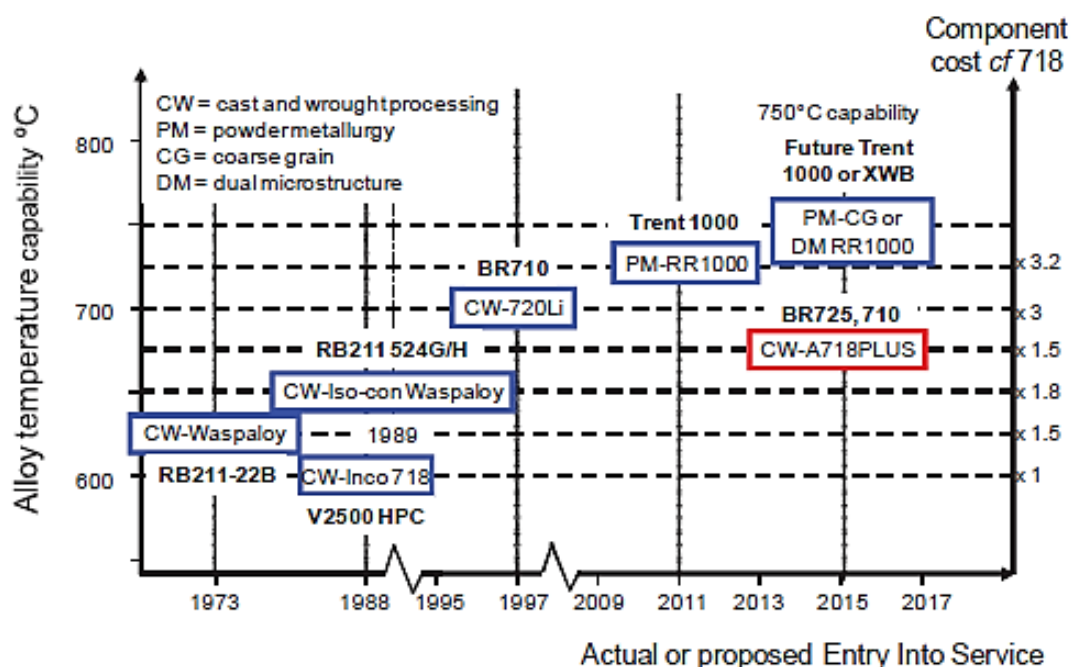


**Figure 2-3: Superalloys used by Rolls-Royce in the manufacturing of high pressure rotative components, Kappmeyer et al. (2012).**

RR1000 machining is further complicated by stricter production standards set for powder metallurgy alloys, compared to those for conventional alloys, in order to ensure enhanced in-service fatigue life. These include:

- Sub-surface strain and distortion to be lower than 10  $\mu\text{m}$ , with no white layer.
- Surface roughness Ra to be lower than 0.8  $\mu\text{m}$ .
- No redeposited material on the finished surface.

Fulfilling these high quality standards has proven detrimental for productivity as the specific machining parameter combinations used to produce the required surface finish results in extensive pick-up occurrence; leading to redundant and costly correction operations. Adding this to RR1000's low machinability and aggressive tool wear rates makes machining these components cost competitive a challenge; setting the foundations for the research conducted in this project. The so-called RR1000 "sensitivity" to pick-up and the defect's rare occurrence in other production lines focused the following literature review on identifying the ways RR1000 differs as a material (i.e. microstructure and mechanical characteristics) from other superalloys and the ways the selected machining strategy may favour pick-up occurrence based on the project hypothesis.

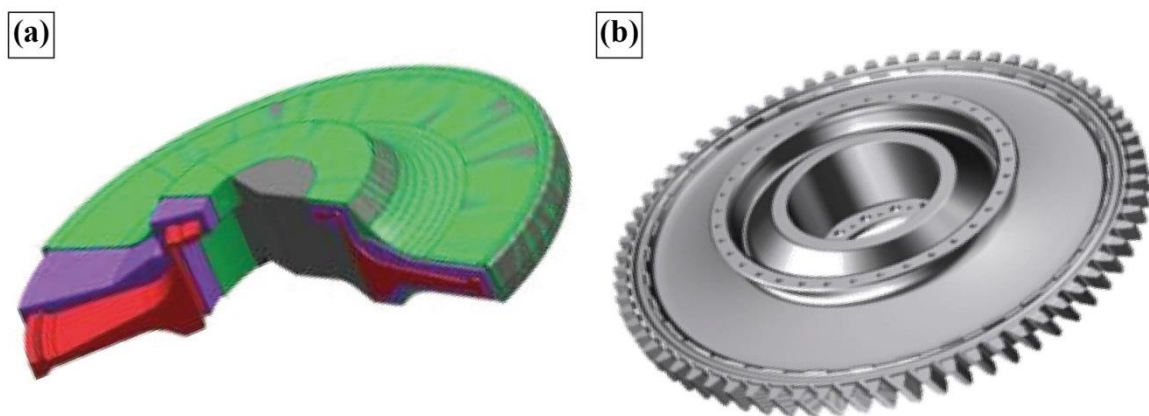


**Figure 2-4: High pressure turbine disc; (a) Forged preform, (b) Finished component,**  
**Kappmeyer et al. (2012).**

## 2.2 NICKEL BASED SUPERALLOYS

### 2.2.1 Introduction

Superalloys are a family of high-temperature metallic alloying systems able to maintain their enhanced static properties, like high strength and toughness, at high temperatures, Figure 2-5. They can also operate in oxidising and corrosive environments and maintain high creep resistance during low cycle loading; making them an ideal material choice for the high heat and high pressure regions of a jet engine. This literature review section reports on the microstructure and mechanical properties of modern polycrystalline nickel based alloys, especially RR1000, focusing on the effect of targeted and no-targeted alloy characteristics on machinability and production efficiency.

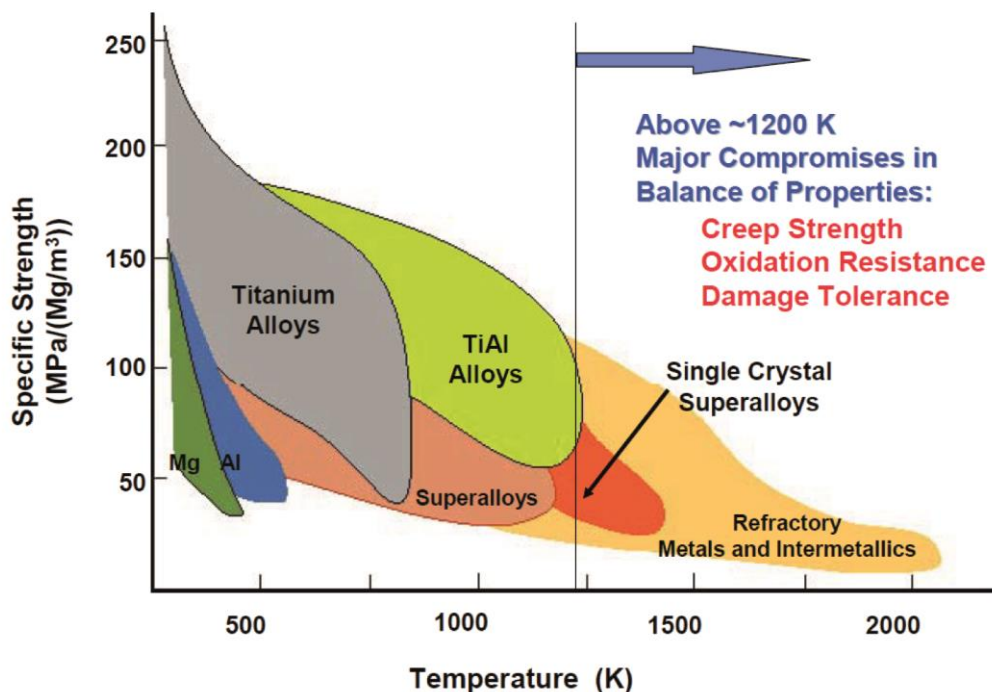


**Figure 2-5: Advanced high strength materials, National Academy of Sciences (2006).**

## 2.2.2 Microstructure and Mechanical Properties of Polycrystalline Superalloys

Nickel (Ni) is the metallic element most commonly used as base material for superalloys due its low diffusion rate and the fact that no phase transformation takes place until it reaches its high melting point (i.e.  $\approx 1455^{\circ}\text{C}$ ), providing the alloy with stability at elevated temperatures. Its face centred cubic (FCC) crystal structure, Figure 2-6, results in the alloy's good ductility and toughness; and while other metals also fit these requirements, they are denser compared to Ni that has density of  $8907 \text{ kg/m}^3$ , and far more expensive, as they belong in the platinum metal family. If other crystal structure metals were to be considered, cobalt (Co) is a good candidate with hexagonally closed-packed (HCP) structure and chromium (Cr) with body-centered cubic (BCC) structure, though cost and brittle characteristics respectively make them better fit as alloying elements for superalloys, Reed (2006).

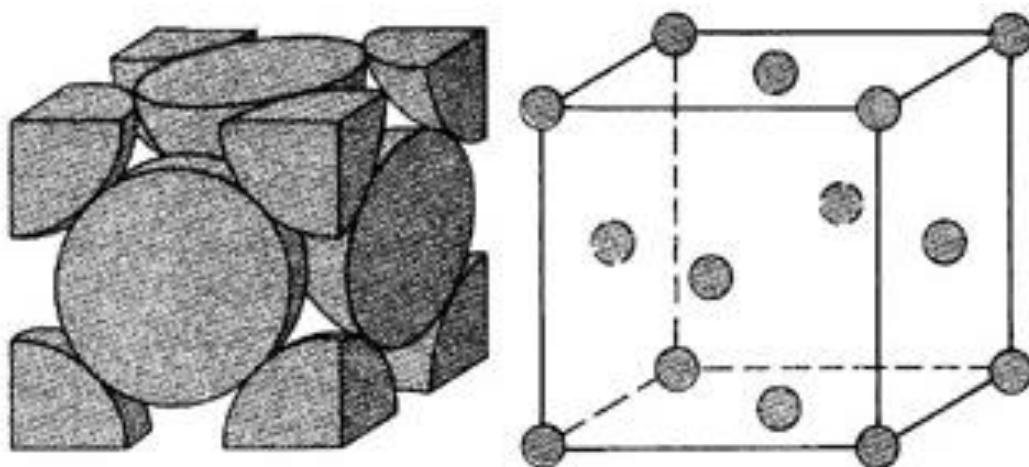


**Figure 2-6: Face centred cubic crystal structure (FCC), Reed (2006).**

Table 2-1 presents the composition of nickel based superalloys used in jet engine production lines, with elements like Co, Cr and molybdenum (Mo) used in addition to Ni to stabilise the alloy matrix. In some cases iron (Fe) is used instead of Co (i.e. for the nickel-iron based Inconel 718) resulting in the alloy's lower service operation temperature but also

reducing its production cost as previously discussed in Figure 2-3. Elements like aluminium (Al), titanium (Ti), tantalum (Ta) and niobium (Nb) bond with Ni and form an ordered phase, coherent with the matrix, called gamma prime ( $\gamma'$ ). The corresponding phase for the Ni-Fe based superalloys is called gamma double prime ( $\gamma''$ ).

**Table 2-1: Composition of wrought superalloys balanced with Ni %weight, Reed (2006).**

	Cr	Co	Fe	Mo	Nb	Al	Ti	Ta	Hf	W	Zr	C	B
RR1000	15.0	18.5		5.0	1.1	3.0	3.6	2.0	0.5		0.06	0.027	0.015
Udimet 720Li	16.0	15.0		3.0		2.5	5.0			1.25	0.05	0.025	0.018
Waspaloy	19.5	13.5		4.3		1.3	3.0					0.080	0.006
Rene 88DT	16.0	13.0		4.0	0.7	2.1	3.7			4.00	0.03	0.030	0.015
Inconel 718	19.0		18.5	3.0	5.1	0.5	0.9					0.040	

Ordered phase precipitates are known to facilitate part of the alloy's strength and thus controlling both their size and volume fraction is crucial for optimising the mechanical properties, Jackson and Reed (1999). The solution and heat treatment temperature defines both the grain structure and size of the large primary  $\gamma'$  precipitates, whilst the amount of precipitate elements in solution and cooling rate affect the formation of smaller secondary and tertiary  $\gamma'$  precipitates, Figure 2-7. The authors found that ageing the tertiary  $\gamma'$  precipitates to a preferred size increases the alloy's resistance to dislocation movements, optimising the tensile strength. The phenomenon was explained by Preuss et al. (2008) that found smaller tertiary  $\gamma'$  precipitates will produce weak dislocation couplings due to the formation of smaller dislocation bowing, Figure 2-8(a), compared to the strong dislocation couplings formed by optimum sized precipitates, which enhance the load transfer from the matrix to the ordered phase, Figure 2-8(b).

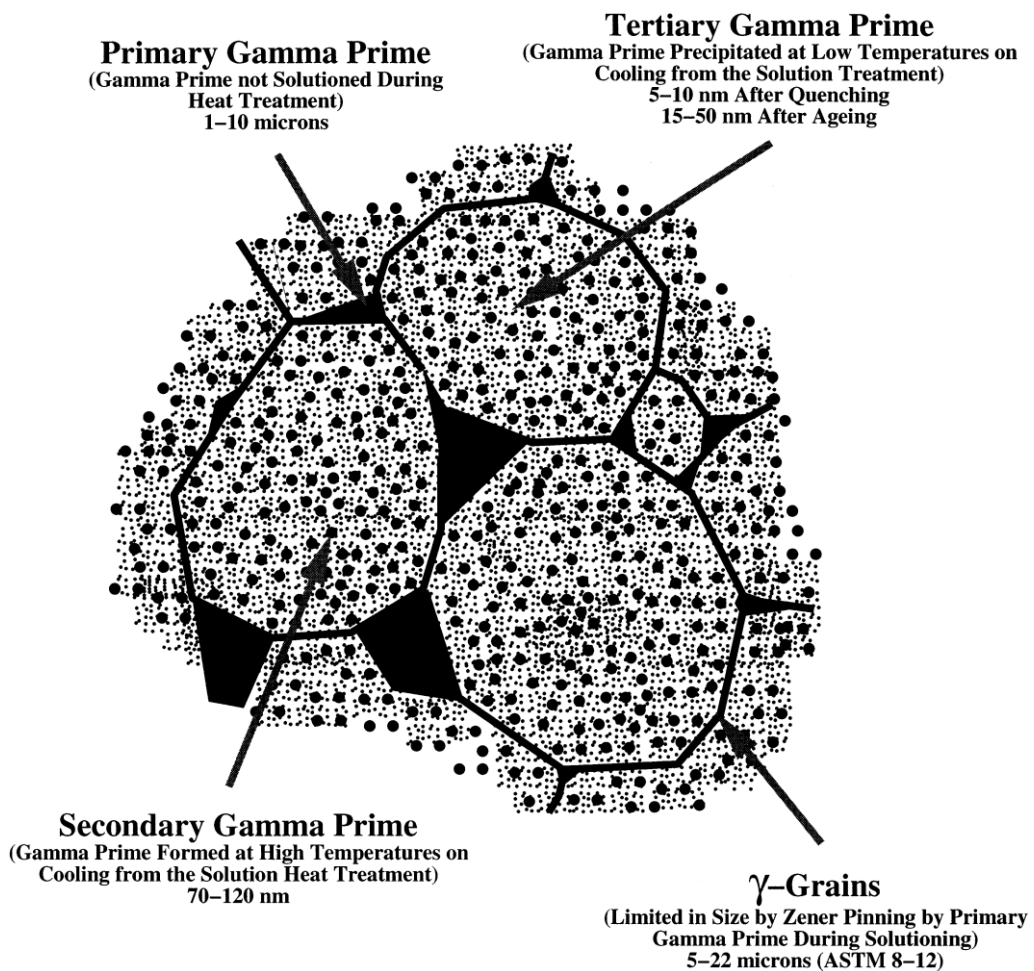


Figure 2-7: Gamma prime precipitation illustration of Udimet 720Li microstructure,

Jackson and Reed (1999).

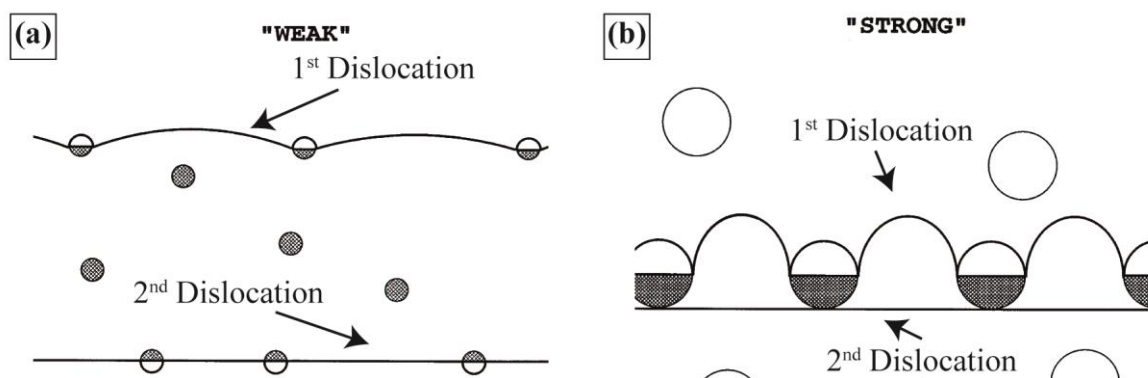
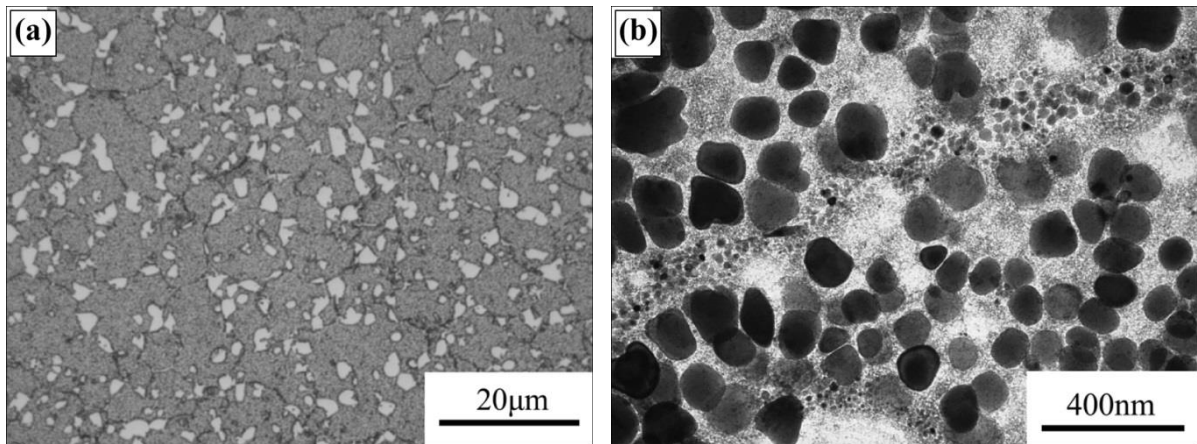


Figure 2-8: Effect of tertiary gamma prime precipitate size on dislocation movement;

(a) Weak coupling, (b) Strong coupling, Jackson and Reed (1999).

In addition to high tensile strength, high  $\gamma'$  volume fraction alloys also exhibit elevated crack growth rates that limit their fatigue life, and thus both the RR1000 composition and microstructure were manipulated in order to balance between low temperature strength and fatigue crack growth, Hardy et al. (2004). This was achieved by increasing the content of Co that promoted the partition of Al, Ti and Ta to  $\gamma'$ , compared to its predecessor U720Li, whilst minimising their content; which limited the overall  $\gamma'$  volume fraction required to achieve the preferred alloy strength. Creep resistance and fatigue life were improved by limiting the Cr content and adding carbon (C), boron (Bo) and zirconium (Zr), whilst adding hafnium (Hf) prevented the extensive presence of carbides,  $M_{23}C_6$  (i.e. a controversial intermetallic phase that benefits creep resistance, though if in excess limits fatigue performance). Furthermore, controlling the RR1000 powder size and powder consolidation route (i.e. hot isostatic pressing and subsequent hot forging processes) below  $\gamma'$  solvus temperature (i.e. 1160 °C), hot extrusion (i.e. to eliminate the effect of powder prior particles boundaries-PPBs) and final quality heat treatment results in fine grain RR1000 material (47%  $\gamma'$  volume fraction) with improved microstructure uniformity compared to cast and wrought alloys, Figure 2-9, Mitchell et al. (2004) and May et al. (2011). All these characteristics add-up to RR1000 exhibiting the enhanced mechanical performance of other superalloys (e.g. U720Li) at higher temperatures, Figure 2-10, making this alloy the primary disc alloy option in Rolls-Royce plc production.

RR1000 is also unique in that a component can be processed to go into service with different microstructures at different disc locations, targeting specific in-service performance and addressing the varying mechanical and thermal stresses acting along the components cross-section, Mitchell et al. (2008). The authors produced fine grain (FG) RR1000 at the bore, which operates at the highest stresses and lower temperatures, following a heat



**Figure 2-9: Fine grain RR1000 microstructure uniformity; (a) Primary gamma prime and (b) Secondary and tertiary gamma prime, Mitchell et al. (2004).**

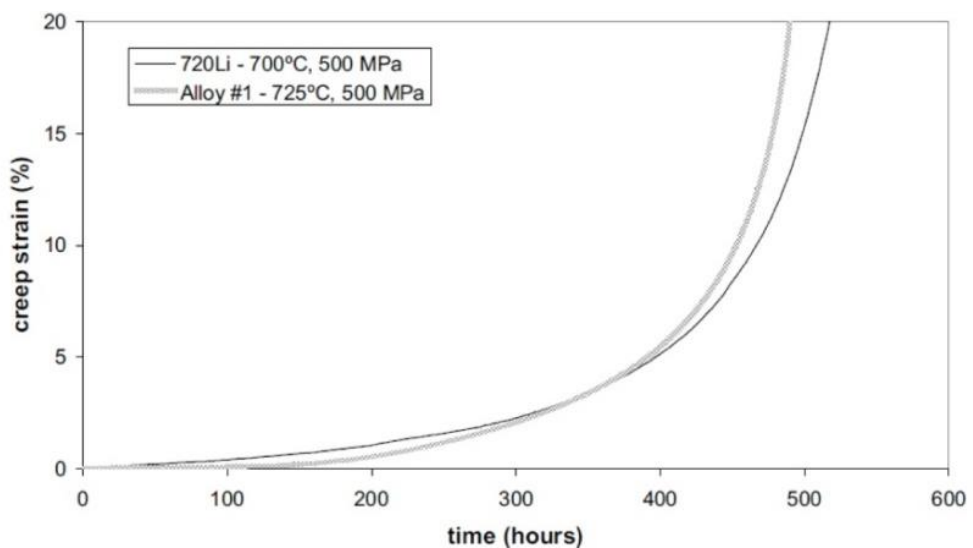


**Figure 2-10: Creep performance comparison between RR1000 and Udimet 720Li, Hardy et al. (2004).**

treatment below the primary  $\gamma'$  solvus temperature (i.e.  $\approx 1120^{\circ}\text{C}$ ) that resulted in 12-16 %volume fraction of primary  $\gamma'$  precipitates (size 1-2  $\mu\text{m}$ ) and restricted grain growth to ASTM 12-11 (average grain size 6-8  $\mu\text{m}$ ), Figure 2-11(a). Coarse grain (CG) RR1000 was produced at the rim, which operates at higher temperatures under lower mechanical stress, following a heat treatment above the primary  $\gamma'$  solvus temperature (i.e.  $\approx 1180^{\circ}\text{C}$ ) resulting in ASTM 7-3 (average grain size 32-135  $\mu\text{m}$ ), Figure 2-11(b). Figure 2-11(c) shows that FG

was engineered for optimum fatigue performance/life and acceptable tensile strength, compared to the CG that targeted improved crack propagation resistance and optimum creep performance, Figure 2-11(d).

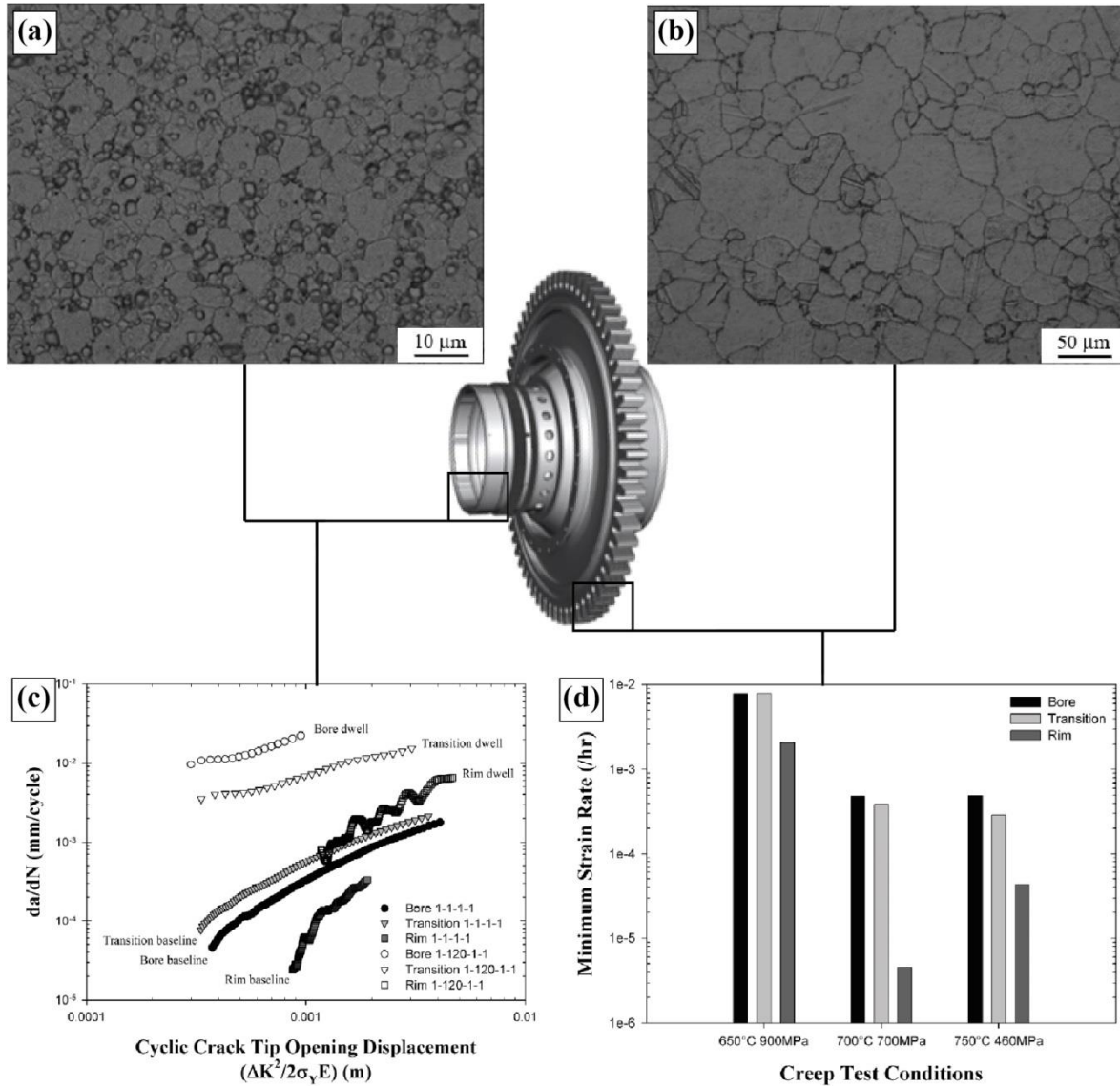


**Figure 2-11: RR1000 dual microstructure turbine disc; (a) FG RR1000, (b) CG RR1000, (c) Fatigue crack growth performance assessment at 700°C and (d) Creep performance assessment, Mitchell et al. (2008).**

Overall significant compromises are required to balance the mechanical properties and achieve improved performance at higher operating temperature; this does, however, mean other non-targeted properties may also vary to different levels. For example, small variations in grain size (i.e. ASTM 10-9 (11-16  $\mu\text{m}$ ) compared to ASTM 12-11 (6-8  $\mu\text{m}$ )) show little effect on tensile strength at room temperature, in the range of 1500-1600 MPa, but a more significant influence on creep resistance, with the finer grain size experiencing higher crack growth rates at elevated temperatures as demonstrated by Hardy et al. (2004). Furthermore, Qiu (2010) showed that the extruded FG material (i.e. ASTM 12-11) exhibits tensile elongation to failure around 10% for both room temperature and 700 °C, in contrast to the CG material (i.e. ASTM 8-7) that experiences more than double the elongation to failure for both temperature conditions, Table 2-2. Banik et al. (2004) reported similar findings with FG RR1000 exhibiting 15-20% less tensile elongation to failure compared to CG Rene 88, showing that ductility is rarely a concern in CG materials (i.e. conventionally processed superalloys). Adding these to the finding by Guédou et al. (2008) that also reported low ductility for FG variations of the high strength powder metallurgy nickel based alloy N18, shows that the phenomenon is linked to the very fine grain structure capability of the powder processed superalloys.

**Table 2-2: RR1000 mechanical properties, Qiu (2010).**

<b>Conditions</b>	<b>20°C</b>			<b>700°C</b>		
	$\sigma_{0.2}$ (MPa)	UTS (MPa)	EL (%)	$\sigma_{0.2}$ (MPa)	UTS (MPa)	EL (%)
	<b>FG RR1000</b>	1075	1575	$\geq 10$	980	1300
<b>CG RR1000</b>	1075	1573	22	963	1453	22

### 2.2.3 Effect of Mechanical Properties and Microstructure in Machining

The mechanical properties targeting enhanced in-service performance, achieved through alloying and microstructure manipulation, are also the reason high strength materials (i.e. titanium or nickel based alloys) are considered difficult to machine. In addition to elevated strength, low machinability materials are usually characterised by high hardness and low thermal conductivity, which factor in high mechanical and thermal loads as well as accelerated tool wear rates during cutting, Ezugwu et al. (1999). These phenomena restrict the machining strategy window, with lower machinability materials being machined at slower cutting speeds and lower material removal rates, Figure 2-12, in order to optimise product quality; proving detrimental for productivity (i.e. RR1000 production line being a valid example).

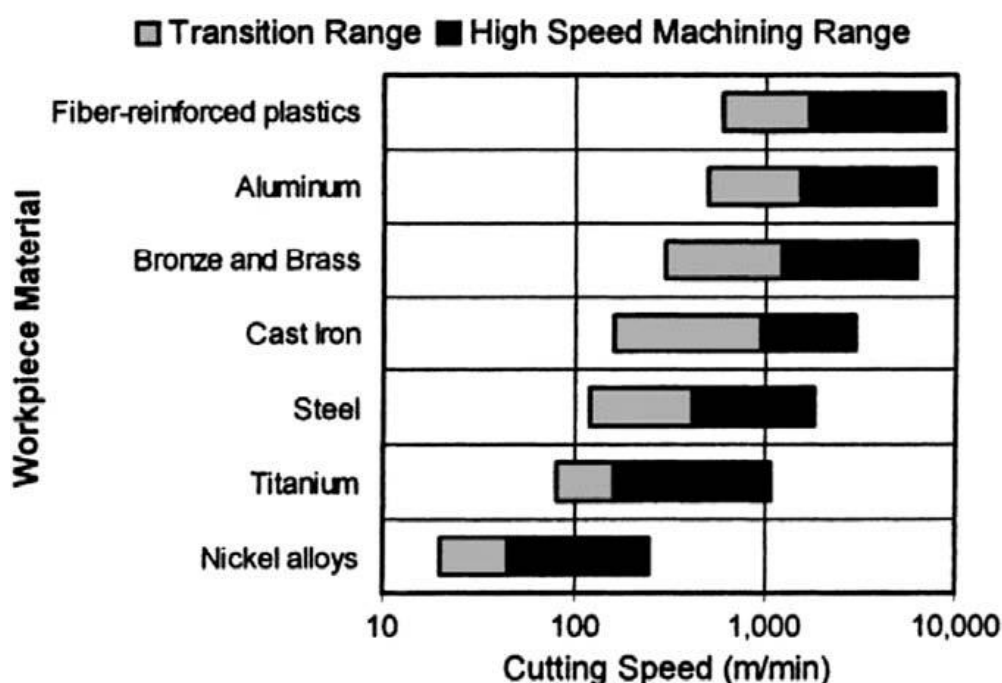


**Figure 2-12: Cutting speeds used for machining different material categories, Schulz and Moriwaki (1992).**

Arrazola et al. (2009) demonstrated the above effect by comparing the machinability of titanium alloys, showing that for identical cutting conditions the stronger, harder and less ductile alloy Ti555.3, produced higher machining forces and different chip formation characteristics than the well-known titanium alloy Ti6Al4V, whilst exceeding the set tool wear criterion when machined at half the cutting speed. When hard turning steel, Poulachon and Moisan (2000) also identified variation in chip morphology, at identical cutting parameters, with decreasing the workpiece's elongation to failure and increasing its hardness and strength (i.e. transformation from continuous to semi-continuous segmented chip to discontinuous chip), Figure 2-13, confirming the integral role of workpiece mechanical properties in chip formation and finished surface deformation. The authors also observed chip deformation mechanism transformation due to increasing machining heat loads at higher cutting speed, a phenomenon proving that machining parameters control the cutting conditions, thus affecting the performance/machinability of alloys and vice versa.

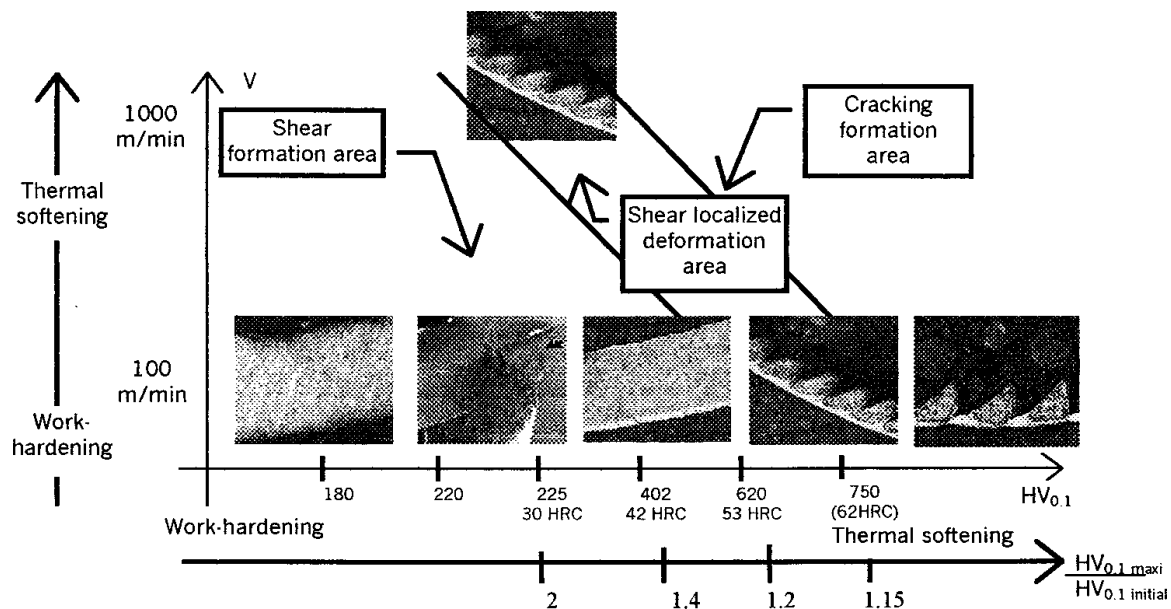


**Figure 2-13: Effect of mechanical properties and cutting speed on 100Cr6 steel chip morphology, Poulachon and Moisan (2000).**

Olovsjö et al. (2010a, 2010b) reported similar findings in nickel-based superalloy machining, as turning the lower strength alloy Waspaloy resulted in better tool life performance (i.e. at least 50% less flank wear) compared to that of the stronger alloy Inconel 718, even though both operations produced similar mechanical machining forces. It was also found that increasing hardness accelerates the flank wear rates independently of the microstructure, whilst varying grain size affected the chip geometry and sub-surface integrity. These phenomena indicate similar deformation characteristics for superalloys to those for steel and titanium alloy machining, suggesting that both the microstructure and targeted or non-targeted mechanical properties have key role in the chip formation mechanism and thus probably have a major role in pick-up occurrence and severity when turning RR1000.

## 2.3 METAL CUTTING

### 2.3.1 Introduction

Metal cutting is a term that defines every machining operation (i.e. milling, turning, drilling, grinding etc.) that requires material removal in order to reform a metal workpiece into a newly shaped component. This involves shearing deformation taking place on the top layer of the workpiece surface, due to its interaction with the cutting tool, and depending on the production stage can be categorised as:

- Roughing cuts, used to give shape to a preform. Aggressive cutting parameters are usually a characteristic at this stage as the objective is removing the majority of excess material at maximum efficiency.
- Semi-roughing cuts, used to prepare the surface for the finishing cuts. Less aggressive parameters are used, compared to roughing, in order to remove material at low tolerance.
- Finishing cuts, used to produce the final product surface. Machining parameters are the least aggressive at this stage in order to achieve high quality product finish according to specific production standards.

The finished surface is the only useful product of machining operations and thus the interest of both the industry and academia is focused on optimising surface integrity, due to its effect on the performance of a component in service. Chips on the other hand are considered the waste by-products, currently presenting no significant interest for research, even though their formation mechanism affects power consumption and controls both the mechanical and thermal loads of the cut, which are defining factors for surface quality.

With pick-up being a surface integrity concern and the thesis hypothesis possibly linking the defect to chip morphology, the following literature review section investigates the basic chip formation physics in order to understand the machining conditions favouring pick-up occurrence in RR1000 finish turning operations.

### **2.3.2 Chip Formation in Turning Operations**

#### *2.3.2.1 Orthogonal Cuts*

Early attempts in investigating chip formation physics, using 2D orthogonal cutting, resulted in observations and prediction models that set the foundations for understanding the principles of this complex shearing process. The orthogonal cut configuration, Figure 2-14(a), simulates chip formation mechanics in their simplest two-dimensional form, with depth of cut and workpiece width (i.e. the flat tool cutting edge is always wider in length than the workpiece's width) being the only dimensional parameters controlling the effective rectangular uncut chip thickness, whilst the cut chip flow is restricted in a single plane along the workpiece-tool interface. The principles learned from this 2D chip formation concept are then used to comprehend the more complex chip formation of the three-dimensional oblique cuts (i.e. feed rate is added to the effective 2D dimensional parameters), Figure 2-14(b), which will be discussed more extensively in section 2.3.2.2.

Merchant (1945) developed a 2D force prediction model, based on the assumption that during cutting all plastic deformation occurs along a single shear plane AB, suggesting that machining forces were a function of the deformed chip thickness and shear angle, Figure 2-15. This enables the calculation of shear plane angle ( $\phi$ ), Equation 2.1, using rake angle ( $\alpha$ ) and chip's thickness ratio, which equals to the ratio of uncut chip thickness (i.e. depth of cut

in orthogonal cutting) and cut/deformed chip thickness. Furthermore, the shear plane area was used to calculate the chip's shear and normal stresses, demonstrating that the work hardening required in chip deformation is linked to physical dimensions defined by the machining parameters and workpiece properties; neither of which were sufficiently defined in the model leading to inaccurate results (e.g. the model failed to predict the effect of cutting speed on shear angle).

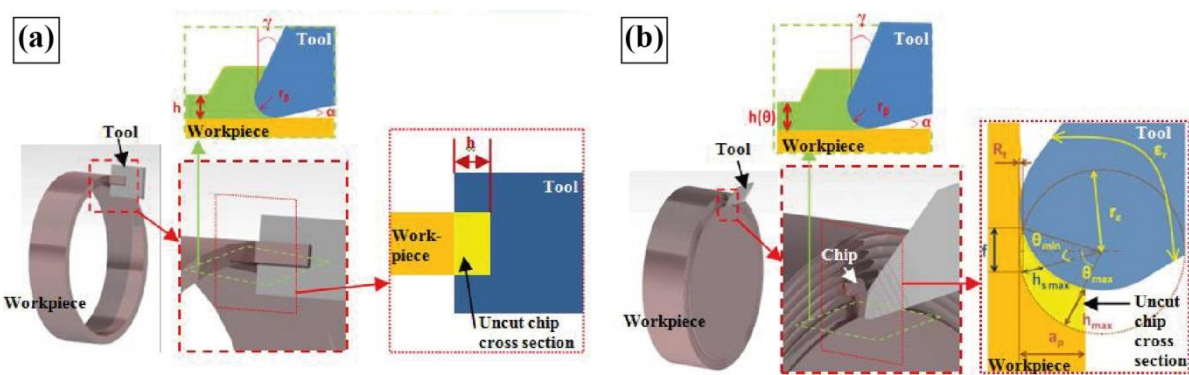


**Figure 2-14: Turning operation configurations; (a) 2D orthogonal cut and (b) 3D oblique cut, Denguir et al. (2014).**

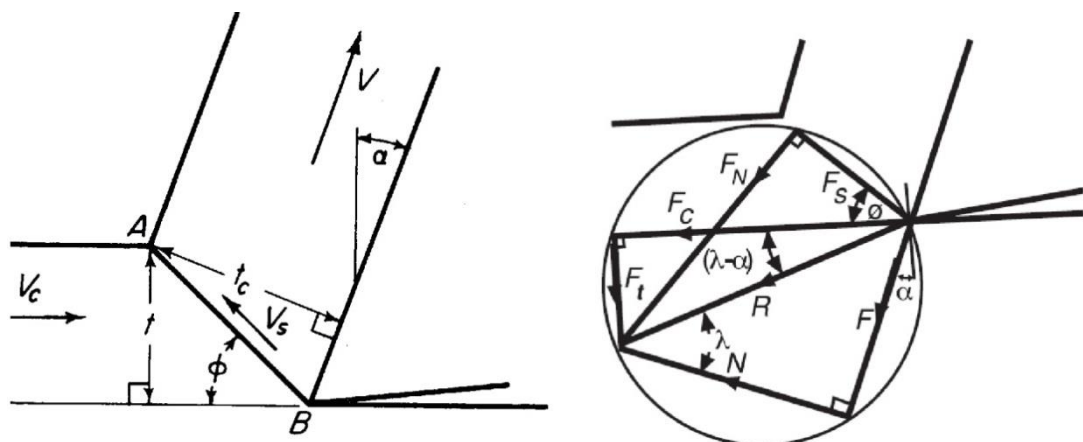


**Figure 2-15: Merchant's cutting force prediction model, Merchant (1945).**

However, using the concept seen in Figure 2-15 and assuming constant chip thickness through its cross-section, Trent and Wright (2000) showed that varying the cutting speed ( $V_c$ )

also varies the shear plane angle ( $\phi$ ), Figure 2-16(a), due to its effect on the magnitude of shearing speed ( $V_s$ ), Equation 2.2, and the speed at which the chip travels away from the tool ( $V$ ), Equation 2.3. For example at constant  $\alpha$ , increasing  $V_c$  also increases  $\phi$  resulting in lower cut chip thickness, which is always larger than the uncut chip thickness. Furthermore, Figure 2-16(b) shows that shear strain ( $\gamma$ ) was defined as the ratio of total material displacement ( $\Delta S$ ) along the shear plane over the thickness of the shearing zone ( $\Delta y$ ), Equation 2.4, and thus the rate of deformation or strain rate ( $\dot{\gamma}$ ) can be expressed as a function of time ( $\Delta t$ ) required to achieve maximum strain. For high ductility materials both  $\Delta y$  and  $\Delta t$  values are high, due to their high plasticity tolerance, suggesting lower chip deformation and thus explaining the often observed findings that higher ductility materials produce thicker chips compared to less ductile materials when machined at identical cutting conditions, also highlighting the effect of material properties on chip formation. Equation 2.5 also expresses  $\dot{\gamma}$  as a function of  $V_s$ , indicating that an infinitely large rake angle (i.e. equal to  $90^\circ$ ) would result in zero strain, thus no deformation, in which case cut chip thickness would be equal to the uncut chip thickness.

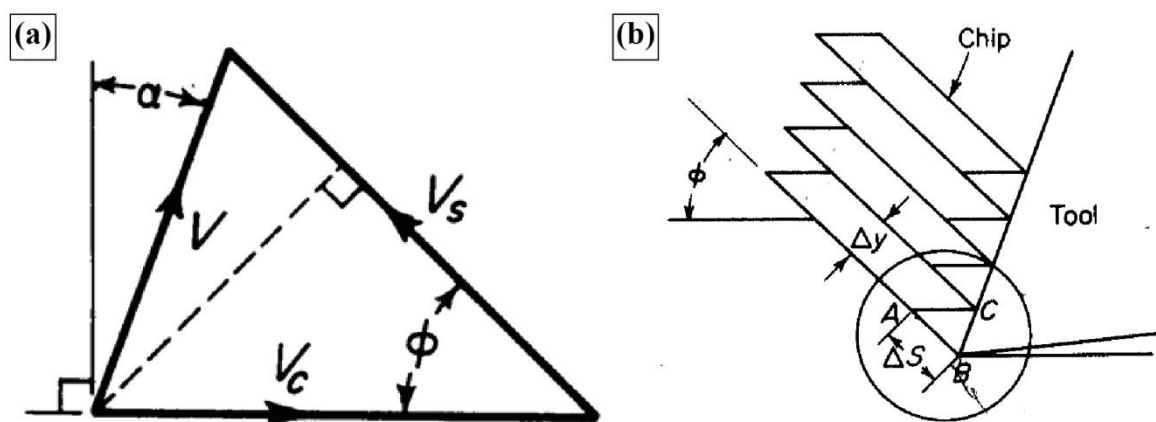


**Figure 2-16: Chip formation physics in orthogonal cutting ; (a) Machining speed vector diagram and (b) Shear-strain model, Trent and Wright (2000).**

The chip single shear plane angle for orthogonal cutting, ( $\varphi$ );

$$\tan\varphi = \frac{\frac{t}{tc} \cos\alpha}{1 - \frac{t}{tc} \sin\alpha} \quad (2.1)$$

The shearing speed and chip speed, ( $V_s$ ) and ( $V$ ) respectively;

$$V_s = \frac{\cos\alpha}{\cos(\varphi - \alpha)} V_c \quad (2.2)$$

$$V = \frac{\sin\varphi}{\cos(\varphi - \alpha)} V_c \quad (2.3)$$

The cutting strain and strain rate, ( $\gamma$ ) and ( $\dot{\gamma}$ ) respectively;

$$\gamma = \frac{\Delta S}{\Delta y} = \frac{V_s}{V_s \sin(\varphi)} \quad (2.4)$$

$$\dot{\gamma} = \frac{\Delta S}{\Delta y \Delta t} = \frac{V_s}{\Delta y} \quad (2.5)$$

Bitans and Brown (1965) proved experimentally this theorem when machining with sharp tools at fixed  $V_c$  and depth of cut, with their findings suggesting that large positive rake angles ( $\alpha$ ) result in insignificant chip deformation, Figure 2-17(a). Decreasing  $\alpha$ , and thus increasing the shearing angle, subjected the chip to higher strain resulting in more severe material distortion and in the case of negative  $\alpha$  even altered the chip's morphology, Figure 2-17(b-c). Furthermore, Figure 2-18 shows that increasing the tool's edge rounding radius ( $r_e$ ) increased the local chip deformation at the cutting edge, also resulting in more severe subsurface distortion, due to more severe ploughing effect of the tool's edge geometry, compared to the minimum deformation detected on the surfaces and chips produced with sharp tools. This phenomenon was caused due to larger part of the chip being deformed at the blunter edge profile where the effective rake angle varies from the tool's top rake angle to  $-90^\circ$ , and thus exhibiting similar characteristics to those discussed for Figure 2-17. Although the benefits of high positive rake angles and sharp tool edges were demonstrated, the authors

highlighted the inability to extensively use these tool geometry characteristics in hard metal turning due to the high machining forces and temperature that often compromise the cutting edge integrity.

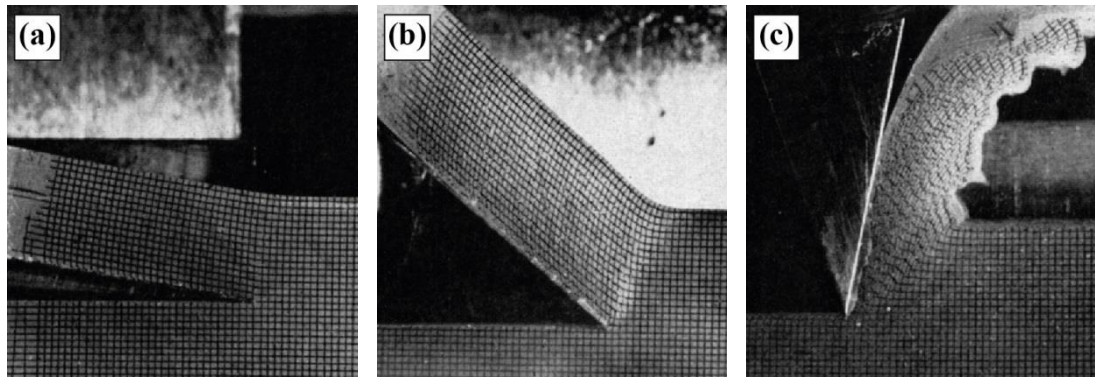


**Figure 2-17: Effect of rake angle on chip formation; (a)  $\alpha = 80^\circ$ , (b)  $\alpha = 50^\circ$ , (c)  $\alpha = -10^\circ$ , Bitans and Brown (1965).**

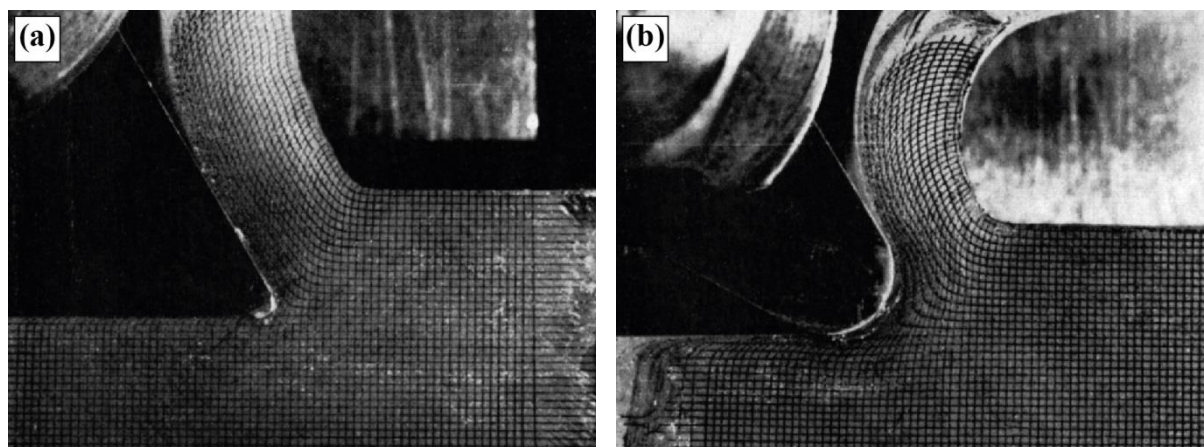


**Figure 2-18: Effect of tool edge rounding radius on chip formation; (a)  $r_e = 0.8$  mm, (b)  $r_e = 3.2$  mm, Bitans and Brown (1965).**

Figure 2-19(a) shows that machining at  $\alpha = -85^\circ$  no chip formation was observed as the cutting tool rubbed across the workpiece, only displacing the workpiece material and forming sideflow. Komanduri (1971) concluded that this phenomenon is a result of material flowing both over and under the cutting edge at high negative rake angles, Figure 2-19(b), as material shearing was being replaced by material dragging. It was calculated that the transformation

between forming and not forming chips occurs at  $-76^\circ$  rake angle, at which point the rake face friction was zero and thus no chip flow was occurring. Furthermore, the observed increase in surface distortion depth, more severe sideflow and chip microstructure recrystallization with increasing negative rake angle suggested a greater ploughing effect and higher strain damage induced by the cut under these conditions.

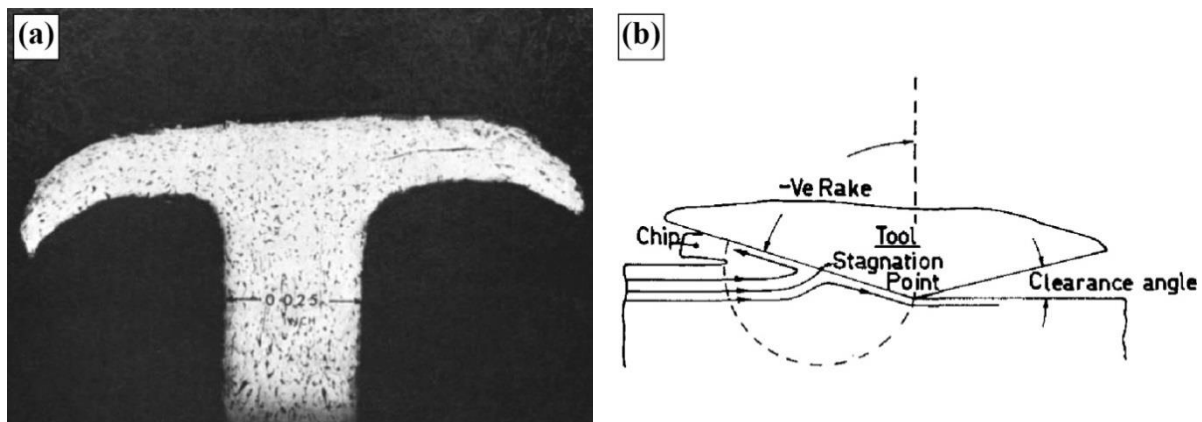


**Figure 2-19: Effect of high negative rake angles; (a) No chip formation and (b) Chip formation minimum conditions, Komanduri (1971).**

Combining all the above findings indicates that chip formation is more complex than the simple single plane shearing process assumed by researchers in the past, with the plastic deformation zone extending in a larger area of the chip (others also consider a secondary shear zone along the tool's rake cause by friction at the chip-tool interface), and chip flow depending on both the workpiece mechanical properties and machining conditions. For simplicity until this point, continuous uniform chip formation was assumed, usually occurring in materials with sufficient ductility, Figure 2-20(a), though other chip morphologies should also be considered like the continuous non-uniform thickness chips affected by the occurrence of built-up edge (BUE) on the cutting tool, Figure 2-20(b), the semi-continuous segmented chips formed when machining low ductility materials under high strain conditions, Figure 2-20(c), and the discontinuous chips formed when machining very brittle materials,

Figure 2-20(d). The latter two chip types lack the uniformity in shear deformation distribution encountered for continuous chips, though their morphology revealed that fracturing (both in microscopic and macroscopic scale) is also a work hardening mechanism present in chip formation, Shaw and Vyas (1993).

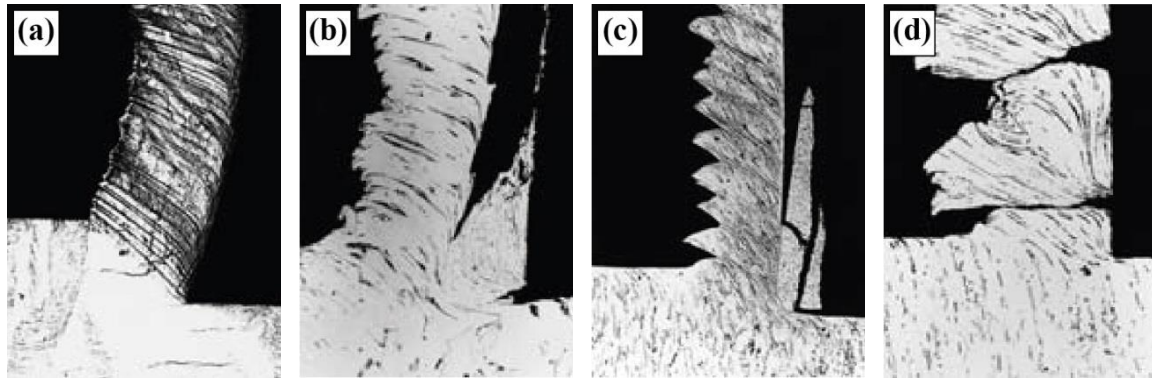


**Figure 2-20: Typical examples of chip types formed in orthogonal cutting; (a) Continuous chip, (b) Continuous chip formed with built-up edge, (c) Semi-continuous segmented chip, (d) Discontinuous chip, Childs et al. (2000).**

Segmented chips form when fracture occurs on the workpiece free surface due to the combined effect of low chip ductility and high deformation conditions acting along the shear plane (often caused by increase in cutting speed combined with low rake angles), Nakayama et al. (1988). König et al. (1993) explained that the cracks nucleate when a critical shear stress value is exceeded at an area of minimum compressive stress (i.e. on the surface), whilst it was demonstrated that their propagation is also affected by the uncut chip thickness. Thick chips produced at high depth of cut ( $a_p$ ) resulted in severe chip segmentation due to the exceeded critical shear stress value being significantly higher than the compressive stress acting nearer the tool edge-chip interface, Figure 2-21(a), compared to thinner segmented chips (at low  $a_p$ ) forming small and frequent cracks, Figure 2-21(b). Furthermore, the latter exhibited similar morphology to continuous chips, supporting the statement that both

shearing and fracturing mechanisms are present in the formation of any chip type. However, the reduction in deformed chip thickness at higher  $V_C$  resulted in more severe chip segmentation due to the higher plastic deformation associated with these cutting conditions, Gatto and Iuliano (1994).

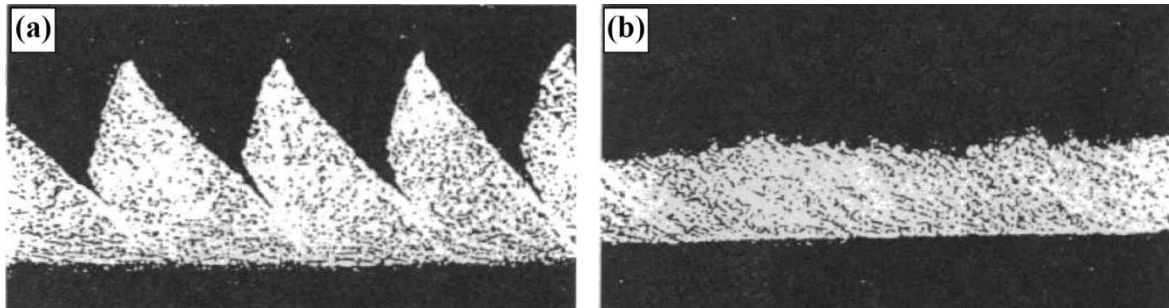


**Figure 2-21: Effect of uncut chip thickness on steel chip segmentation; (a) Thick chip at high  $a_p$ , (b) Thin chip at low  $a_p$ , König et al. (1993).**

Another theory states that segmented chips form purely due to adiabatic shear caused by the material's poor thermal properties, suggesting that the low thermal conductivity and low specific heat transfer coefficient of materials, like those of titanium alloys, lead to material softening during cutting and the formation of adiabatic shear bands, Komanduri and Von Turkovich (1981). Figure 2-22(a) shows that most plastic deformation was restricted to the shear bands, also causing material recrystallization due to the excessive localised mechanical strains and heat loads, whilst the rest of the chip volume showed minimal deformation. More recent findings suggest that chip segmentation is a combination of both cyclic crack formation on the workpiece surface and adiabatic shear for the work-hardened area of the chip, Shaw and Vyas (1998), whilst micro-fracturing is part of the deformation mechanism, Figure 2-22(b). The only point of disagreement among researchers is that of the dominant mechanism, with some suggesting that adiabatic shear causes the crack initiation and propagation, Barry and Byrne (2002), whilst others argue that crack initiation defines the

shear bands occurrence frequency, Vyas and Shaw (1999). However, they all agree that both the material properties (i.e. lack in ductility and poor heat properties) and machining parameters affect the machining condition influencing this chip formation mechanism.

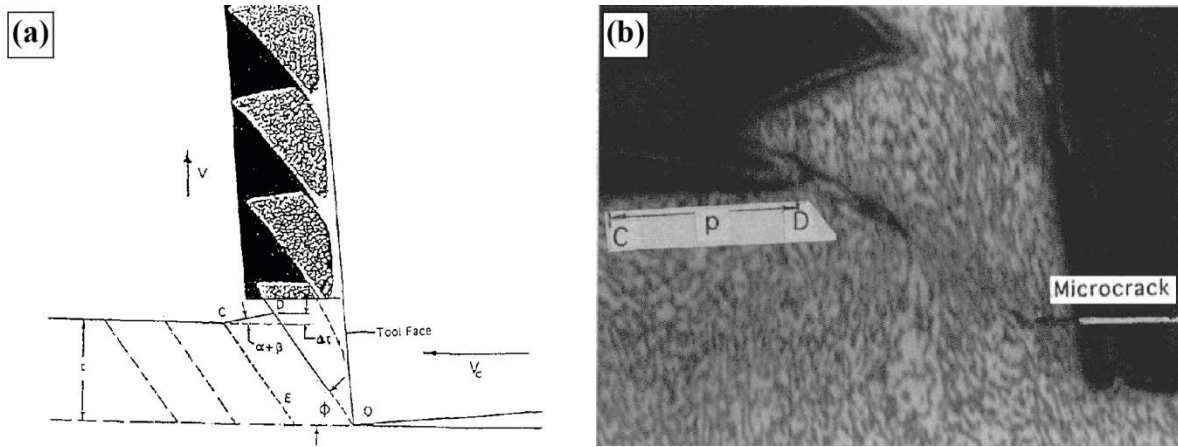


**Figure 2-22: Shear band formation in segmented chips; (a) Adiabatic shear mechanism, (b) Fracturing mechanism, Vyas and Shaw (1999).**

Okushima and Hitomi (1961) found that machining even less ductile materials under extreme strain conditions or very brittle materials form discontinuous chips due to crack propagation near the cutting edge area causing complete chip fracture, Figure 2-23(a). Deformation in the shearing zone “AOB” was found to be lower than that in other chip types, suggesting brittleness favours high localised plasticity at low deformation rates. Using FEM simulation, Guo and Yen (2004) demonstrated that this phenomenon results in instant formation of an internal crack, which then propagates along the shearing plane OB towards a second crack formed near the free surface, causing the chip to fail, Figure 2-23(b). The cyclic repetition of discontinuous chip formation also varied the mechanical loads during machining (i.e. drop in shearing stresses due to the chip failure) resulting in non-uniform subsurface deformation and proving the direct effect of chip formation on surface and sub-surface integrity, Obikawa et al. (1997).

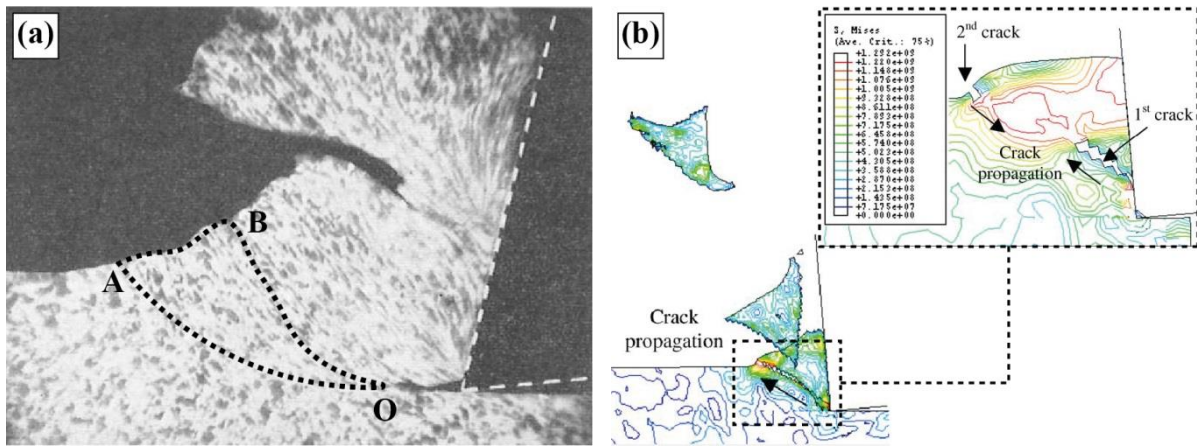


**Figure 2-23: Discontinuous chip formation; (a) Brittle fracture, Okushima and Hitomi (1961), (b) FEM simulation, Guo and Yen (2004).**

When machining Inconel 718 at fixed depth of cut, Komanduri and Schroeder (1986) found that increasing  $V_C$  transformed the continuous ribbon shaped chips produced at  $V_C = 15\text{-}90 \text{ m/min}$ , Figures 2-24 (a-b), into smaller discontinuous chips, Figures 2-24 (c-d), whilst chip segmentation and semi-continuous chip formation occurred at  $V_C \geq 60 \text{ m/min}$ . Similar trends were observed when machining steels, Dolinšek et al. (2004), and titanium alloys, Sima and Özal (2010), proving that any material is able to produce any chip type depending on the machining conditions created by the machining parameters. The workpiece properties at corresponding conditions (e.g. effect of temperature on stress-stain relationship) influence the chip deformation rate tolerance and thus the chip formation mechanism transformation threshold (i.e. from uniform plastic deformation to localised plastic deformation combined with ductile failure to complete ductile failure). Indicative of this temperature, material properties and chip formation relationship are also the data presented by Joshi et al. (2013) who observed reduction in the alloy Ti6Al4V chip segmentation size, shear bands thickness and sub-surface distortion depth when heating-up the workpiece prior machining (i.e. in the range of  $40\text{-}350^\circ\text{C}$ ); proving that reducing the alloy's strength at higher preheating temperatures resulted in lower alloy resistance to deformation, and thus less deformation

work was required to form the chip and finished surface. Overall, the investigation so far revealed that both shearing and fracturing deformation mechanisms are involved in chip formation and surface deformation, whilst the effect of parameters on machining conditions and their interaction with the workpiece's properties define the chip material flow and the finished surface integrity. Finally, the lack of reference to numerous models developed in an effort to capture the essence of this complex relationship is because they are predicting chip flow trends according to the physics already discussed, Figures 2-25(a-b), as they require calibration (i.e. using experimental data) to define their empirical constant values.

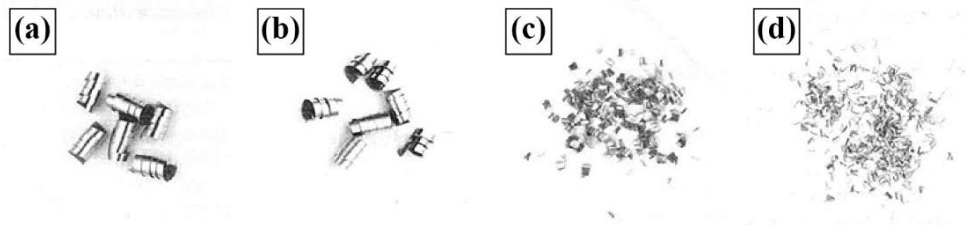


**Figure 2-24: Chip formation mechanism transformation when machining Inconel 718; Continuous ribbon shaped chips (a)  $V_C = 15 \text{ m/min}$ , (b)  $V_C = 90 \text{ m/min}$ , Discontinuous chips (c)  $V_C = 122 \text{ m/min}$  (d)  $V_C = 213 \text{ m/min}$ , Komanduri and Schroeder (1986).**

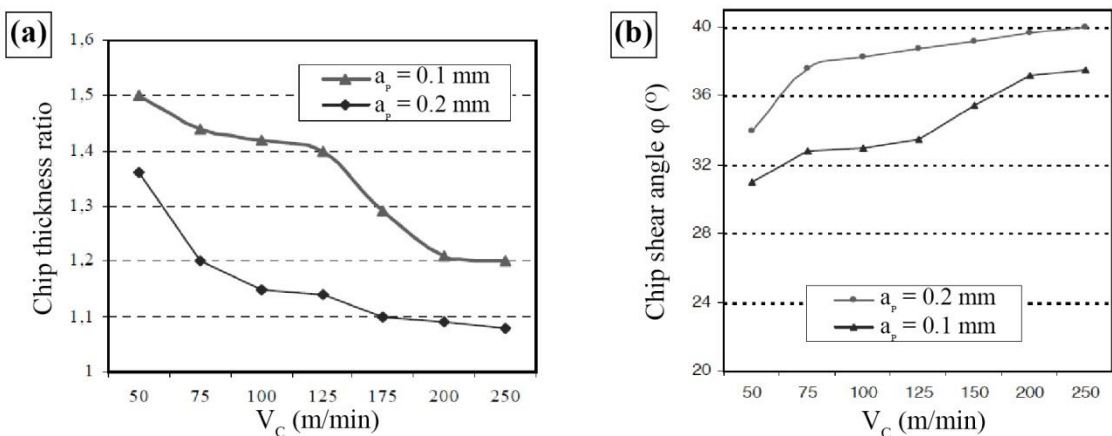


**Figure 2-25: Predicted chip flow data at varying  $V_C$  when machining Ti6Al4V; (a) Effect on chip thickness, (b) Effect on chip shear angle, Daymi et al. (2009).**

### 2.3.2.2 *Oblique Turning*

Within this section the geometrically complex deformation mechanism of oblique turning cuts is explained using the orthogonal machining chip formation physics and observations described above. In contrast to orthogonal cutting, in oblique turning the workpiece surface is considered infinitely wider than the tool's width (i.e. or diameter for round tools), and thus a number of tool passes are required for machining the full surface, Figure 2-26(a), whilst the tool is continuously fed along the workpiece at constant feed rate ( $f$ ) and fixed depth of cut ( $a_p$ ). Combined, these dimensional machining parameters produce non-uniform uncut chip geometry profiles, in contrast to the uniform rectangular shaped chips in orthogonal cutting, resulting in variation of the machining conditions acting along the tool's cutting edge (i.e. varying heat loads and mechanical strains), affecting the chip formation and workpiece deformation, Kishawy et al. (2006). Furthermore, the resultant machining force ( $F$ ) acting on the cutting tool represents the summation of three force vectors due to the added effect of feed rate, Figure 2-26(b), with feed force ( $F_f$ ) measuring the workpiece resistance to the tool's displacement along z-axis, whilst cutting force ( $F_c$ ) and push-off force ( $F_p$ ) acting on the x-y plane are similar to those found in 2D orthogonal cutting. Further discussion on machining forces will follow in section 2.3.4.1.

Bushlya et al. (2015) demonstrated that in oblique turning, uncut chip morphology is controlled by the tool geometry, whilst they highlighted that secondary tool characteristics often ignored by researchers (i.e. rake angle ( $\alpha$ ) and cutting edge rounding ( $r_e$ )) may result in significant errors when calculating the uncut chip area and chip volume machined per unit time. The authors observed that using sharp tools results in more uniform chip flow distribution along the cutting edge, similar to the orthogonal machining, Figure 2-27(a), in

contrast to nose-radius and round tools that produce less uniform chip profiles, Figure 2-27(b-c). The latter two tool options though improve surface integrity and ensure enhanced control over the surface roughness; making them ideal tool options for finishing operations.

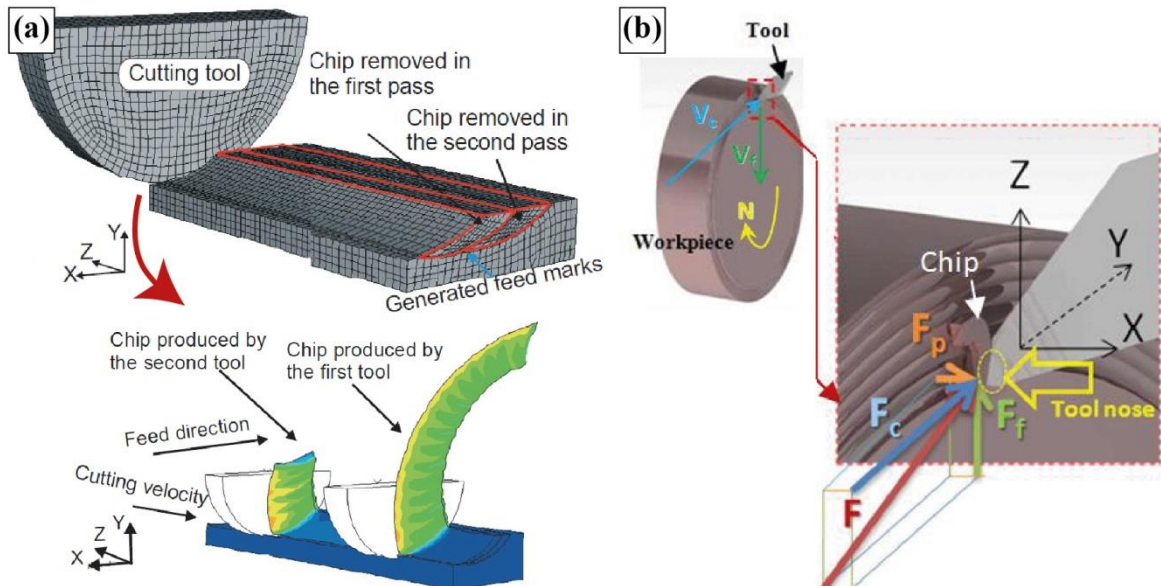


**Figure 2-26: Illustrations of oblique turning with round tools; (a) Chip formation process, Kishawy et al. (2006), (b) Machining force configuration, Denguir et al. (2014).**

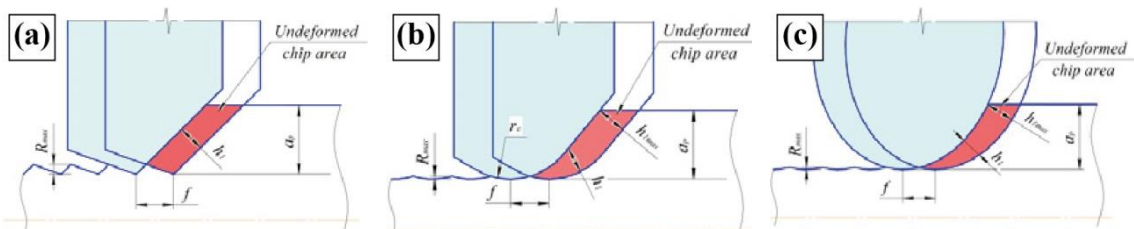


**Figure 2-27: Effect of tool geometry on uncut chip cross-section in oblique turning; (a) Sharp tool, (b) Nose-radius tool, (c) Round tool, Bushlya et al. (2015).**

However, this investigation focuses on the chip profile produced by round tools only, as they are primary tool options in RR1000 final production stages and they produce the most common chip geometry in finish turning operations. Figure 2-28 shows the workpiece-round tool interaction interface projection during machining, indicating that the uncut chip

morphology, and area, is controlled by the values of tool radius ( $r_n$ ), depth of cut ( $a_p$ ) and feed rate ( $f$ ). Uncut chip thickness varies continuously along the tool's cutting edge, with the chip's thinner section (i.e. chip forming at the trailing edge) forming the finished surface, whilst chip thickness increases in the feed direction until it reaches a maximum uncut thickness ( $h_{max\_u}$ ). This value corresponds to the uncut chip thickness described in orthogonal cutting and thus it's often used to calculate the chip compression ratio (CCR) that defines the overall chip deformation rate (i.e. ratio of maximum uncut and maximum cut chip thickness). For a more advanced analysis though, the 3D chip profile is divided in an infinite number of thin 2D segments (e.g. A to B, C to D...etc.) vertical to the cutting edge, for which orthogonal cutting conditions are assumed, whilst the uncut thickness of each segment ( $h_{seg}$ ) can be calculated using Equation 2.6, Denguir et al. (2014).

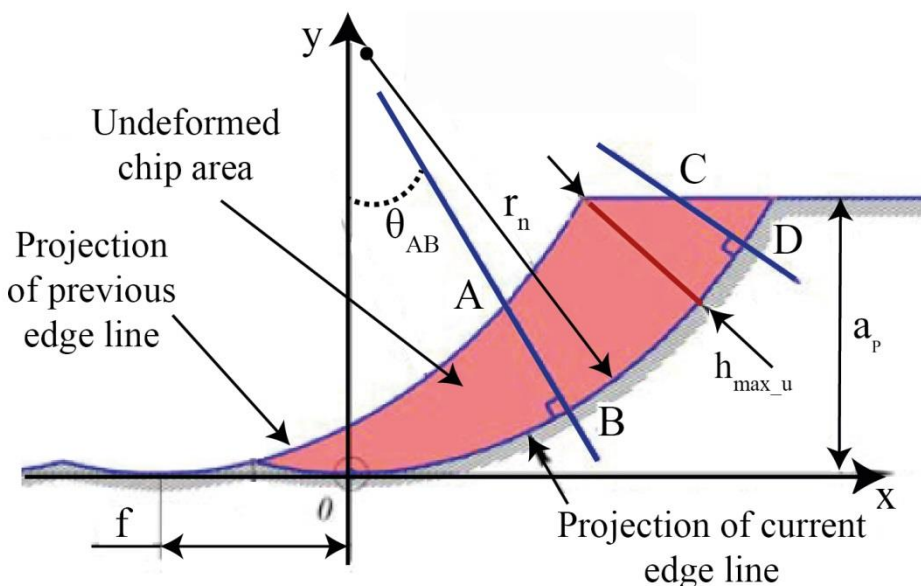


**Figure 2-28: Round tool uncut chip geometry in oblique turning, Bushlya et al. (2015).**

The uncut thickness of each segment along the chip profile formed in oblique turning cuts with round tools, ( $h_{seg}$ );

$$h_{seg} = r_n + f * \sin(\theta) - \sqrt{r_n^2 - f^2 * \cos^2(\theta)} \quad (2.6)$$

The effect of differential chip thickness in 3D turning is especially noticeable when forming segmented chips, with severe segmentation occurring at the chip's thicker/leading edge compared to the more uniform continuous chip formation at its thin/trailing edge, Figure 2-29(a). Furthermore, increasing maximum uncut chip thickness using smaller  $r_n$  (for constant  $V_C$ ,  $a_p$  and  $f$ ) results overall in more severe chip segmentation compared to thinner chips produced with larger  $r_n$ , Figure 2-29(b). Both observations coincide to the phenomenon described in Figure 2-21, for orthogonal cutting chips at different  $a_p$ , and when combined to the fact that increasing  $f$  has a similar effect in chip morphology, Kishawy (1998), confirms that 2D chip formation physics apply in 3D machining, even though cutting conditions vary along the oblique turning cutting edge. The author used this concept of non-uniform deformation to also explain the occurrence of serrations on the hard steel AISI 1550 chip's thin edge, Figures 2-29(a-b), suggesting they form due to lateral chip flow (in addition to chip flow along the tool's rake) acting as a machining stress relieve mechanism, Figure 2-30.

El-Wardany and Elbestawi (1998) explained that chip thinning parameters (i.e. high  $r_n$  and low  $f$ ) increase heat loads and compressive stresses in the chip, whilst resulting in more material being machined at the tool's cutting edge, favouring the occurrence of serrations below a so-called "critical" minimum chip thickness value. Consequently, cutting edge roundness ( $r_e$ ) was also found to have significant effect on the phenomenon's severity due to its control over the amount of chip thin trailing edge material being machined at differential negative rake angles. Thus larger  $r_e$  increases local plasticity and forces more chip material to be "side-squeezed", producing both chip serrations and the surface defect known as side-flow (further details in section 2.3.3.1). This also explains the increase in the phenomenon's severity with increasing tool wear, as machining with a worn tool has a similar effect to

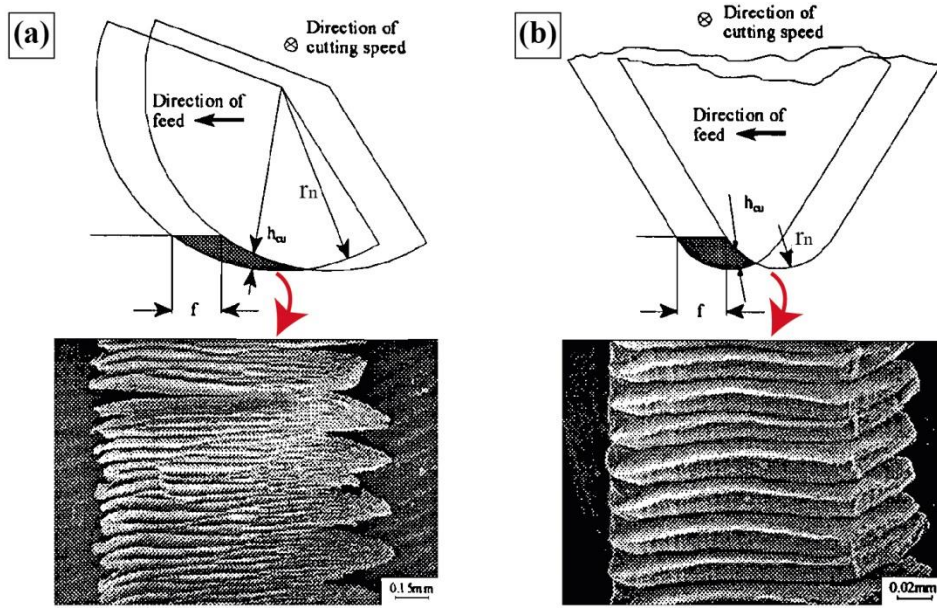


**Figure 2-29: Effect of uncut chip thickness on chip segmentation and edge serration when turning hard steel AISI 1550; (a)  $r_n = 3.6$  mm, (b)  $r_n = 1.2$  mm, Kishawy (1998).**

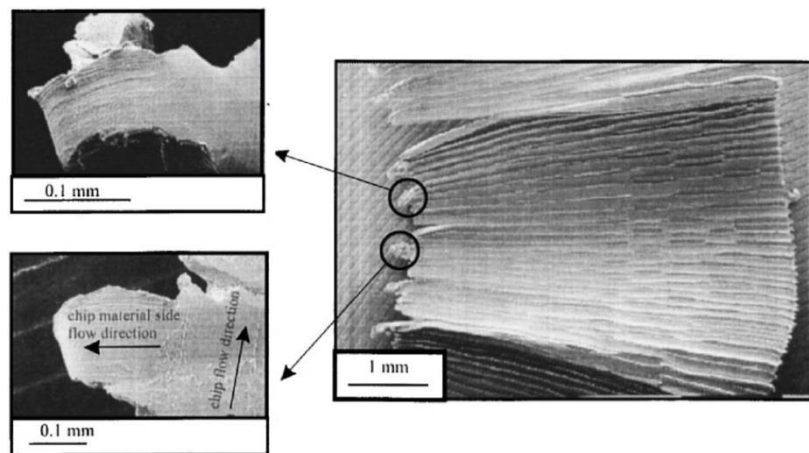


**Figure 2-30: Chip lateral flow when turning of hard steel at  $V_C = 160$  m/min,  $f = 0.05$  mm and  $a_p = 4$  mm, El-Wardany et al. (2000b).**

machining with a blunder tool, resulting in higher deformation stresses and heat loads at the cutting edge. Furthermore, the model developed to predict chip sideflow indicates that machining conditions suggesting extensive ploughing at the cutting trailing edge-finished surface interface (i.e. reduction in cutting force and increase in push-off force) also favour the occurrence of chip serrations. The model also suggests that a small enough  $r_n$  with sharp edge

could eliminate the phenomenon's occurrence, whilst specific combination of parameters could be used to reduce its severity.

Thakur et al. (2009) observed similar so-called "saw-tooth" trailing edge chips when turning Inconel 718 with tungsten-carbide tools at  $f = 0.08$  mm/rev and  $V_C \geq 50$  m/min, Figure 2-31, suggesting they formed due localised thermal softening of the workpiece (as a result of its low thermal conductivity) that decreases the chip's ability to accommodate work hardening at its thin edge. Even though the authors limited their discussion concerned with this phenomenon and provided no further details about the chip formation impact on surface integrity, it is evident in Figures 2-30(b-c) that increasing  $V_C$  affected both the geometry and occurrence frequency of these serrations. Furthermore, the chip's irregular edge morphology when machining at  $V_C = 40$  m/min reveals that the statement of no serrations occurring at these conditions maybe false. Overall, this phenomenon is not widely reported in literature concerned with superalloy machining, even though its presence is visible in figures published by researchers like Pawade et al. (2008) for high speed finish turning Inconel 718 with ceramic tools at  $f = 0.05\text{-}0.15$  mm/rev.

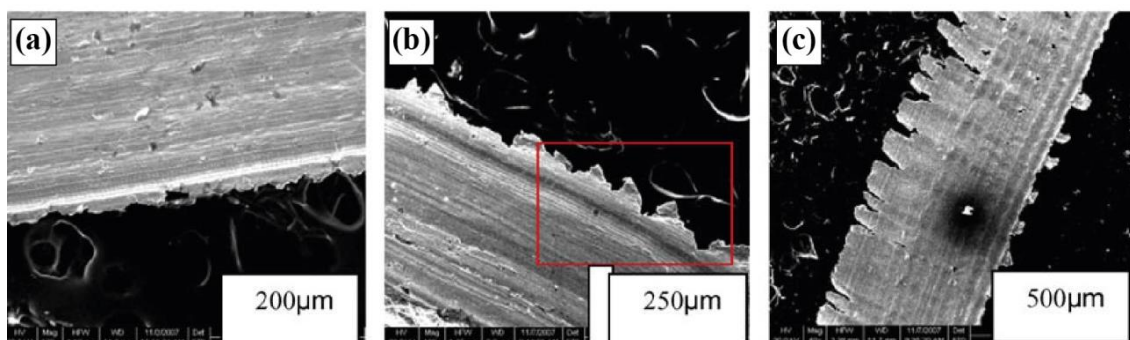


**Figure 2-31: Chip edge serrations when turning Inconel 718 at  $f = 0.08$  mm/rev,  $a_p = 0.5$  mm and  $r_n = 0.8$  mm; (a)  $V_C = 40$  m/min, (b)  $V_C = 50$  m/min, (c)  $V_C = 60$  m/min, Thakur et al. (2009).**

Kumar et al. (2002) also failed to discuss serration formation at the chip's trailing edge when finish milling hard steel ASSAB 718 at  $f = 0.05$  mm/tooth, however, these findings show that the phenomenon is not exclusive in turning, while physics appear identical for both operations. Furthermore, it is evident that both the serration size and morphology were affected by the machining conditions created when using tool coatings compared to uncoated tools, Figures 2-32(a-b), or applying different cooling processes, Figures 2-32(b-d), verifying that the phenomenon is also linked to the machining dynamics and not just to the uncut chip geometry dimensions.

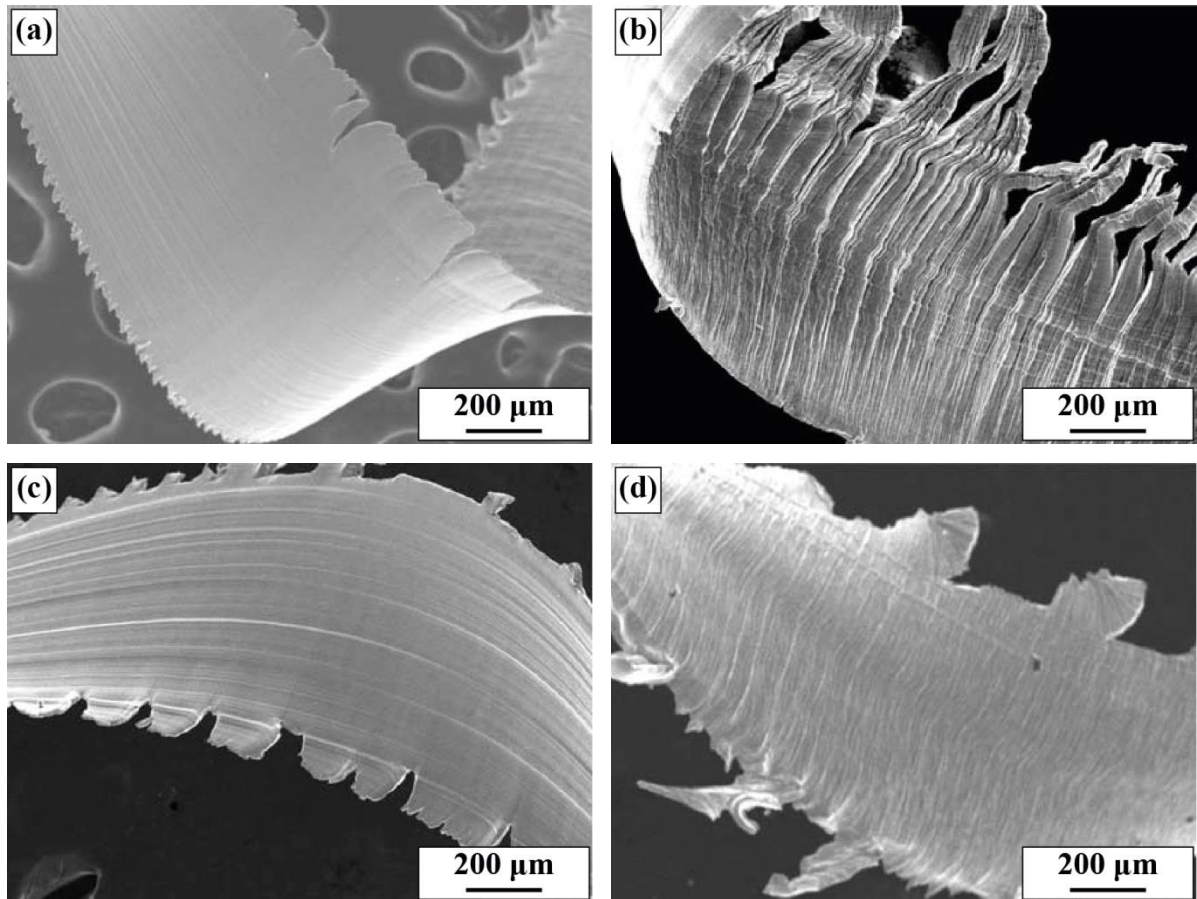


**Figure 2-32: Chip edge serrations when milling hard steel ASSAB 718 at  $V_C = 150$  m/min,  $f = 0.05$  mm/tooth and  $a_p = 0.35$  mm; Uncoated tool (a) Dry cut, Coated tool (b) Dry cut, (c) Conventional cooling , (d) High pressure cooling, Kumar et al. (2002).**

Finally, Asai and Kobayashi (1990) observed the phenomenon's occurrence when micro-turning aluminium alloys to a mirror surface finish at  $f = 0.02$  mm/rev and  $V_C = 450$  m/min, supporting further the theory for non-uniform chip deformation as they found that machining shearing angle varied along the differential chip thickness profile. Their findings also indicate that any material type would produce chip serrations at permitting machining conditions, which similar to other chip morphology characteristics, like chip segmentation, is defined by both the machining parameters and materials properties.

### **2.3.3 Surface Integrity**

This section aims to correlate specific machining conditions affecting the finished surface integrity to those controlling the chip formation mechanism in order to understand further the 'physics' of machining, whilst focusing on identifying similarities in the RR1000 machining strategy and the literature reporting favourable conditions for the occurrence of surface defects, especially pick-up. Furthermore, an insight is provided in terms of Rolls-Royce's plc decision driving factors that led to establishing stricter RR1000 production standards, only achieved following specific production parameters.

#### *2.3.3.1 Sub-surface Integrity*

Hardy et al. (2014) found that acceptable surface finish (i.e. low surface roughness Ra) results in good RR1000 fatigue in-service performance only when combined with good sub-surface integrity. Low cycle fatigue testing revealed that sub-surface distortion damage below 10  $\mu\text{m}$  from the RR1000 finished surface (and in the absence of a phenomenon known as white layer), Figures 2-33(a-b), minimises the design compromise in fatigue in-service

performance, compared to that of an optimum damage-free component, explaining Rolls-Royce's specific powder alloy production requirements for sub-surface strain and distortion depth profile to be lower than 10  $\mu\text{m}$  with no white layer present.

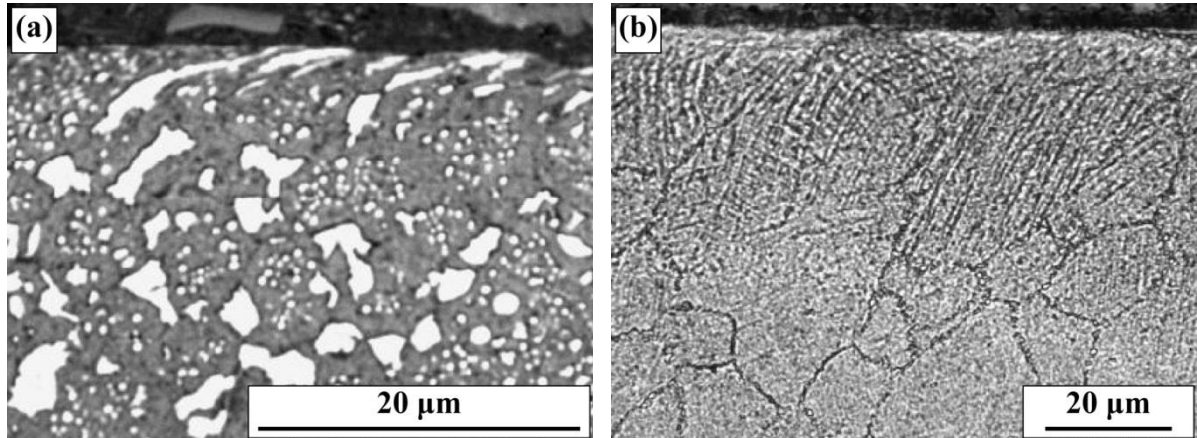


**Figure 2-33: Acceptable sub-surface damage when machining RR1000; (a) Fine grain material, (b) Coarse grain material, Hardy et al. (2014).**

When turning Inconel 718, Sharman et al. (2006) found that for finishing machining conditions (i.e. fixed  $a_p = 0.25 \text{ mm}$ , while varying  $V_C = 40\text{-}120 \text{ m/min}$  and  $f = 0.15\text{-}0.25 \text{ mm/rev}$ ) tool wear had the most significant effect on sub-surface integrity. Using new tools resulted in minimal sub-surface material distortion, Figure 2-34(a), and shallow work hardening depth profiles of the finished surfaces, compared to machining with worn tools under higher mechanical loads that produced up-to three times thicker sub-surface distortion layers, Figure 2-34(b), and deeper sub-surface work hardening profiles. Increasing cutting speed (i.e.  $V_C \geq 80 \text{ m/min}$ ) when machining with worn tools also had significant effect on sub-surface integrity degradation, indicating higher deformation strain rates at these conditions in alignment with the findings reported for chip formation. However, higher  $V_C$  resulted in lower residual tensile stresses, for both new and worn tools, even though increasing  $V_C$  is supposed to produce higher cutting temperatures, which should have had an

opposite effect. The authors explained that this phenomenon occurred due to the faster chip flow (at higher  $V_C$ ) limiting time for heat diffusion towards the finished surface, meaning that the chips were those subjected to higher heat loads. Using similar principles, they also explained that the lower tensile stresses detected when machining with uncoated tools were produced due to more heat being dissipate through the tool's body and less through the surface, in contrast to machining with coated tools at identical cutting parameters, which produced higher tensile stresses due to the heat-resistant coating limiting heat dissipation through the tool and thus subjecting both chip and surface to higher thermal loads.

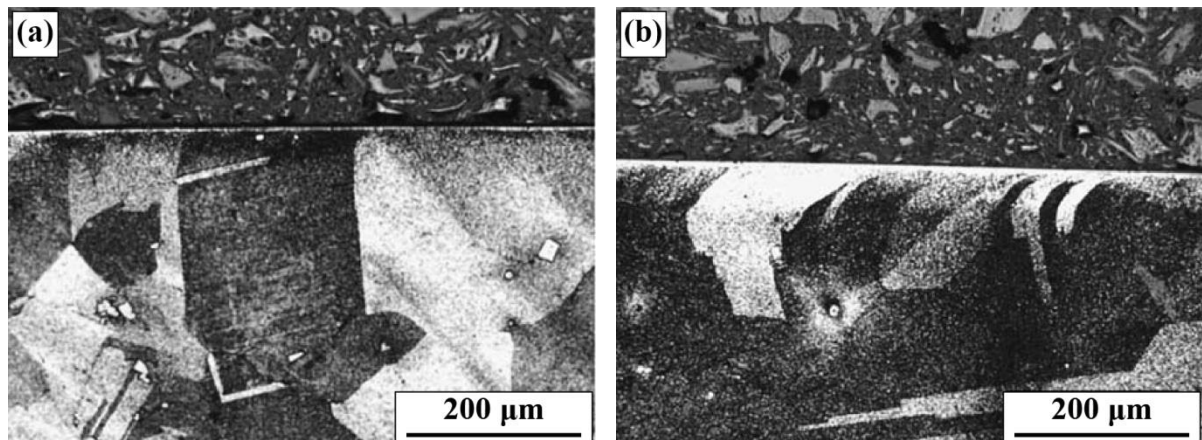


**Figure 2-34: Sub-surface distortion when finish turning Inconel 718; (a) New tool, (b) Worn tool, Sharman et al. (2006).**

Li et al. (2009) reported identical trends in residual stresses when face-finish turning RR1000 at varying cutting speeds, even though tensile stress values in the cutting direction were found at least 400 MPa higher than those previously reported for Inconel 718; indicative of the mechanical properties effect on machining conditions and especially temperatures. The authors, however, provided no explanation for the increase in tensile stresses observed with increasing tool radius (i.e. from  $r_n = 0.8$  mm to  $r_n = 6.0$  mm) at identical material removal rates. Sharman et al. (2015), who also observed similar residual stress behaviour when

turning Inconel 718 as well as increased sub-surface distortion layer depth with increasing tool radius (i.e.  $r_n = 2.0\text{-}6.0$  mm), suggested that lower maximum uncut chip thickness values ( $h_{max\_u}$ ), produced at larger  $r_n$  and fixed cutting parameters, increase the ploughing energy of the cut (due to more material being machined at the tool's cutting edge); subjecting both the surface and chip to higher heat and strain loads, which explains the increase in residual stresses. Furthermore, they illustrated that machining with larger  $r_n$  at fixed  $h_{max\_u}$  results in thinner chip profiles, with more material being machined below the tool's cutting edge rounding, especially at the trailing edge that is responsible for forming the finished surface, Figures 2-35(a-b). This, based on the suggested theory, also explains the increase in residual tensile stresses with increasing  $r_n$  at fixed  $h_{max\_u}$  (i.e. tensile stresses almost doubled with double tool radius) as shown in Figure 2-36. However, increasing  $f$  also resulted in higher residual stresses, even though thicker chip profiles were produced, with the authors suggesting that increasing the material volume removed required more deformation work for machining (i.e. high machining forces), which probably also caused increase in cutting temperatures. Matsumoto et al. (1999) found that increasing the material removal rate due to increasing the  $a_p$  had less effect on residual stresses, supporting further the concept that sub-surface integrity is defined by the conditions at the chip's trailing edge.

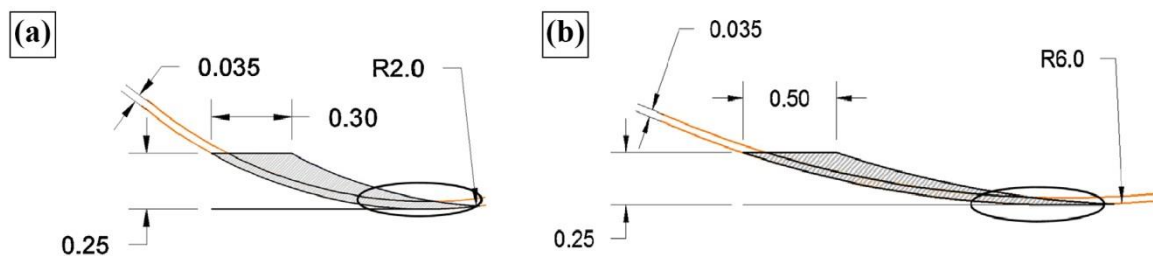


**Figure 2-35: Chip cross-section profiles for varying tool radius at fixed maximum uncut chip thickness  $h_{max\_u} = 0.145$  mm; (a) Thick chip, (b) Thin chip, Sharman et al. (2015).**

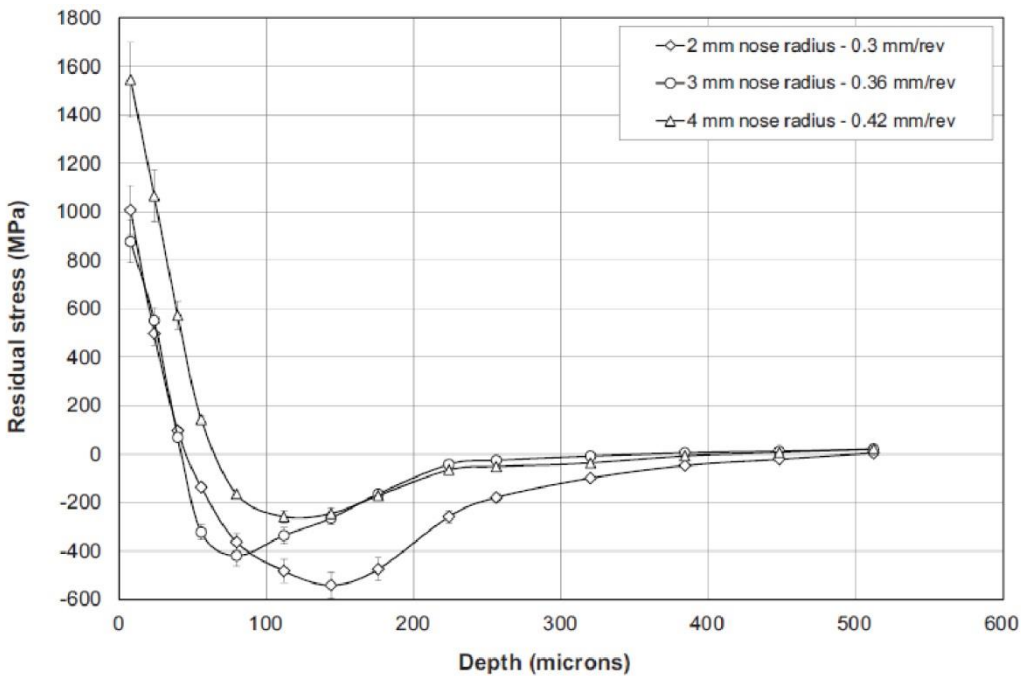


**Figure 2-36: Effect of tool radius on residual stresses in the cutting direction when finish turning Inconel 718 at fixed maximum uncut chip thickness  $h_{max\_u} = 0.145$  mm,  $V_C = 40$  m/min and worn tools; Sharman et al. (2015).**

Chou and Song (2004) found that using similar aggressive finish parameters in hard turning steel AISI 52100, like high  $f$  and high  $V_C$  (i.e.  $f = 0.3$  mm/rev and  $V_C = 120\text{-}180$  m/min), resulted in excessive machining stresses and heat loads, causing extensive transformation/recrystallization of the sub-surface material, a phenomenon known as white layer. They also observed that increasing  $r_n$  from 0.8 to 2.4 mm at  $f = 0.05$  mm/rev results in deeper white layer penetration due to higher machining temperatures developed on the finished surface, suggesting that chip thinning conditions increase the cut's ploughing energy and thus subjecting both the chip and surface at higher heat loads, in agreement with the residual stresses scenarios presented above. White layer was also detected in finish turning Inconel 718, Figures 2-37(a-b), though in this case the phenomenon was only observed at  $V_C \geq 300$  m/min for semi-worn or worn tools, indicative of 1. the alloy's enhanced deformation

and heat resistance properties compared to hard steels, and 2. demonstrating the amount of strain and heat developed in superalloy chip formation for white layer to form on a material that is stable until it exceeds its high performance limits, Bushlya et al. (2011).

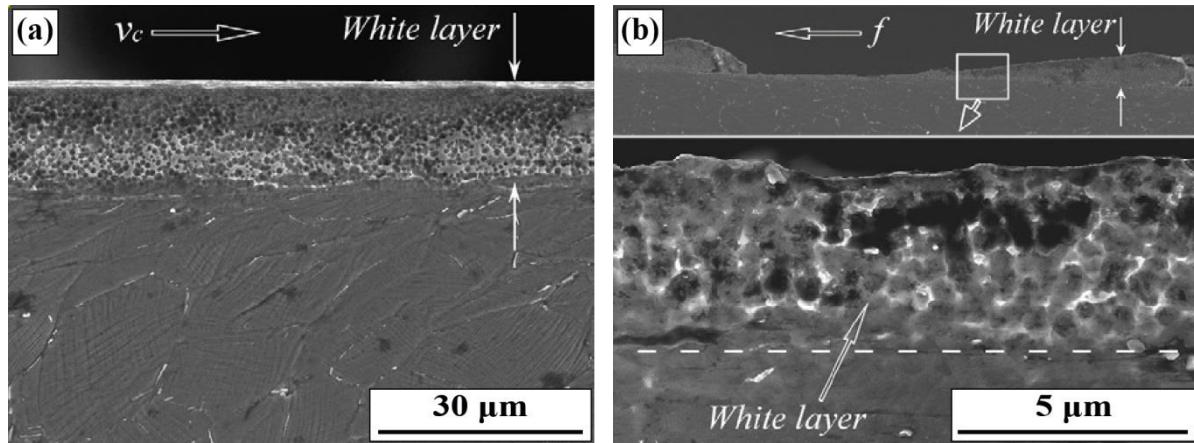


**Figure 2-37: White layer formation when turning Inconel 718 with worn tool at  $V_c = 300 \text{ m/min}$ ,  $a_p = 0.3 \text{ mm}$  and  $f = 0.2 \text{ mm/rev}$ ; (a) Cutting direction, (b) Feed direction, Bushlya et al. (2011).**

With sub-surface integrity being influenced by machining thermodynamics, coolant application is a machining solution employed to reduce both the severity of white layer, Bushlya et al. (2011), and surface tensile stresses, Arunachalam et al. (2004a), compared to those detected in dry machining, due its effect on suppressing machining temperatures (discussed further in section 2.3.5). Furthermore, using sharper tool edge rounding, previously shown to reduced localised deformation in the chips, was also found to produced shallower sub-surface distortion and lower surface tensile residual stresses compared to using tools with larger edge rounding or chamfered edge, Thiele et al. (2016). Combined with the fact that sharper tools resulted in at least double tool life compared to blunder tools when finish turning Ti6Al4V, verifies that these conditions favour reduction in mechanical and heat activated plastic deformation of the chips, surfaces and tools, Hughes et al. (2004).

### 2.3.3.2 Surface Finish

Further to RR1000's specific production standards, Hardy et al. (2014) explained that acceptable surface finish requires both low surface roughness values and a defect-free surface, as defects like the pick-up surface deposits present a major concern for further reduction in the component's fatigue life due to the risk of being shot peened on the finished surfaces (which may act as stress concentration areas or crack initiation points).

While sub-surface deformation is affected by the cut's thermomechanical dynamics, surface finish is vastly controlled by the geometrical aspects of cutting, with Ardi et al. (2014) suggesting that smoother finished surface topography is produced when using low f values, Figure 2-38(a), also improving fatigue life performance compared to that of a rougher machined surface produced at higher f, Figure 2-38(b). Surface finish is most commonly derived/quantified using surface roughness Ra, also known as average roughness, which measures the absolute mean height deviation of the surface, created by the machining mark peaks and valleys alternation, from a theoretical surface centreline over a specific length (L), Figure 2-39. The simplicity in calculating this specification, Equation 2.7, set Ra as one of the easier and most commonly used quality control markers in high quality machining production lines, Thomas (1981), with RR1000 components requiring average Ra less than 0.8  $\mu\text{m}$ , even though the production target is in the range of 0.4-0.5  $\mu\text{m}$ .

The average finished surface roughness, (Ra):

$$\text{Ra} = \frac{1}{L} \int_0^L |z| dx = \frac{1}{n} \sum_{i=1}^n |z_i| \quad (2.7)$$

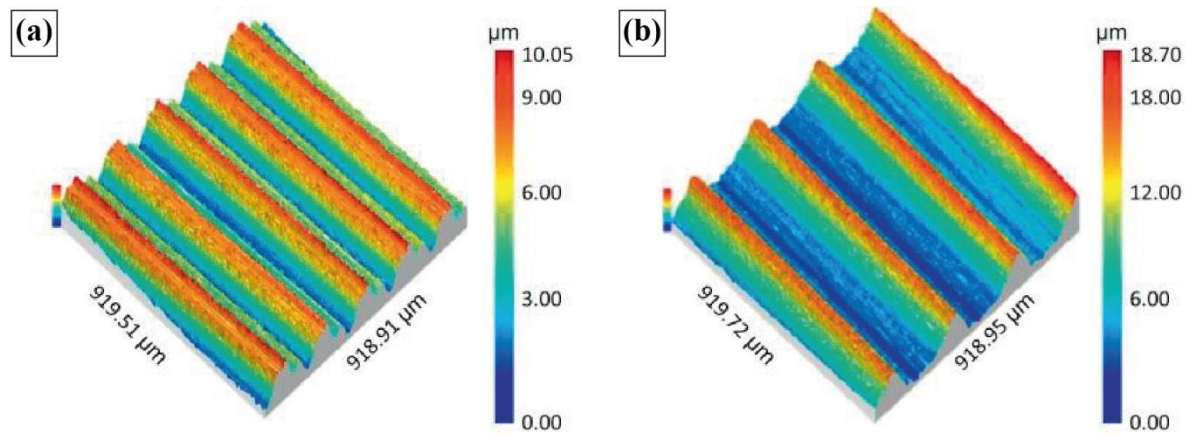


**Figure 2-38: 3D reconstruction of Udimet 720 finish turned surface topography, (a) Low feed rate, (b) High feed rate, Ardi et al. (2014).**

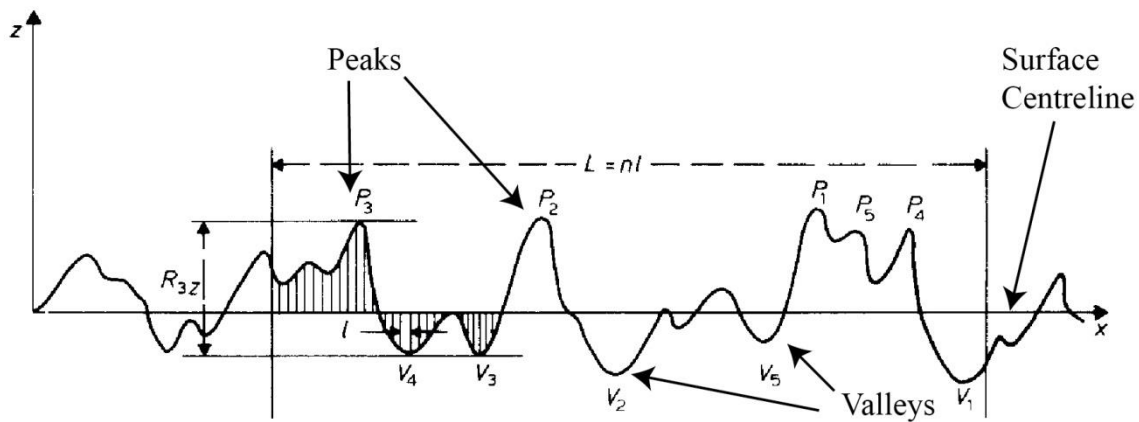


**Figure 2-39: 2D surface finish profile illustration, Thomas (1981).**

Ezugwu et al. (1999) found that  $f$  has the most significant effect on  $R_a$  values when turning Inconel 718 with new tools, due to its effect on both the spacing between the machining mark peaks and the depth of the valleys, indicating that decreasing  $f$  produced lower  $R_a$  values whilst small variations in  $r_n$  and  $V_C$  appear to be insignificant, Figure 2-40. However, large variations in  $r_n$  at fixed  $f$ , also resulted in lower  $R_a$  values, due to the spacing of the peaks being constant while the depth of the valleys decreased, which can be explained by the relationship  $R_a = f^2 / 32r_n$  used to approximately calculate theoretical  $R_a$  values.

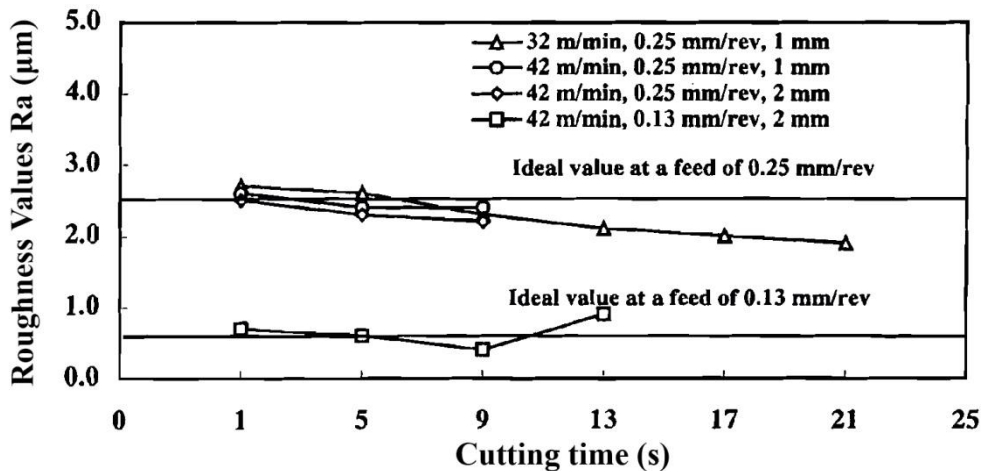


**Figure 2-40: Effect of machining parameters on finish turned Inconel 718 surface roughness Ra values, Ezugwu et al. (1999).**

Furthermore, Ezugwu and Tang (1995) observed increase in surface roughness with increasing machining time when turning cast iron G17 and Inconel 718, suggesting that tool wear results in rougher surfaces, independently of the machined material. Kishawy and Elbestawi (2001) reported similar findings when turning hard steel D2, though they also found that increasing  $V_C$  from 350 m/min to 500 m/min accelerated the tool wear rate, which resulted in more degradation of the surface finish, indicating the indirect effect of  $V_C$  on surface roughness. At identical tool wear conditions though, neither  $V_C$  nor  $a_p$  appear to have significant effect on Ra values as they are not geometry defined parameters of the finish machined surface, except when they result in the formation of surface defects, El-Wardany et al. (2000a).

Increase in surface roughness Ra, from 0.5 to 0.9  $\mu\text{m}$ , was also observed with the occurrence of more frequent and severe parent material deposits on dry turned Inconel 718 surfaces, machined with TiAlN coated carbide tools at  $f = 0.1 \text{ mm/rev}$  while increasing  $V_C$  from 40 to 80 m/min, respectively, Arunachalam and Mannan (2003). It was suggested that dry machining combined with increasing  $V_C$  resulted in high surface temperatures that

favoured a so called “chip welding mechanism” of smeared metal and adhered micro-chips, Figure 2-41, though no further evidence were provided. Arunachalam et al. (2004b) used the same concept to explain the defect-free surfaces detected when machining Inconel 718 at identical cutting parameters under cooled conditions, suggesting that applying coolant caused the reduction of surface temperature and led to the defect elimination.

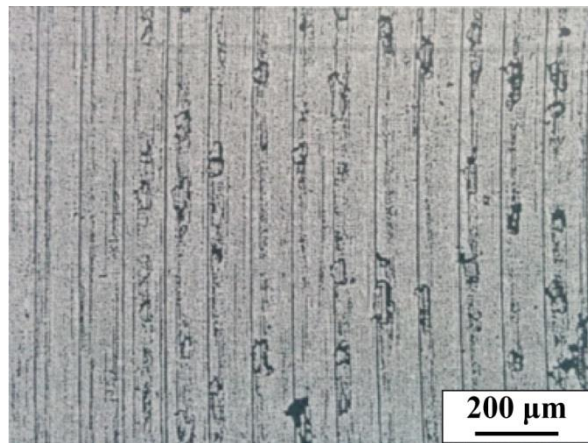


**Figure 2-41: Parent material surface deposits on dry turned Inconel 718 at  $V_C = 80$  m/min and  $f = 0.1$  mm/rev , Arunachalam and Mannan (2003).**

Similar parent material deposits, in this case called “residual” chip and metal debris, were also seen by Pawade et al. (2007) when dry turning Inconel 718 using ceramic tools at high cutting speeds and low feed rates (i.e.  $V_C = 125\text{-}475$  m/min and  $f = 0.05\text{-}0.15$  mm/rev), with the authors suggesting the same deposition mechanism concept discussed above. The presented findings partially support this theory as defect severity increased with increasing  $V_C$  from 125 m/min to 300 m/min, Figures 2-42(a-b), though further increase of  $V_C = 475$  m/min resulted in reduction of the parent material deposits contradicting the statement that higher temperature would result in the welding of more chips, Figures 2-42(c). The authors failed to comment both on this phenomenon as well as the occurrence of the surface defect called sideflow at these cutting conditions.

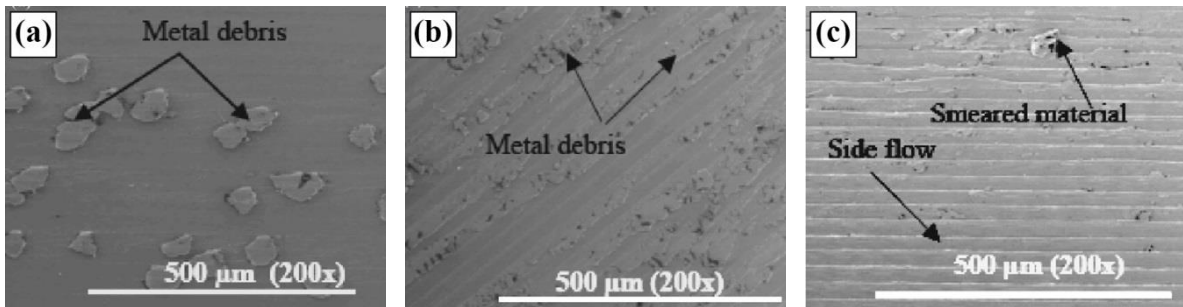


**Figure 2-42: Surface defects in high speed machining of Inconel 718 at  $f = 0.05$  mm/rev;**

**(a)  $V_C = 125$  m/min, (b)  $V_C = 300$  m/min, (c)  $V_C = 425$  m/min, Pawade et al. (2007).**

Bresseler et al. (1997) also reported deposition of chip fragments on the finished surfaces among other defects, like the formation of grooves and cavities, when machining hard steels at  $V_C = 107$  m/min and  $f = 0.075$  mm/rev with new round ceramic tools, Figures 2-43(a,c,d). These deposits were not reported at higher  $V_C$ , though similar to the findings above these conditions favoured the formation of more severe sideflow, Figure 2-43(b). Kishawy and Elbestawi (1999) explained that material being squeezed to the sides at the chip's thin edges results in lateral material flow, leaving material uncut along the machining marks, Figure 2-44(a), which is only considered a roughness concern for surface integrity. Figure 2-44(b) links the chip serrations detected on the chip's thin trailing edges at corresponding cutting conditions to sideflow, suggesting that cutting parameters favouring thin chip geometry, high plasticity and accelerated tool wear rates also result in more severe sideflow presence and notch tool wear.

Zhou et al. (2012) also found that dry turning Inconel 718 using worn ceramic tools at  $V_C = 200$  m/min,  $f = 0.1$  mm/rev and  $a_p = 0.3$  mm resulted in more severe parent material deposits and formation of secondary defects like sideflow, carbide tearing, cracking, cavities and grooves, compared to machining with new tools, Figures 2-45(a-b). Coolant application reduced the defect presence on finished surfaces, improving the overall surface quality for

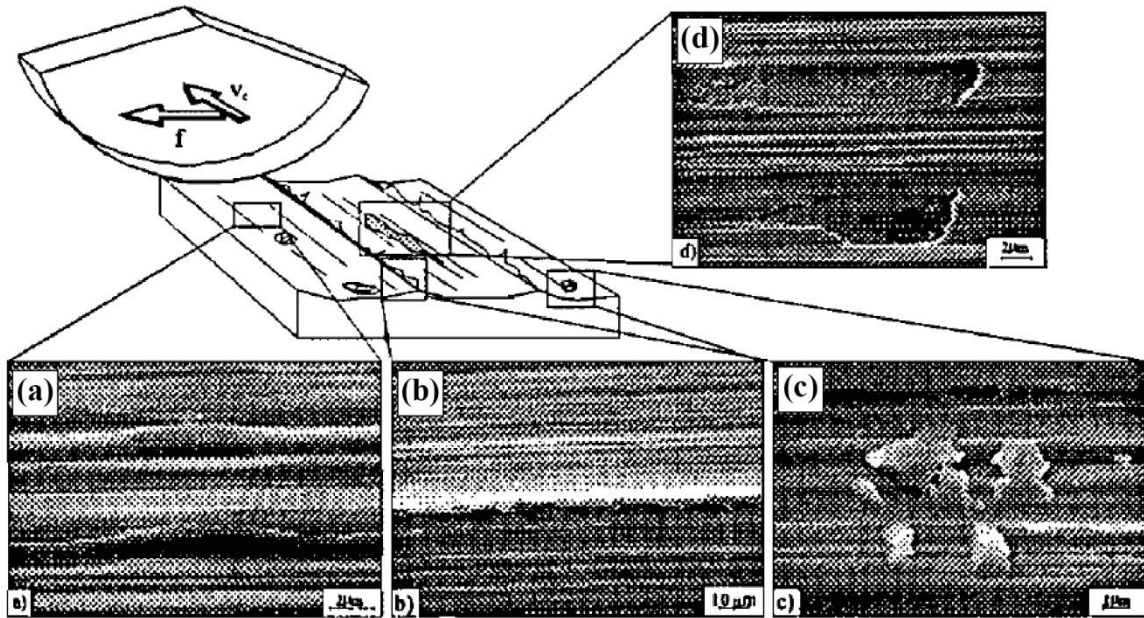


**Figure 2-43: Surface defects in hard turning steel AISI 4615 with ceramic tools at  $V_c = 107 \text{ m/min}$ ,  $r_n = 4.7 \text{ mm}$ ,  $a_p = 0.125 \text{ mm}$  and  $f = 0.075 \text{ mm/rev}$ ; (a) Grooves, (b) Sideflow, (c) Material deposits, (d) Cavities, Bresseler et al. (1997).**

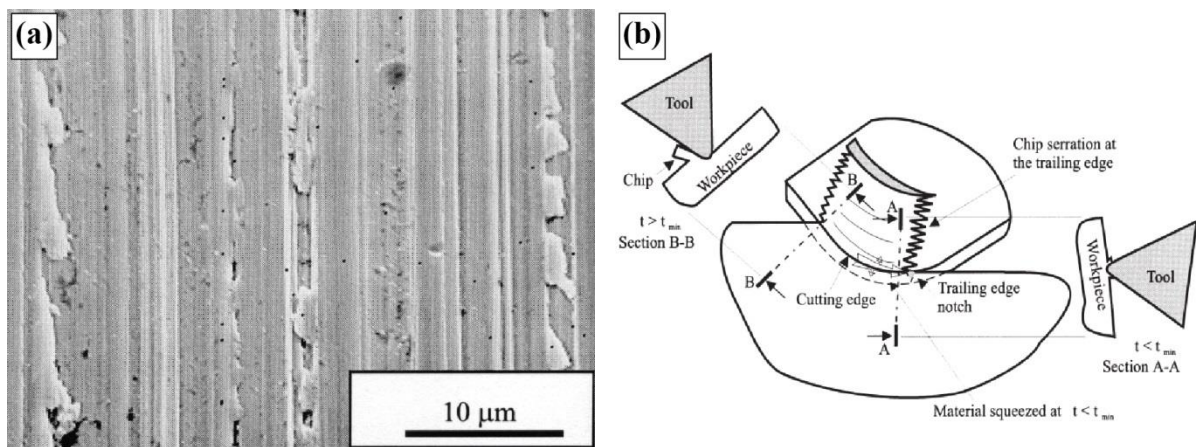


**Figure 2-44: Material side flow in hard turning; (a) Surface defects, (b) Defect formation mechanism, Kishawy and Elbestawi (1999).**

both worn and unworn tool conditions compared to those in dry cuts, Figures 2-45(c-d), though no reasoning was discussed. Furthermore, the authors observed that the deposits, either related to built-up edge (BUE) or chip adherence on the surface, were more severe at

low  $f$  values independently of the other machining parameters, suggesting that the defect formation was related to higher cut ploughing energy at these conditions, though no further evidence were provided in terms of the origin of either deposit type.

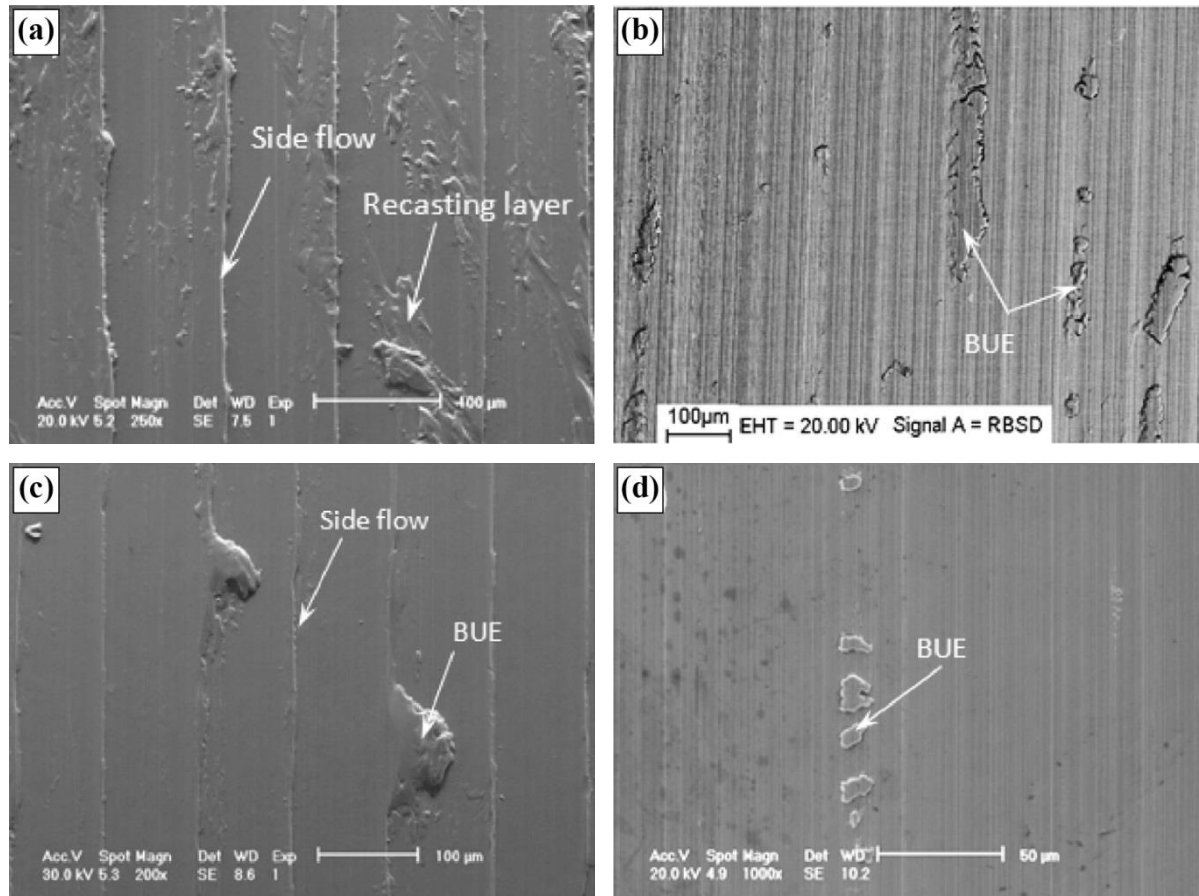


**Figure 2-45: Effect of cooling conditions on surface defects when turning Inconel 718 at  $V_C = 200$  m/min,  $a_p = 0.3$  mm and  $f = 0.1$  mm/rev; Dry cuts (a) Worn tool, (b) New tool, Cooled cuts (c) Worn tool, (d) New tool, Zhou et al. (2012).**

However, Axinte et al. (2006) observed severe parent material deposits, also known as pick-up, smeared on the finished surfaces along the cutting direction when turning RR1000 with round S05F grade (i.e. TiCN/Al<sub>2</sub>O<sub>3</sub>/TiN) carbide tools under flood cooling conditions, Figure 2-46(a). The defects were detected for all assessed parameters, though increasing material removal rates ( $Q$ ), due to the increase in  $V_C$ , combined with high tool wear resulted

more frequent defect deposition, Figures 2-46(b-c), whilst these conditions also resulted in white layer formation, Figure 2-46(d). The authors suggested that pick-ups originated from transferring adhered material present on the tool's cutting edge to the finish turned surface, though no evidence were provided to validate this theory. The low surface roughness values (i.e.  $R_a \leq 0.5 \mu\text{m}$ ) indicate that the cuts were performed at low  $f$ , whilst  $R_a$  appears unaffected by the pick-up deposition.

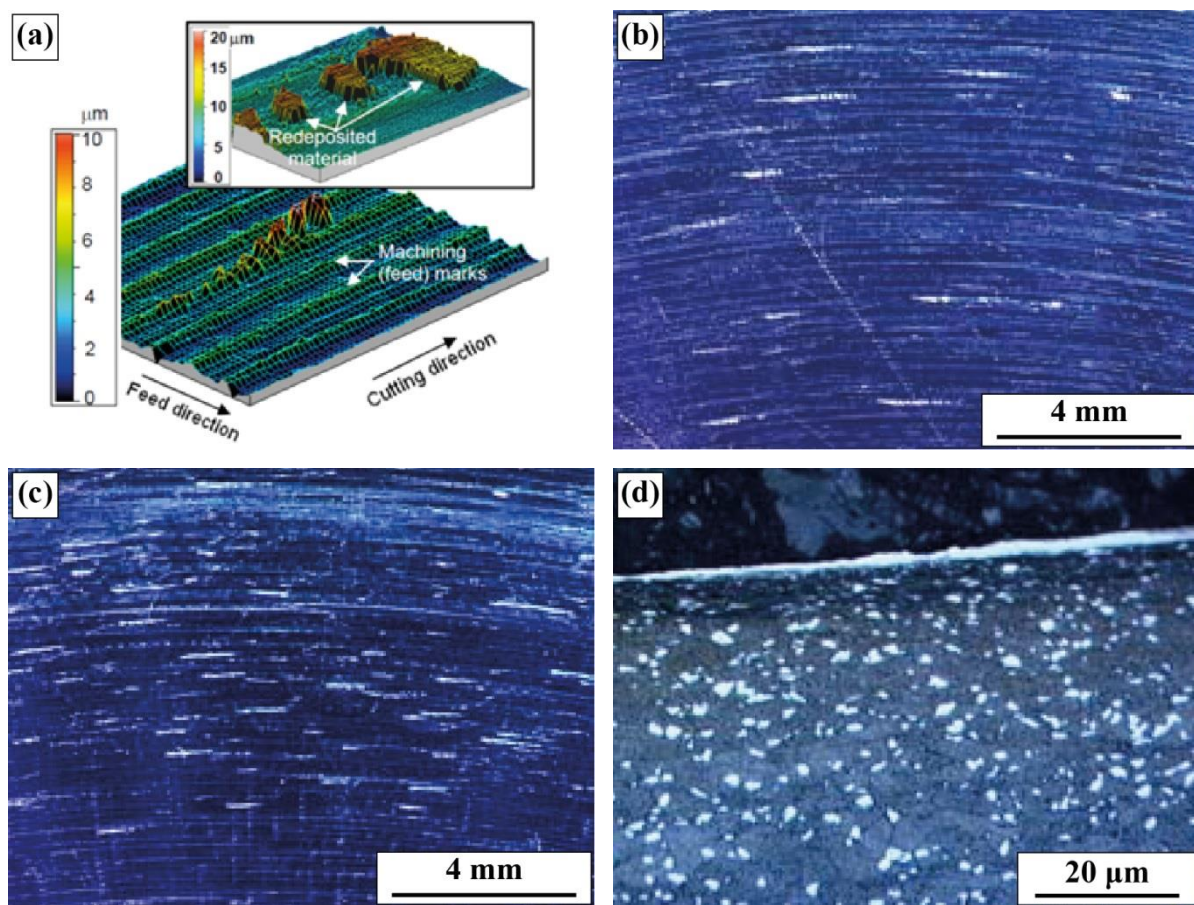


**Figure 2-46: RR1000 finish turned surface integrity; (a) Pick-up 3D morphology, Pick-up deposits (b)  $Q = 30 \text{ mm}^3/\text{sec}$ , (c)  $Q = 37 \text{ mm}^3/\text{sec}$ , (d) Sub-surface damage at  $Q = 37 \text{ mm}^3/\text{sec}$ , Axinte et al. (2006).**

Acceptable RR1000 surface roughness values (i.e.  $R_a \leq 0.8 \mu\text{m}$ ) with pick-up present, Figure 2-47(a) were also produced on finish drilled and milled RR1000 surfaces machined

under cooled conditions and acceptable tool wear, Soo et al. (2011). Similar deposits were also observed by Hood et al. (2016) in drilling and milling Udimet 720, indicating parent material deposits (i.e. pick-up) are not exclusive to turning operations, whilst Sharman et al. (2008) stated that these deposits are not uncommon in hole making operations as a result of chip entrapment between the workpiece and the drilling flute. Figure 2-47(b) shows that the smeared press-welded chips on the finish drilled Inconel 718 surfaces appear as white layer with no further sub-surface damage detected as a result of the defect deposition. The authors stated that the major concern with these deposits in the aerospace industry is that they could potentially cover-up other surface defects critical for fatigue performance, like cracks and cavities.

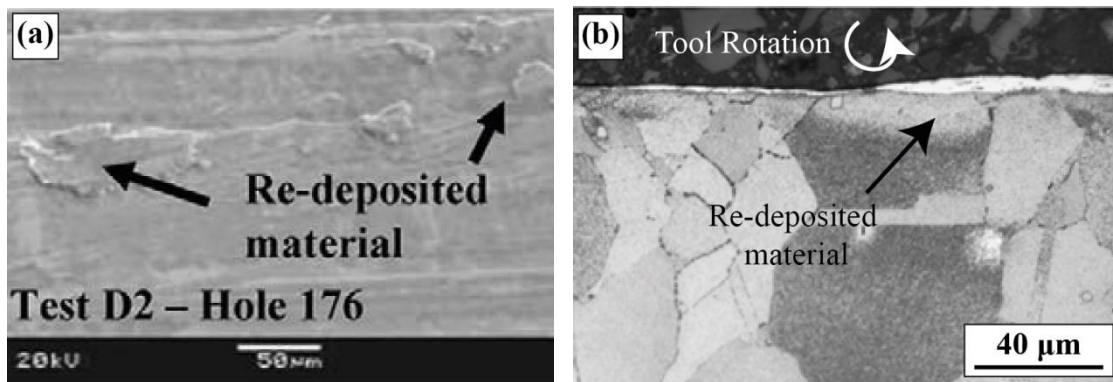


**Figure 2-47: Parent material deposits in hole making operations; (a) Drilling RR1000, Soo et al. (2011), (b) Milling Inconel 718, Sharman et al. (2008).**

### 2.3.4 Cutting Mechanics and Temperatures

Up to this point, chip formation and surface integrity revealed that the ‘physics’ of every cut are dictated by the combined resisting effort of mechanical and thermal loads towards the work put into reforming a workpiece to a preferable shape. Within this section, the relationship between the magnitude of machining forces and temperatures with the material mechanical properties and cutting parameters would be explained, whilst taking into consideration factors altering cutting dynamics during machining (e.g. tool wear).

#### 2.3.4.1 *Cutting Forces*

Crawforth et al. (2016) and Arrazola et al. (2009) demonstrated that machining high strength titanium alloys at identical cutting parameters, for orthogonal and oblique turning respectively, resulted in a range of machining loads depending on both alloy composition and mechanical characteristics, with those demonstrating higher strength and hardness at elevated temperatures also producing higher machining forces. However, Olovsjo and Nyborg (2012) found that turning Waspaloy produced higher machining loads compared to those when turning the stronger, harder and less ductile Inconel 718, whilst the coarse grain microstructure variants of both alloys also resulted in higher forces than those produced for the fine grain variants. Based on these findings, the authors suggested that the material’s resistance to deformation (indicated by the area under the stress-strain curves) defines the deformation work required when machining, and thus a high ductility and relatively strong material may produce higher machining loads than a higher strength and relatively brittle material (conditions that were also proven to affect chip deformation rate, see section 2.3.2).

Thiele and Melkote (1999), who also observed higher resultant machining force when increasing AISI 52100 steel workpiece hardness, reported increase in mechanical loads when turning at higher  $f$ , due to increasing the overall chip material volume removed per unit time, as well as when using tools with larger  $r_e$ , due to increasing the cut's ploughing energy. This explains the significantly higher cutting forces detected when machining Inconel 718 with worn tools, compared to using new tools, as it essentially means machining with blunder tool edges, Figure 2-48, whilst the new tool data show reduction of the machining forces with increasing  $V_C$ . Ng and Aspinwall (2002) explained that increasing  $V_C$  increases the chip shearing angle which forms thinner chips, thus reducing the machining forces acting on the tool, except for conditions of extreme heat for which sharp reduction in mechanical loads may be the consequence of the workpiece's thermal softening.

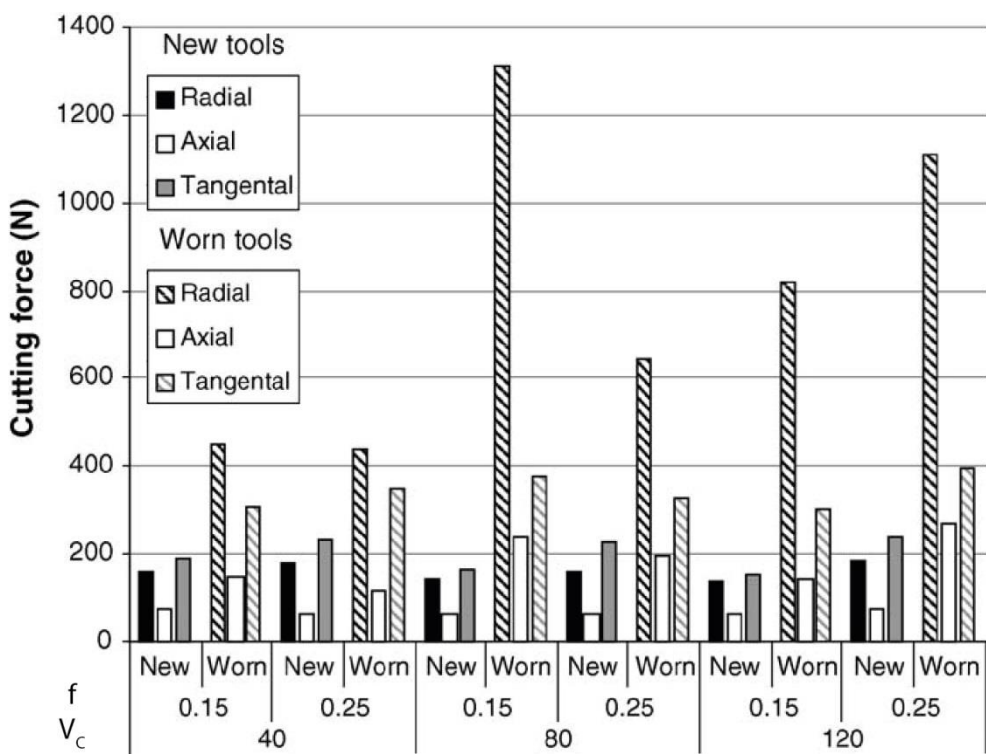


**Figure 2-48: Effect of cutting parameters and tool wear on Inconel 718 turning forces;**

Sharman et al. (2006).

Huang and Liang (2003) reported higher forces in steel machining when using tools with high cubic born nitride (CBN) content compared to those recorded for tools with lower CBN content at identical cutting parameters, Figure 4-49(a), suggesting that the poorer low CBN tool thermal conductivity resulted in higher cutting temperatures causing thermal softening of the workpiece, Figure 2-49(b). Furthermore, Devillez et al. (2007) demonstrated that orthogonal cutting Inconel 718 with coated tools resulted in lower machining forces than those recorded for the uncoated tools, with the authors suggesting that coatings reduced friction between the chip-tool-workpiece interfaces due to their better tribological properties, even though the phenomenon was not validated for higher material removal rates. Assessing though the performance of similar conditions when machining Inconel 825 at low  $f$ , Thakur et al. (2014) reported that uncoated tools produced thicker chips than the coated tools, indicating that factors affecting the cut's thermodynamics also affect chip formation; thus controlling indirectly the machining loads magnitude. Li et al. (2014) also stated that the so-called 'thermomechanical' conditions effect on chip formation was responsible for the oscillating thermal and mechanical loads recorded when forming segmented chips, with peak cutting temperatures and lower cutting forces recorded when forming shear bands (i.e. chip thermal softening), whilst machining loads peaked when shearing the chip segments at lower cutting temperature, Figure 2-50.

It is therefore clear that the cutting parameters and workpiece properties define the work required for machining, which in its own turn affects the balance between the interacting relationship of mechanical and heat loads. Heat influences the chip and surface tolerance to deformation with the cutting forces simply representing the workpiece physical response to chip formation and surface deformation.

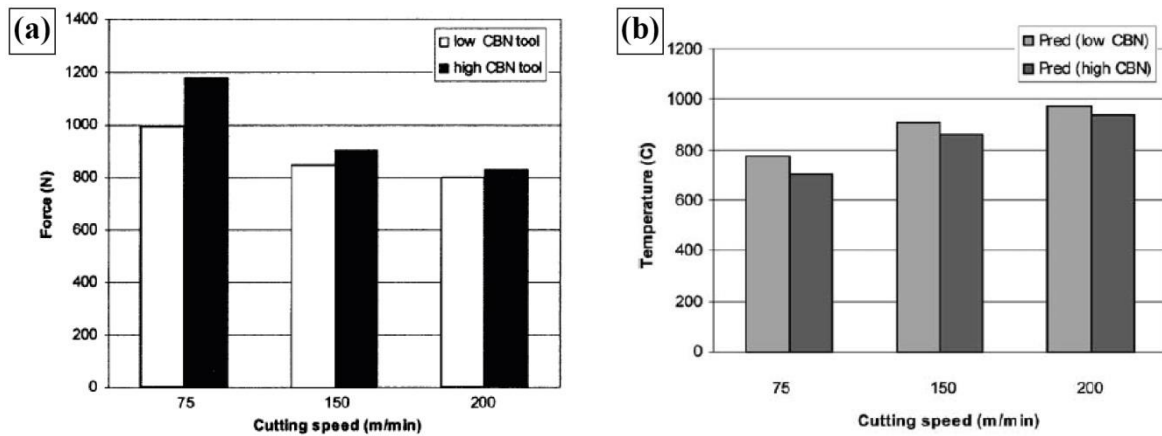


**Figure 2-49: Effect of the tool's CBN content on AISI H13 steel machining conditions;**

**(a) Cutting forces, (b) Predicted cutting temperature; Huang and Liang (2003).**

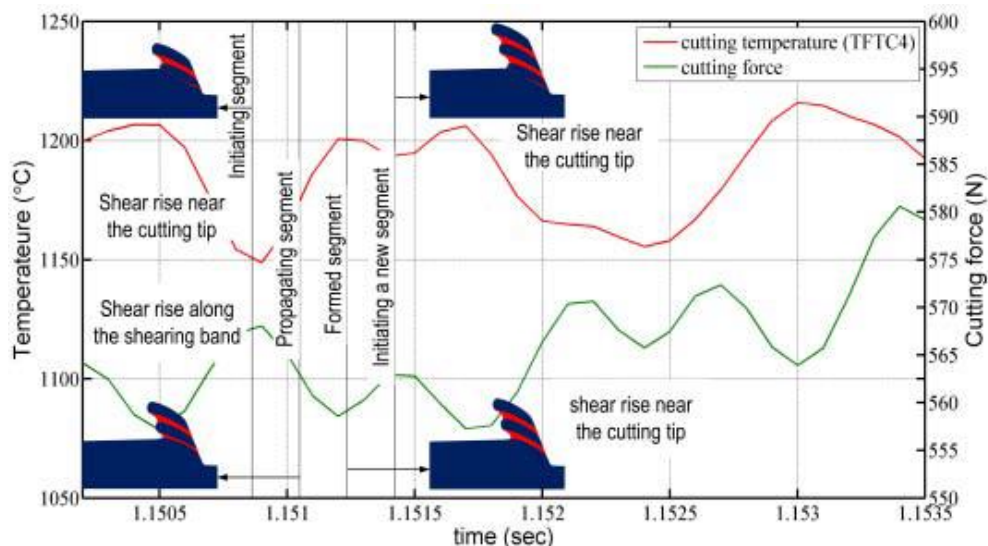


**Figure 2-50: Temperature and cutting force relationship in segmented chip formation,**

**Li et al. (2014).**

### 2.3.4.2 Cutting Temperatures

Parameters controlling heat generation and heat dissipation are critical in machining as the majority of work put into plastically deforming the chip and surface transforms into heat. Strength being the major material property resisting deformation affects cutting temperatures the most, whilst poor workpiece thermal conductivity, like those of high strength titanium

and nickel based alloys, increases further the temperatures developed in the cutting zone. Figure 2-51(a) illustrates that heat is primarily generated in the primary and secondary chip deformation zones (of which a very small amount is friction related), which also explains the fact that higher temperatures are developed closer to the cutting edge.

The magnitude of cutting temperatures is also affected by the selection of machining parameters, with conditions increasing the cut's ploughing energy (e.g. chip thinning conditions and large edge rounding) and those increasing the overall work required for machining (e.g. increase in the material volume removed per unit time) resulting in higher heat levels, Chen et al. (2006) and Nedic and Eric (2014), while it was demonstrated that increasing cutting speed ( $V_C$ ) has the most steep effect in cutting temperature increase, El-Wardany et al. (1996). Kitagawa et al. (1997) reported cutting temperatures up to 1000°C for titanium alloys and 1200°C for nickel alloys, whilst more moderate finishing conditions when machining Inconel 718 produced temperatures in the range of 800-900°C at the tool's cutting edge, Figure 2-51(b). Simulation models developed by Ozel et al. (2011) to examine Inconel 718 chip formation turning conditions confirmed these experimental trends, with lower cutting temperatures detected at  $V_C = 30$  m/min compared to those found at  $V_C = 70$  m/min (verifying the residual stress findings indirectly suggesting higher heat loads at high  $V_C$  conditions, discussed in section 2.3.3.1), whilst in both cases higher heat loads were observed in the cutting zones compared to those at the tool edges, Figure 2-52.

Komanduri (1982) stated that for all cutting conditions the majority of heat is dissipated through the chip, explaining the hotter chip surfaces reported above, whilst it was demonstrated that higher  $V_C$  values reduce the percentage of heat dissipated through the tool and the workpiece subjecting the chip at even higher heat loads. Smart and Trent (1975b) explained that this variation in heat flux is promoted by the  $V_C$  increase and/or the machining

of less ductile material variants, either of which result in lower chip thickness deformation ratio values that accelerates material flow through the cutting zone and thus concentrating the majority of heat in the chip. Furthermore, heat flux was found to be affected by the tool material thermal conductivity and the tool coating grade, both of which control the heat diffusion rate through the tool body, Ostafiev et al. (1999). Chinchanikar and Choudhury (2014) demonstrated the TiAlN coating resulted in lower cutting temperature compared to the superior thermal barrier multilayer coating TiCN/Al<sub>2</sub>O<sub>3</sub>/TiN, suggesting that the coating's insulating performance controls the amount of heat reflected back to the cutting zone and thus affecting the maximum cutting temperature. Finally, Huda et al. (2002) observed reduction in the overall cutting temperature due to coolant application on the tool's rake face compared to those detected in dry machining at identical cutting parameters, indicating that coolant acts as heat removal agent and thus cooling performance is another factor affecting the cut's heat flux balance, which would be discussed further in section 2.3.5.

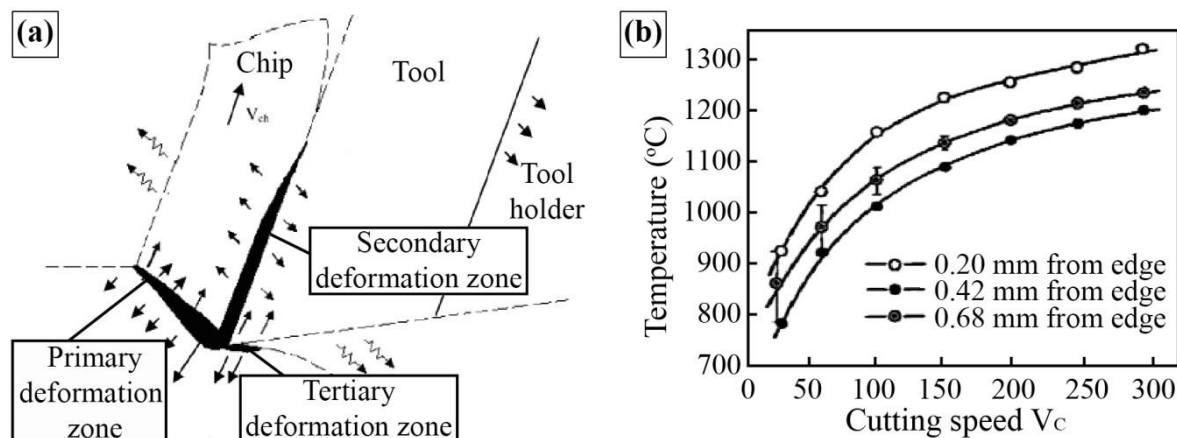


**Figure 2-51: Thermodynamics in material removal operations; (a) Heat generation and dissipation areas, Abukhshim et al. (2006), (b) Cutting temperatures in turning Inconel**

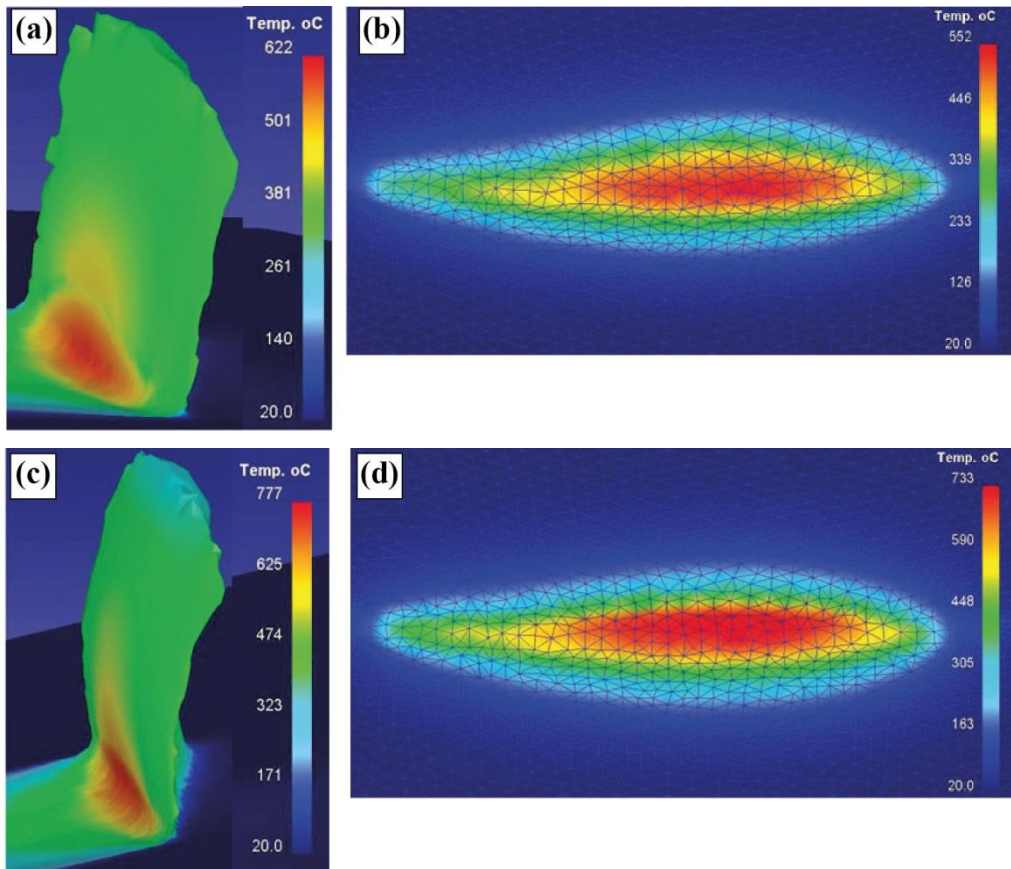


**Figure 2-52: Cutting speed effect on Inconel 718 cutting temperatures;  $V_C = 30 \text{ mm/min}$**

(a) Chip and (b) Tool,  $V_C = 70 \text{ mm/min}$  (c) Chip and (d) Tool, Ozel et al. (2011).

#### 2.3.4.3 Effect on Tool Performance

Tool wear has already been proven a major factor affecting both chip formation and surface quality, whilst tool life is often used to quantify workpiece machinability. More difficult to machine materials, like nickel based alloys compared to iron based steels, result in poorer tool life at identical cutting parameters due to subjecting the tool edges in higher mechanical and thermal machining loads, Wright and Chow (1982). Higher workpiece strength and hardness were linked to accelerated tool wear rates, Arrazola et al. (2009), which was even verified when Olovsjo and Nyborg (2012) reported lower mechanical loads for machining Inconel 718 compared to machining Waspaloy, with the stronger and harder alloy still

resulting in almost double flank wear. Therefore to withstand plastic deformation, tools are manufactured using harder materials than the machined workpieces, with carbide and ceramic tools being ideal choices for conventional and high speed machining of strong alloys, respectively. Coating these tools with thermal barriers was found to improve flank wear life up to 10 times and reduce crater (rake) wear rate by up to 100 times compared to uncoated tools, Dearnley and Trent (1982), whilst the performance gap between different coating types is significantly smaller, Sharman et al. (2001). This also explains the fact that major coated tool wear mechanisms, like uniform flank wear and rake crater wear seen in Figures 2-53(a-b), are usually formed due to diffusion wear (in addition to abrasive wear) which is heat activated. Furthermore, Figure 2-53(c) shows notch wear forming at the maximum depth of cut point, which is a phenomenon often linked to burr formation, Chandrasekaran and Johansson (1994), whilst Kishawy and Elbestawi (1999) reported severe notch wear at the tool's trailing edge due to formation of chip sideflow, Figure 2-53(d).

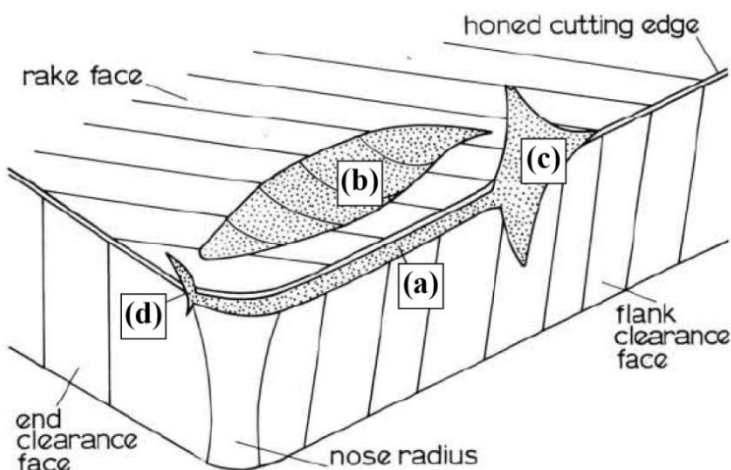


**Figure 2-53: Tool wear mechanisms of coated tools; (a) Flank wear, (b) Crater Wear, (c) Notch wear - Leading edge, (d) Notch wear - Trailing edge, Dearnley and Trent (1982).**

Xue and Chen (2011) also detected the formation of adhered layer on both rake and flank tool faces when machining nickel based superalloy GH4169 with coated tools at  $V_C \leq 82$

m/min, Figures 2-54(a-b), which according to the authors protected the tools from excessive mechanical-abrasive wear, though it accelerated diffusion wear. Furthermore, the severe adhered material stacking observed at the tool's leading cutting edge area when machining at  $V_C = 82$  m/min and its more extensive presence at lower cutting speeds, indicated that the phenomenon (also known as built-up edge) was promoted by cooler cutting conditions, whilst the frequent failure of this unstable adhesive wear mechanism let to plucking of the tool's coated surfaces as well as severe notch wear. However, higher cutting speed ( $V_C = 115$  m/min) increased the cutting temperature accelerating diffusion wear, which replaced the rake face adhered layer seen at lower  $V_C$  with the formation of craters, Figure 2-54(c), while flank face adhered layer remained unaffected, Figure 2-54(d).

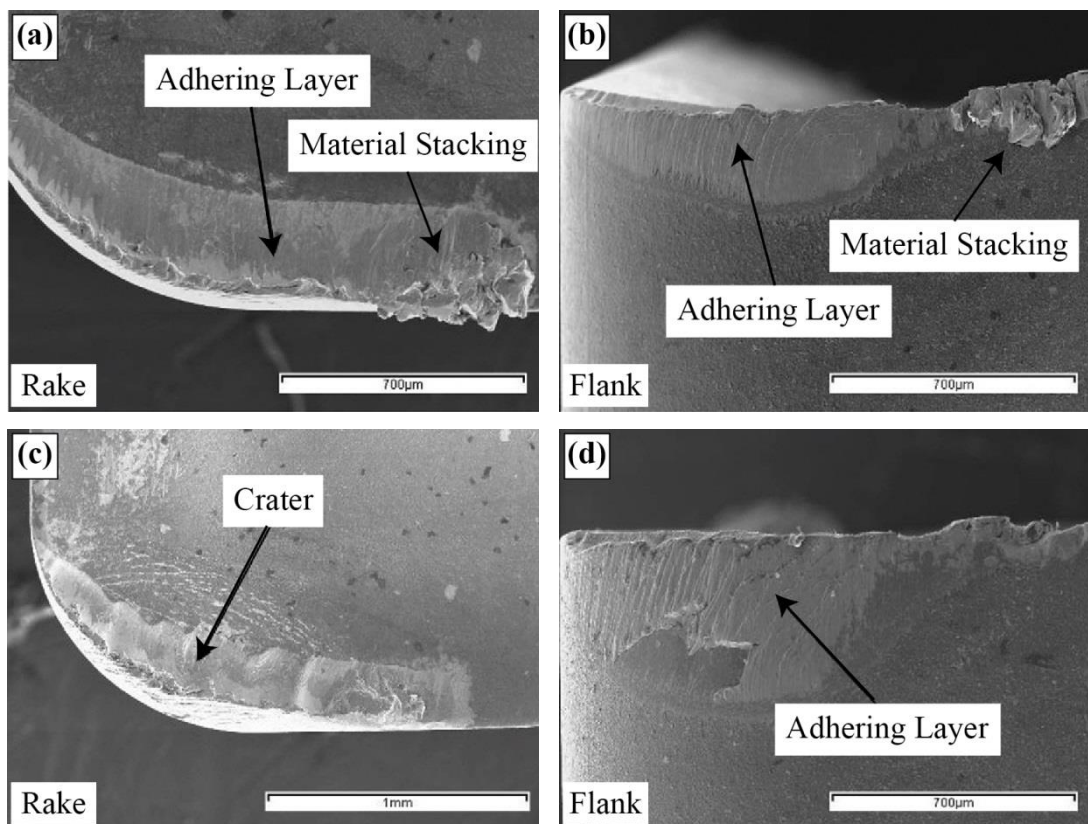


**Figure 2-54: Tool wear mechanisms when turning GH4169 at  $f = 0.13$  mm/rev and  $a_p = 1.2$  mm; (a-b)  $V_C = 82$  m/min, (c-d)  $V_C = 115$  m/min, Xue and Chen (2011).**

Ezugwu et al. (1999) and Bhatt et al. (2010) observed the same transformation in dominant wear mechanisms presented above when turning Inconel 718 at varying cutting speed ( $V_C$ ), whilst excessive flank face wear was the primary tool failure mode; same as when machining AISI 52100 steel with CBN tools, Huang and Liang (2005). Furthermore, they all agreed that tool life reduced, independently of the tool grade, with increasing depth of cut, feed rate and cutting speed due to the higher material removal rates resulting in higher cutting temperatures. Interestingly, however, Bhatt et al. (2010) also found that the single coating layered (TiAlN) tool outperformed the triple coating layered (TiCN/Al<sub>2</sub>O<sub>3</sub>/TiN) tool when machining Inconel 718 at conventional cutting speeds ( $V_C \leq 75$  m/min), while their comparable tool life performance was reversed at  $V_C = 100$  m/min. Even though provided no further explanation was provided, linking this phenomenon to the significantly reduced thermal conductivity of Al<sub>2</sub>O<sub>3</sub> with higher temperatures (from 36.0 W m<sup>-1</sup> K<sup>-1</sup> at ambient temperature to 6.1 W m<sup>-1</sup> K<sup>-1</sup> at 1273 K), Grzesik (1998), explains its superiority at high speed conditions compared to other thermal barriers. This phenomenon proves once more the tool wear performance dependency to cutting temperatures, whilst indirectly confirming the effect of increasing  $V_C$  on machining temperature and thus the chip formation mechanics.

Finally, Cantero et al. (2013) observed that machining Inconel 718 under cooled conditions improved tool life compared to dry machining, whilst Dhar and Kamruzzaman (2007) found that tool life also depends on the selected cooling strategy. For example in steel turning, cryogenic cooling produced the lowest cutting temperature resulting in extended tool life, compared to conventional cooling that resulted in higher tool wear rates due to hotter cutting conditions, whilst for both cases tools performed better than those used in dry machining.

### 2.3.5 Cooling Strategy

So far, it was demonstrated that coolant application acts as heat sink affecting both cutting heat flux and overall cutting temperatures, and thus controlling the magnitude of surface residual stresses and tool life performance during machining. Dahlman (2002) though suggested that it's the overall coolant momentum increase that results in lower tool temperature (i.e. combined effect of coolant pressure ( $P$ ) and coolant flow rate ( $\lambda$ )), with higher  $\lambda$  having greater effect on temperature reduction and high  $P$  producing lower temperatures at identical coolant momentum conditions.

Furthermore, Klocke et al. (2011) reported up to 30% reduction in tool interface temperature when turning Inconel 718 using higher  $P$  and  $\lambda$ , Figure 2-55, with the data indicating that above a so-called ‘critical’ coolant momentum value (cutting parameters depended) the effect on temperature remains constant. Figure 2-56 also shows decrease in tool temperature with increasing  $P$  when turning Ti6Al4V, though temperature at the tool’s interface increased with increasing  $\lambda$  at identical  $P$  conditions. The authors suggested that reducing cutting temperatures resulted in lower thermal conductivity and higher strength of the workpiece, increasing heat dissipation through the tool and causing higher chip deformation mechanical and thermal loads, respectively, explaining this phenomenon. Same principles apply for the findings by Palanisamy et al. (2009) that observed variation in chip formation (i.e. more frequent Ti6Al4V chip segmentation and thicker shear bands) with increasing  $P$ , from 6 to 90 bar at identical machining parameters. The phenomenon is indicative of more work required to deform the cooler and thus stronger chips produced at high  $P$  conditions, showing that improved cooling performance has opposite effect to that of increasing cutting speed (discussed in section 2.3.2).

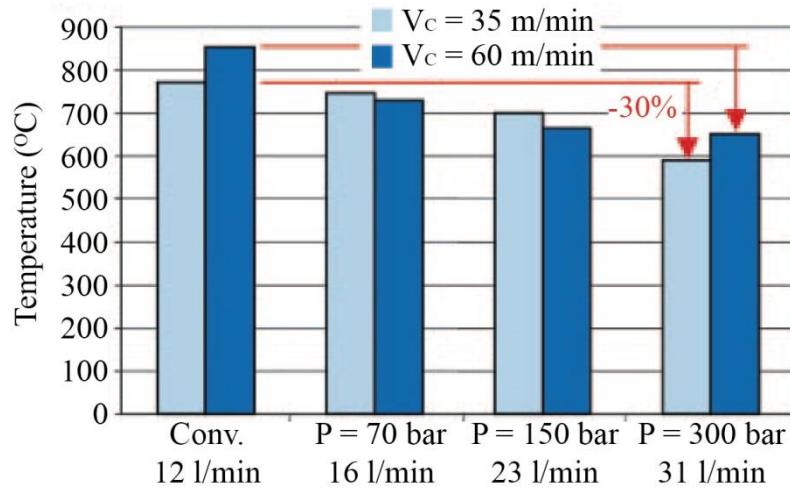


**Figure 2-55: Cooling strategy effect on tool temperatures when turning Inconel 718 at  $a_p = 1 \text{ mm}$  and  $f = 0.2 \text{ mm/rev}$ , Klocke et al. (2011).**

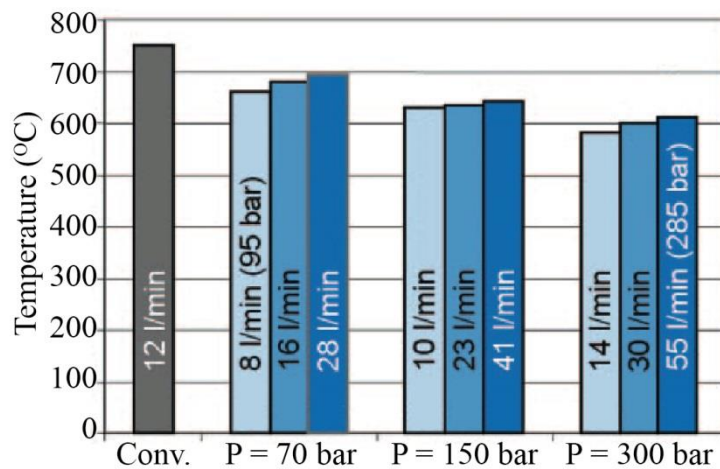


**Figure 2-56: Cooling strategy effect on tool temperatures when turning Ti6Al4V at  $a_p = 1 \text{ mm}$  and  $f = 0.2 \text{ mm/rev}$ , Klocke et al. (2011).**

Sanchez et al. (2012) observed variation in steel SAE EV-8 chip morphology (i.e. chip ribbon length and spiral diameter) when altering coolant delivery strategy, i.e. flood cooling the cutting zone, Figure 2-57(a), versus using focused cooling at identical flow rate ( $\lambda$ ), Figure 2-57(b), or cooling different cutting interfaces, Figures 2-57(b-d). They also found that cooling process affects chip shearing, with higher pressure and flow rate conditions resulting in both thicker chips (i.e. reduced shearing angle) and lower cutting temperatures.

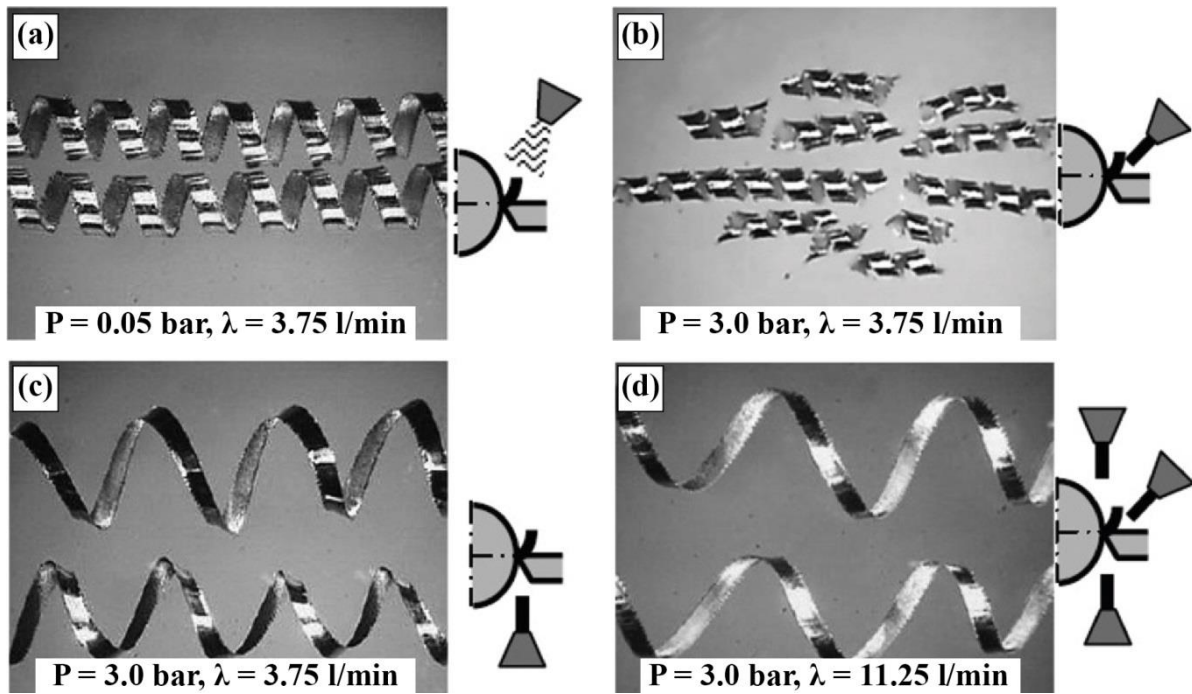


**Figure 2-57: Effect of cooling strategy performance and coolant supply jet configuration on chip morphology when turning steel SAE EV-8; (a) Conventional flood cooling, (b) Focused rake cooling, (c) Focused flank cooling, (d) Focused multi-face cooling, Sanchez et al. (2012).**

Sørby and Tønnessen (2006) and Diniz and Micaroni (2007) though observed that for constant  $P$  and  $\lambda$  when turning Ti6Al4V and hard steels, respectively, the combination of rake and flank face cooling out-performed in tool life the more conventional rake-only cooling strategy. Li (1995) also demonstrated that flank face cooling produced similar rake temperature distribution to that of rake face cooling, though it reduced peak temperature on the flank by up to 30% at high  $\lambda$ . Combined these evidences explain the findings by Sharman et al. (2008) that reported only compressive surface residual stresses when turning Inconel 718 while supplying coolant in the flank face zone, whilst the rake-only cooling strategy produced tensile stresses (i.e. the highest were reported when flood cooling though their value reduced with increasing  $P$  and  $\lambda$ ), as these data are indicative of reduced cutting

temperatures developed in the cutting zone close to the cutting edge and finished surface under flank face cooling conditions. Furthermore, the phenomenon aligns with the flank clearance cooling strategy proposed by Smart and Trent (1975a) as the most appropriate for nickel turning, due to their findings suggesting that dry machining this material type results in peak tool cutting temperature at the flank face, Figure 2-58(a). Figure 2-58(b) shows that the suggested cooling strategy resulted in lower temperature profiles along the tool's cutting profile compared to that of rake cooling, Figure 2-58(c). The authors suggested that exposing the hotter part of the tool to coolant supply reduced localised heat concentration; accelerating heat dissipation and thus limiting temperature distribution.

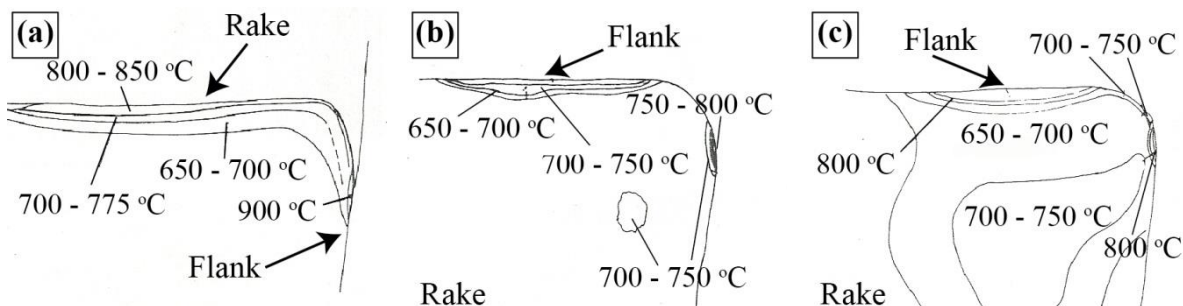


**Figure 2-58: Effect of cooling strategy on tool temperatures when turning nickel at  $V_C = 46 \text{ m/min}$ ,  $a_p = 1.25 \text{ mm}$  and  $f = 0.25 \text{ mm/rev}$ ; (a) Dry machining – Tool cross-section, (b) Flank face cooling, (c) Rake face cooling, Smart and Trent (1975a).**

It is clear that selecting an optimum cooling strategy for enhancing control over machining ‘dynamics’, known to have major effect on surface integrity and chip formation, requires considering three basic key process variables affecting its overall performance:

- Cooling pressure ( $P$ ),
- Coolant flowrate ( $\lambda$ ),
- Cooling position.

## 2.4 SUMMARY

Within this literature review it was found that machining ‘mechanics’ are defined by the workpiece physical ‘response’ to plastic deformation during the complex shearing and fracturing process of chip formation and surface reformation. This explains the impact of workpiece properties (i.e. strength, ductility, heat conductivity etc.) and selected machining parameters (i.e.  $V_C$ ,  $a_p$ ,  $f$ ,  $r_n$  and tool coating etc.) on the mechanical and heat machining conditions, which affect tool life, surface integrity and chip tolerance to plasticity. Furthermore, literature outlined some key differences between FG RR1000 production line and other superalloys like 1. FG RR1000 exhibits lower ductility than other nickel based superalloys and 2. FG RR1000 strict production standards only allow for specific parameters to be used during machining, for example for low feed rates. Both conditions have major role in the FG RR1000 turning operations, which are vulnerable to frequent pick-up occurrence on finished surfaces, whilst similar defects are also common in hole making operations.

Beyond this, little information is available in literature describing the occurrence conditions of pick-up on RR1000. Overall, detailed studies of pick-up and surface defects in turning operations are limited but indicate that surface deposits occur when materials that have good high temperature strength are machined dry, at a low feed rate ( $f$ ), whilst severity increases with increasing cutting speed ( $V_C$ ), Table 2-3. With the exception of Zhou et al. (2012) who reported reduction in surface deposits with coolant application and increasing feed rate, researchers have failed to identify that low  $f$  is a common factor in pick-up development on machined surfaces. They also failed to identify that similar parameters favouring the presence of this defect, especially low  $f$ , often resulted in the formation of serrations at the chip’s thin trailing edge, Table 2-4. El-Wardany and Elbestawi (1998) for example linked these chip

'thinning' conditions to chip serrations and the surface defect called sideflow, though neither provided evidence or discussed any possible link to this phenomenon and pick-up.

Consequently, there is a gap identified in literature concerning the origin of pick-up, its formation mechanism as well as its deposition mechanism. The proposed theory that high surface temperature is responsible for pick-up deposition was considered insufficient, as high heat loads during cutting may well serve as favouring condition, though it does not reveal the defect's causing mechanism. The same stands for the findings indicating pick-up reduction at high  $f$  and/or under cooled conditions, as no further explanation was provided about the effect of these parameters on pick-up formation mechanism and the extent of surface integrity improvement. Therefore, this work aims to:

- Identify the origin of pick-up formation and deposition on RR1000 surfaces.
- Investigate possible link between pick-up and the chip deformation mechanism, especially serration formation.
- Investigate the effect of microstructure and mechanical properties on pick-up presence and severity.
- Enhance understanding about the effect of machining parameters on chip formation and pick-up severity.
- Investigate the possible link (and reasoning) between coolant application and reduction of pick-up damage.
- Examine the effect of machining strategies on pick-up formation mechanism beyond the fixed RR1000 production process, like using sharper tools or enhanced cooling performance, proven to reduce severity of machining conditions with promising improvements on other machining elements (i.e. tool life and surface integrity).

**Table 2-3: Summary of surface material deposit observations in literature.**

<b>Author(s)</b>	<b>Operation</b>	<b>Parameters</b>	<b>Remarks</b>
Arunachalam and Mannan (2003)	Turning	Inconel 718 $V_C = 40\text{-}80 \text{ m/min}$ $r_n = 0.8\text{-}1.6 \text{ mm}$ $f = 0.10 \text{ mm/rev}$ $a_p = 0.50 \text{ mm}$	Increasing $V_C$ resulted in more severe material surface deposits. The authors suggested that high surface temperatures promoted the phenomenon.
Arunachalam et al. (2004b)	Turning	Inconel 718 $V_C = 125\text{-}475 \text{ m/min}$ $r_n = 0.8 \text{ mm}$ $f = 0.05\text{-}0.15 \text{ mm/rev}$ $a_p = 0.50\text{-}1.00 \text{ mm}$	Material surface deposit severity increased at higher $V_C$ . The authors suggested that high surface temperatures promoted the phenomenon.
Pawade et al. (2007)	Turning	AISI 4615 steel $V_C = 90\text{-}250 \text{ m/min}$ $r_n = 0.4\text{-}3.2 \text{ mm}$ $f = 0.05\text{-}0.10 \text{ mm/rev}$ $a_p = 0.125 \text{ mm}$	Serrations formed at the thin chip trailing edges were linked to the formation of the surface defect known as sideflow.
Bresseler et al. (1997)	Turning	Inconel 718 $V_C = 100\text{-}400 \text{ m/min}$ $r_n = 1.2 \text{ mm}$ $f = 0.10\text{-}0.20 \text{ mm/rev}$ $a_p = 0.3 \text{ mm}$	Increasing $f$ and applying coolant reduced the severity and occurrence rate of surface deposits.
Kishawy and Elbestawi (1999)	Turning	RR1000 $Q = 20\text{-}37 \text{ mm}^3/\text{sec}$ $r_n = 0.8\text{-}1.2 \text{ mm}$ Flood cooling	Low surface roughness Ra values suggest the use of low $f$ in these experiments. More severe pick-up occurrence was observed at high $Q$ .
Zhou et al. (2012)	Turning		
Axinte et al. (2006)	Turning		
Soo et al. (2011)			
Hood et al. (2016)	Drilling and	RR1000 Udimet 720	Pick-ups were also observed in hole-making operations for a range of superalloys.
Sharman et al. (2008)	Milling	Inconel 718	

**Table 2-4: Summary of chip edge serration observations in literature.**

<b>Author(s)</b>	<b>Operation</b>	<b>Parameters</b>	<b>Remarks</b>
Kishawy (1998)	Turning	AISI 1550 steel $V_C = 90\text{-}200 \text{ m/min}$ $r_n = 1.2\text{-}3.6 \text{ mm}$ , $f = 0.05\text{-}0.20 \text{ mm/rev}$ $a_p = 4.0 \text{ mm}$	Serrations were formed at the thin chip trailing edges, due to high plastic deformation of the chip material machined below the tool edge rounding.
El-Wardany et al. (2000b)	Turning	AISI 4615 steel $V_C = 90\text{-}250 \text{ m/min}$ $r_n = 0.4\text{-}3.2 \text{ mm}$ $f = 0.05\text{-}0.10 \text{ mm/rev}$ $a_p = 0.125 \text{ mm}$	Larger chip serrations were observed under chip thinning conditions, i.e. at higher $r_n$ and lower $f$ values.
El-Wardany and Elbestawi (1998)	Turning	Inconel 718 $V_C = 40\text{-}60 \text{ m/min}$ $r_n = 0.8 \text{ mm}$ , $f = 0.08 \text{ mm/rev}$ $a_p = 0.5 \text{ mm}$	Serrations were observed at the chip's thin trailing edge when machining at $V_C \geq 50 \text{ m/min}$ .
Thakur et al. (2009)	Turning	Inconel 718 $V_C = 125\text{-}475 \text{ m/min}$ $r_n = 0.8 \text{ mm}$ , $f = 0.05\text{-}0.15 \text{ mm/rev}$ $a_p = 0.5\text{-}1.0 \text{ mm}$	Serrations appear to form at thin chip trailing edges, though no explanation was provided by the authors.
Pawade et al. (2008)	Turning	Aluminium alloys $V_C = 450 \text{ m/min}$ $r_n = 5.0 \text{ mm}$ $f = 0.02 \text{ mm/rev}$ $a_p = 0.002 \text{ mm}$	Serrations appear to form at thin chip trailing edges, though no explanation was provided by the authors.
Asai and Kobayashi (1990)	Micro-Turning	ASSAB 718 steel $V_C = 150 \text{ m/min}$ $f = 0.05 \text{ mm/tooth}$ $a_p = 0.35 \text{ mm}$	Varying cooling conditions appear to affect serration formation at the chip's thin trailing edge.
Kumar et al. (2002)	Milling		

## 3 EXPERIMENTAL WORK

### 3.1 INTRODUCTION

In order to successfully fulfil the aims of this work a series of experimental trials were designed based on the literature review findings, focusing on exploring the performance of cutting conditions both in and out of FG RR1000 validated production strategy boundaries.

Phases 1-2 of experiments were designed to investigate pick-up for FG and CG RR1000 and compare their performance to the baseline Alloy 718 material. Phase 1 trials were conducted at fixed low feed rate and a variety of material removal rates, under dry conditions, to identify the key parameters promoting the occurrence of parent material deposition when turning superalloys. Phase 2 of experiments investigated the role of coolant application on RR1000 chip morphology, serration formation and surface finish, especially pick-up deposition. Therefore, Phase 2a run under minimum cooling conditions and Phase 2b under conventional low pressure cooling supply in order to compare the findings to the dry cuts conducted in Phase 1. Furthermore, Phase 2b examined the effect of feed rate on serration formation and pick-up at specific identical material removal rates.

Phase 3 of experiments was designed to assess the impact of cooling performance, i.e. flow rate, pressure and cooling position, on FG RR1000 chip formation, aiming to identify an optimised production line cooling strategy, focusing on conditions that could possibly reduce pick-up occurrence risk. Finally, Phase 4 examines the possible effects of tool related parameters on chip formation and pick-up origin, i.e. tool radius, edge rounding and coating.

## 3.2 EXPERIMENTAL PROCESS

### 3.2.1 Pick-up Investigation Trials (Phases 1-2)

Face turning trials were conducted using a Cincinnati Hawk 300 horizontal lathe, used for oblique turning cuts, equipped with a Kistler 9121 dynamometer in series to a 5070A 8-channel charger amplifier and a 5697A analogue to digital data acquisition system to collect 1000 force readings per sec (1000 Hz), Figure 3-1(a). All experiments were run to a fixed spiral cutting length with the tool moving in the feed direction across the rotation axis, while the workpiece rpm increased with the cut progression in order to maintain a constant cutting speed ( $V_C$ ), Figure 3-1(b).

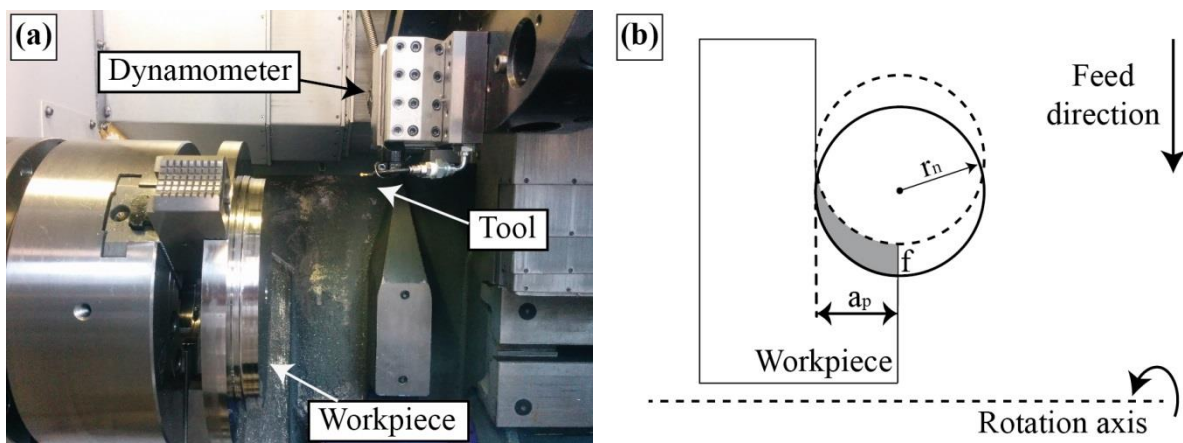


**Figure 3-1: Trials Phases 1-2; (a) Machining setup, (b) Experimental configuration.**

Sandvik Corocut 1-2 round (RO) tools used for profiling, Figure 3-2(a), were selected for the purposes of these experiments, representing more than 85% of the tools used in FG RR1000 finish turning operations. Each experiment was run using new N123F2-0300-RO S05F tool, which is the middle range tool radius ( $r_n$ ) option used in these operations by Rolls-Royce plc; with  $r_n = 1.5$  mm, 7° clearance angle, 7° positive rake angle, built-in chip breaker and edge rounding ( $r_e$ ) measured at 35 $\mu$ m ( $\pm 2\mu$ m), Figure 3-2(b). S05F is the primary coated

fine grain carbide cutting tool option for these finishing operations, selected for its high temperature and wear resistant performance provided by the  $4\mu\text{m}$  TiN/Al<sub>2</sub>O<sub>3</sub>/TiCN chemical vapour deposited (CVD) coating layer, Figure 3-2(c). An appropriate tool holder configuration, 570-25NG-2020 tool shank combined with a 570-25L123G13C tool blade, was used to ensure  $90^\circ$  angle of attack in regards to the face of the workpiece and allow the natural rake and flank clearance angles of the tool.

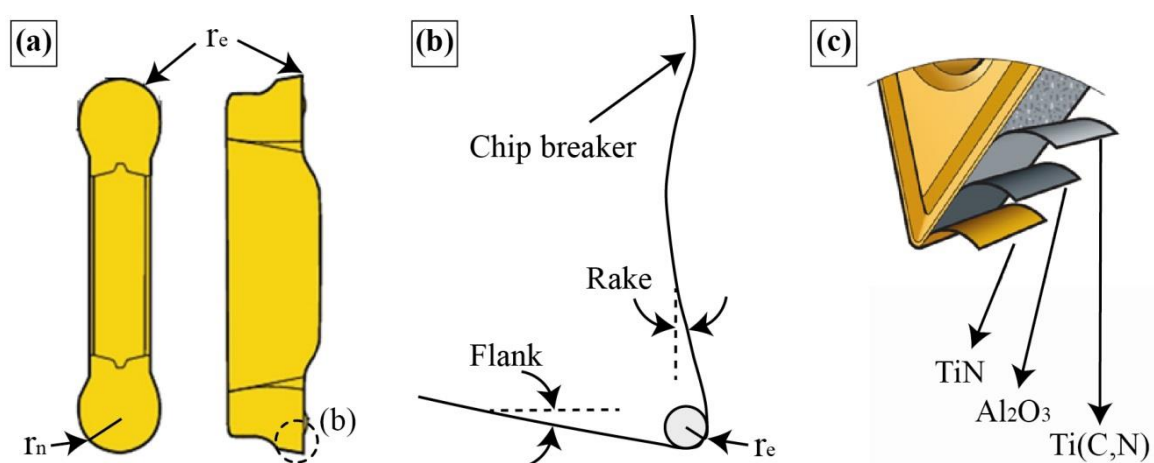


**Figure 3-2: Cutting tools used in the experimental trials; (a) Tool geometry, (b) Cutting edge cross-section, (c) S05F coating grade. {Courtesy of Sandvik}**

The RR1000 material used in this work, chemical composition 15% Cr, 18.5% Co, 5% Mo, 3% Al, 3.6% Ti, 2% Ta, 0.5% Hf, 0.06% Zr, 0.027% C, 0.015% B and Ni balance, was subjected to two different heat treatments, below and above the strengthening solvus temperature. This produced material for machining trials with fine grain (FG) microstructure of average grain size ASTM 12.0-11.5 (i.e.  $5\text{-}7 \mu\text{m}$ ) and primary  $\gamma'$  particles of  $2\text{-}3 \mu\text{m}$  in cross-section, Figure 3-3(a-b), and coarse grain (CG) microstructure of average grain size ASTM 8.5-8.0 (i.e.  $16\text{-}20 \mu\text{m}$ ), Figure 3-3(c), respectively. Furthermore, Alloy 718 with a chemical composition of 53.8% Ni, 18.1% Cr, 5.5% Nb, 2.9% Mo, 1% Ti, 0.55% Al, 0.25% C, 0.06% Mn, 0.04% Si and Fe balance in weight percent was also used for the purposes of

the experiments, heat treated to an average grain size of ASTM 5.5-5.0 (i.e. 48-57  $\mu\text{m}$ ), Figure 3-3(d). Grain size was measured using a Nikon Eclipse LV150 microscope calibrated according to the ASTM E112 standards, ASTM International (2013).

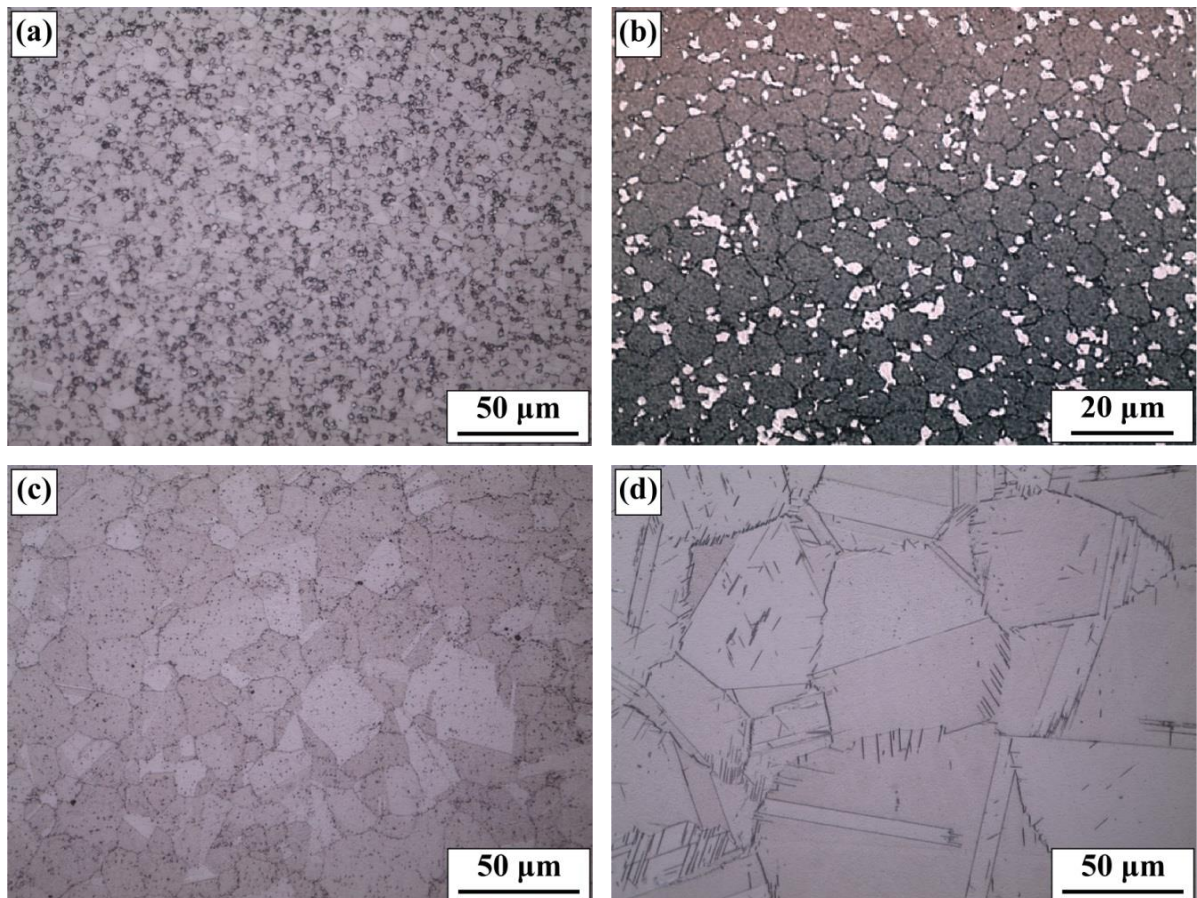


**Figure 3-3: Microstructure of machined superalloys; (a) FG RR1000-Kalling's N°2, (b) FG RR1000-10% Phosphoric acid, (c) CG RR1000-Kalling's N°2 and (d) Alloy718-Kalling's N°2.**

All workpieces were subjected to Vickers hardness assessment using a Mitutoyo hardness testing machine HM-101 at 1kgf load and 15 seconds dwell time. Figure 3-4 shows that at room temperature, FG RR1000 exhibits the highest average hardness at 471.8 HV, followed by CG R1000 at 453.4 HV and Alloy 718 at 447.5 HV. Finally, Table 3-1 summarises other major mechanical properties of the materials used in these experiments, particularly evident

is the difference in the temperature operational capability of these superalloys, with both RR1000 variants maintaining sufficient strength at 700°C compare to 540°C for Alloy 718.

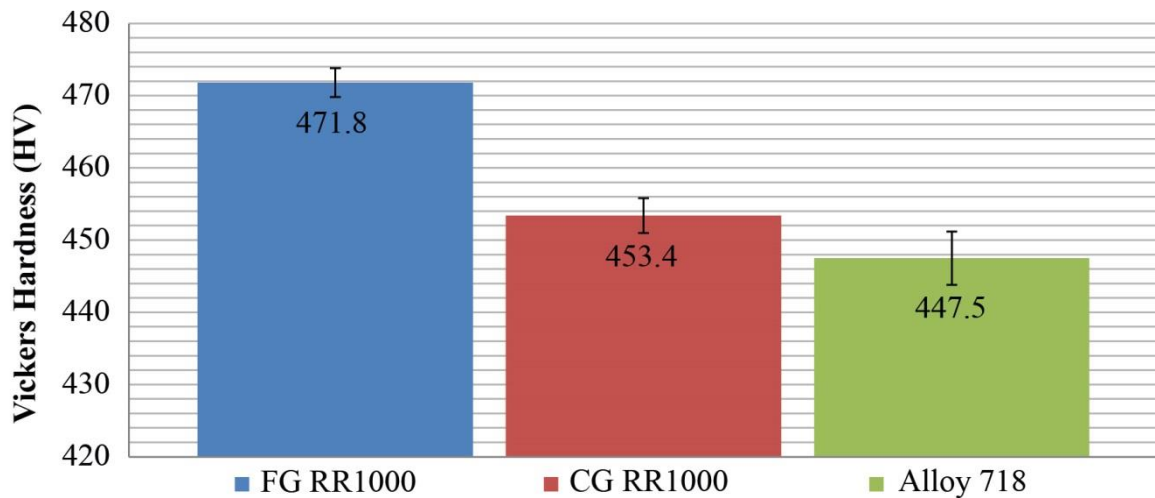


**Figure 3-4: Average Vickers hardness of the machined workpieces measured at 1kgf load and 15 seconds dwell time.**

**Table 3-1: Machined superalloys mechanical properties; FG and CG RR1000, Qiu (2010), Alloy 718, Donachie and Donachie (2002).**

Conditions	20°C			540°C			700°C		
	$\sigma_{0.2}$ (MPa)	UTS (MPa)	EL (%)	$\sigma_{0.2}$ (MPa)	UTS (MPa)	EL (%)	$\sigma_{0.2}$ (MPa)	UTS (MPa)	EL (%)
<b>FG RR1000</b>	1075	1575	$\geq 10$	-	-	-	980	1300	$\geq 10$
<b>CG RR1000</b>	1075	1573	22	-	-	-	963	1453	22
<b>Alloy 718</b>	1185	1435	21	1065	1275	18	-	-	-

### 3.2.1.1 Dry Trials (Phase 1)

To identify the origin of pick-up formation and deposition on machined surfaces and investigate the effect of microstructure and mechanical properties on the defect severity and presence, FG RR1000, CG RR1000 and Alloy 718 have been investigated under dry conditions, aiming to promote pick-up occurrence. A range of material removal rates ( $Q$ ) were assessed, by varying cutting speed ( $V_C$ ) and depth of cut ( $a_p$ ), Table 3-2, with all experiments conducted at fixed low feed rate ( $f = 0.12 \text{ mm/rev}$ ), for a fixed spiral length of 83 m.

**Table 3-2: List of machining parameters used in the dry turning trials.**

		$Q (\text{mm}^3/\text{sec})$	$V_C (\text{m/min})$	$a_p (\text{mm})$
FG RR1000	$V_C$	7.8	30	0.13
		13	50	0.13
	$a_p$	15	30	0.25
		25	50	0.25

### 3.2.1.2 Minimum Cooling Trials (Phase 2a)

This work focuses on setting the baseline concerning the effect of coolant application on FG RR1000 finishing turning operations compared to the dry cuts conducted in Phase 1. For this purpose, limited coolant supply was provided at the cutting zone using a low pressure (LP) pump set at 4 bar pressure supplying 0.9 l/min flow rate of Hocut 795B coolant (7% concentration) through a 1 mm diameter pipe, Figure 3-5(a), aligned for rake face cooling, Figure 3-5(b). In addition to the cutting parameters assessed in Phase 1, experiments were also conducted at  $V_C = 70 \text{ m/min}$  in order to investigate the process performance at higher material removal rates, Table 3-3. All experiments were run at constant  $f = 0.12 \text{ mm/rev}$  for a

fixed spiral length of 185 m. Repeat cuts of 111 m fixed spiral length were conducted in order to provide surface samples for further investigation.

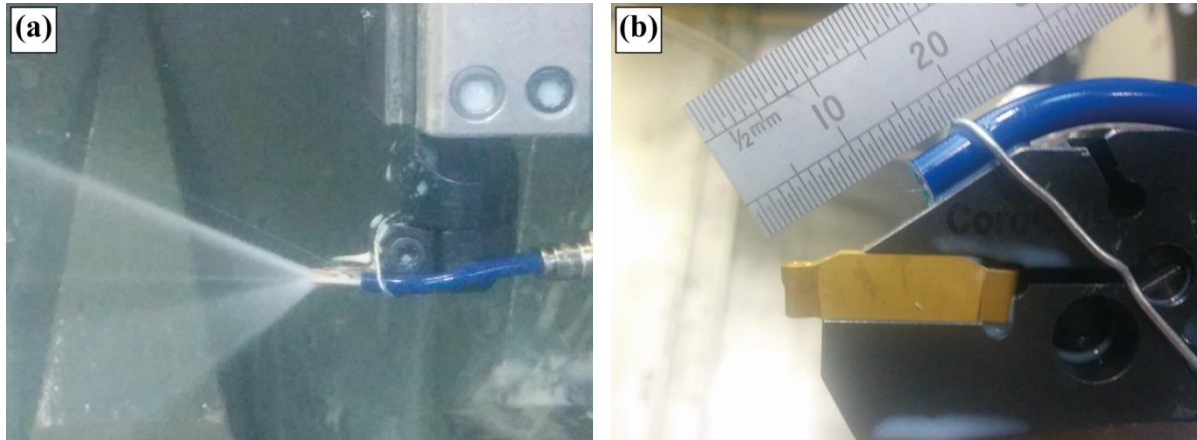


**Figure 3-5: Minimum cooling conditions; (a) Coolant supply, (b) Cooling setup.**

**Table 3-3: Material removal rates ( $Q \text{ mm}^3/\text{sec}$ ) used in the minimum cooling trials.**

	$a_p = 0.13 \text{ mm}$	$a_p = 0.25 \text{ mm}$
$V_C = 30 \text{ m/min}$	7.8	15.0
$V_C = 50 \text{ m/min}$	13.0	25.0
$V_C = 70 \text{ m/min}$	18.2	35.0

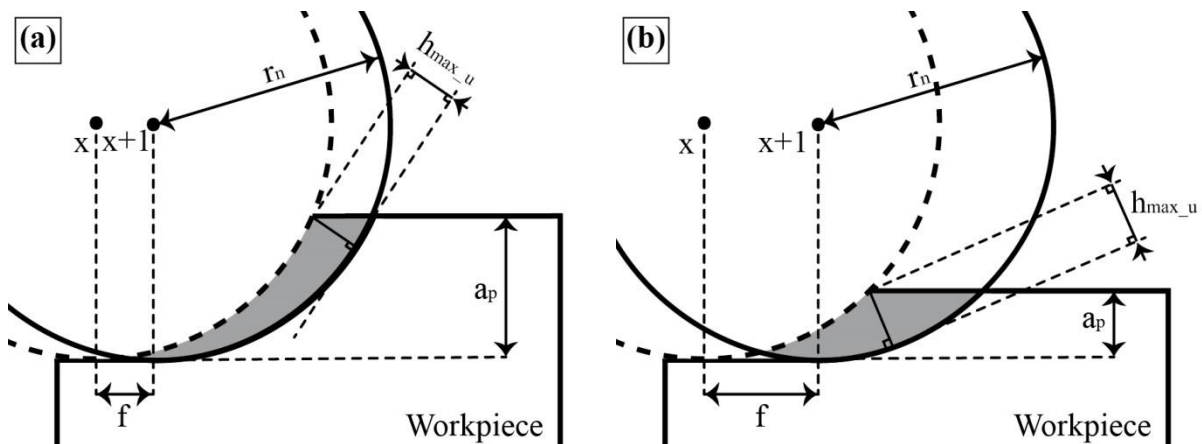
### 3.2.1.3 Low Pressure Cooling Trials (Phase 2b)

The coolant supply setup used in Phase 2a, Figure 3-5(a), was also used to assess the performance of improved low pressure (LP) cooling conditions on FG RR1000, CG RR100 and Alloy 718 machining. In this case, rake face cooling directed at the cutting zone was provided using a low pressure pump to deliver Hocut 795B coolant (7% concentration) at 12 bar pressure and flowrate of 1.9 l/min through 1 mm diameter pipe for all assessed conditions. In addition to the combinations of parameters assessed in Phase 2a, experiments were also designed to investigate the effect of feed rate on serration formation and pick-up at

specific material removal rates when machining FG RR1000. This was achieved by varying both  $a_p$  and  $f$  in order to assess the performance of different uncut chip geometries at identical  $Q$  and corresponding  $V_C$  conditions, Table 3-4. The uncut chip geometry in regards to the selected cutting conditions as the cutting tool moves from cutting position  $x$  to cutting position  $x+1$  are shown in Figure 3-6(a) for the low  $f$  and high  $a_p$  and Figure 3-6(b) for the high  $f$  and low  $a_p$  conditions. A fixed spiral cutting length of 111 m was used for all cuts.

**Table 3-4: List of machining parameters used in the LP cooling trials.**

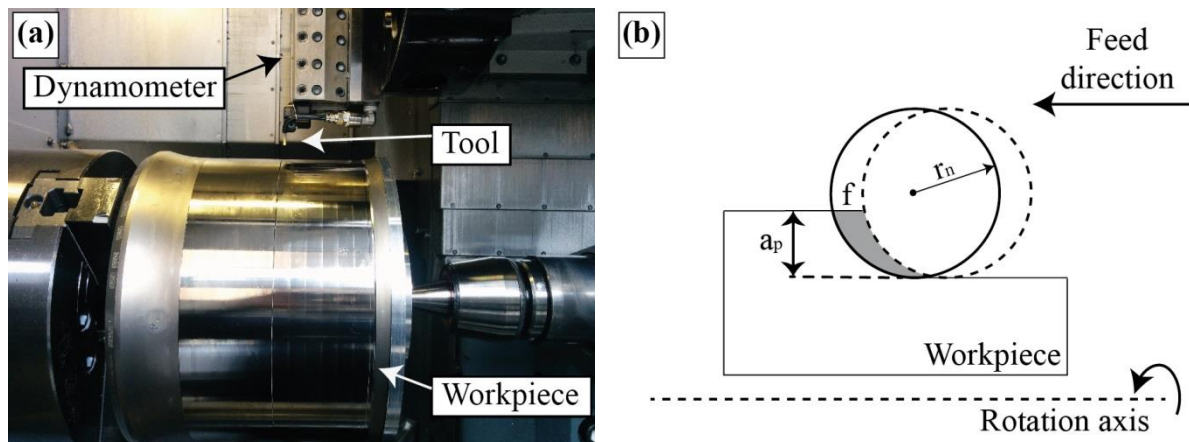
Workpiece	$Q$ (mm <sup>3</sup> /sec)	$V_C$ (m/min)	$a_p$ (mm)	$f$ (mm/rev)
FG RR1000	15	30		
CG RR1000	25	50	0.25	0.12
Alloy 718	35	70		
	15	30		
FG RR1000	25	50	0.12	0.25
	35	70		



**Figure 3-6: Illustration of uncut chip cross-section geometry; (a)  $f = 0.12$  mm/rev and  $a_p = 0.25$  mm and (b)  $f = 0.25$  mm/rev and  $a_p = 0.12$  mm.**

### 3.2.2 Cooling Performance Investigation Trials (Phase 3)

These experiments focus on assessing the performance of cooling conditions similar to those found in FG RR1000 line as well as the impact of different cooling strategies on the FG RR1000 machining. For these purposes, workpiece outer diameter (OD) turning trials were conducted using a Cincinnati Hawk 300 horizontal lathe, used for oblique turning cuts, equipped with the same force measurement configuration used in Phases 1-2 experiments, Figure 3-7(a). Each experiment was run using new N123F2-0300-RO S05F tools (identical to those in previous phases), whilst all experiments were run to a fixed spiral cutting length of 111 m, with the tool moving in the feed direction along the rotation axis at  $f = 0.12 \text{ mm/rev}$ ,  $a_p = 0.25 \text{ mm}$ . The workpiece rpm was kept constant with the cut progression in order to maintain a constant cutting speed ( $V_C$ ), Figure 3-7(b). Appropriate tool holder configurations were used to achieve  $90^\circ$  angle of attack in regards to the workpiece OD and allow the natural rake and flank clearance angles of the tool.



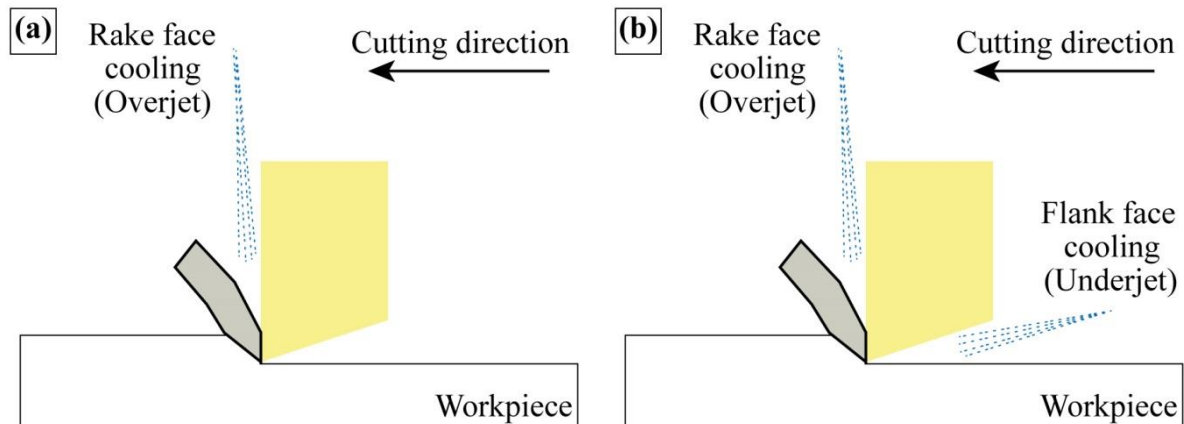
**Figure 3-7: Phase 2 trials; (a) Experimental configuration and (b) Machining diagram.**

Table 3-5 shows that  $V_C$  was varied to achieve a range of material removal rates, whilst all cutting parameter combinations were assessed under three different cooling conditions, assessing the effect of coolant flow rate ( $\lambda$ ), coolant pressure (P) and cooling position on FG

RR1000 machining. Both low and high external pumps were used to supply 12 bar and 70 bar pressure of Hocut 795B coolant (7% concentration) respectively, in the former case through a 2 mm diameter external pipe fixed on the 570-25LF-2020 tool shank combined with a 570-25L123G13B tool blade and in the latter case through QS-LF123F20C2020F tool holder body, Table 3-5. When cooling the tool's rake face only using an overjet  $\lambda$  was identical for both low and high P conditions, Figure 3-8(a), while cooling both the tool's rake and flank faces using overjet and underjet resulted in higher  $\lambda$ , Figure 3-8(b).

**Table 3-5: List of machining parameters used in Phase 3 trials.**

Cooling Setup	P (bar)	$\lambda$ (l/min)	Cutting Parameters
2 mm output for flank face cooling	12	< 6.5	$V_C = 30, 50, 70 \text{ m/min}$
1.4 mm output for flank face cooling	70	< 6.5	for
1.4 mm output for flank face cooling and 1.4 mm output for rake face cooling	70	< 9.1	$Q = 15, 25, 35 \text{ mm}^3/\text{sec}$



**Figure 3-8: Cooling process configurations; (a) Rake face cooling only and (b) Rake and flank cooling.**

### 3.2.3 Chip Formation Trials (Phase 4)

All experiments were conducted under dry conditions using Phase 3 machining configuration, Figure 3-7, though shorter experimental cuts (approximately 15 m in spiral cutting length) were run to collect chip samples and measure cutting forces, aiming to develop an effective quick study machining testing model that can predict pick-up occurrence risk using limited machining resources.

Figure 3-9 shows the tool path programmed to run a series of short cuts for every experiment, using a new cutting tool and enabling the assessment of different feed rate ( $f$ ) at fixed cutting speed ( $V_C$ ), depth of cut ( $a_p$ ) and tool radius ( $r_n$ ), Table 3-6. A 570-25NG-2020 tool shank combined with a 570-25L123G13C tool blade was used with the new N123F2-0300-RO tools ( $r_n = 1.5$  mm), whilst LF123J13-2020BM toolholder was used with the new N123J2-0600-RO tools ( $r_n = 3.0$  mm), both resulting in 90° angle of attack in regards to the workpiece OD. Furthermore, the performance of process variables uncommon to FG RR1000 production was also assessed:

1. The effect of customised sharper tool edge rounding (i.e.  $r_e \approx 15\mu\text{m}$  (+/- 2 $\mu\text{m}$ )) compared to the standard tool edge rounding (i.e.  $r_e \approx 35\mu\text{m}$  (+/- 2 $\mu\text{m}$ )).
2. The performance of fine carbide tools when uncoated and coated with 1105 coating grade compared to the validated S05F coating grade. S05F is the high temperature resistant 4 $\mu\text{m}$  TiN/Al<sub>2</sub>O<sub>3</sub>/TiCN chemical vapour deposited (CVD) coating used in all previous experiments, Figure 3-2(c), while 1105 is a high temperature resistant single layer TiAlN physical vapour deposited (PVD) coating.

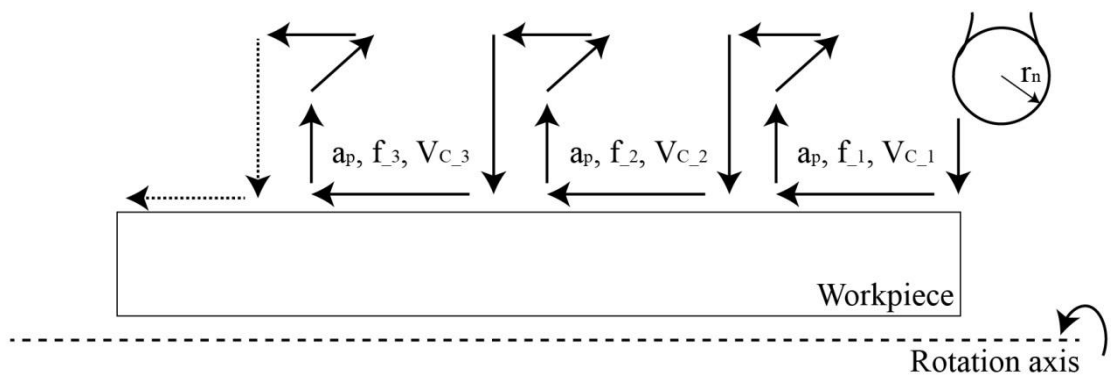


**Figure 3-9: Phase 4 quick study machining experimental configuration.**

**Table 3-6: List of machining parameters used in the Phase 4 trials.**

$V_C$ (m/min)	$r_n$ (mm)	$a_p$ (mm)	$f$ (mm/rev)			Coating	$r_e$ ( $\mu m$ )	
50	1.5	0.24	0.12	0.24	0.36	S05F	35	
50	3.0	0.24	0.12	0.24	0.36	S05F	35	
50	3.0	0.24	0.12	0.24	0.36	S05F	15	
30	3.0	0.24	0.12	0.24	0.36	S05F	15	
30	3.0	0.12	0.12	0.24	0.36	S05F	15	
50	3.0	0.24	0.12			1105	15	
50	3.0	0.12	0.12			1105	15	
30	3.0	0.12	0.12			Uncoated	15	
50	3.0	0.12	0.12			Uncoated	15	
**	50	1.5	0.12	0.12	0.18	0.24	S05F	35

\*\* Only this cut covered an overall 333 m in spiral length to produce surfaces for optical inspection.

### 3.3 DATA ANALYSIS METHODS AND EQUIPMENT

Optical analysis of the worn tools, chips and workpiece surfaces produced for each experiment was undertaken using a Zeiss Stemi 2000 optical stereoscope or similar. A more detailed and higher magnification analysis of the chips was also performed using a Philips XL 30S field emission gun scanning electron microscope (SEM) operated at 20 kV, whilst the microstructural analysis and chip cross-section profile analysis were performed using a Nikon Eclipse LV150. Where appropriate samples were prepared using a standard ground and polishing methodology to 0.05  $\mu\text{m}$  surface finish, whilst for producing chip cross-sections the samples were ground in order for the sections to pass as close as possible through the chip's spiral centreline to produce more representative results, with minimum distortion.

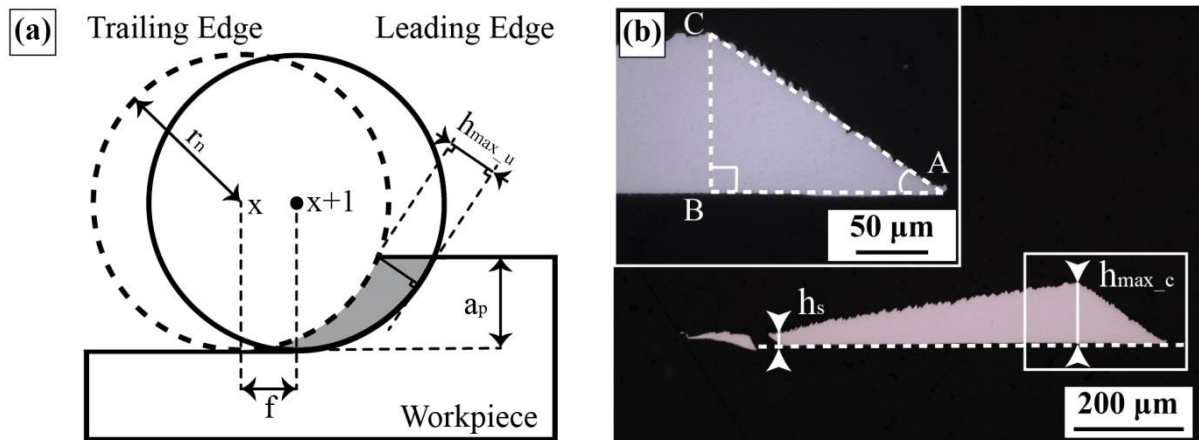
Furthermore, the possibility of tool wear affecting the presented data was taken into consideration when designing the experiments (thus the short spiral lengths adopted for all experiments), in addition to the surface damage assessment representing the surface integrity observed in the full length of every cut. Whilst to ensure the validity of the chip formation data, only chips produced at the early steady state cutting stages were assessed, at which point there is minimum tool wear.

Figure 3-10(a) shows the uncut geometry of the chip as the cutting tool moves from cutting position ( $x$ ) to cutting position ( $x+1f$ ) in regards to the selected feed rate. The effect of  $a_p$ ,  $f$  and  $r_n$  on the calculation of the theoretical value for maximum uncut chip thickness ( $h_{\max\_u}$ ) is shown in Equation 3.1, derived from the formulas shown in Appendix 1, Chou and Song (2004). Figure 3-10(b) shows an example chip cross-section, indicating the maximum cut chip thickness ( $h_{\max\_c}$ ), as a result of chip deformation, and the maximum serration thickness ( $h_s$ ), as a result of chip fracture during machining.  $h_{\max\_c}$  measures the maximum

vertical distance from the tangent to the back face of the chip forming the right angle triangle, ABC, as shown in Figure 3-10(b). To accurately measure the dimensions of the chip 3D scanning of the chip samples was undertaken using an Alicona InfiniteFocus 3D optical microscope, to measure length AC and angle  $\hat{A}$  that were then used to calculate the length of BC, i.e.  $h_{\max\_c}$ , using Equation 3.2.

$$h_{\max\_u} = r_n - \sqrt{(r_n^2 + f^2 - 2 * f * \sqrt{(2 * a_p * r_n - a_p^2)})} \quad (3.1)$$

$$BC = AC * \sin(\hat{A}) \quad (3.2)$$



**Figure 3-10: Chip cross-section geometry; (a) Uncut, (b) Cut.**

Figure 3-11 shows example 3D chip scans from which the average values of the data points selected in the red cross-sections (width of 200  $\mu\text{m}$ ) were used to plot corresponding chip profiles. Figure 3-11(a) shows an example dataset produced to measure length AC and Figure 3-11(b) shows the best fit for angle  $\hat{A}$  at the leading edge of the chip. At least 5 measurements each of length AB and angle  $\hat{A}$  were taken from two different samples of the same experiment, resulting in the calculation of 25 values for the length BC.  $h_{\max\_c}$  was defined as the mean value of the BC calculations, with its measurement error ( $\varepsilon$ ) calculated at

confidence level of 95% (i.e.  $z = .95$ ). This then enabled the calculation of CCR, the ratio of  $h_{max\_c} / h_{max\_u}$ . 3D scanning was also used to measure the spacing between the serrations ( $d_s$ ), Figure 3-11(c), and the maximum serrat thickness ( $h_s$ ), Figure 3-11(d). However, for the latter case the width of the selected data points was reduced to 20  $\mu\text{m}$  in order to measure the maximum thickness value at the deepest point of the serrat. The average of the 3 largest values was then used to calculate  $h_s$ . Appendix 2 shows an example of these calculations based on the 3D scanning measured values.

In terms of the collected machining force data, the presented values were calculated using recorded readings from the initial 20 seconds of the cut's steady state to minimise the effect of tool wear, with:

- Cutting force ( $F_C$ ) was defined as the force load component vector parallel to the direction of cutting;
- Push-off force ( $F_P$ ) was defined as the force load component vector vertical to the direction of cutting;
- Feed force ( $F_F$ ) was defined as the force load component vector opposing the tool's movement in the feed direction.

Furthermore, the  $F_C$ ,  $F_P$  and  $F_F$  values represent raw force data from single trial runs for each set of parameters as the restrictions in resources did not allow for repeatability trial tests. However, many of the cutting parameter combinations were repeated in order to assess the effect of cooling performance on the machining process, also allowing for the identification of specific trends in the machining forces at corresponding machining conditions. In terms of the uncertainty/error values indicated in the force data, these were calculated based on the

standard deviation of the force readings collected during the initial 20 seconds of each cut at confidence level of 95% (i.e.  $z = .95$ ).

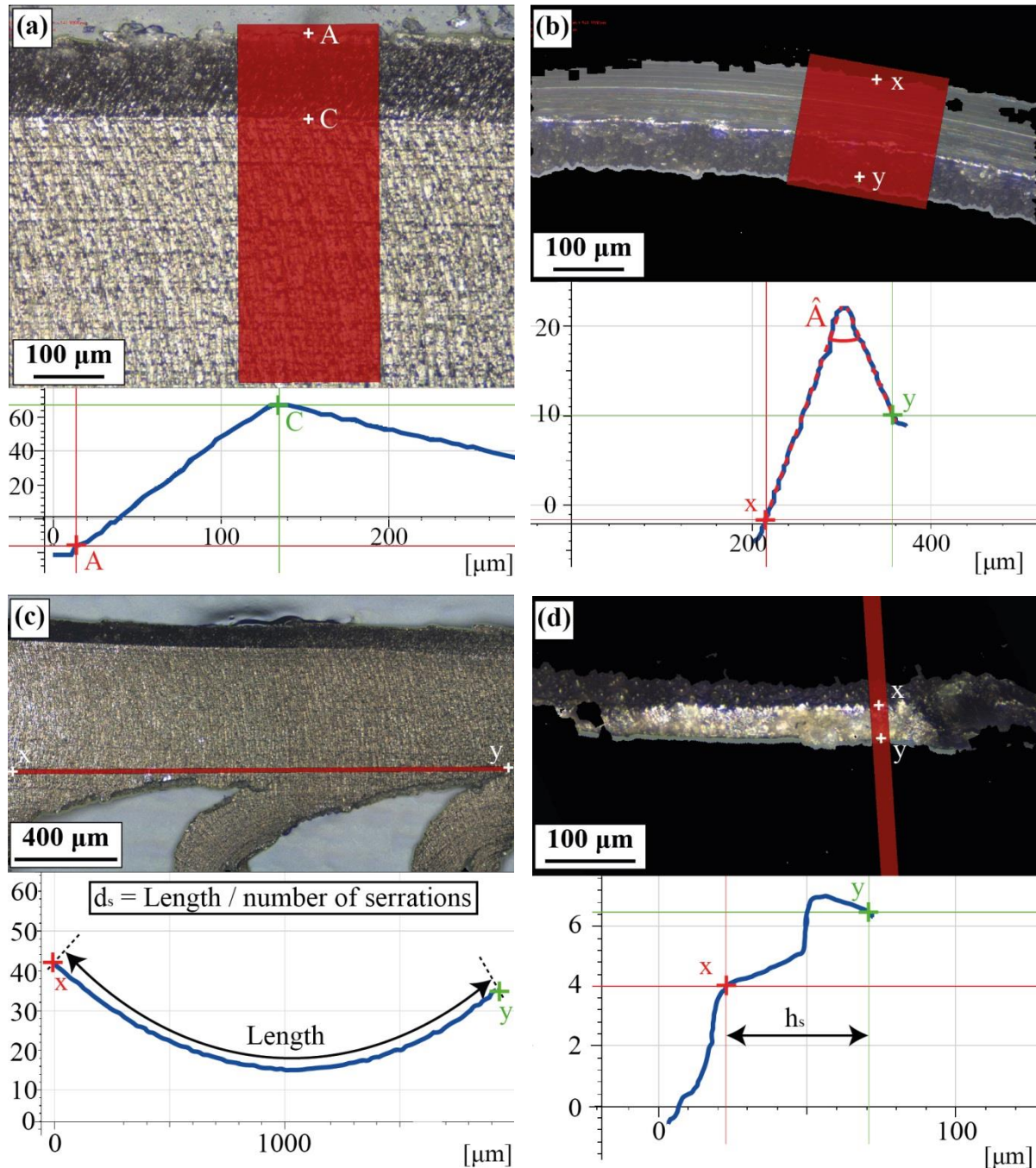


**Figure 3-11: Examples of the chip 3D scans; (a) Length AC, (b) Angle  $\hat{A}$ , (c) Serration spacing  $d_s$ , (d) Maximum serratation thickness  $h_s$ .**

In terms of calculating the specific cutting load ( $\text{N/mm}^2$ ) of each cut, two methodologies were used:

- The traditional approach reported in literature, which calculates the specific cutting load by dividing the average  $F_C$  value over the uncut chip cross-section area (i.e.  $\approx f * a_p$ ).
- The proposed less conventional method, which calculates the specific cutting load by dividing the average  $F_C$  value over the cut/deformed chip cross-section area ( $S$ ).  $S$  was calculated under the assumption that the chip cross-section is triangular, as seen in Figure 3-10(b), using  $h_{\max\_c}$  values extracted from the 3D scans as the height of the triangular profile and the chip's uncut width ( $w$ ) as the base of the triangular profile, see Appendix 1.

The purpose for proposing the less conventional methodology rises from the fact that the traditional force analysis (i.e. using the uncut chip cross-section area) contradicts with the established machining principles discussed in the literature review, which state that: 1. machining forces originate due to the deformation process; 2. machining forces are affected by the cut/deformed chip geometry; 3. machining forces are controlled by parameters affecting the 3D machining mechanics (i.e.  $V_C$ ). Furthermore, based on the fact that findings reported in section 2.3.4.1 link the force values to the chip's deformed geometry (i.e. decreasing the chip's cut/deformed thickness due to higher  $V_C$  resulted in the reduction of machining forces), it is the author's belief that analysing the machining forces using the deformed chip geometry data is a better practice. A comparison of both methodologies is presented based on actual force data from the Dry Trials (see section 4.2.1.3 – Figure 4-20), explaining further the reasons for using the less conventional analysis route in the full length of this thesis. However, it should be stated that primarily the proposed force analysis concept

aims to highlight the contradictions in the traditional force analysis method, while providing an alternative methodology for calculating the specific cutting load.

Finally, a Mitutoyo SJ-400 surface roughness tester was used to record the roughness Ra values from at least 5 different points on each finished surface, focusing on areas with the most severe surface damage. The presented values were then averaged unless stated otherwise.

# 4 RESULTS AND DISCUSSION

## 4.1 INTRODUCTION

This chapter describes all the experimental data and analysis as well as discussing the findings. The work is presented in the following order: dry machining, minimum cooling application, low pressure cooling application and comparison of rake-only against rake-flank cooling. After each section a detailed discussion is presented, which builds on the previous discussions to identify the major machining parameters for serration formation and pick-up deposition. To explore the conclusions derived from these discussions, the final section presents a set of experimental tests based on varying feed rate, coating grade, tool radius and tool edge rounding, all with the intention to independently validate the key factors controlling these phenomena.

## 4.2 PICK-UP INVESTIGATION TRIALS

### 4.2.1 Dry Trials (Phase 1)

#### 4.2.1.1 Surface Integrity

All dry experimental trials produced surfaces with distinct, but varying severity levels of parent material deposits known as pick-up. Figure 4-1(a) shows typical examples of these deposits observed when machining FG RR1000 at  $V_C = 30$  m/min and  $a_p = 0.25$  mm. Three pick-up types were observed:

- **Type 1**, streaks of smeared material residue producing relatively low surface roughness, while the defect's cross-section revealed similar microstructure to thin white layer suggesting severe material ploughing during deposition, Figure 4-1(b);
- **Type 2**, minor pick-up deposits ranging in length from 10-100  $\mu\text{m}$  in the cutting direction, leading to minor protrusions (thickness of few microns) with their microstructure severely more distorted compared to the workpiece, Figure 4-1(c);
- **Type 3**, major pick-up deposits ranging in length from 200-500  $\mu\text{m}$  in the cutting direction, leading to significant protrusions which appear of uniform thickness in the cutting direction, Figure 4-1(d), whilst they formed triangular dissenting profile in the feed direction, Figure 4-1(e).

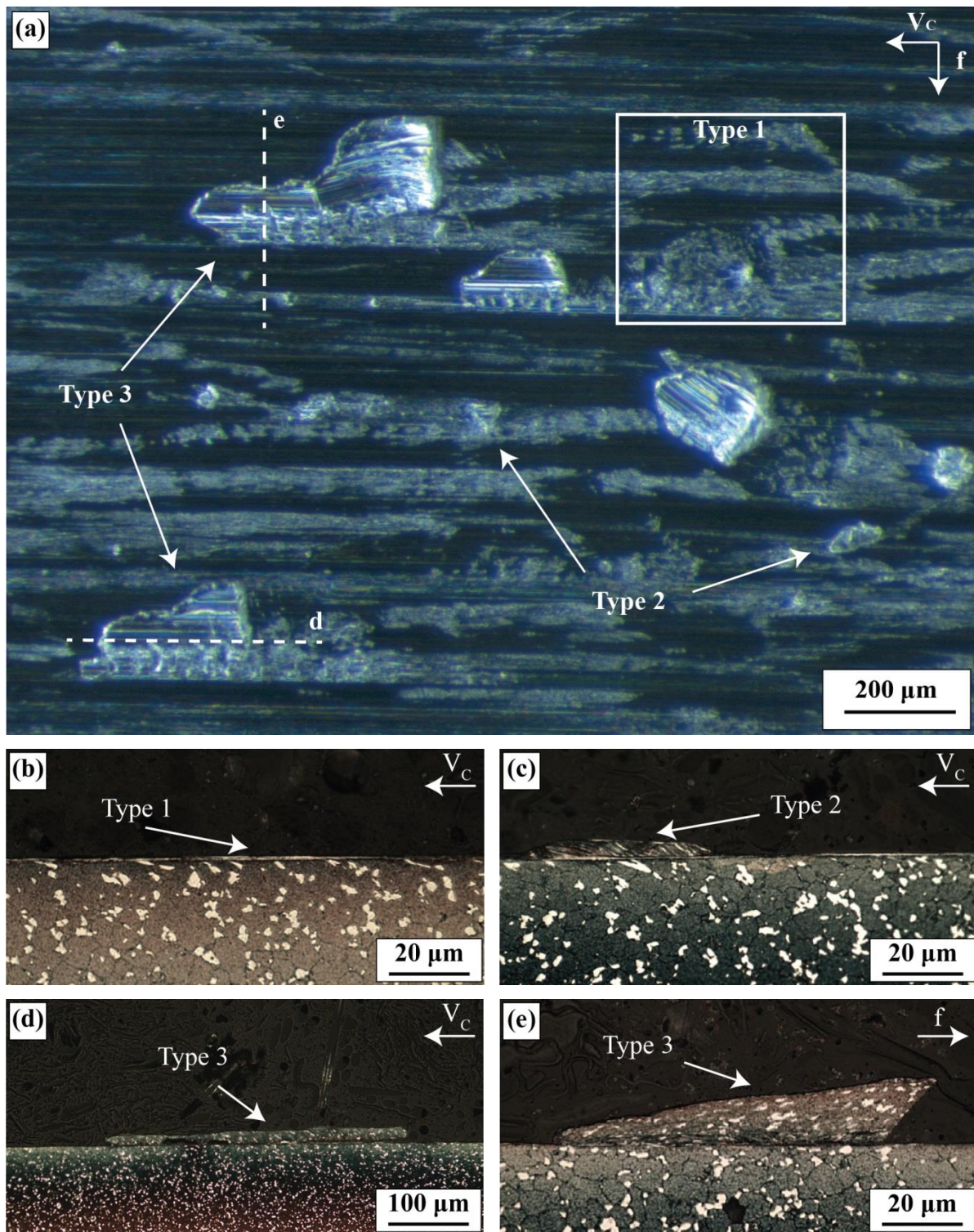


**Figure 4-1:** Typical examples of pick-up deposits in RR1000 dry machining; (a) Surface finish, (b) Type 1 pick-up cross-section, (c) Type 2 pick-up cross-section, (d-e) Type 3 pick-up cross-sections.

Further observations typical in these experiments were: 1. Tool marks on the top face of pick-up deposits, formed parallel to the cutting direction, in addition to the smearing residue produced when major pick-ups partially deposited on the surface, Figure 4-2(a), and 2. The tool was heavily coated with small chip pieces at the end each cut, Figure 4-2(b). A further phenomenon detected when turning FG RR1000 cuts at  $V_C = 30$  m/min and  $a_p = 0.25$  mm was increase in pick-up severity with the progression of the cut. Figure 4-2 shows the surface state at the beginning of the cut with the majority of pick-ups being Type 1, Figure 4-2(c), whilst a more intense level of damage, due to the occurrence of Type 3 pick-ups, was observed near the end of the cut, Figure 4-2(d).

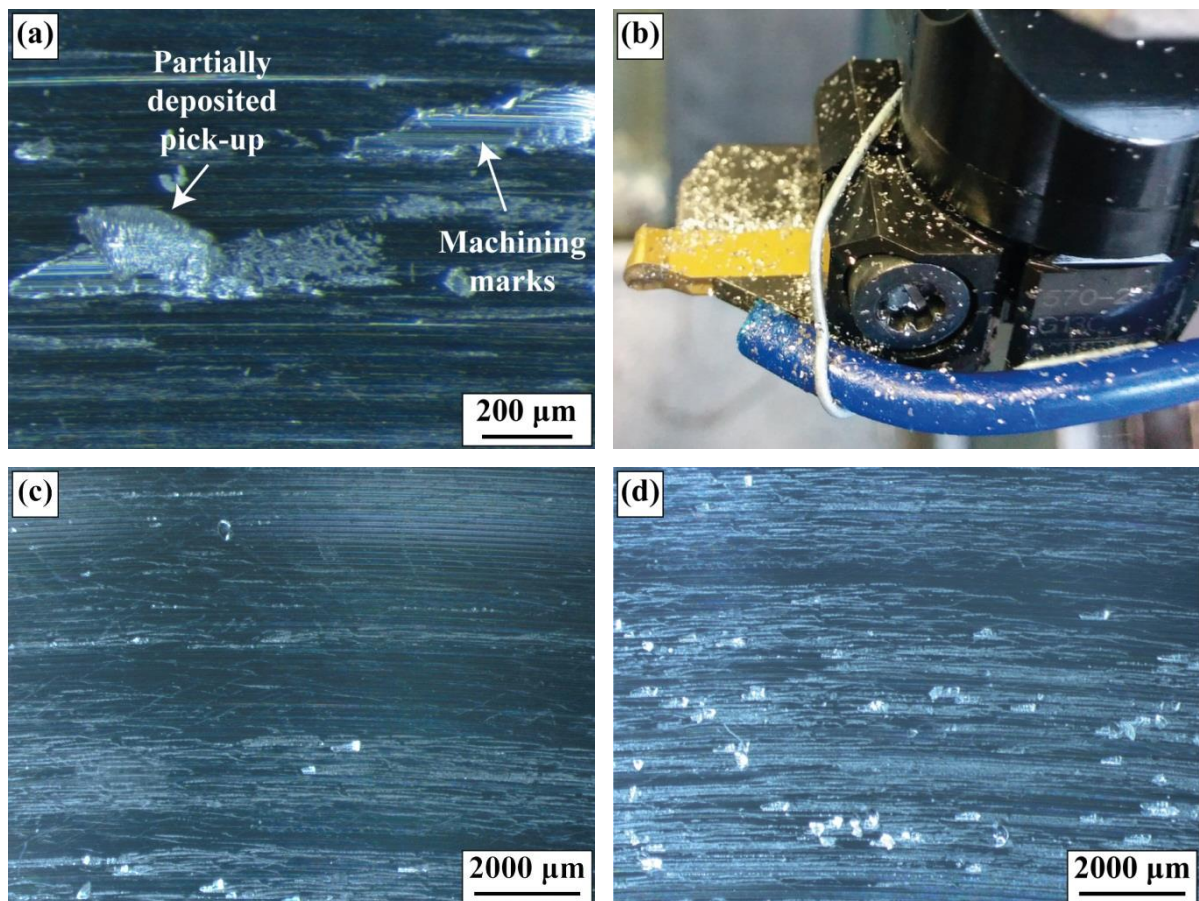


**Figure 4-2: Further observations; (a) Pick-up deposit characteristics, (b) Tool state - end of the cut, FG RR1000 pick-up severity (c) Start of the cut and (d) End of the cut.**

Figure 4-3 shows the finished surfaces for all FG RR1000 experiments. Low  $a_p$  conditions resulted in the deposition of all three pick-up types, with similar defective surface area coverage and surface roughness Ra ranging from 0.64 to 1.36  $\mu\text{m}$ , for both the  $V_C$  conditions, Figures 4-3(a-b). For  $a_p = 0.25 \text{ mm}$  and  $V_C = 30 \text{ m/min}$ , a larger proportion of the surface was covered with streaks of smearing residue (Type 1) and more frequent minor and major pick-up deposits (Type 2 and 3 respectively), compared to  $a_p = 0.13 \text{ mm}$  conditions, leading to Ra values of up to 2.88  $\mu\text{m}$ , Figure 4-3(c). Whilst for  $V_C = 50 \text{ m/min}$  and  $a_p = 0.25 \text{ mm}$  conditions, Figure 4-3(d), resulted in the maximum coverage of the surface with Type 1 smearing residue in addition to Type 2 and random oversized Type 3 pick-ups, resulting in a surface roughness of 0.64  $\mu\text{m}$ .

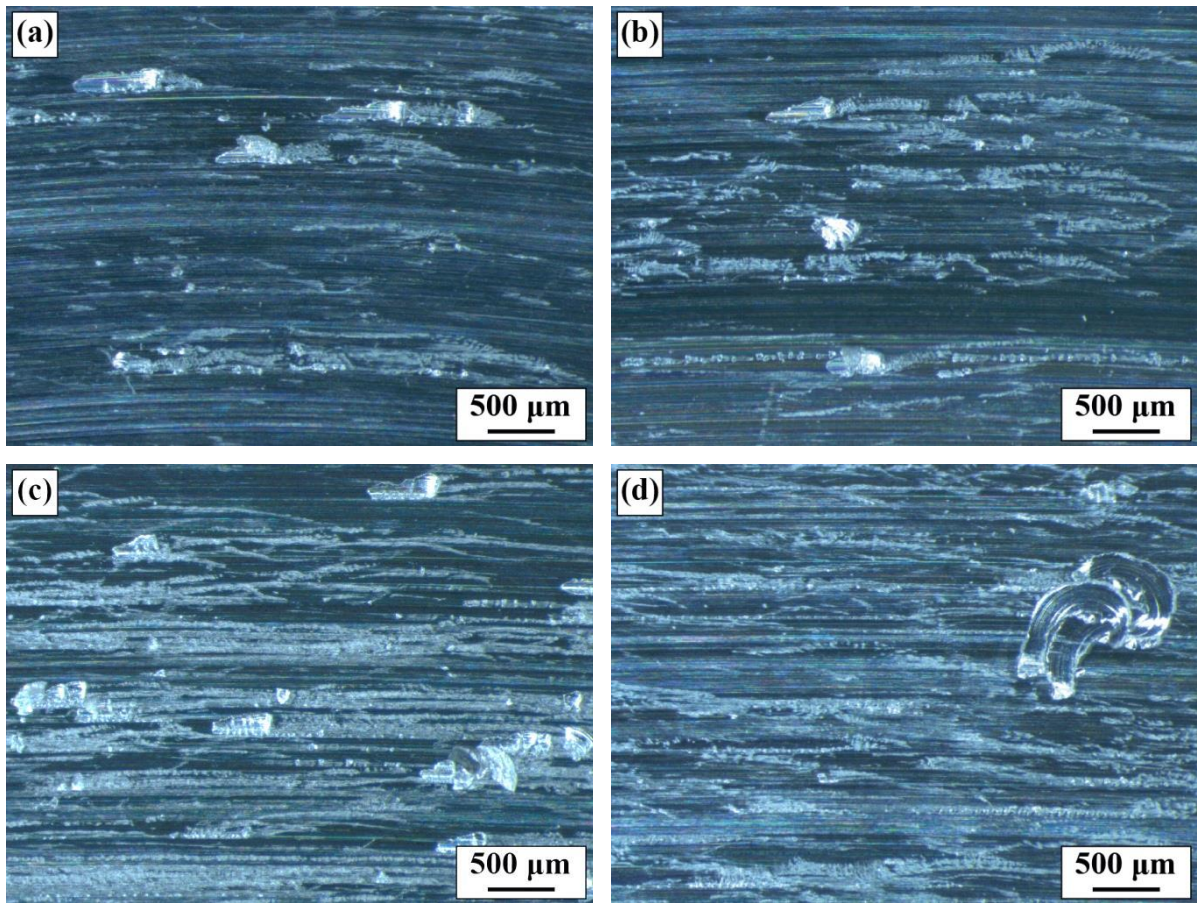
Figure 4-5 shows the finished surfaces for all CG RR1000 experiments. Figure 4-5(a) shows that  $a_p = 0.13 \text{ mm}$  and  $V_C = 30 \text{ m/min}$  resulted in sporadic deposition of minor pick-up (Type 2) in addition to minimum smearing residue (Type 1), resulting in  $\text{Ra} = 0.33 \mu\text{m}$  and producing the least amount of surface damage observed overall for all the dry RR1000 surfaces investigated. Increasing  $V_C$ , at  $a_p = 0.13 \text{ mm}$ , resulted in sporadic occurrence of all three pick-up types and a Ra increase to 0.44  $\mu\text{m}$ , Figure 4-5(b). Machining at  $a_p = 0.25 \text{ mm}$  and  $V_C = 30 \text{ m/min}$  resulted visually in the most severe surface damage for the CG material due to frequent minor pick-up deposition (Type 2) with Ra values up to 1.31  $\mu\text{m}$ , Figure 4-5(c). The highest material removal rate (Q) conditions,  $V_C = 50 \text{ m/min}$  and  $a_p = 0.25 \text{ mm}$ , resulted in  $\text{Ra} = 0.79 \mu\text{m}$  because of minor pick-up deposition, similar to the defects observed at low  $V_C$  conditions, in addition to the occurrence of major pick-up deposits (Type 3), which were deposited at the end of the smearing residue projected path, Figure 4-5(d).

Figure 4-7 shows the finished surfaces for all dry Alloy 718 experiments. All three pick-up types were detected on the surface machined at  $a_p = 0.13$  mm and  $V_C = 30$  m/min, resulting in a surface roughness  $R_a = 3.8 \mu\text{m}$ , Figure 4-7(a). For  $V_C = 50$  m/min and  $a_p = 0.13$  mm, only random minor pick-ups were deposited, reducing both the surface damage and roughness ( $R_a = 1.22 \mu\text{m}$ ) compared to the low  $V_C$  conditions, Figure 4-7(b). The most severe damage in these experiments was observed at  $a_p = 0.25$  mm and  $V_C = 30$  m/min, which resulted in  $R_a = 4.52 \mu\text{m}$  and the machined surface completely covered with minor pick-ups, Figure 4-7(c), in contrast to  $V_C = 50$  m/min conditions that produced the least damaged dry machined Alloy 718 surface with  $R_a = 0.78 \mu\text{m}$  and sporadic minor pick-up deposits only, Figure 4-7(d).

Table 4-1 summarises the average subsurface deformation depth for all dry machined surfaces, with both RR1000 variants demonstrating enhanced resilience to machining induced subsurface damage at all assessed cutting conditions (neither sample excited distortion depth of 2  $\mu\text{m}$ ), Figures 4-4 and 4-6. However, Alloy 718 produced at least 400% thicker subsurface distortion profiles compared to RR1000, Figures 4-8(a-b), whilst  $V_C = 50$  m/min and  $a_p = 0.25$  mm conditions (i.e. high Q) resulted in double the damage depth compared to  $V_C = 30$  m/min, Figures 4-8(c-d). Finally, pick-up deposition (of any type) appears to have inflicted no added mechanical subsurface damage compared to that observed in defect-free surface areas for each corresponding material.

**Table 4-1: Average subsurface deformation depth of dry machined superalloys.**

	<b>FG RR1000</b>	<b>CG RR1000</b>	<b>Alloy 718</b>
<b><math>V_C = 30 \text{ m/min } a_p = 0.13 \text{ mm}</math></b>	$1.2 \mu\text{m} \pm 0.1$	$1.3 \mu\text{m} \pm 0.1$	$6.6 \mu\text{m} \pm 0.3$
<b><math>V_C = 50 \text{ m/min } a_p = 0.13 \text{ mm}</math></b>	$1.4 \mu\text{m} \pm 0.1$	$1.4 \mu\text{m} \pm 0.2$	$6.8 \mu\text{m} \pm 0.2$
<b><math>V_C = 30 \text{ m/min } a_p = 0.25 \text{ mm}</math></b>	$1.8 \mu\text{m} \pm 0.2$	$1.1 \mu\text{m} \pm 0.1$	$7.5 \mu\text{m} \pm 0.2$
<b><math>V_C = 50 \text{ m/min } a_p = 0.25 \text{ mm}</math></b>	$1.6 \mu\text{m} \pm 0.1$	$1.6 \mu\text{m} \pm 0.1$	$15.9 \mu\text{m} \pm 0.5$



**Figure 4-3: FG RR1000 dry turning surface damage;  $a_p = 0.13 \text{ mm}$  (a)  $V_C = 30 \text{ m/min}$  and (b)  $V_C = 50 \text{ m/min}$ ,  $a_p = 0.25 \text{ mm}$  (c)  $V_C = 30 \text{ m/min}$  and (d)  $V_C = 50 \text{ m/min}$ .**

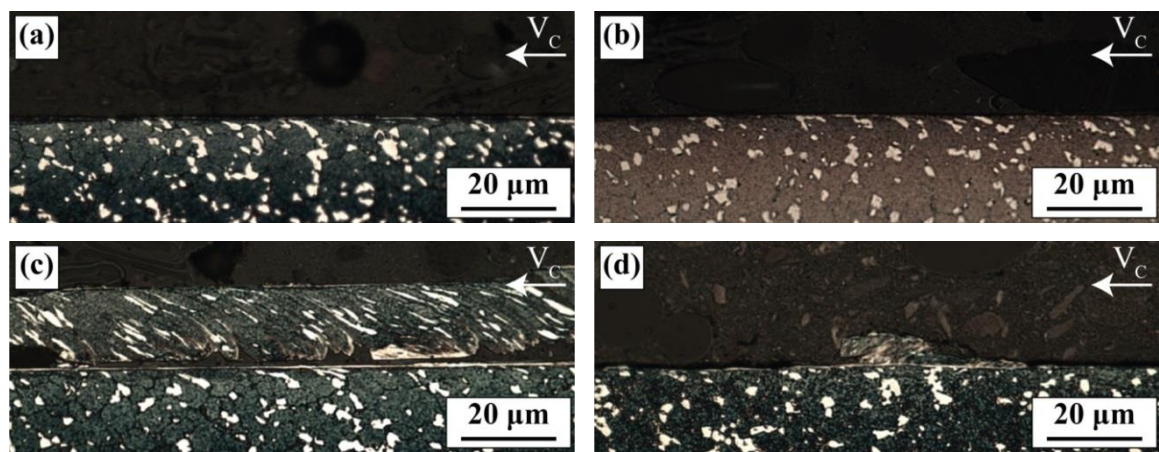


**Figure 4-4: FG RR1000 dry turning subsurface deformation;  $a_p = 0.13 \text{ mm}$  (a)  $V_C = 30 \text{ m/min}$  and (b)  $V_C = 50 \text{ m/min}$ ,  $a_p = 0.25 \text{ mm}$  (c)  $V_C = 30 \text{ m/min}$  and (d)  $V_C = 50 \text{ m/min}$ .**

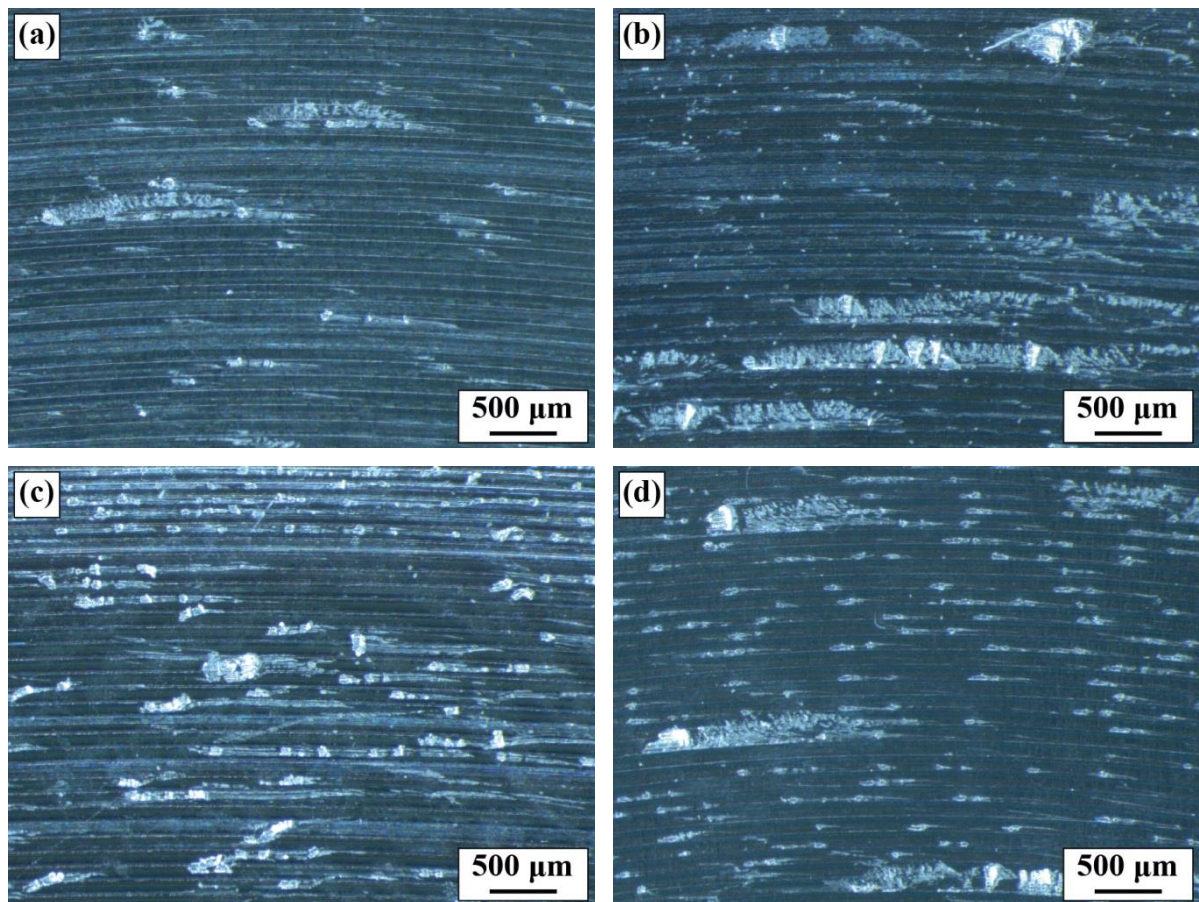


**Figure 4-5: CG RR1000 dry turning surface damage;  $a_p = 0.13 \text{ mm}$  (a)  $V_C = 30 \text{ m/min}$  and (b)  $V_C = 50 \text{ m/min}$ ,  $a_p = 0.25 \text{ mm}$  (c)  $V_C = 30 \text{ m/min}$  and (d)  $V_C = 50 \text{ m/min}$ .**

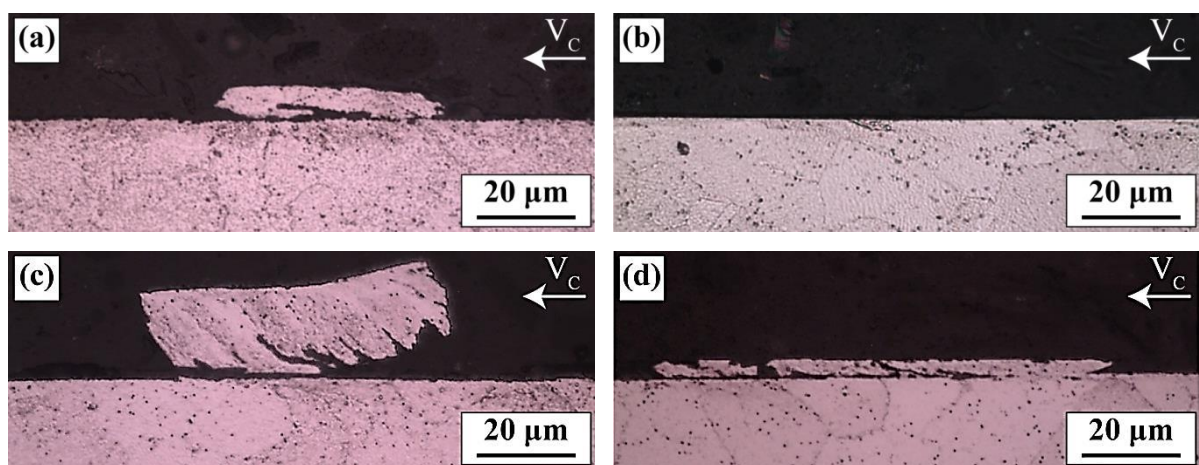


**Figure 4-6: CG RR1000 dry turning subsurface deformation;  $a_p = 0.13 \text{ mm}$  (a)  $V_C = 30 \text{ m/min}$  and (b)  $V_C = 50 \text{ m/min}$ ,  $a_p = 0.25 \text{ mm}$  (c)  $V_C = 30 \text{ m/min}$  and (d)  $V_C = 50 \text{ m/min}$ .**

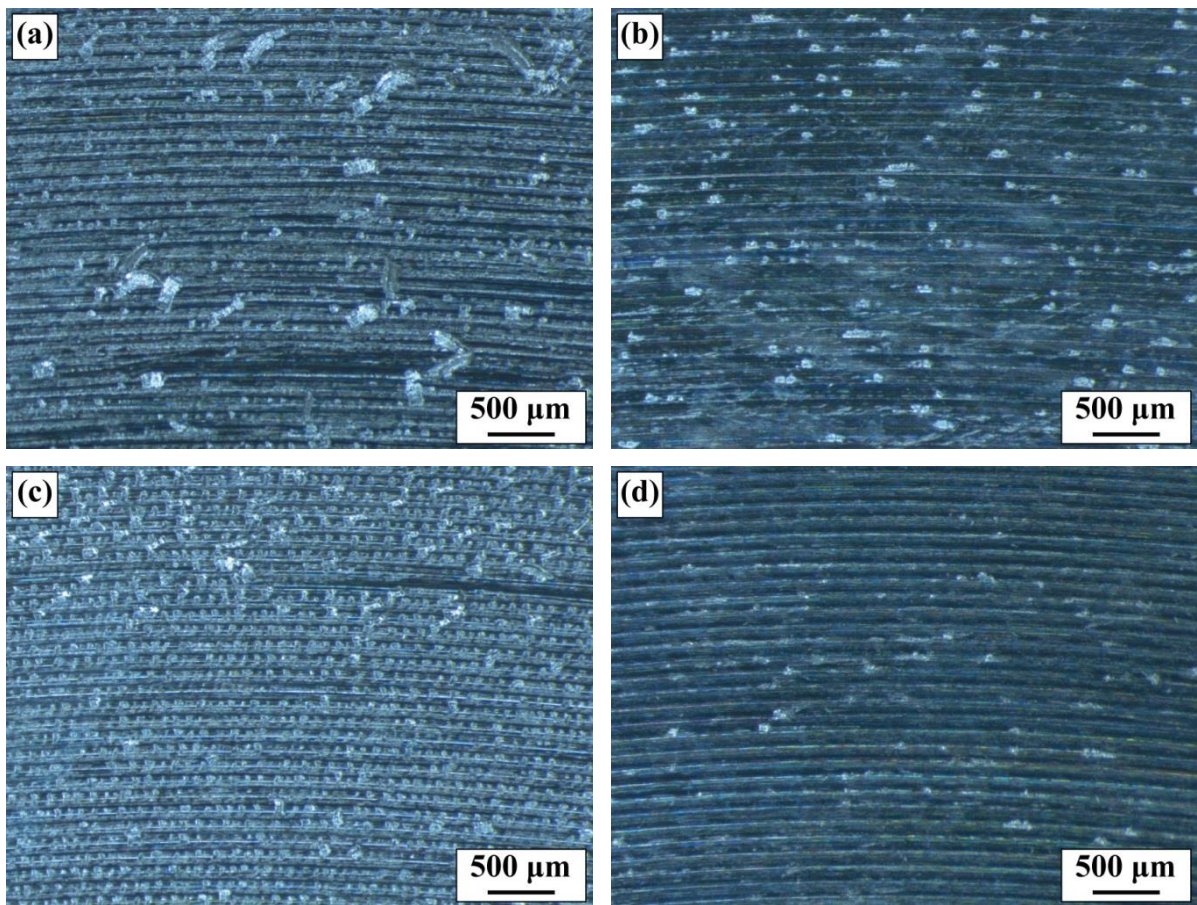


**Figure 4-7:** Alloy 718 dry turning surface damage;  $a_p = 0.13 \text{ mm}$  (a)  $V_c = 30 \text{ m/min}$  and (b)  $V_c = 50 \text{ m/min}$ ,  $a_p = 0.25 \text{ mm}$  (c)  $V_c = 30 \text{ m/min}$  and (d)  $V_c = 50 \text{ m/min}$ .

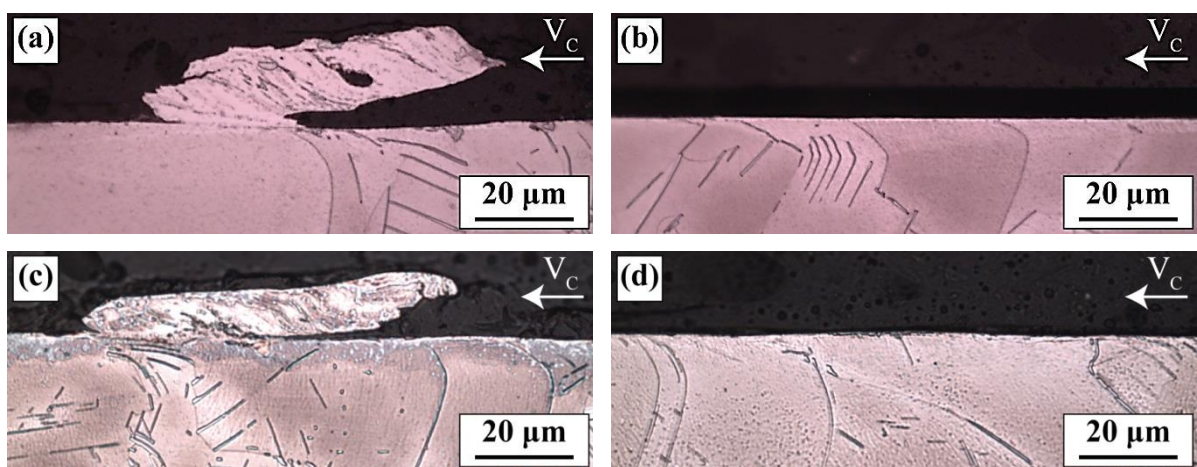


**Figure 4-8:** Alloy 718 dry turning subsurface deformation;  $a_p = 0.13 \text{ mm}$  (a)  $V_c = 30 \text{ m/min}$  and (b)  $V_c = 50 \text{ m/min}$ ,  $a_p = 0.25 \text{ mm}$  (c)  $V_c = 30 \text{ m/min}$  and (d)  $V_c = 50 \text{ m/min}$ .

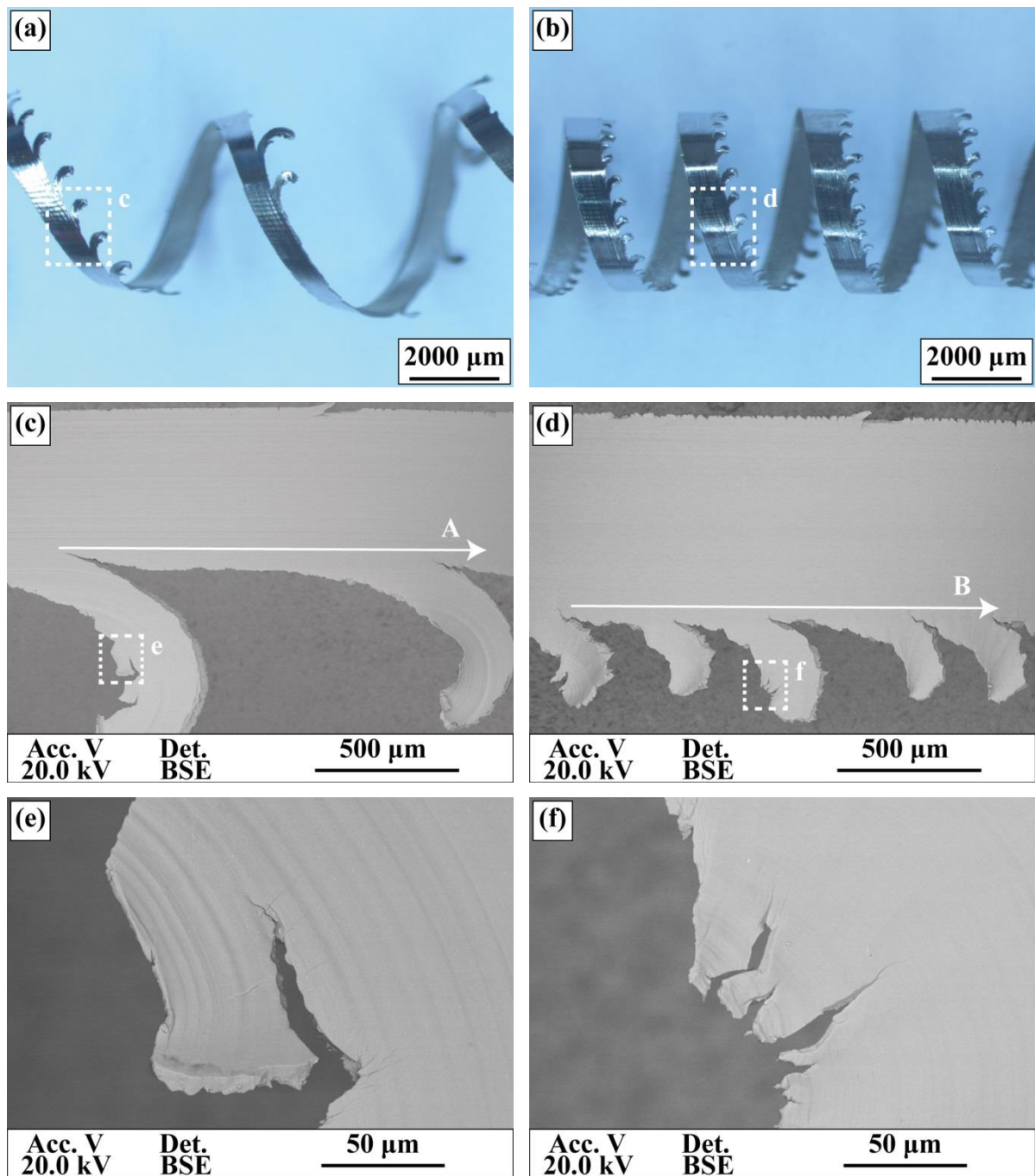
#### 4.2.1.2 Chip Formation and Geometry

Figure 4-9 shows the FG and CG RR1000 chip morphology formed at  $Q = 25 \text{ mm}^3/\text{sec}$ , for  $V_C = 50 \text{ m/min}$  and  $a_p = 0.25 \text{ mm}$ . Continuous ribbon chips with hook shaped serrations forming at the thin trailing edge, Figures 4-9(a-b), were characteristic for all investigated machining conditions. The chip's serrated area was formed by the trailing edge of the tool that also shaped the finished surface, whilst both the serration size and frequency varied for the two alloy variants, with the FG chips having larger and thus less frequent serrations. It is also interesting to note that a large number of the FG serrations fractured-off, especially at high  $a_p$  conditions, compared to the CG chips, as evidenced by the large number of missing serrations in Figure 4-9(a) compared to those in Figure 4-9(b). The large serrations, shown in Figure 4-9(c) for the FG material and Figure 4-9(d) for the CG material, are regarded as primary serrations, propagating against the chip flow, shown by the direction of the arrows A and B. These primary serrations appear to reach a consistent maximum thickness/depth before initiation of the next serration, which are similar in size to the major pick-up deposits (Type 3) detected on the RR1000 finished surfaces. The main body of the chip corresponds to the thicker edge of the chip that also experiences the formation of small serrations machined by the leading edge of the round insert. Figures 4-9(e-f) shows the formation of smaller secondary serrations at the edge of the primary serrations, which have the same size as the minor pick-up deposits (Type 2) detected on RR1000 machined surfaces.

Serrations occurred for the full length of the chip except at the very beginning of the cut for all machined materials. In early stages of machining, the cut is considered to be in an unsteady state, as the tool has yet to fully engage with the workpiece. Figure 4-10 shows a typical example of the chip formation timeline, in this case for FG RR1000 at  $V_C = 50 \text{ m/min}$

and  $a_p = 0.13$  mm, from a point where the tool had yet to engage with the workpiece, position (x), up to a point where the cut had reached the steady state, position (x+4f). At position (x+1f) the round tool engaged the workpiece, machining off a very small part of the surface for a full revolution of the workpiece that lasted approximately 0.6 seconds at the corresponding  $V_C$ . At positions (x+2f) and (x+3f) the tool advanced (at the fixed feed rate (f)) further in the feed direction in both cases increasing the uncut chip area and thus the amount of material removed, resulting in increased chip width and machining forces. Finally, at position (x+4f) the cut passed into a steady state as the tool had engaged fully with the maximum uncut chip area, forming a chip with a thin trailing edge that resulted in the formation of the hook shaped serrations for the rest of the cut. No serrations were formed on the chips with the thicker trailing edges produced in the early positions (x+1f) to (x+3f).

Closer inspection of the chip serrations, formed for FG RR1000 at  $V_C = 50$  m/min and  $a_p = 0.25$  mm, Figures 4-11(a-b), revealed the formation of cracks at the chip's thin trailing edge, Figures 4-11(c,e), in addition to micro-cracks forming along the serration path, Figure 4-11(d). The examination of the chip fracture surfaces, Figure 4-11(f), revealed the formation of a smooth surface fracture approximately 3-5  $\mu\text{m}$  thick, indicating a thin brittle fracture zone, forming just below the back face of the chip that was in contact with the cutting insert. The dimple formation below the crack initiation zone indicates that the fracture mechanism of the bulk chip material, forming both serration types until they reached a critical chip thickness (or until they met another crack in which case the serration breaks-off), is ductile in nature.



**Figure 4-9: Chip serration geometry in dry turning of RR1000 at  $V_C = 50 \text{ m/min}$  and  $a_p = 0.25 \text{ mm}$ ; (a) FG chip geometry, (b) CG chip geometry, (c) FG primary serrations, (d) CG primary serrations, (e) FG secondary serrations and (f) CG secondary serrations.**

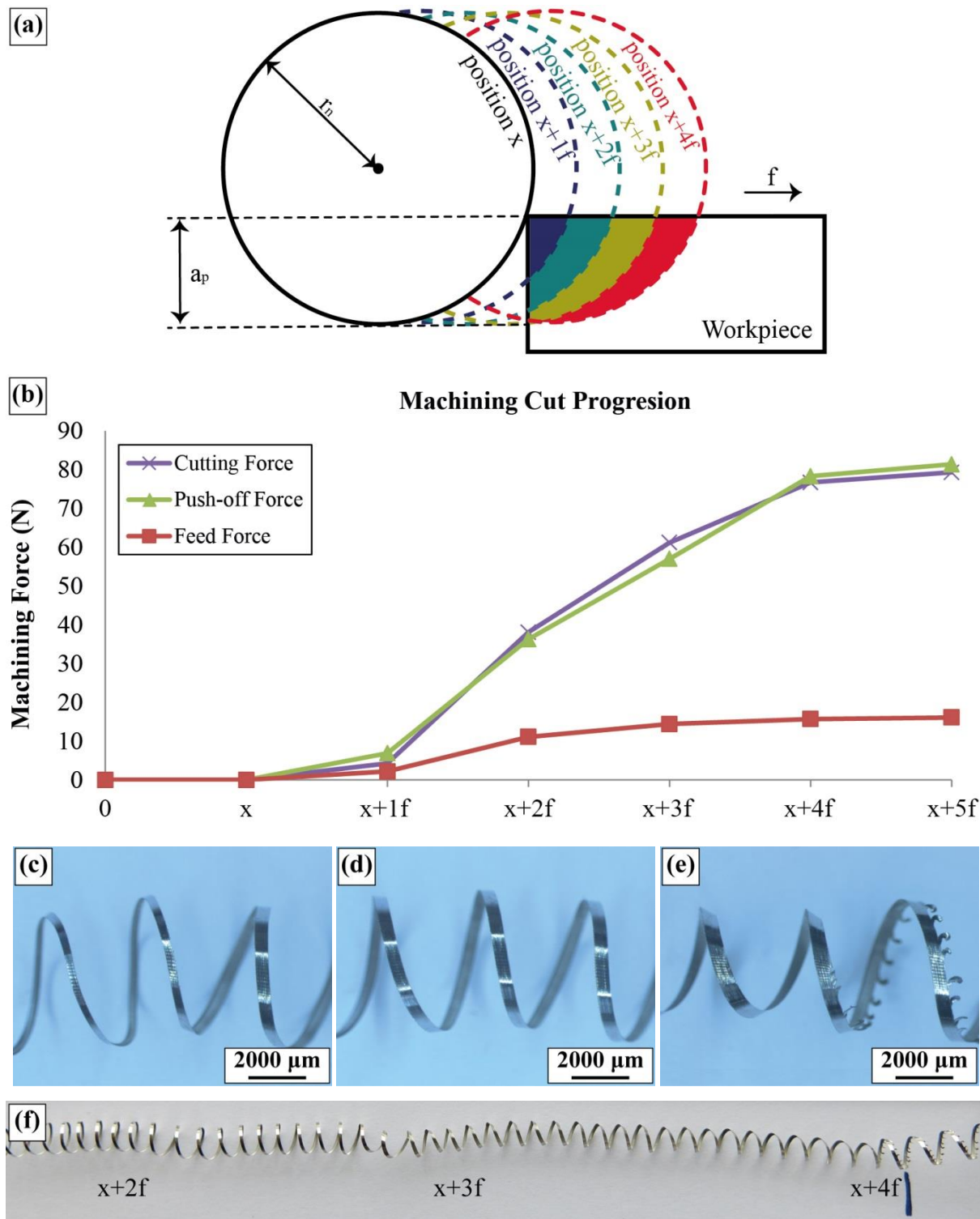


**Figure 4-10: Chip formation mechanism during the unsteady state of the cut; (a) Uncut chip geometry, (b) Machining forces, (c) Chip morphology at  $x+2f$ , (d) Chip morphology at  $x+3f$ , (e) Chip morphology at  $x+4f$ , (f) Continues chip morphology.**

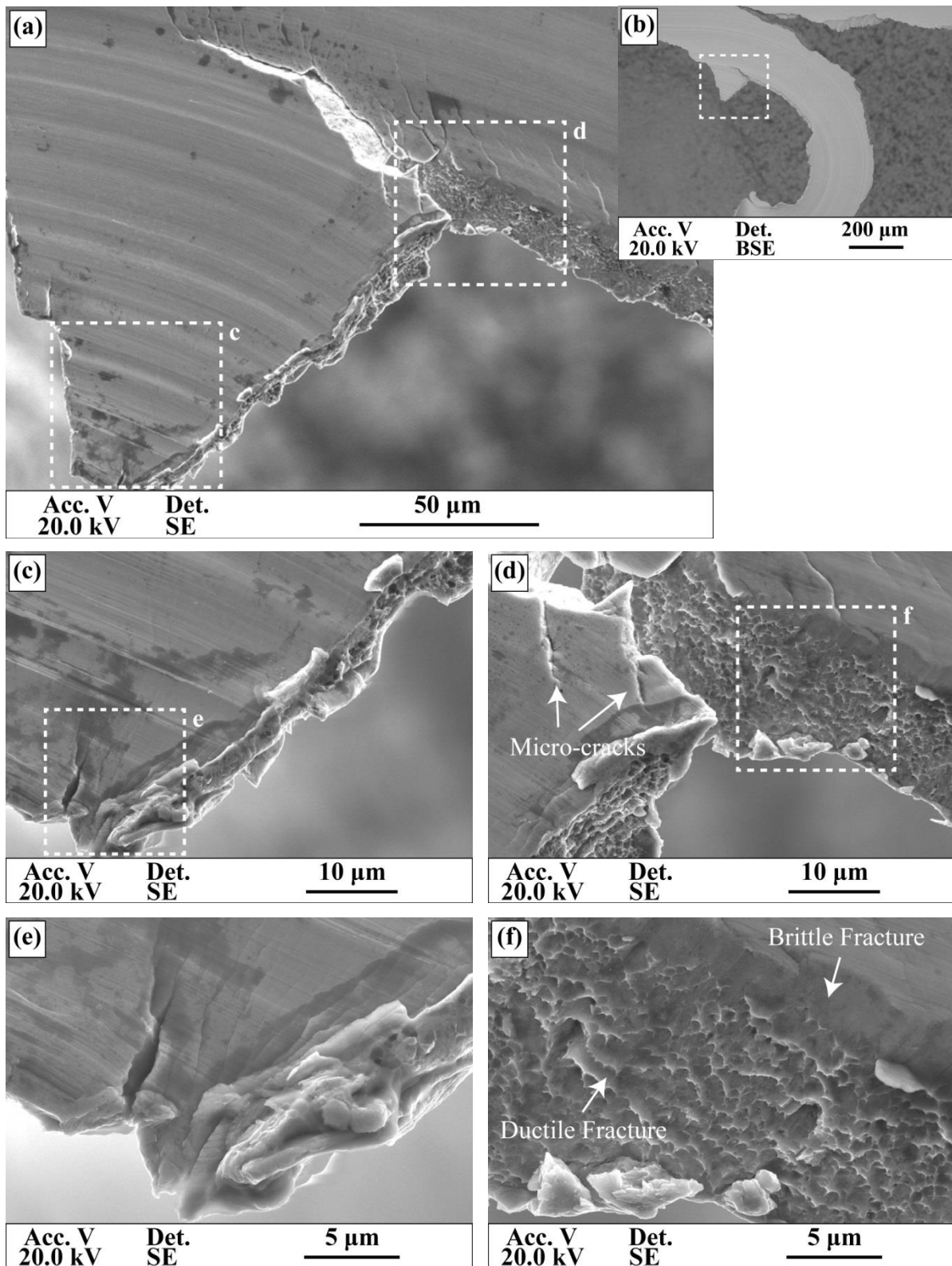


**Figure 4-11: FG RR1000 chip serraions failure at  $V_C = 50$  m/min and  $a_p = 0.25$  mm;**

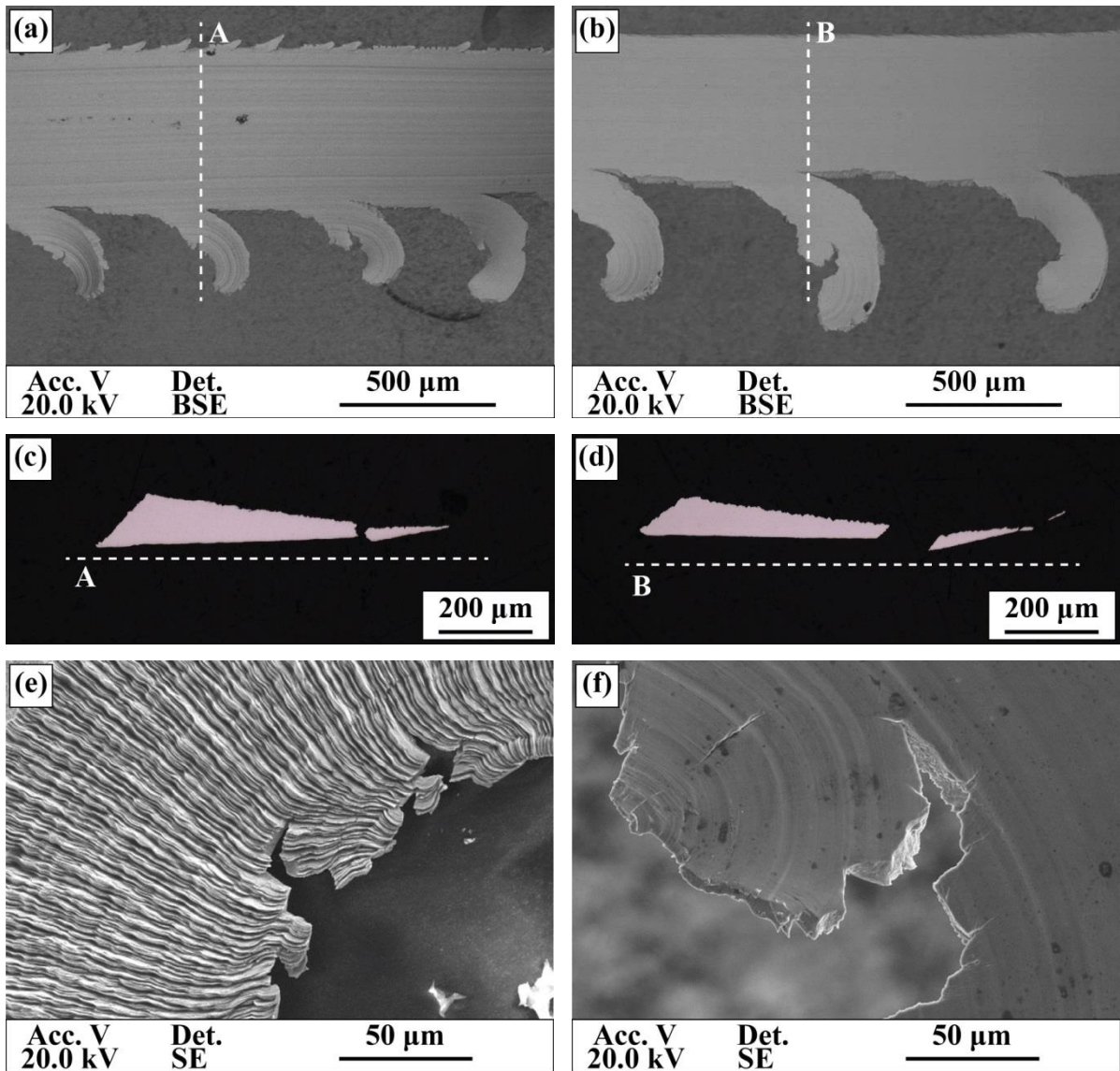
**(a,b) Chip serraions, (c,e) Crack nucleation at trailing edge, (d,f) Fractured surfaces.**

Figure 4-12 shows the effect of increasing  $V_C$  on FG RR1000 chip formation at  $a_p = 0.13$  mm. The chips produced at  $V_C = 30$  m/min formed smaller and more frequent primary serrations, Figure 4-12(a), compared to the larger serrations formed at  $V_C = 50$  m/min, Figure 4-12(b). However, the cross-sections of both primary serrations are similar in geometry to the Type 3 pick-up cross-section in the feed direction seen in Figure 4-1(e). Low  $V_C$  conditions also resulted in thicker chip cross-section (A) and smaller secondary serrations, Figures 4-12(c,e), compared to the thinner chip cross-section (B) and larger secondary serrations produced at  $V_C = 50$  m/min, Figures 4-12(d,f).

These observations are confirmed by the FG chip geometry data, gathered by 3D scanning, Table 4-2. Both  $h_{max\_c}$  and CCR values reduced when increasing  $V_C$  at corresponding  $a_p$  conditions. For example, analysis of the chips examined in Figure 4-12 shows that the chips machined at  $V_C = 30$  m/min and  $a_p = 0.13$  mm had  $CCR = 1.96$  compared those produced at  $V_C = 50$  m/min and  $a_p = 0.25$  mm with  $CCR = 1.32$ . The data also suggest that low  $a_p$  conditions resulted in higher CCR compared to high  $a_p$  and corresponding  $V_C$  conditions. The maximum primary serrat thickness ( $h_s$ ) and primary serrat spacing ( $d_s$ ) increased with increasing  $a_p$ , with the data suggesting that  $a_p$  had the most significant effect on these values as high  $a_p$  approximately doubled  $d_s$  and increased  $h_s$  by almost 10  $\mu\text{m}$ , compared to the low  $a_p$  cases.

**Table 4-2: Chip formation geometry data for dry machined FG RR1000.**

	$h_{max\_c}$ ( $\mu\text{m}$ )	$\epsilon$ ( $z = .95$ )	CCR	$h_s$ ( $\mu\text{m}$ )	$d_s$ ( $\mu\text{m}$ )
<b><math>V_C = 30</math> m/min <math>a_p = 0.13</math> mm</b>	87.8	$\pm 1.2$	1.96	31.8	542
<b><math>V_C = 50</math> m/min <math>a_p = 0.13</math> mm</b>	59.1	$\pm 1.0$	1.32	33.4	665
<b><math>V_C = 30</math> m/min <math>a_p = 0.25</math> mm</b>	100.5	$\pm 1.1$	1.60	42.2	1072
<b><math>V_C = 50</math> m/min <math>a_p = 0.25</math> mm</b>	78.3	$\pm 1.4$	1.25	41.8	1010



**Figure 4-12: Effect of cutting speed on FG RR1000 chips machined at  $a_p = 0.13$  mm;**  
**Chip geometry (a)  $V_c = 30$  m/min and (b)  $V_c = 50$  m/min, Chip cross-section (c)  $V_c = 30$  m/min and (d)  $V_c = 50$  m/min, Secondary chip serrations (e)  $V_c = 30$  m/min and (f)  $V_c = 50$  m/min.**

Figure 4-13 shows the effect of  $a_p$  on the formation of both serraion types in CG machining. Figure 4-13(a) shows the formation of smaller primary serrations at  $a_p = 0.13$  mm and  $V_c = 30$  m/min, compared to those formed when increasing  $V_c$ , Figure 4-13(b). Similar to FG findings, the larger primary serrations are associated with the increase in size and

occurrence rate of the secondary serrations, the formation of which did not occur for CG and  $a_p = 0.13$  mm and  $V_C = 30$  m/min, Figure 4-13(c), even though cracks were detected on the thin edge of the primary serrations, Figure 4-13(e). However, increasing  $a_p$  to 0.25 mm resulted in nucleation of identical cracks that acted as initiation points for the secondary serrations on the edges of the primary serrations, Figure 4-13(d). The crack nucleation mechanism and the fractured chip surface shown Figure 4-13(f) reveal the serration formation for CG is identical to the mechanism described for FG.

The CG chip formation data, Table 4-3, show that  $h_{max\_c}$  and CCR follow the same trend observed in the FG machining, i.e. they reduced with increasing  $V_C$  and CCR reduced with increasing  $a_p$  at corresponding  $V_C$  conditions. However, varying the cutting parameters had no significant effect on the  $h_s$  as the values ranged between 31-33  $\mu\text{m}$  for all the machining conditions except for the  $a_p = 0.13$  mm and  $V_C = 50$  m/min, which resulted in  $h_s = 35.2 \mu\text{m}$ . Finally, increasing  $a_p$  from 0.13 to 0.25 mm almost doubled  $d_s$ , explaining the difference primary serraion size observed in Figure 4-13(a-b), though  $V_C = 50$  m/min and  $a_p = 0.25$  mm resulted in the reduction of  $d_s$  compared to the lower  $V_C$  conditions.

**Table 4-3: Chip formation geometry data for dry machined CG RR1000.**

	$h_{max\_c}$ ( $\mu\text{m}$ )	$\epsilon$ ( $z = .95$ )	CCR	$h_s$ ( $\mu\text{m}$ )	$d_s$ ( $\mu\text{m}$ )
<b><math>V_C = 30</math> m/min <math>a_p = 0.13</math> mm</b>	93.7	$\pm 1.3$	2.09	30.9	347
<b><math>V_C = 50</math> m/min <math>a_p = 0.13</math> mm</b>	79.7	$\pm 1.5$	1.78	35.2	500
<b><math>V_C = 30</math> m/min <math>a_p = 0.25</math> mm</b>	116.3	$\pm 1.0$	1.85	32.9	632
<b><math>V_C = 50</math> m/min <math>a_p = 0.25</math> mm</b>	107.1	$\pm 1.3$	1.71	30.8	423

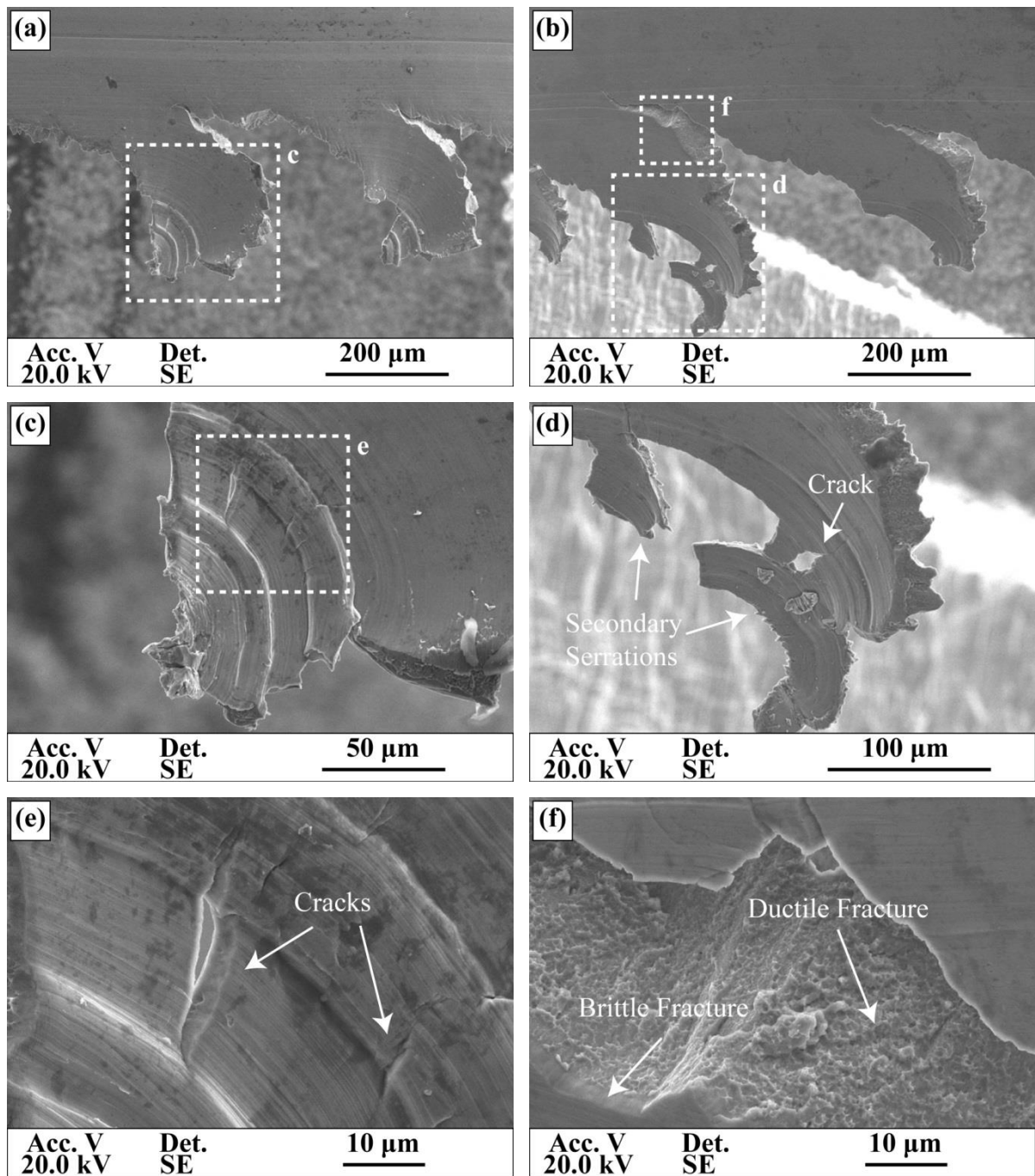


**Figure 4-13: Effect of the depth of cut on CG RR1000 chip serrations formed at  $V_C = 30$  m/min; (a,b) Primary serrations at  $a_p = 0.13$  mm and  $a_p = 0.25$  mm respectively, (c) Lack of secondary serrations at  $a_p = 0.13$  mm, (d) Secondary serrations at  $a_p = 0.25$  mm, (e) Crack nucleation at  $a_p = 0.13$  mm, (f) Serration fracture surface at  $a_p = 0.25$  mm.**

Whilst the majority of RR1000 chips consisted of both primary and secondary serrations, machining Alloy 718 resulted in the formation of primary serrations only, with continuous ribbon chips produced for all assessed cutting conditions. At  $V_C = 30$  m/min and  $a_p = 0.13$  mm, two types of serrated edges were formed randomly across the chip length, with parts of the trailing edge forming ribbon shape serrations, Figure 4-14(a), and other parts of the trailing edge forming small frequent serrations, Figure 4-14(b). Both primary serration types were similar in size and shape to the major and minor pick-ups detected on the corresponding surface. Figure 4-14(c) shows the ribbon serrations formed against chip flow resulting in large sections of the thin edge showing no evidence of serration formation when inspected optically, Figure 4-14(e), which maybe a phenomenon that has misled researchers in the past into suggesting Alloy 718 serrations only occur at  $V_C \geq 50$  m/min and similar cutting conditions, Thakur et al. (2009). Figure 4-14(d) shows that the small serrations also formed against the chip flow although they propagated initially in the feed direction until they reached a maximum serration depth similar to the RR1000 findings. Furthermore, micro-cracks were nucleated along the serration path and dimple formation was detected on the chip's fractured surfaces, indicating the ductile nature of the failure, Figure 4-14(f).

Increasing  $V_C$ ,  $Q = 13$  mm<sup>3</sup>/sec, or  $a_p$ ,  $Q = 15$  mm<sup>3</sup>/sec formed large rectangular shape serrations similar in size to the pick-ups detected on the corresponding surfaces, Figures 4-15(a-b). For both cases, serrations propagated in the feed direction until they reached a maximum chip thickness and then then propagated against the chip flow, with the serrations formed at  $V_C = 50$  m/min and  $a_p = 0.13$  mm exhibiting less tearing compared to those formed at  $V_C = 30$  m/min and  $a_p = 0.25$  mm, Figures 4-15(c-d). The latter combination of parameters also resulted in crack nucleation on the primary serration surface though similar to CG (at  $a_p = 0.13$  mm and  $V_C = 30$  m/min) no secondary serrations were formed, Figure 4-15(d).

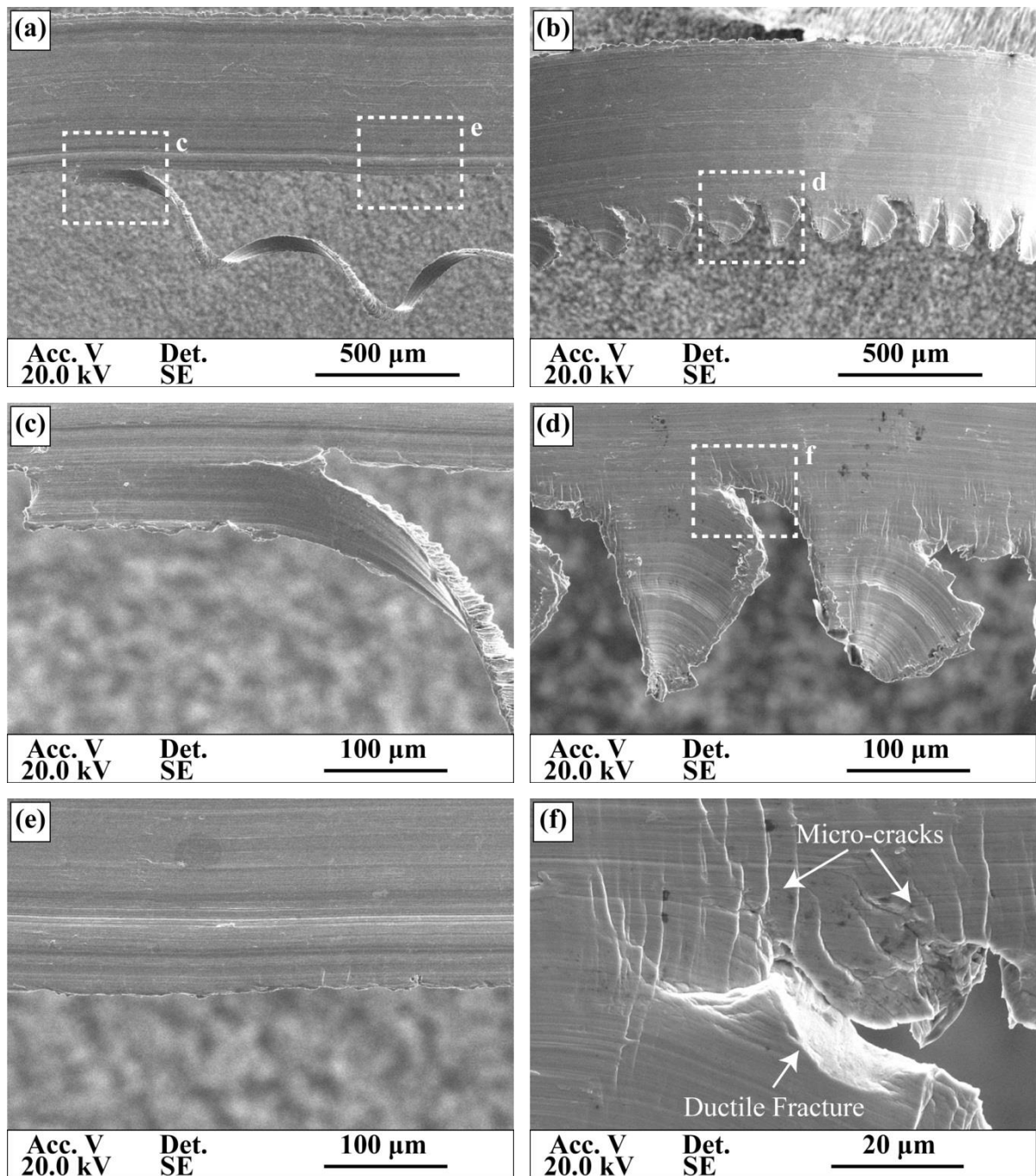


**Figure 4-14: Alloy 718 chips machined at  $V_C = 30 \text{ m/min}$  and  $a_p = 0.13 \text{ mm}$ ; (a,b) Chip morphology, (c,d) Primary serration formation, (e,f) Chip fractured surface.**

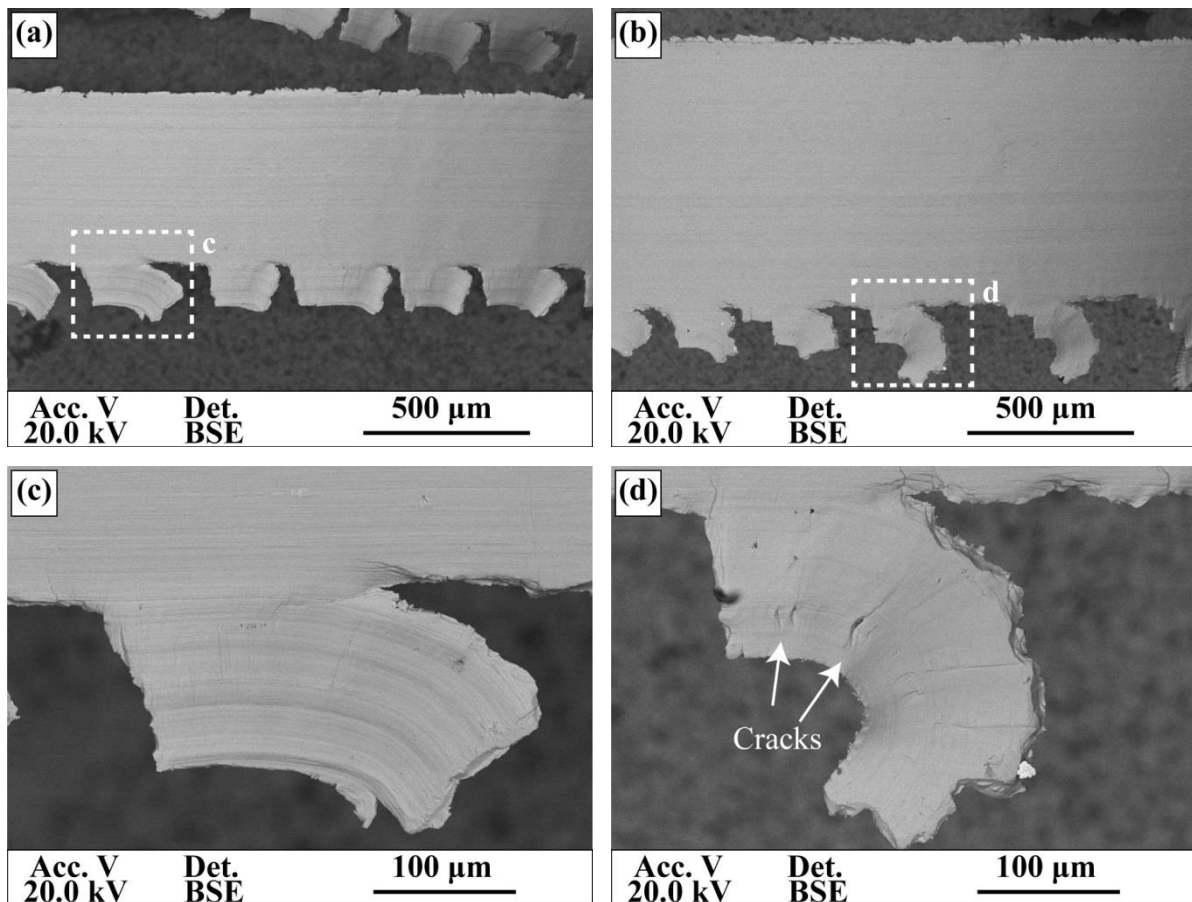


**Figure 4-15: Effect of cutting speed and depth of cut when machining Alloy 718; Chip morphology (a)  $V_C = 50$  m/min and  $a_p = 0.13$  mm, (b)  $V_C = 30$  m/min and  $a_p = 0.25$  mm, Serrations (c)  $V_C = 50$  m/min and  $a_p = 0.13$  mm, (d)  $V_C = 30$  m/min and  $a_p = 0.25$  mm.**

Rectangular shape serrations were also detected at  $V_C = 50$  m/min and  $a_p = 0.25$  mm, Figure 4-16(a), though in this case smaller and more frequent serrations were formed compared to  $V_C = 30$  m/min and  $a_p = 0.25$  mm. The phenomenon was also detected when machining CG RR1000, with the serrations exhibiting limited tearing in the chip flow direction and tendency to propagate in the feed direction even though  $h_s$  was not significantly affected by the variation in cutting parameters. Figure 4-16(b) shows that these conditions also resulted in crack nucleation on the primary serraion surface, a phenomenon detected only at high  $a_p$  when machining Alloy 718.

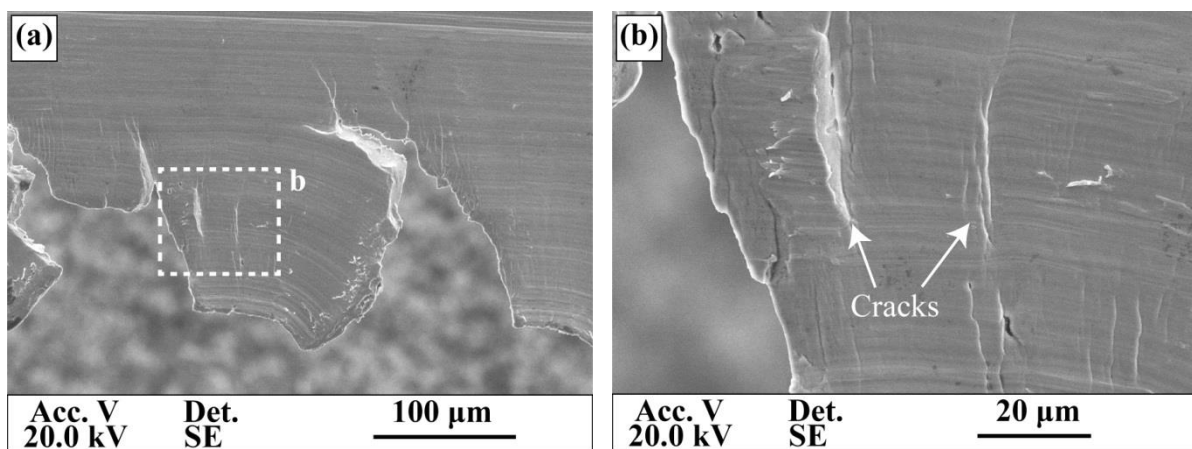


**Figure 4-16: Alloy 718 serrations formed at  $V_C = 50$  m/min and  $a_p = 0.25$  mm; (a)**

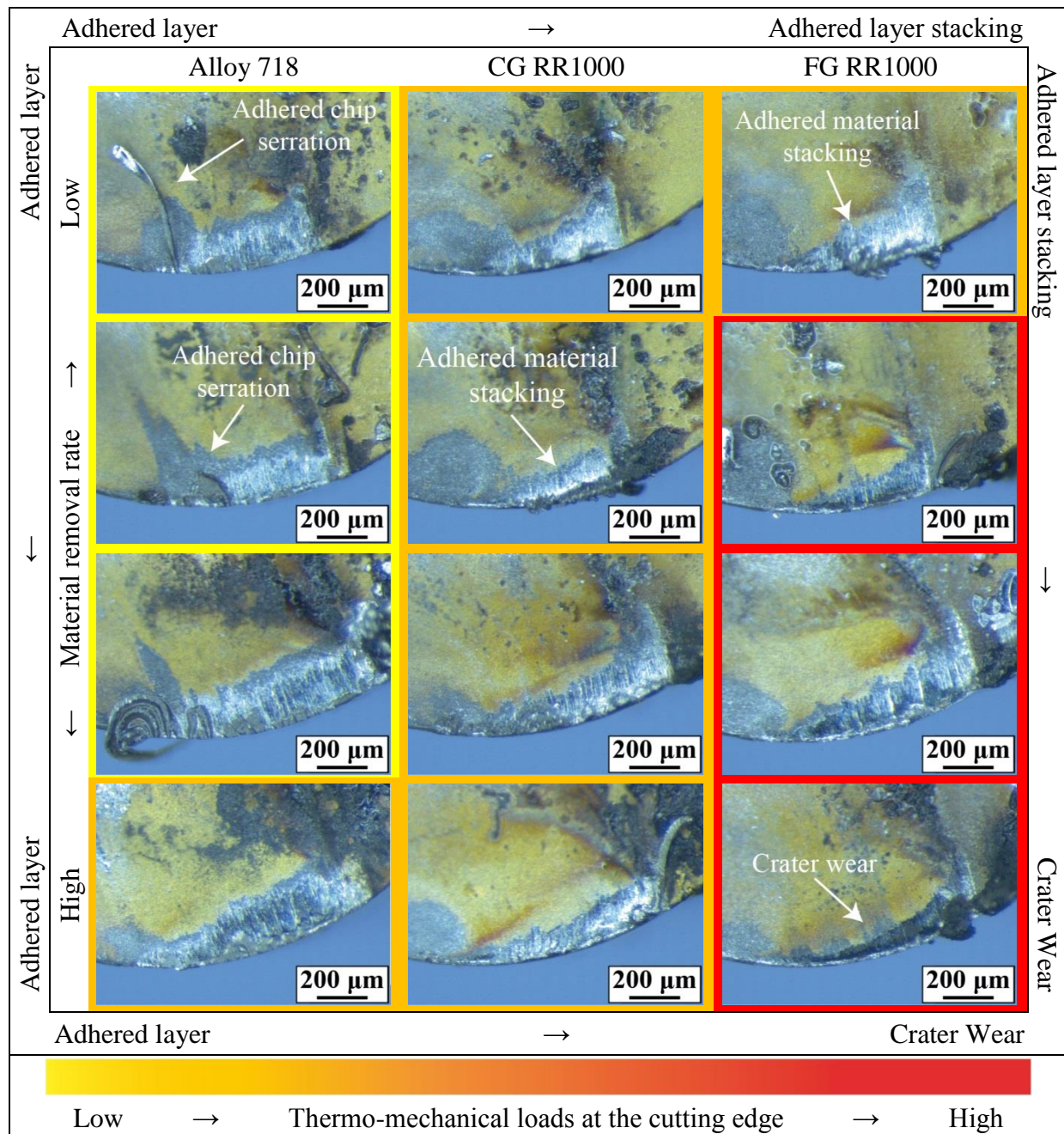
**Serration morphology, (b) Crack formation.**

Table 4-4 shows the Alloy 718 chip geometry data, gathered by 3D scanning. Chips formed at  $V_C = 30$  m/min and  $a_p = 0.13$  mm resulted in  $h_s = 15.8$   $\mu\text{m}$  and  $d_s = 214$   $\mu\text{m}$  explaining the small serrations shown in Figure 4-14(b). Increasing  $Q$  increased  $h_s$ , which was found to be in the range of 25-26  $\mu\text{m}$  for all other machining parameter combinations, also explaining the increase in  $d_s$  and the large serrations detected in Figures 4-15(c-d). Overall machining Alloy 718 produced thicker chips compared to both RR1000 variants even though chip formation trends were identical for all superalloys, with Alloy 718  $h_{\max,c}$  and CCR also reducing with increasing  $V_C$ , and CCR reducing with increasing  $a_p$  at corresponding  $V_C$  conditions.

**Table 4-4: Chip formation geometry data for dry machined Alloy 718.**

	$h_{\max,c}$ ( $\mu\text{m}$ )	$\epsilon$ ( $z = .95$ )	CCR	$h_s$ ( $\mu\text{m}$ )	$d_s$ ( $\mu\text{m}$ )
$V_C = 30$ m/min $a_p = 0.13$ mm	104.4	2.0	2.34	15.8	214
$V_C = 50$ m/min $a_p = 0.13$ mm	93.9	1.4	2.10	24.7	299
$V_C = 30$ m/min $a_p = 0.25$ mm	136.9	1.9	2.18	25.2	330
$V_C = 50$ m/min $a_p = 0.25$ mm	120.9	1.9	1.92	24.2	236

Figure 4-17 shows the tool rake face wear mechanisms detected when turning superalloys at increasing material removal rates ( $Q$ ) under dry conditions. All Alloy 718 machining tools formed thin adhered material layer at the rake faces, whilst fractured primary serrations were detected adhered at the tool's trailing cutting edge. Machining CG RR1000 resulted in adhered material stacking at the tool's leading edge, whilst the phenomenon was also observed when turning FG RR1000 at low  $Q$ . However, increasing  $a_p$  and  $V_C$  when turning FG RR1000, eliminated material stacking and resulted in crater wear formation, with the most severe and distinct crater observed at  $V_C = 50$  m/min and  $a_p = 0.25$  mm. Trent and Wright (2000) observed similar transformation in tool wear mechanisms (i.e. from thin metal adhered layer to severe material stacking and then crater wear) when machining steel at increasing  $Q$ , especially due to the effect of higher  $V_C$ , suggesting that these wear mechanisms may serve as rough markers in understanding the cutting thermo-mechanical conditions at the tool/chip interface. The presence of thin adhered material layer at the tool cutting faces is common in metal cutting, whilst according to the authors the formation of adhered material stacking is an indication of "seizure" occurring at the cutting zone. Desaigues et al. (2016) explained that this phenomenon, also known as built-up edge (BUE), usually occurs at low  $V_C$  when chip material is under high stress and at a viscous state (with high friction between the tool/chip interface). Finally, Liao and Shiue (1996) and Hua and Shivpuri (2005) demonstrated that crater formation usually occurs due to the combined effect of high heat and high stresses promoting diffusion and abrasion wear respectively, explaining its occurrence at higher material removal rates. Overall, the variations in the rake wear mechanisms shown in Figure 4-17 suggested a range of thermo-mechanical loads acting at the tool's cutting edges, depending on both the cutting parameters and the workpiece microstructure and properties.



**Figure 4-17: Tool rake face wear mechanisms for dry machined superalloys.**

Furthermore, Figure 4-18(a) shows an example of the indentations detected only on finished FG RR1000 surfaces, whilst Figure 4-18(b) demonstrates that the phenomenon was caused by tool fragments being pressed into the surface during machining. Gatto and Iuliano (1994) observed accelerated tool disintegration and tool fragments pull outs when machining under high heat and plasticity conditions, possibly linking this phenomenon to the more

aggressive wear observed in Figure 4-17 when machining FG RR1000 compared to that for CG RR1000 and Alloy 718. It is also critical to protect surfaces from such defects, as machining related crack formation has been proven in the past to reduce the component's fatigue performance, Sharman et al. (2001).

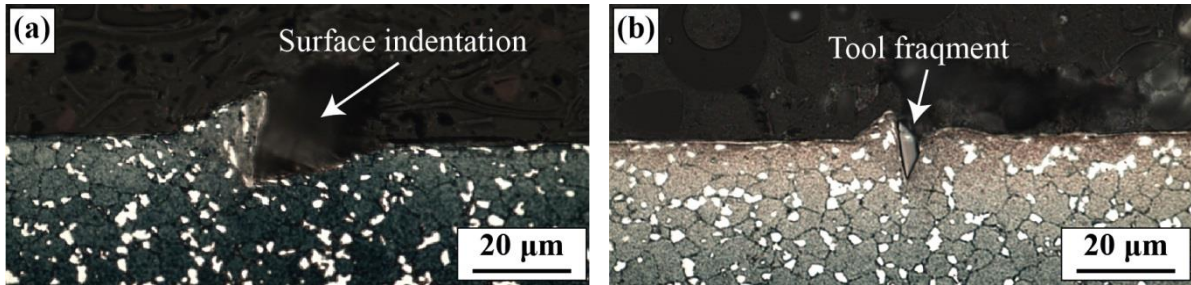


**Figure 4-18: Examples of FG RR1000 surface indentations; (a)  $V_C = 30 \text{ m/min}$  and  $a_p = 0.13 \text{ mm}$ , (b)  $V_C = 30 \text{ m/min}$  and  $a_p = 0.25 \text{ mm}$ .**

#### 4.2.1.3 Cutting Forces

Figure 4-19 shows that dry conditions resulted in similar machining forces for all three alloys, which exhibited identical variation trends at corresponding machining parameters independent of their composition and microstructure. Olovsjo and Nyborg (2012) reported that semi-rough turning of different Waspaloy and Inconel 718 microstructure variants affected tool wear, though the effect on machining forces was considered insignificant, a phenomenon that explains the minor differences observed when machining superalloys at these less aggressive finishing conditions. Overall machining force reduction was observed with increasing  $V_C$ , especially due to reduction in the cutting forces, a phenomenon that Trent and Wright (2000) linked to the reduction in the cut chip thickness and the change in shearing angle at higher  $V_C$ . Furthermore, the cutting force ( $F_C$ ) was always higher than the push-off force when machining at high  $a_p$ , compared to higher push-off forces when machining at low

$a_p$ . This suggests that higher  $a_p$  conditions result in higher cutting forces due to the deformation of larger uncut chip area compared to lower  $a_p$  values at corresponding  $V_C$ , whilst the push-off force is more related to the contact length of cutting edge and thus the amount of work going into shaping the new surface and shearing the chip during machining. At  $a_p = 0.13$  mm the uncut chip area was approximately halved compared to  $a_p = 0.25$  mm explaining the lower cutting force values, though the cutting edge contact length was only reduced by approximately 30% explaining the higher push-off forces (compared to the cutting forces) at these conditions. Finally, feed force was identical for all alloys at corresponding cutting conditions and was only affected by the depth of cut variation showing that this force output represents the elastic reaction of the tool as it was pressed against the workpiece in the feed direction.

Figure 4-20 shows that calculating the specific cutting load acting at the tool's edge using the traditional methodology resulted in overall higher values compared to those found when using the less conventional proposed calculation methodology. This can be explained by the fact that the uncut chip cross-section area used as the denominator when normalizing the  $F_C$  values in the case of the traditional calculation methodology is always smaller than the cut/deformed chip cross-section area used in the case of the proposed calculation methodology. Furthermore, in the case of the traditional methodology normalising the  $F_C$  values using the uncut chip area means that the effect of  $V_C$  on the machining process is not taken into consideration; even though it has been demonstrated in Figures 4-19(a-c) that increasing  $V_C$  reduced the overall machining forces. As a result Figure 4-20(a) exhibits the same trends as the Figures 4-19(a-c) in terms of the alloy microstructure effect on the machining process at corresponding parameters, indicating that this analysis method adds very little value to the collected data.

In the case of the proposed less conventional specific cutting load calculation methodology, Figure 4-20(b), using the cut/deformed chip area takes into consideration the effect of all parameters involved in the machining process. Therefore, the thicker chips produced at  $V_C = 30$  m/min were found to apply lower specific cutting loads compared to the thinner chips produced at  $V_C = 50$  m/min due to their larger cross-section area (even though their formation involved higher  $F_C$  values). These findings align with the chip formation principles reported in the literature review section 2.3.2.1 stating that increasing  $V_C$  increases the strain (thus more work is required to deform the chip at those conditions). In terms of the actual calculated values, the specific cutting load acting at the tool edge was found to be always higher for the FG RR1000, compared to that of CG RR1000 and Alloy 718, while the effect of higher  $Q$  achieved at high  $a_p$  conditions appears insignificant for all microstructures. Finally, the effect of  $V_C$  increase on Alloy 718 was identical to that of CG RR1000; even though machining CG RR1000 resulted in higher specific cutting loads at all machining conditions.

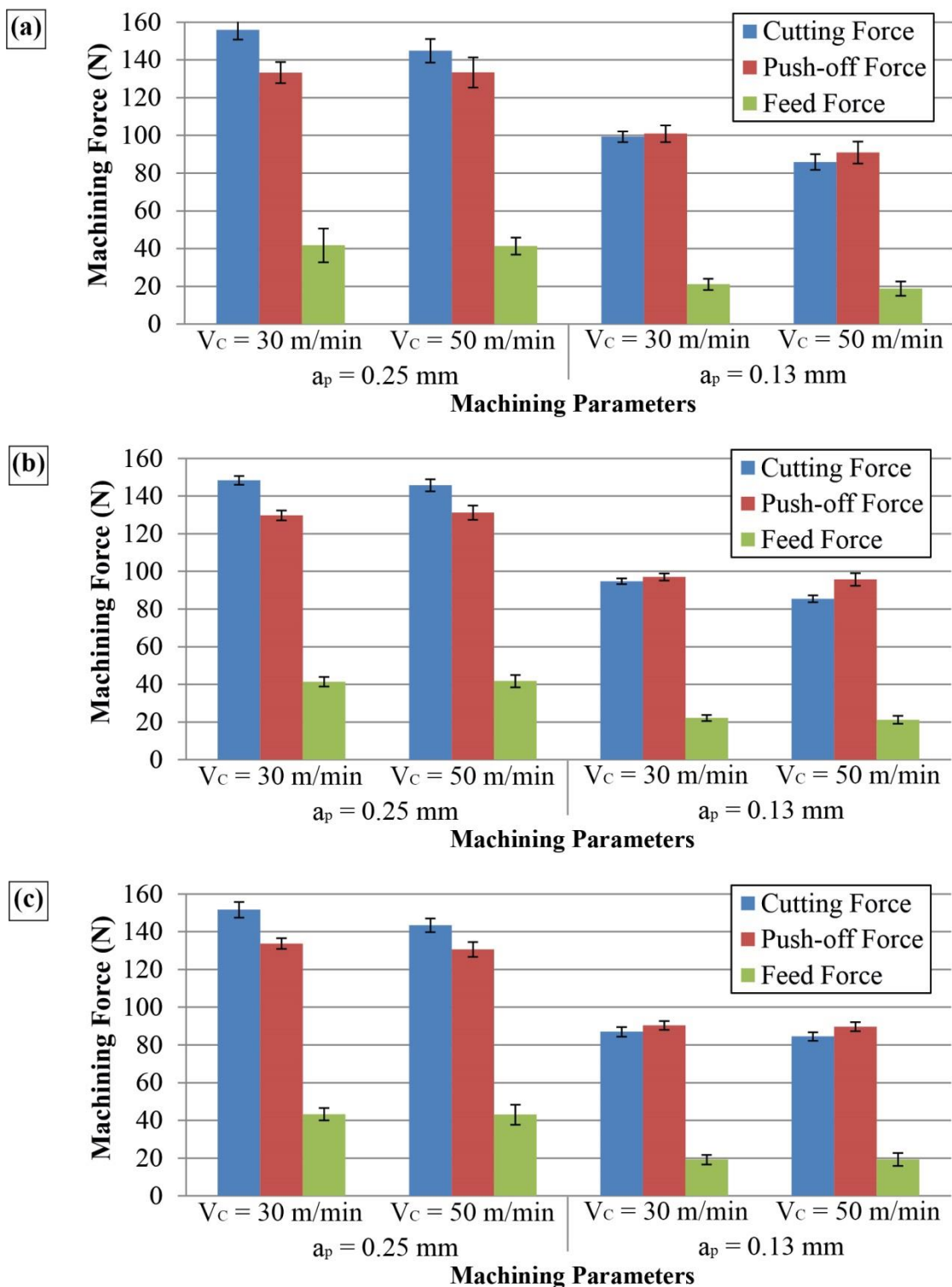
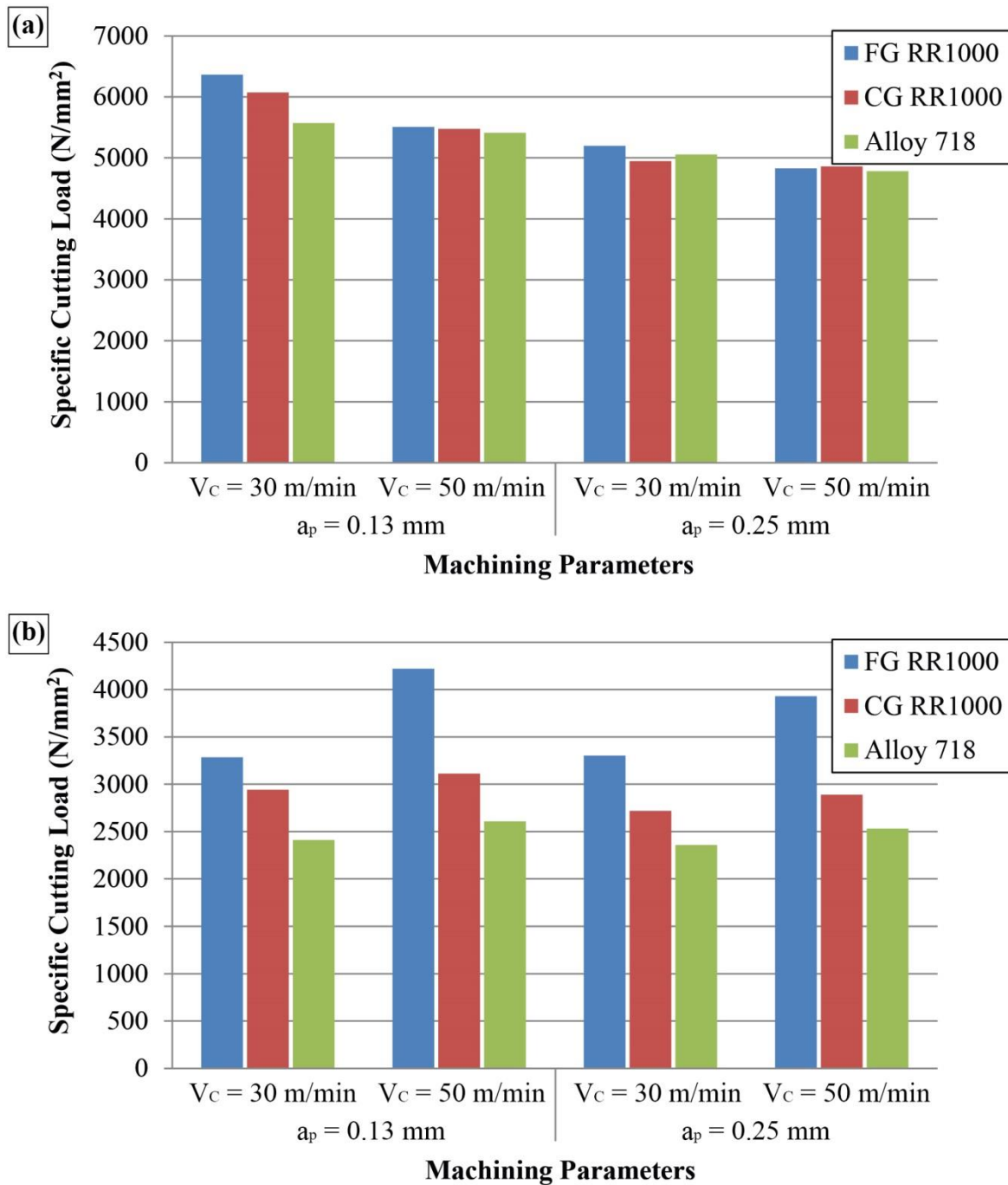


Figure 4-19: Machining forces for dry conditions; (a) FG RR1000, (b) CG RR1000, (c)

Alloy 718. (Error bars show the standard deviation)



**Figure 4-20: Effect of machining parameters and microstructure on specific cutting load when dry turning superalloys; (a) Traditional calculation methodology, (b) Proposed calculation methodology.**

#### *4.2.1.4 Discussion - Dry Trials (Phase 1)*

The results show a clear link between the fracture of primary and secondary chip serrations produced when machining all three superalloys to the surface deposits of parent material known as pick-up. The size of minor (Type 2) and major (Type 3) pick-up reveal that they originated from the deposition of secondary and primary serrations respectively, with the smearing residue streaks (Type 1) forming by smearing serrations that may not always deposit on the finished surfaces. Furthermore, key observations of: 1. the identical shape of FG RR1000 Type 3 pick-up and primary serration cross-sections in the feed direction, 2. the tool marks on the top of the defects and 3. the chip pieces coating the tool at the end of every cut, 4. the adhered fractured serrations at the tool's trailing edge, confirm that pick-up deposits consist of fractured chip serrations that were smeared and pressed on to the workpiece by the cutting tool. Pick-up deposition mechanism thus appears to link well with the trapped chip theory proposed by Sharman et al. (2008) for milling and drilling operations, though the deposits in turning can only occur at the cutting zone during serration formation in contrast to drilling operations for which the chip could be trapped at any point of the tool/workpiece interface (i.e. during extraction).

The serrations initiated from brittle cracks nucleated on the chips trailing edges, forming initially a shallow brittle fracture zone followed by dimple formation (i.e. ductile fracture) of the chip bulk, Figures 4-11(f), 4-13(f) and 4-11(f), demonstrate that deforming the chip thin trailing edge exceeded the chip's material damage strain threshold leading to fracture, serration formation and often to serration failure. According to Steglich et al. (2010) dimple formation indicates the formation of voids as a result of the high triaxiality stresses loading in the specimen, revealing that simple shearing deformation was limited, i.e. specimens

failure in a ductile manner by void formation and their coalescence. Basaran (2011) explained that higher principal triaxial loads also results in a higher ratio of the mean principal stresses value over the von Mises corresponding value which limits the ability of material to deform plastically by dislocation motion leading to premature failure in the elastic region or at much lower levels of plastic strain than in a simple shear test. Taken in combination with the dimple formation observed in the serration fracture zone of both primary and secondary serrations, it is suggested that serration formation occurred due to excessive triaxiality at the chip's thin trailing edge. Absence of serration formation at the thicker chip trailing edges machined at the very beginning of the cuts and the fact that the serrations initiated as soon as a thin trailing edge profile was machined, Figure 4-10, show that the chip's trailing edge tolerance to damage is affected by the chip thickness as well as the amount of plastic deformation at the chip edge. These evidences align to those presented by El-Wardany and Elbestawi (1998) that reported occurrence of serrations below a so-called "critical" minimum chip thickness value, linking the phenomenon to the variable chip thickness profile across the tool edge in oblique turning cuts. The chip's thin trailing edge is machined below the tool's cutting edge rounding at varying effective rake angles, that range from the tool's top rake angle to negative rake of  $-90^\circ$ , which are conditions found to increase the cut's ploughing effect and result in higher localised chip deformation at the shearing zone, Komanduri (1971).

Primary serrations appear to reach a consistent maximum thickness at which point their propagation stopped as the chip was able to support the level of deformation within the chip, forcing the initiation of the next serration. For RR1000 experiments, serration spacing ( $d_s$ ) doubled and serration maximum thickness ( $h_s$ ) increased by more than  $10 \mu\text{m}$  for both  $V_C$  conditions at  $a_p = 0.25 \text{ mm}$ , compared to the  $h_s$  values at  $a_p = 0.13 \text{ mm}$  that ranged between

31.8-33.4  $\mu\text{m}$ . This trend was not as significant when increasing depth of cut ( $a_p$ ) for CG RR1000 as  $h_s$  ranged from 31-35  $\mu\text{m}$ , however the  $a_p = 0.25 \text{ mm}$  and  $V_C = 30 \text{ m/min}$  conditions resulted in formation and fracture of secondary serrations, a phenomenon that was not present at  $a_p = 0.13 \text{ mm}$  and  $V_C = 30 \text{ m/min}$ . Furthermore, increasing  $a_p$  at  $V_C = 30 \text{ m/min}$  reduced CCR by 0.36 for FG and 0.24 for CG, which indicates variation of the chip flow (i.e. change in the shear angle) with increasing  $Q$  due to higher  $a_p$ . Machining at fixed  $f = 0.12 \text{ mm/rev}$  though means that the uncut chip thickness variation rate across the cutting edge is identical for both  $a_p$  conditions, Figure 4-21, and thus the chip shearing strain at constant  $V_C$  should also be identical for each corresponding material. This is further supported by the unaffected specific cutting loads due to  $a_p$  variation, Figure 4-20, indicating comparable strains for both  $a_p$  conditions. Thus, the difference detected in chip compression ratios at the two  $a_p$  conditions for corresponding microstructures, Figure 4-21, suggests that varying  $a_p$  alters the strain rate, indicating variation in the chip plasticity behaviour. This may link to the higher machining forces observed at high  $a_p$ , as Chen et al. (2006) and Nedic and Eric (2014) proved that the higher mechanical loads, due to increase in the uncut material removal volume, indicate more shearing work, thus more energy and higher heat loads during machining. In addition, Sadat and Reddy (1992) linked directly the reduction in surface tensile residual stresses when turning Inconel 718 to the lower thermal loads achieved at lower  $a_p$ . Therefore, it is possible that higher cutting temperature is one of the factors affecting CCR variation with increasing  $a_p$ , explaining the change in material flow. Finally, the lower deformation work required when turning CG RR1000 (i.e. CG specific cutting load is always lower than that of FG) and CG's higher strength and ductility at elevated temperatures giving this material higher deformation tolerance, explain the less significant effect of  $a_p$  variation on CG CCR and serration formation.

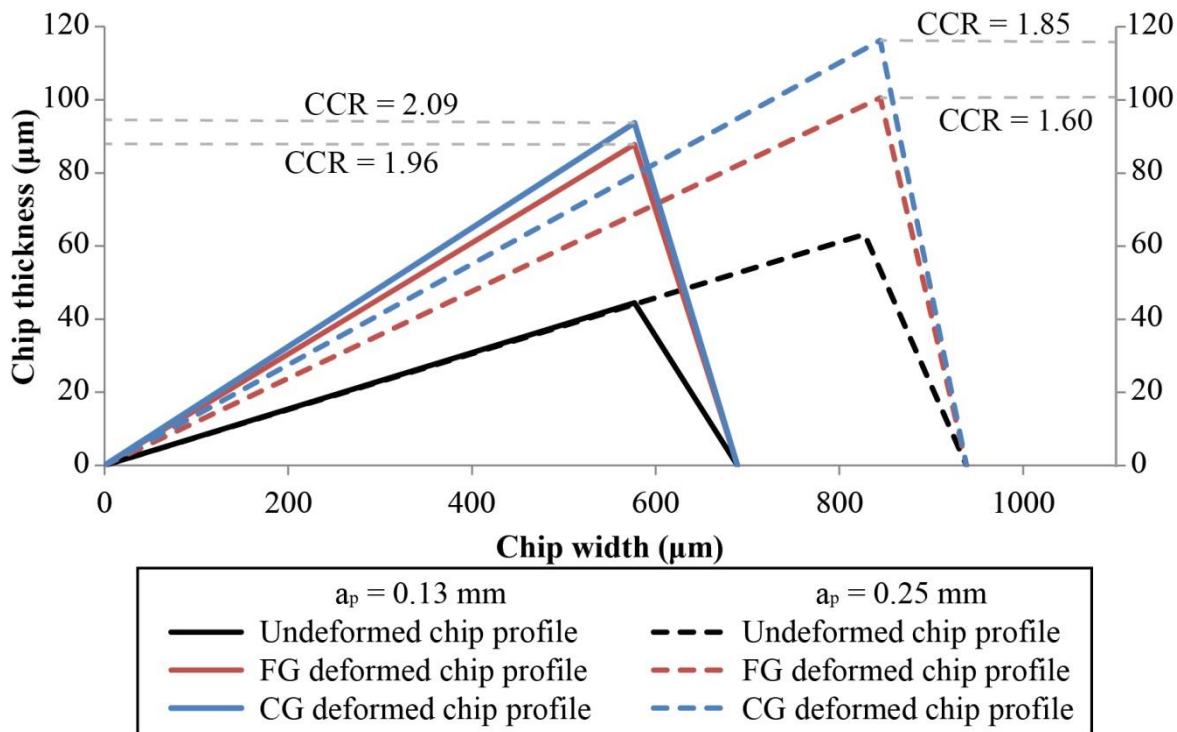


**Figure 4-21: Illustration of the depth of cut effect on FG and CG RR1000 chip deformation at  $V_C = 30$  m/min compared to the non-deformed chip thicknesses at corresponding conditions.**

Furthermore, both RR1000 variants experienced reduction in chip thickness with increasing  $V_C$  due to change in shearing angle, as discussed by (Trent & Wright, 2000), however the effect was more significant for the thinner FG chips, as CCR reduced by 0.64 at  $a_p = 0.13$  mm and 0.35 at  $a_p = 0.25$  mm, compared to less than half the reduction detected for the thicker CG chips at the corresponding conditions (i.e. 0.31 at  $a_p = 0.13$  mm and 0.14 at  $a_p = 0.25$  mm). Increasing  $V_C$ , however, was shown by Kitagawa et al. (1997) and Ozel et al. (2011) to increase machining heat loads, whilst turning superalloys under finishing conditions resulted in temperatures excess of  $800^\circ\text{C}$ . These evidences combined to the higher sensitivity of FG properties to temperature variation, explain the different plasticity performance of the two alloy variants with increasing  $V_C$  and FG's higher sensitivity to the variation of cutting conditions. In addition, the higher FG localised mechanical loads, which also explain the tool

crater wear formation in FG machining, indicate higher strain when machining the less ductile FG chips at high  $V_C$ , forcing the chips to prematurely reach maximum strain leading to higher strain rates and significantly lower thicknesses (i.e. higher shearing angle) than the corresponding CG chips. Finally, FG exhibiting overall lower ductility explains the inability of FG chips to withstand the propagation of both serration types, leading to the presence of all three pick-up types on the FG surfaces. On the other hand the CG's superior ductility resulted in the majority of the deposits detected on the CG surfaces being minor pick-ups (Type 2) demonstrating that CG chips were able to maintain structural integrity of their primary serrations and thus explaining the absence of severe chip smearing residue damage (Type 1) from CG surfaces.

Machining Alloy 718 resulted in overall the thickest chips and smallest serrations, due the lowest serration thickness values produced in these experiments, indicating that this alloy exhibits higher plasticity tolerance than both FG and CG RR1000 at corresponding cutting parameter combinations. However, evidences like 1. Alloy 718 having the lowest specific cutting loads at the tool's edge and 2. Rake tool wear indicating the least aggressive machining conditions when machining Alloy 718, suggest that the strain required for deforming Alloy 718 chips and possibly the heat loads developed during machining are lower than those when machining RR1000. This, however, did not prevent pick-up occurrence on Alloy 718 surfaces that was found to be more severe at  $V_C = 30$  m/min, whilst  $V_C = 50$  m/min resulted in the least surface damage; contradicting the RR1000 observations that indicated less severe pick-up occurrence at lower  $Q$ . Combining though the Alloy 718 surface finish findings with serration formation shows that the most severe deposits occurred when dry machining produced ductility conditions that favoured an unstable transformation in the serration formation mechanism. For example, machining Alloy 718 at  $V_C = 30$  m/min and  $a_p$

$a_p = 0.13$  mm resulted in unstable serration formation producing two types of serrations, Figure 4-14(a-b), that although they had penetrated to the shallowest thickness overall, they frequently fractured-off completely and deposited on the surface in the form of pick-ups. Increasing cutting speed (i.e.  $V_C = 50$  m/min and  $a_p = 0.13$  mm) formed larger serrations that penetrated to higher serraion thickness relieving the machining strain at the chip's thin edge; thus limiting their tendency for fracturing-off and resulting in less severe pick-up. Alloy 718 pick-up severity also increased with increasing  $a_p$  at  $V_C = 30$  m/min, even though identical serraion morphology and similar chip compression ratio were produced to those formed at  $V_C = 50$  m/min and  $a_p = 0.13$  mm, (i.e. CCR = 2.18 and CCR = 2.10 respectively), which suggests similar chip strain rates for both cases. However, the crack nucleation on the serraion surface and excess serraion tearing observed at  $V_C = 30$  m/min and  $a_p = 0.25$  mm, are indicative of lower chip trailing edge plasticity tolerance at these conditions, leading to more unstable serraion formation compared to  $V_C = 50$  m/min and  $a_p = 0.13$  mm, Figures 4-15(c-d). These findings and the effect of  $a_p$  on Alloy 718 CCR at  $V = 30$  m/min, Figure 4-22, add to the FG and CG RR1000 findings suggesting that high  $a_p$  conditions limit the chips tolerance to plasticity compared to low  $a_p$  conditions, possibly due to the effect of higher cutting temperatures produced when increasing the chip material volume removed. Increasing  $V_C$  to 50 m/min at  $a_p = 0.25$  mm, increased the chip strain, similar to FG and CG RR1000, though instead of promoting serraion failure and pick-up deposition, serraion formation mechanism transformed once more to a stable state, producing more frequent serrations that exhibited limited tearing and fracturing-off, also resulting in improved surface finish.

Furthermore, specific characteristics common in Alloy 718 and CG RR1000 machining, like: 1. similar CCR reduction rates when increasing  $V_C$  at corresponding  $a_p$  conditions, 2. identical trend in  $d_s$  variation with increasing  $Q$  and 3. similar effect of  $V_C$  on the specific

cutting loads variation, indicate comparable performance between the two ductile and coarse grain workpieces. This is further supported by the fact that when the deformed chip profile thickness variation of Alloy 718 and CG RR1000 matched at  $V_C = 30$  m/min for  $a_p = 0.25$  mm and  $a_p = 0.13$  mm respectively (i.e. suggesting similar strain rates), Figure 4-22, both alloys produced primary serrations only with cracks forming on their surface, whilst these serrations were similar in morphology, size and thickness. Further increase in machining strain and heat loads (due to higher  $V_C$  and  $a_p$ ) resulted in similar chip and serra formations trends for both alloys, though the thicker Alloy 718 chips and the formation of Alloy 718 primary serrations only, confirm that this material exhibited higher plasticity tolerance than CG RR1000 at corresponding machining parameters.

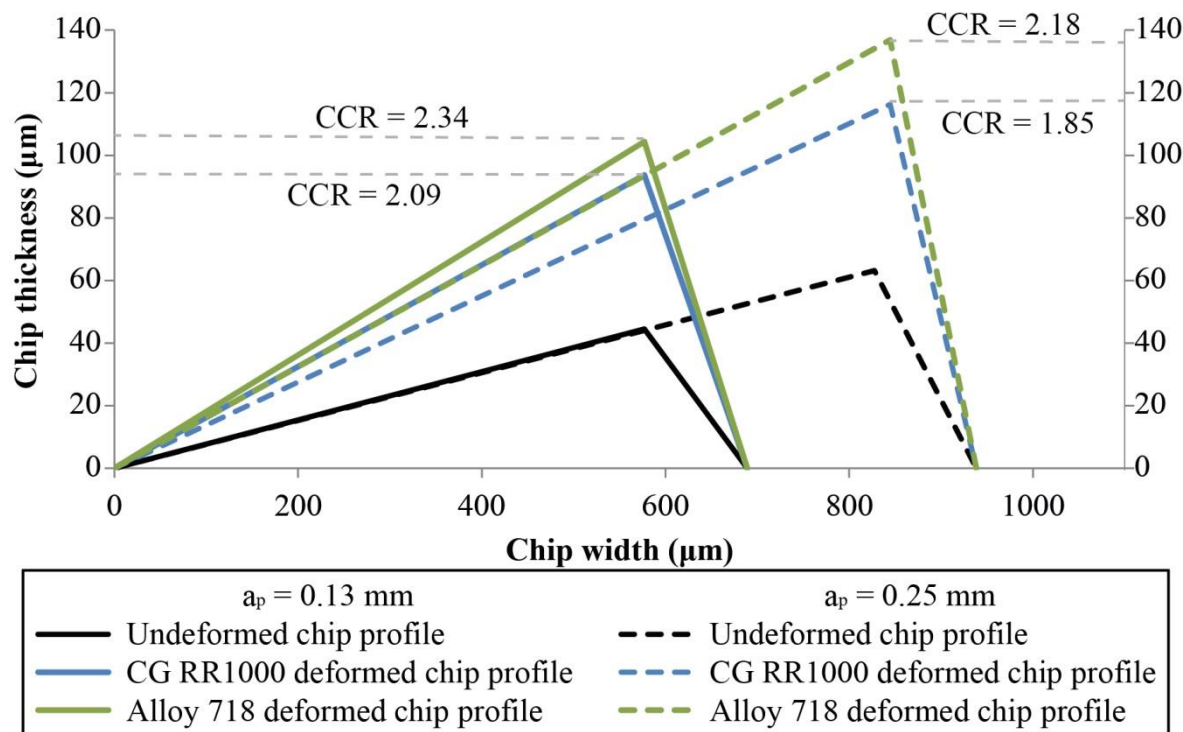


**Figure 4-22: Illustration of the depth of cut effect on CG RR1000 and Alloy 718 chip**

**deformation at  $V_C = 30$  m/min compared to the non-deformed chip thicknesses at corresponding conditions.**

Summarizing the findings, the serration formation is linked to the limited ability of the chip's thin trailing edge, machined with round inserts, to support the imposed strain at high temperatures within the chip, though the extent of the fractures and the formation of primary or primary and secondary serrations is defined by the ductility performance of the machined material at corresponding cutting conditions. For RR1000 machining, the increase in cutting temperatures and machining strains, due to increase in  $Q$  is key in the reduction of chip's ductility, increasing the serration fracture likelihood and increasing the risk of pick-up severity. Machining the more ductile Alloy 718, however, demonstrated that the relationship between chip ductility conditions and pick-up damage is more complex than the linear relationship shown when machining RR1000, with the serration fracturing-off tendency depending on whether the ductility conditions at the chip's edge favour the serration propagation to failure independently of their propagation thickness. This phenomenon also explains the common failure of the smaller RR1000 secondary serration which although propagated in lower thickness their tendency to failure is higher than that of the primary serrations especially when machining CG RR1000. Furthermore, it is now possible to explain the reason behind the concurrent emergence of serrations during machining and enhanced levels of pick-up deposits with the introduction of P/M superalloys in the production of jet engine rotative components. The strict machining standards for these high strength alloys require very low Ra values that dictate the use of low feed rates in oblique turning cuts, resulting in the machining of very thin chips and causing the formation and fracture of these serrations leading to pick-up. It is thus suggested that if the strict Ra conditions are to be maintained when machining the low ductility FG RR1000, temperature and cutting strains should be controlled by optimising the cutting strategy by coolant application and optimised tool geometry, in order to control the serrations formation and fracture taking into

consideration that reducing the serration thickness and size to the minimum may not be the optimum solution for pick-up elimination.

## 4.2.2 Minimum Cooling Trials (Phase 2a)

### 4.2.2.1 Surface Integrity

Minimum cooling conditions resulted in Type 2 sporadic minor pick-up deposits on surfaces machined at  $V_C = 30\text{-}50 \text{ m/min}$ . The defects consisted of a series of pick-up protrusions, which were smeared along the cutting direction and contained between the feed marks, Figures 4-23(a-b). Figure 4-23(c) shows that  $V_C = 70 \text{ m/min}$  resulted in the increase of pick-up damage due to the occurrence of severe Type 1 pick-up smearing residue combined with partial parent material deposits, Figure 4-23(d), and in many cases major Type 3 pick-up protrusions, Figure 4-23(e). Tool marks were also detected on the protrusion's top faces revealing pick-ups were smeared on the surface by the cutting tool, Figure 4-23(f). These severe pick-ups were smeared in the cutting direction, similar to the minor defects, though they were found to extent further than the machining mark's width (i.e.  $120 \mu\text{m}$ ) opposite to the tool feed direction, whilst they never overlapped the leading machining marks in the feed direction, suggesting that the defects were reduced in their current size and shape by the next tool pass, Figure 4-24(a). In addition to pick-ups, secondary defects like long machining grooves along the feed marks were also formed by the following tool pass, which similar to the findings by Bailey (1977) appear to have been caused by non-uniform trailing cutting edge profile due material build-up, Figure 4-24(b).

Machining at  $a_p = 0.13 \text{ mm}$  resulted in similar surface damage as the  $a_p = 0.25 \text{ mm}$  conditions, though at  $V_C = 70 \text{ m/min}$  severe surface damage due to Type 3 pick-ups was only detected at the beginning of the cut, Figures 4-25(a-b). Whilst the surface machined towards the end of the cut had similar finish to the lower  $V_C$  conditions, with minor pick-up deposits (Type 2) and long grooves along the trailing end of the machining marks, Figures 4-25(c-d).

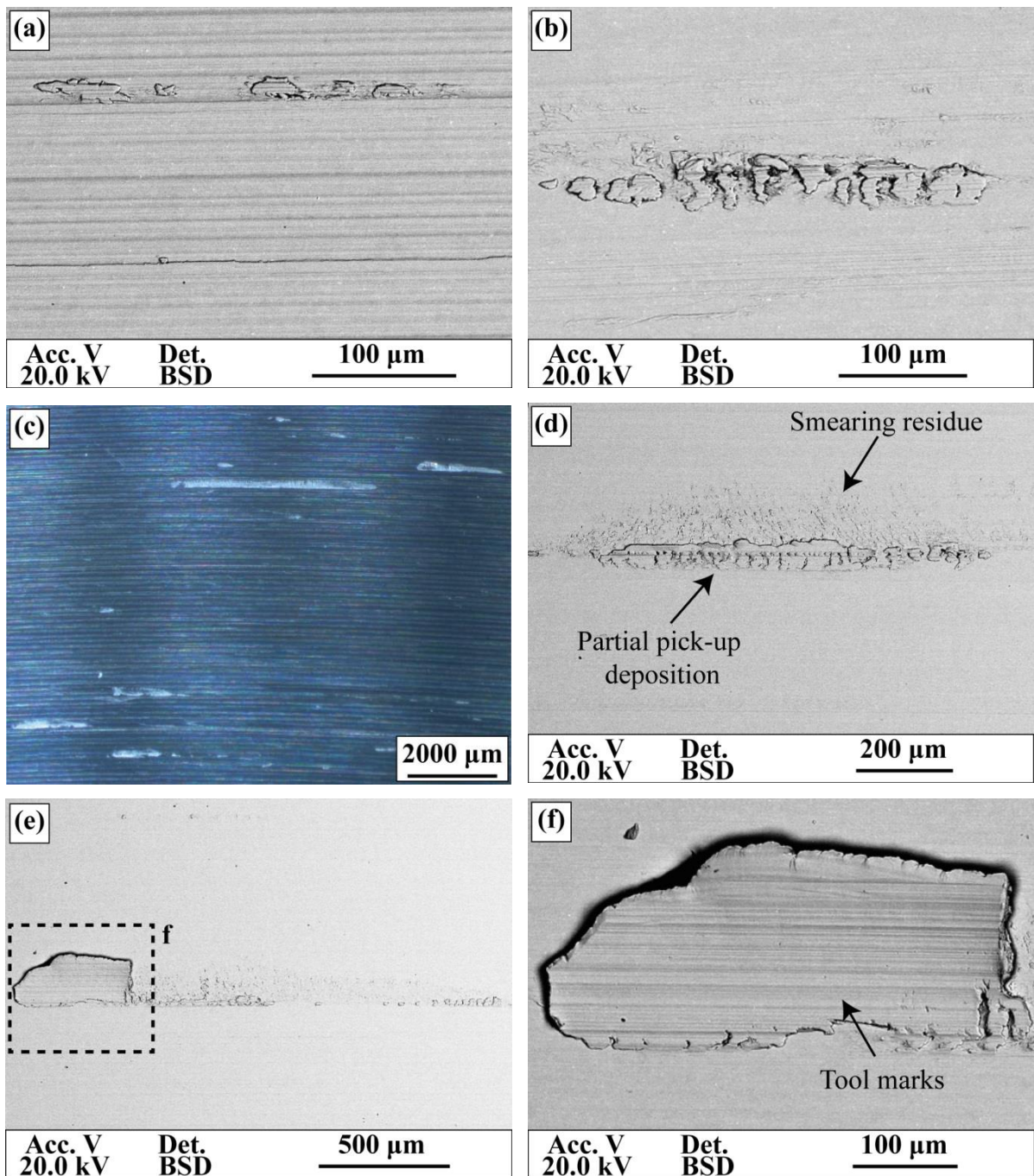


**Figure 4-23: Surface defects for minimum cooling at  $a_p = 0.25$  mm; (a)  $V_C = 30$  m/min, (b)  $V_C = 50$  m/min, (c-f)  $V_C = 70$  m/min.**

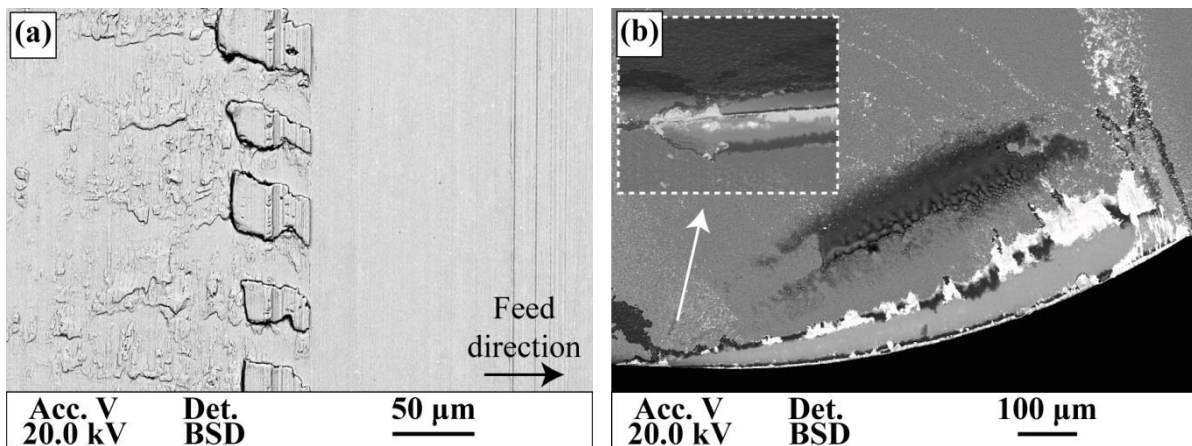


**Figure 4-24:** Pick-up deposition and cut progression effect on surface finish; (a) Surface damage and (b) Tool rake wear at  $V_C = 70 \text{ m/min}$  and  $a_p = 0.25 \text{ mm}$ .

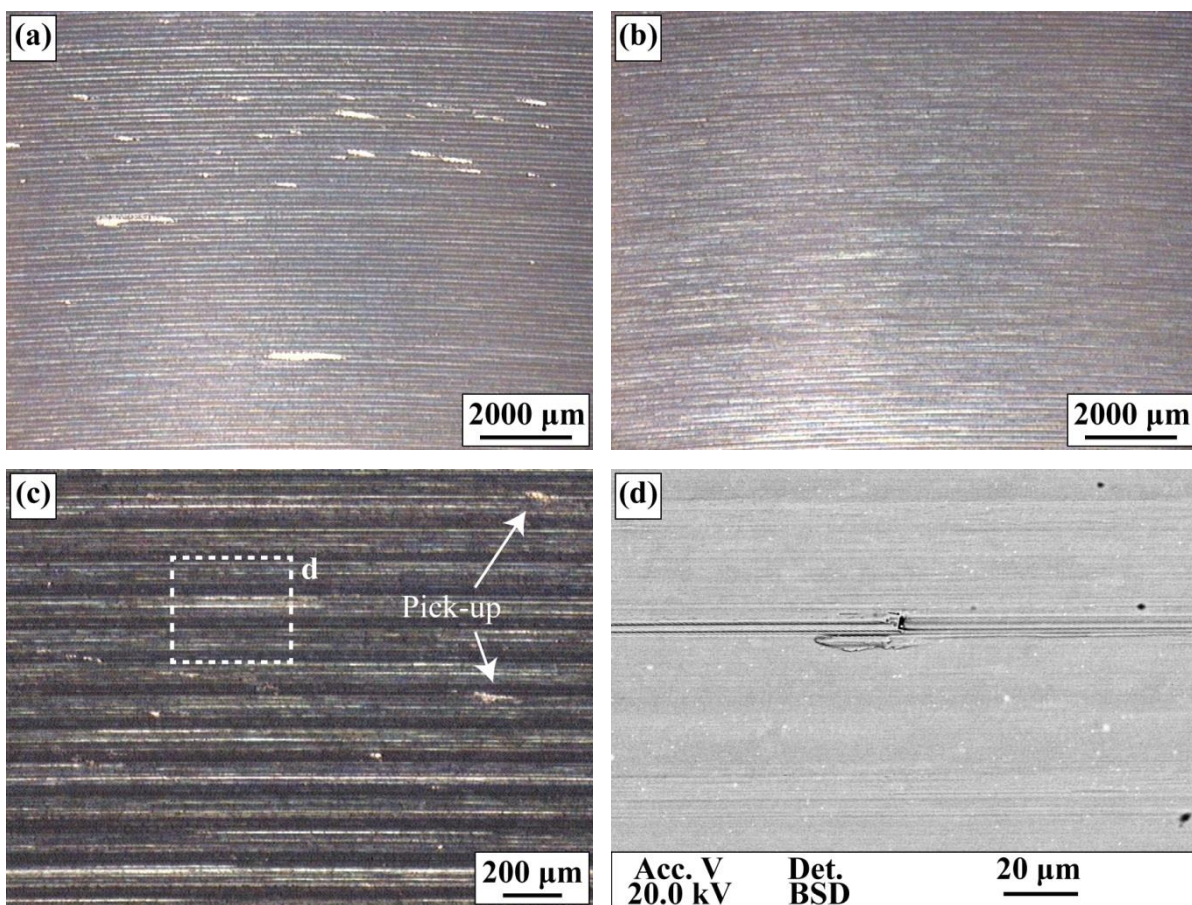


**Figure 4-25:** Surface finish at  $V_C = 70 \text{ m/min}$  and  $a_p = 0.13 \text{ mm}$ ; (a) Beginning of the cut, (b) End of the cut and (c-d) Minor surface defects.

Both pick-up damage severity and material removal rate had negligible effect on surface roughness Ra, with the average values ranging between 0.25-0.31  $\mu\text{m}$  Ra for all the minimum cooling experiments. Figure 4-26(a) shows that the major pick-ups detected at  $V_C = 70 \text{ m/min}$  exceeded 30  $\mu\text{m}$  in maximum protrusion height (i.e. similar in to the maximum primary serration thickness), whilst calculating surface roughness Ra using the 3D scans verified that the pick-up's size, geometry and especially the occurrence rate effect on average Ra is insignificant at these conditions, Figure 4-26(b). This also suggests that optical inspection is currently the only process capable of detecting the presence of pick-up in production, as the Ra measurements taken across the feed direction using the conventional stylus technique is not sensitive enough to capture random pick-up deposits on the surface.

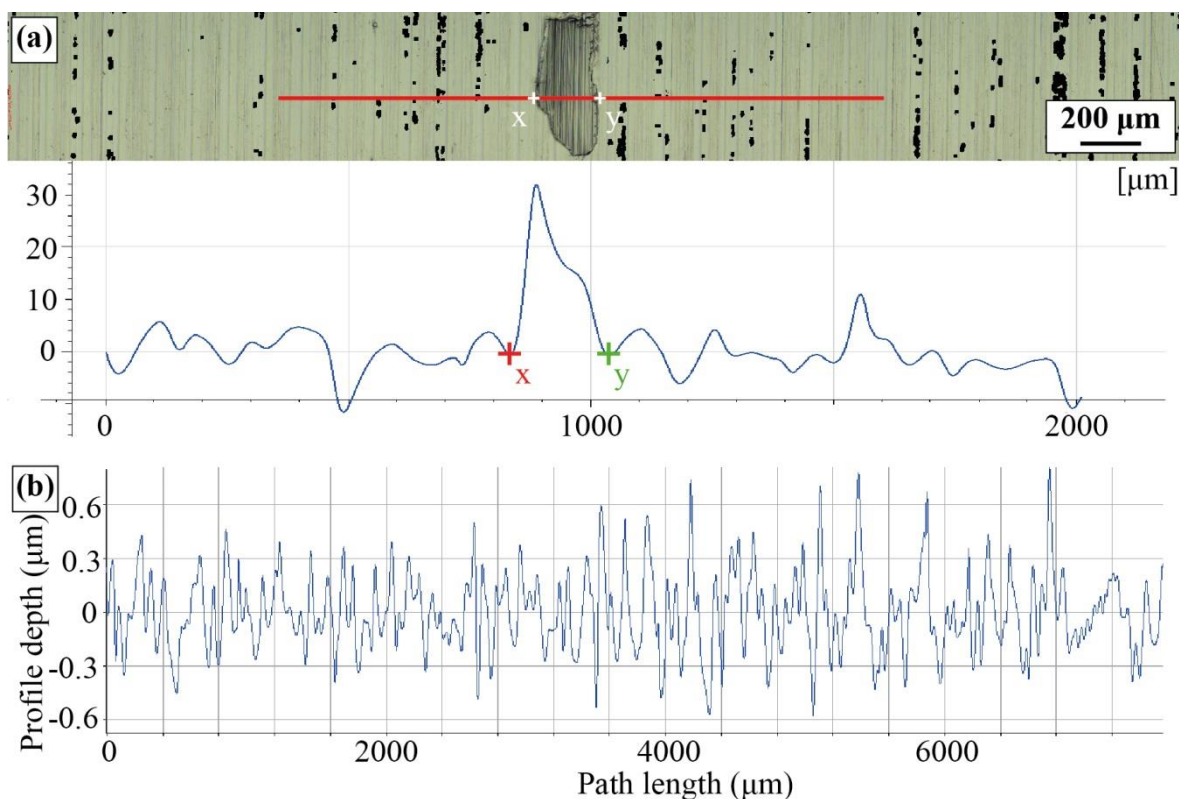


**Figure 4-26: 3D scan of Type 3 pick-up detected in FG RR1000 machining at  $V_C = 70 \text{ m/min}$  and  $a_p = 0.25 \text{ mm}$ ; (a) 2D profile, (b) Surface roughness Ra estimation.**

Furthermore, neither the minimum cooling conditions nor the varying cutting parameters appear to have had any impact on subsurface deformation, similar to previous experiments, as the distortion depth of all samples never exceeded the 2  $\mu\text{m}$  from the surface, Figure 4-27.

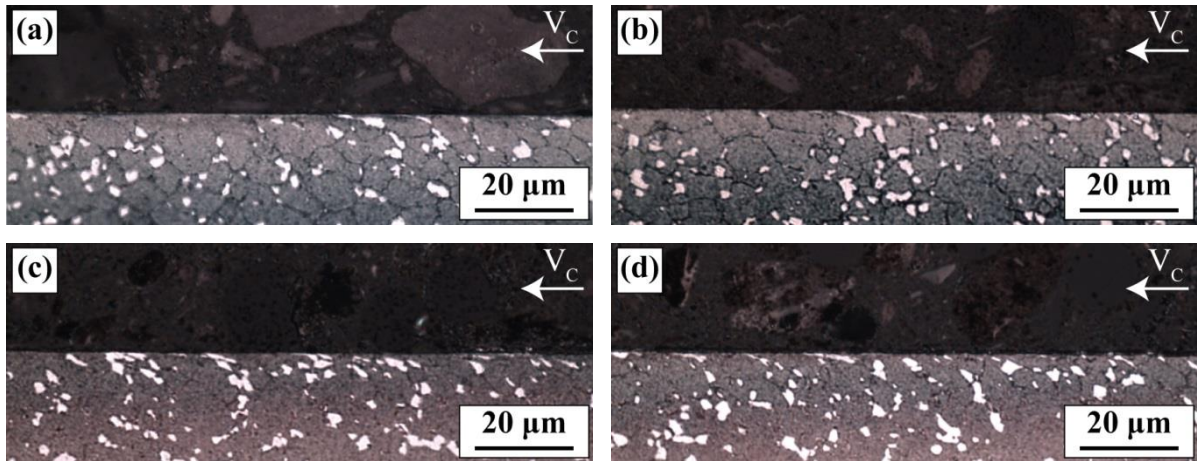


**Figure 4-27: FG RR1000 subsurface deformation at minimum cooling conditions;  $V_C = 30 \text{ m/min}$**  (a)  $a_p = 0.13 \text{ mm}$  and (b)  $a_p = 0.25 \text{ mm}$ ,  $V_C = 70 \text{ m/min}$  (c)  $a_p = 0.13 \text{ mm}$  and (d)  $a_p = 0.25 \text{ mm}$ .

#### 4.2.2.2 Chip Geometry

Continuous ribbon chips with primary hook shape serrations and secondary serrations, forming at their trailing edges, were produced for all assessed minimum cooling conditions. In contrast to the FG RR1000 dry cuts, the serration size decreased with increasing  $V_C$ , whilst their morphology appears unaffected by the variation in  $a_p$  conditions, Figure 4-28. The chip geometry data, gathered by 3D scanning, confirm these observations, Table 4-6, as the highest serration thicknesses ( $h_s$ ) were produced at  $V_C = 30 \text{ m/min}$ , explain the larger serration size and high serration spacing ( $d_s$ ) at these conditions. Increasing  $V_C$  resulted in lower chip compression ratios (CCR), due to decreasing the cut chip thicknesses ( $h_{\max_c}$ ), which at  $V_C = 70 \text{ m/min}$  and  $a_p = 0.25 \text{ mm}$  were very close to the minimum theoretical value

of CCR = 1. The values of  $h_s$  and  $d_s$  also reduced at  $V_C \geq 50$  m/min, explaining the smaller and more frequent serrations detected with increasing  $V_C$ .

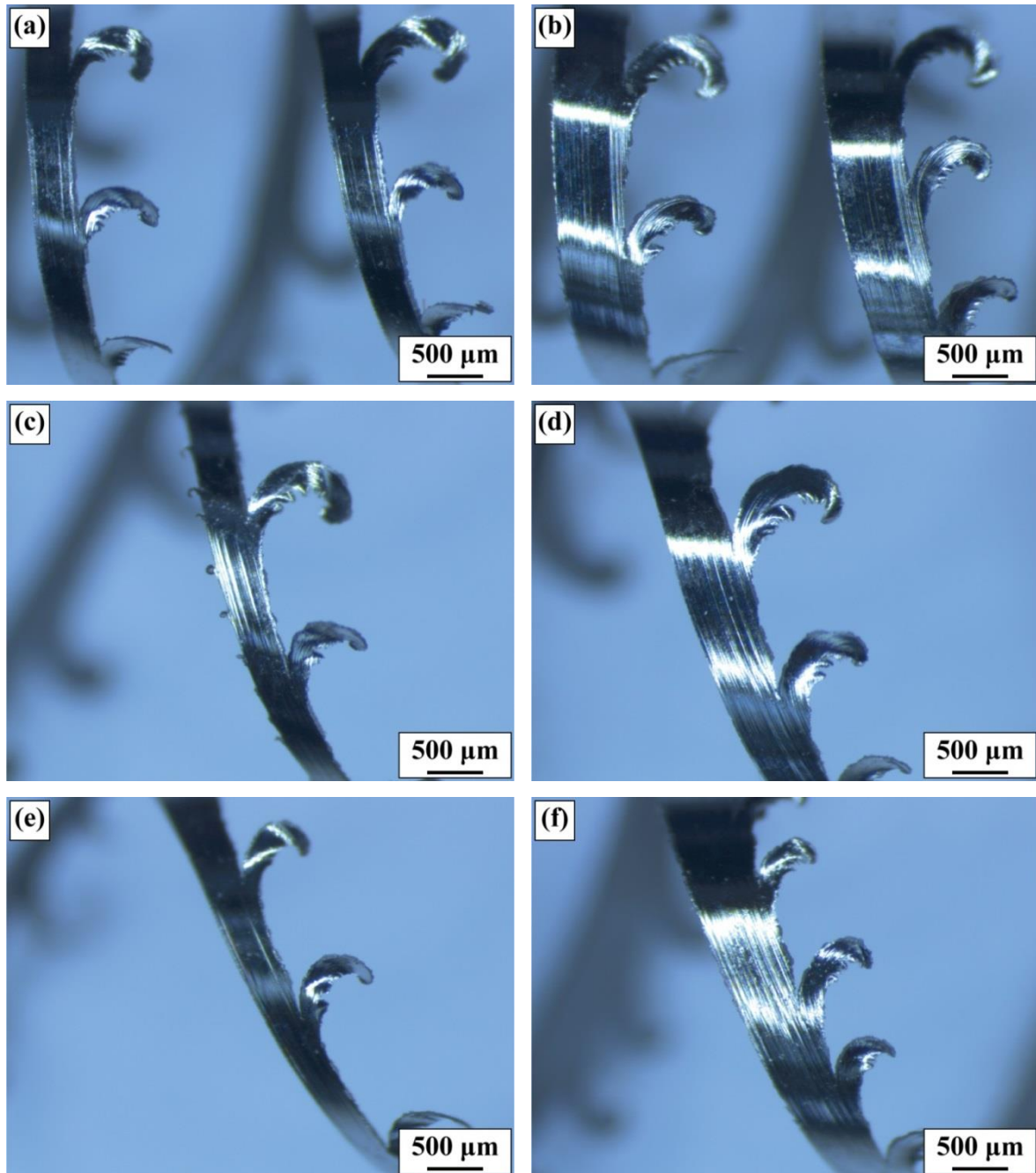


**Figure 4-28: Chip formation at minimum cooling conditions;  $V_C = 30$  m/min (a)  $a_p = 0.13$  mm and (b)  $a_p = 0.25$  mm,  $V_C = 50$  m/min (c)  $a_p = 0.13$  mm and (d)  $a_p = 0.25$  mm,  $V_C = 70$  m/min (e)  $a_p = 0.13$  mm and (f)  $a_p = 0.25$  mm.**

**Table 4-5: FG RR1000 chip formation geometry data for minimum cooling trials.**

	$h_{max\_c}$ ( $\mu\text{m}$ )	$\epsilon$ ( $z = .95$ )	CCR	$h_s$ ( $\mu\text{m}$ )	$d_s$ ( $\mu\text{m}$ )
<b><math>V_C = 30 \text{ m/min } a_p = 0.13 \text{ mm}</math></b>	92.4	$\pm 1.1$	2.07	53.3	1562
<b><math>V_C = 50 \text{ m/min } a_p = 0.13 \text{ mm}</math></b>	65.9	$\pm 1.8$	1.47	42.2	1217
<b><math>V_C = 70 \text{ m/min } a_p = 0.13 \text{ mm}</math></b>	61.0	$\pm 1.5$	1.36	40.6	1178
<b><math>V_C = 30 \text{ m/min } a_p = 0.25 \text{ mm}</math></b>	114.5	$\pm 1.3$	1.82	60.9	1569
<b><math>V_C = 50 \text{ m/min } a_p = 0.25 \text{ mm}</math></b>	74.8	$\pm 0.7$	1.19	41.5	1012
<b><math>V_C = 60 \text{ m/min } a_p = 0.25 \text{ mm}</math></b>	70.6	$\pm 0.9$	1.12	41.8	896

Further observations of the minimum cooling experiments include 1. random tendency of primary serration formed at  $V_C = 70 \text{ m/min}$  to fracture off during machining, Figure 4-29(a-b), explaining the severe pick-up defects detected at the corresponding surfaces caused by deposition of the failed primary serrations, 2. evidence of secondary serration failure explaining the occurrence of minor pick-ups, Figure 4-29(c) and 3. adherence of fractured secondary serrations at the tool's trailing cutting edge verifying that the fractured-off serrations were trapped between the tool and workpiece interface before being deposited on the surfaces, Figure 4-29(d).

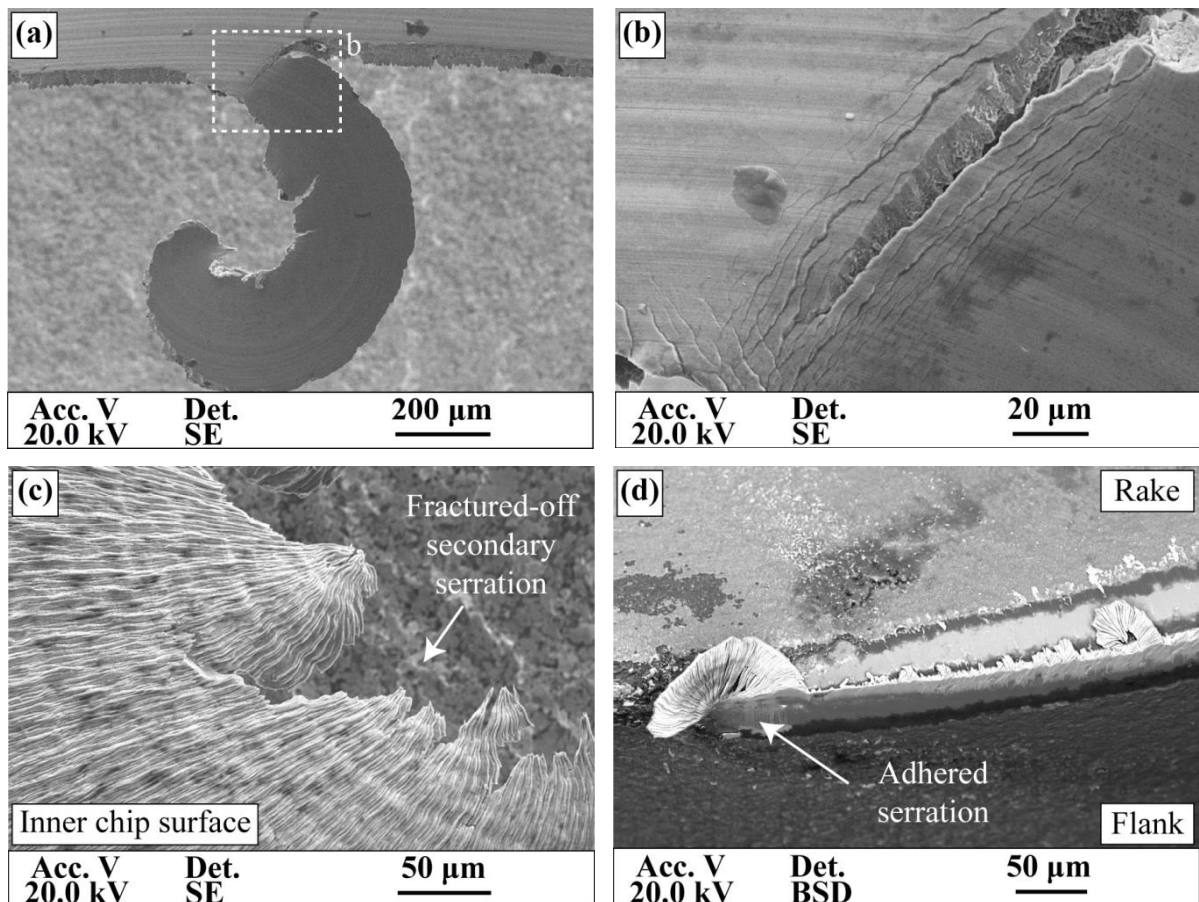


**Figure 4-29: Further observations at  $V_C = 70$  m/min and minimum cooling conditions;**

**$a_p = 0.25$  mm (a) Serration geometry and (b) Serration partial fracture,  $a_p = 0.13$  mm**

**(c) Secondary serration geometry and (d) Secondary serration adherence on the tool.**

Rake face wear mechanisms were also affected by the variation in  $V_C$ , while they appear identical for both  $a_p$  conditions. Figures 4-30(a-b) shows that severe material stacking occurred  $V_C = 30$  m/min, compared to the corresponding  $a_p = 0.25$  mm dry cut that resulted in crater wear. Increasing  $V_C \geq 50$  m/min, for minimum cooling conditions, resulted in crater formation and reduction in the chip/tool contact area, Figure 4-30(c-d). The tools used at higher  $V_C$  conditions also show evidence of severe oxidation, usually associated to higher cutting temperatures at these conditions, Figure 4-30(d).

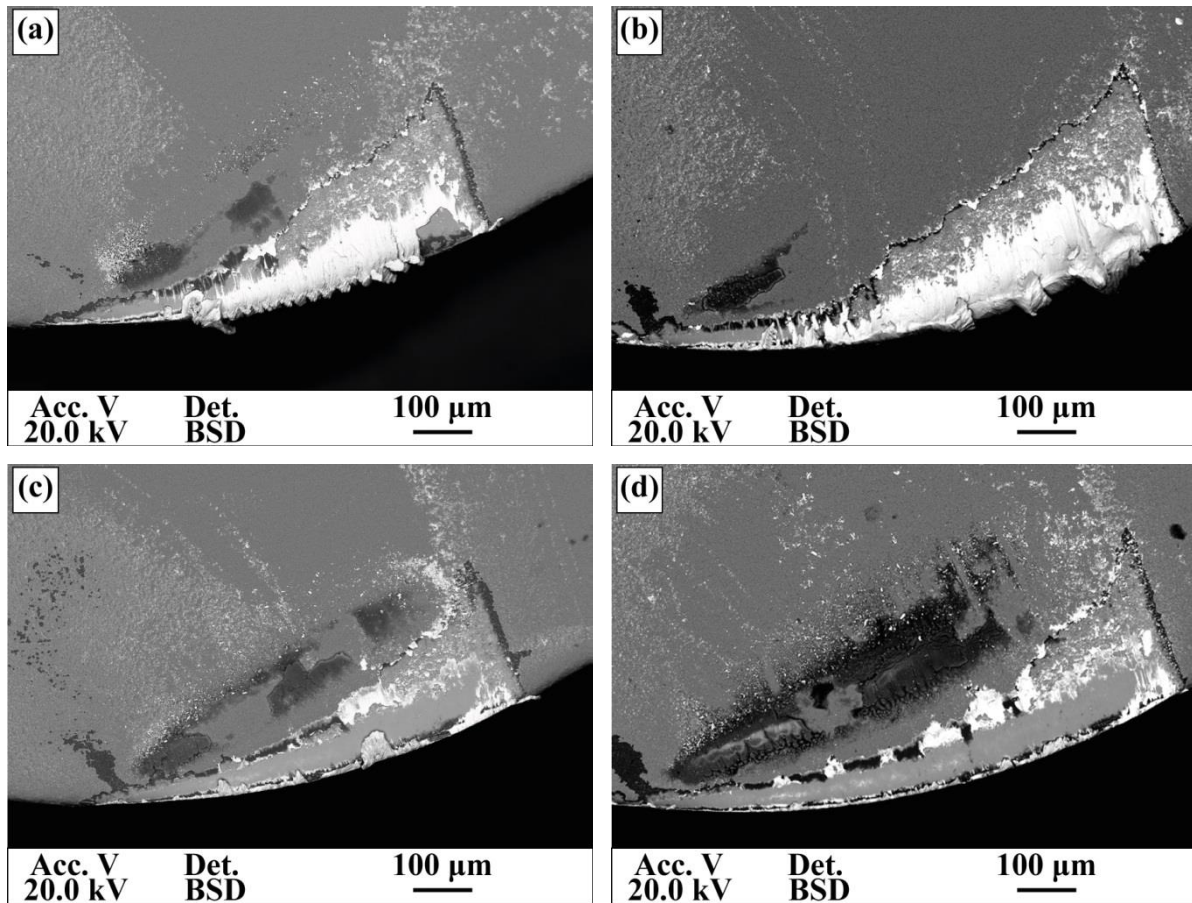
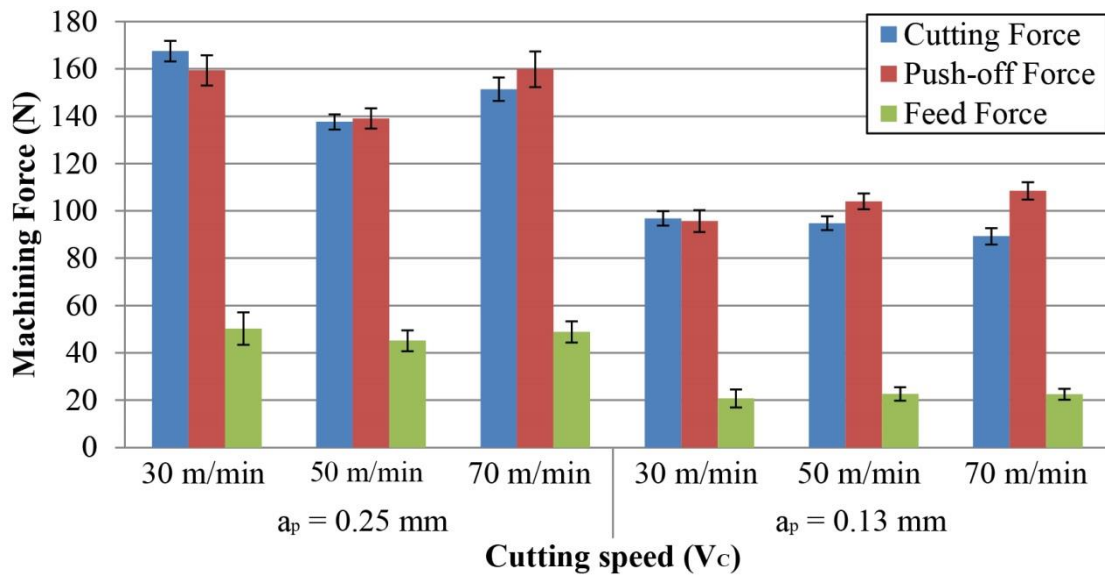


**Figure 4-30: Rake tool wear for minimum cooling conditions;  $V_C = 30 \text{ m/min}$  (a)  $a_p = 0.13 \text{ mm}$  and (b)  $a_p = 0.25 \text{ mm}$ ,  $V_C = 50 \text{ m/min}$  (c)  $a_p = 0.13 \text{ mm}$  and (d)  $a_p = 0.25 \text{ mm}$ .**

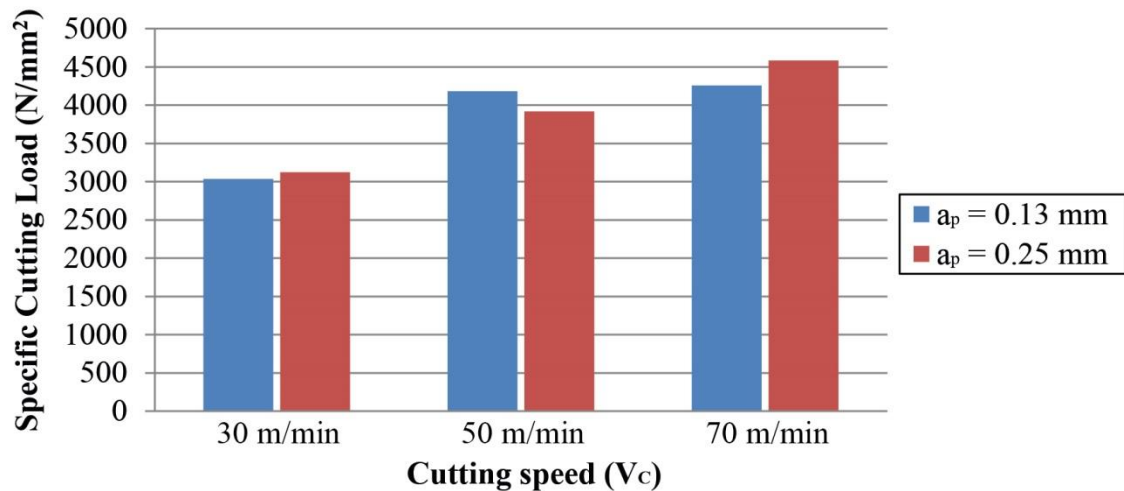
#### 4.2.2.3 Cutting Forces

Figure 4-31 shows the FG RR1000 machining forces for minimum cooling conditions, which similar to the dry machining conditions were found higher for  $a_p = 0.25 \text{ mm}$  compared to those for  $a_p = 0.13 \text{ mm}$ , and were reduced with the increase  $V_C$  from 30 to 50 m/min. At  $V_C = 70 \text{ m/min}$  and  $a_p = 0.13 \text{ mm}$  forces followed the trend observed at lower  $V_C$  conditions, as the cutting force reduced and push-off force increased, whilst at  $V_C = 70 \text{ m/min}$  and  $a_p = 0.25 \text{ mm}$  both the cutting and push-off forces increased compared those recorded at  $V_C = 50 \text{ m/min}$ . The phenomenon was seen in a number of Inconel 718 machining publications (see

Figure 2-48 by Sharman et al. (2006), Thakur et al. (2009) etc.) though neither provided an explanation. However, Figure 4-32 shows that similar to the dry cuts the specific cutting load acting at the tool edge increased with increasing  $V_C$ , whilst the effect of  $a_p$  was found to be less significant.



**Figure 4-31: FG RR1000 machining forces for minimum cooling conditions. (Error bars show the standard deviation)**



**Figure 4-32: Effect of machining parameters on specific cutting load at  $f = 0.12 \text{ mm}$  and minimum cooling conditions.**

### 4.2.3 Low Pressure Cooling Trials (Phase 2b)

#### 4.2.3.1 Surface Integrity

Figure 4-33 shows the surfaces produced at identical material removal rate ( $Q = 15 \text{ mm}^3/\text{sec}$ ) for  $V_C = 30 \text{ m/min}$  under low pressure (LP) cooling conditions. Both surfaces were defect free, though the surface machined at  $f = 0.12 \text{ mm/rev}$  and  $a_p = 0.25 \text{ mm}$  shows smoother surface finish due to the shorter distance between the feed marks, as a result of the lower feed rate, Figure 4-26(a), compared to the surface machined at  $f = 0.25 \text{ mm/rev}$  and  $a_p = 0.12 \text{ mm}$ , Figure 2-26(b). These observations were confirmed by the surface roughness  $R_a$  values, with those collected for the low  $f$  resulting in average  $R_a = 0.25 \mu\text{m}$  and those collected for the high  $f$  resulting in average  $R_a = 0.47 \mu\text{m}$ . A similar trend was detected for all assessed conditions with increasing  $V_C$  having negligible effect on the measured average  $R_a$  values.

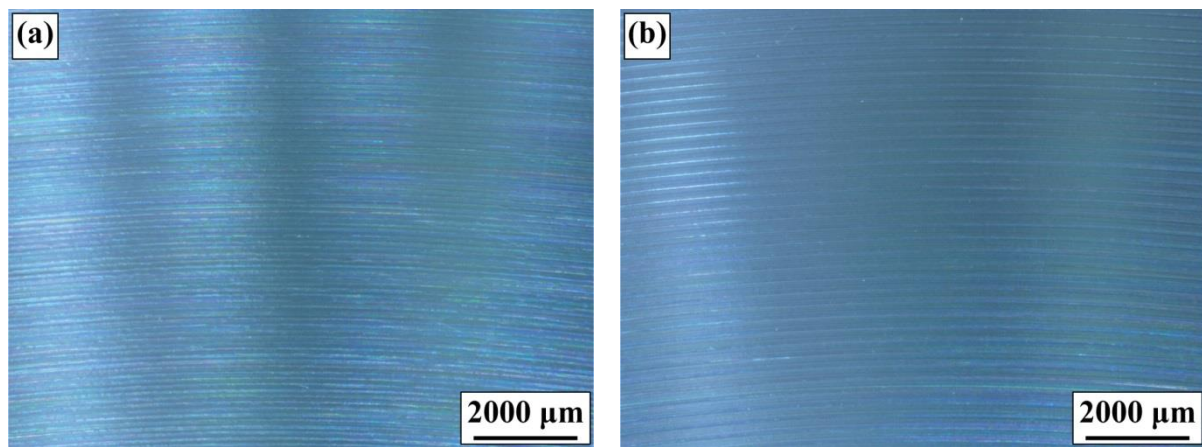


**Figure 4-33: Surface finish at  $V_C = 30 \text{ m/min}$  and LP cooling conditions; (a)  $f = 0.12 \text{ mm/rev}$  and  $a_p = 0.25 \text{ mm}$ , (b)  $f = 0.25 \text{ mm/rev}$  and  $a_p = 0.12 \text{ mm}$ .**

However, increasing  $V_C \geq 50 \text{ m/min}$  resulted in sporadic pick-up deposits on the surfaces machined at low  $f$  and high  $a_p$  conditions, Figures 4-34 (a-b). In both cases, small chip pieces were smeared along the cutting direction, resulting either in smearing residue damage up to

500  $\mu\text{m}$  long or in several distinct Type 2 minor pick-up deposits contained between the feed marks in the cutting direction. all surfaces machined at high  $f$  and low  $a_p$  conditions were pick-up free, regardless the increase in  $Q$  and  $V_C$ , though machining at  $f = 0.25 \text{ mm/rev}$  produced subsurface damage depth in the range of 3.5-3.7  $\mu\text{m}$ , Figure 4-35(b), compared to the maximum value of 1.6  $\mu\text{m}$  found for all samples machined at  $f = 0.12 \text{ mm/rev}$ , Figure 4-35(a).

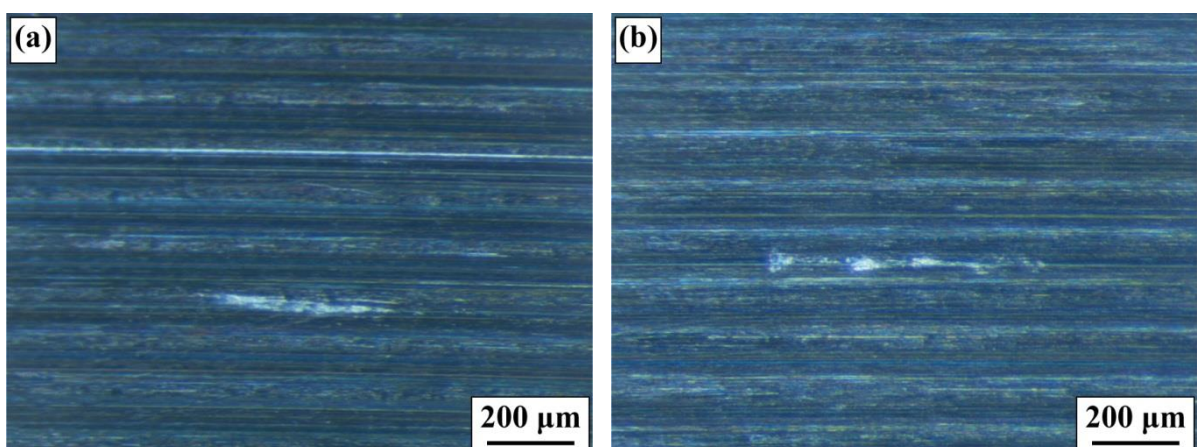


**Figure 4-34: Pick-up when machining FG RR1000 at  $f = 0.12 \text{ mm/rev}$ ; (a)  $V_C = 50 \text{ m/min}$  and (b)  $V_C = 70 \text{ m/min}$ .**

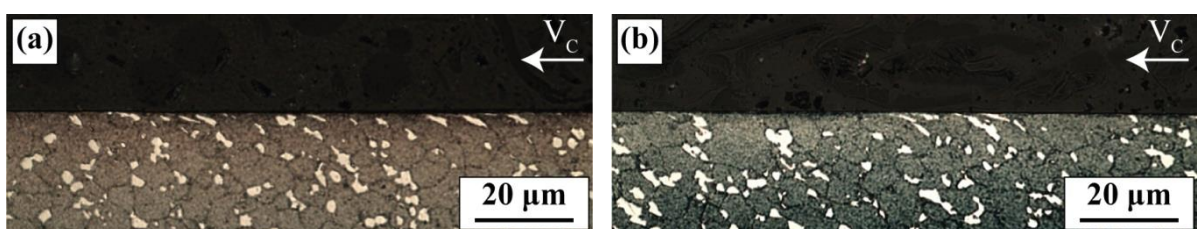


**Figure 4-35: FG RR1000 subsurface deformation under LP cooling conditions;  $V_C = 70 \text{ m/min}$  (a)  $f = 0.12 \text{ mm/rev}$  and  $a_p = 0.25 \text{ mm}$ , (b)  $f = 0.25 \text{ mm/rev}$  and  $a_p = 0.12 \text{ mm}$ .**

Figures 4-36(a,c) show similar minor sporadic Type 2 pick-ups deposits when machining CG RR1000 and Alloy 718 at  $V_C = 30 \text{ m/min}$ . Increasing  $V_C$  produced pick-up free Alloy 718 surfaces, Figure 4-36(d), in contrast to severe Type 1 smearing and Type 2 pick-ups detected when turning CG RR1000 at  $V_C = 70 \text{ m/min}$ , Figure 4-36(c). These deposits are

similar in size to those detected in FG machining, though in this case they occurred frequently only within the first half of the cut, similar to the phenomenon described in FG RR1000 machining at  $V_C = 70$  m/min and minimum cooling conditions.

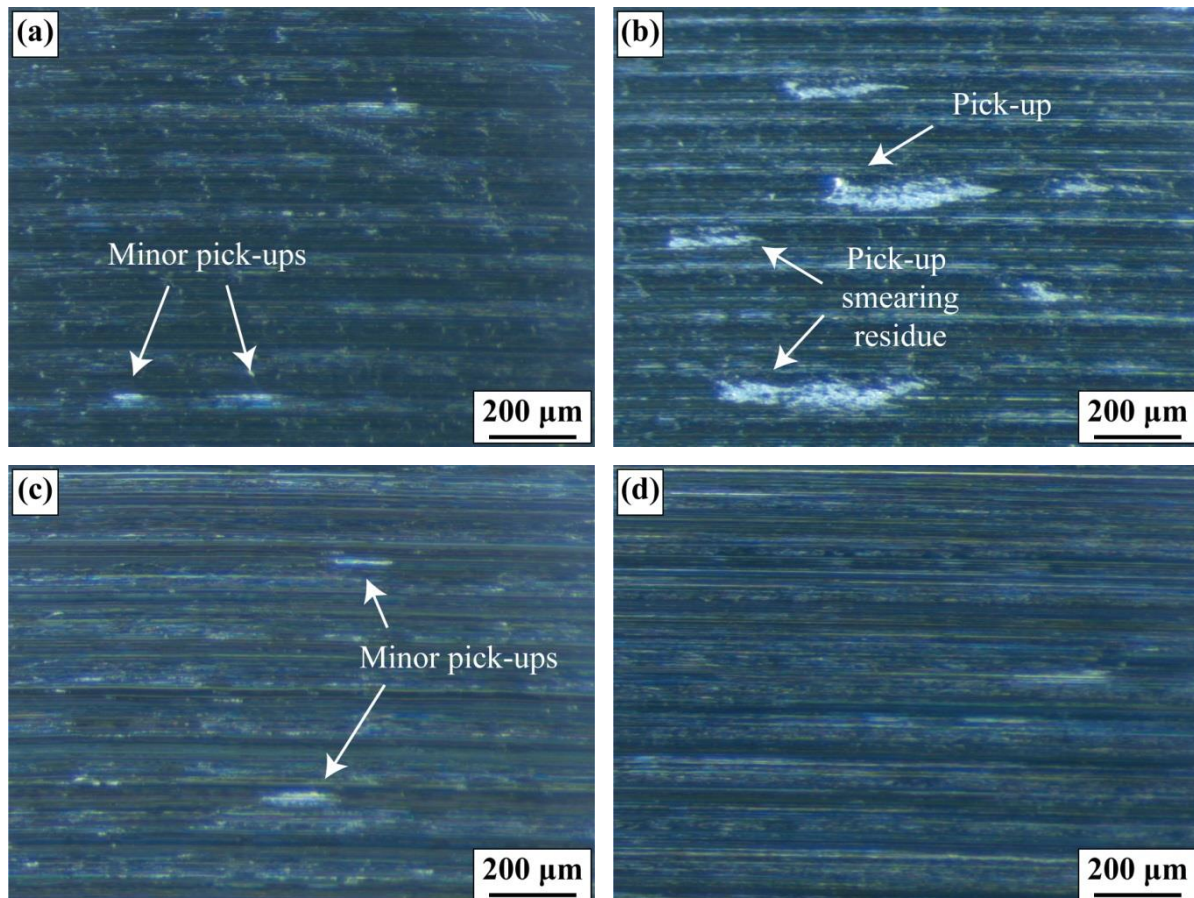


**Figure 4-36: Pick-up deposits at  $f = 0.12$  mm/rev; CG RR1000 (a)  $V_C = 30$  m/min and (b)  $V_C = 70$  m/min, Alloy 718 (c)  $V_C = 30$  m/min and (d)  $V_C = 70$  m/min.**

In terms of the subsurface damage, similar to dry machining the CG RR1000 deformation depth was limited below the 2  $\mu\text{m}$  for all machining conditions, Figure 4-37(a-b), whilst Alloy 718 deformation depth was found in the range of 5.5-5.8  $\mu\text{m}$  at  $V_C \leq 50$  m/min, Figure 4-37(c) and 8.9  $\mu\text{m}$  at  $V_C = 70$  m/min.

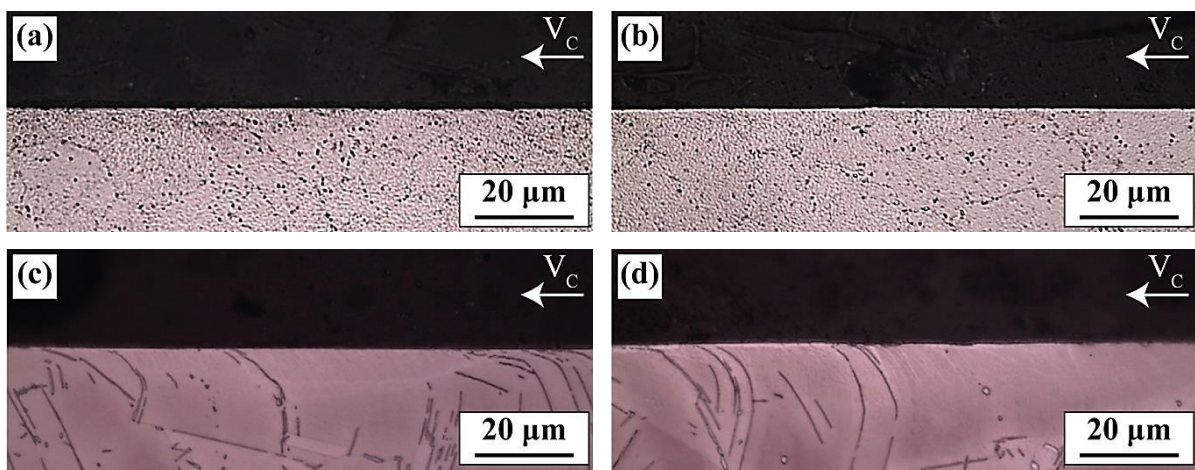
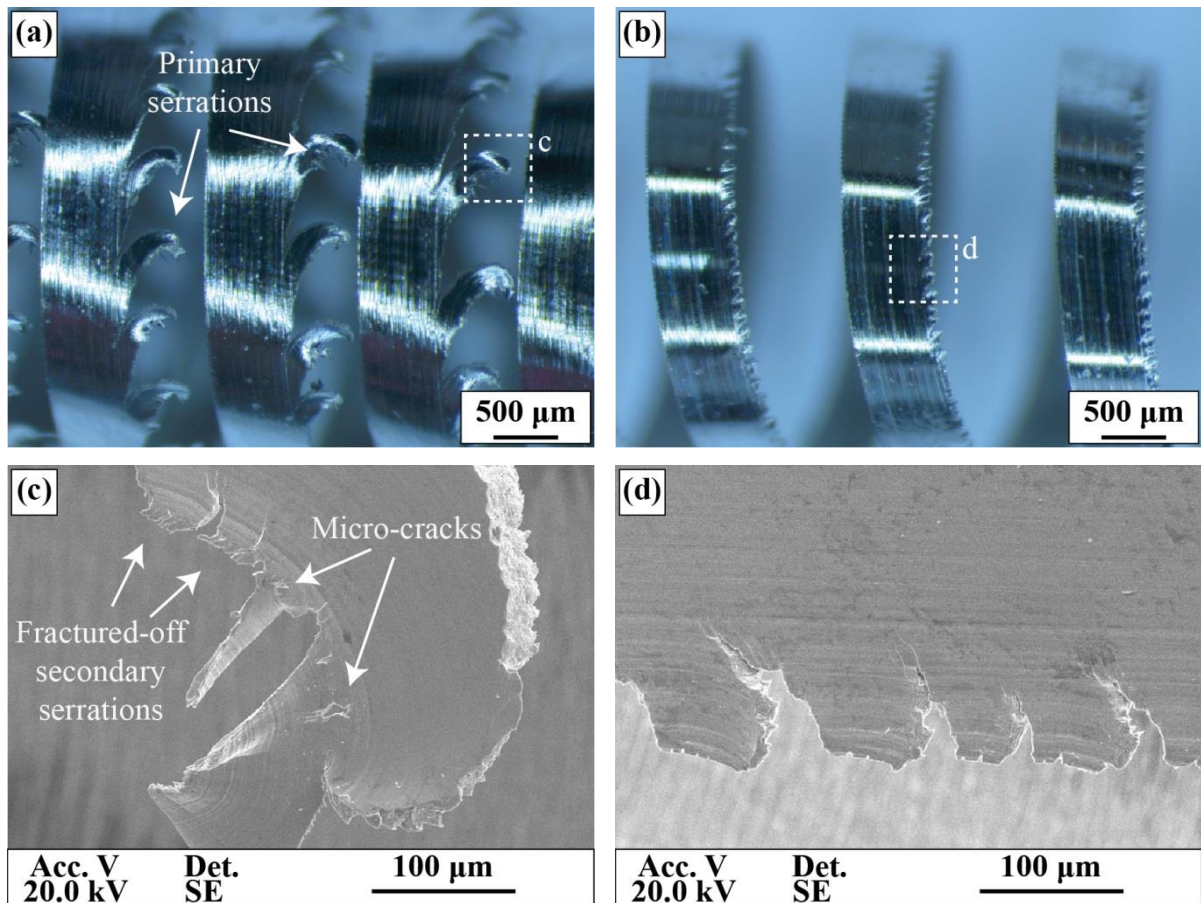


**Figure 4-37: Subsurface deformation at  $f = 0.12 \text{ mm/rev}$ ; CG RR1000 (a)  $V_C = 30 \text{ m/min}$  and (b)  $V_C = 70 \text{ m/min}$ , Alloy 718 (c)  $V_C = 30 \text{ m/min}$  and (d)  $V_C = 70 \text{ m/min}$ .**

#### 4.2.3.2 Chip Geometry

Continuous ribbon chips were produced for all cutting conditions with varying serration geometries forming at the chip's trailing edges depending on the machining parameters and workpiece microstructure. Figure 4-38 shows the FG RR1000 chip morphology produced at  $V_C = 30 \text{ m/min}$  (i.e.  $Q = 15 \text{ mm}^3/\text{sec}$ ) under LP cooling conditions. Large hook shape primary serrations were formed at low  $f$  conditions, Figure 4-38(a), compared to small and more frequent primary serrations detected at high  $f$  conditions, Figure 4-38(b). Secondary serrations, were only observed at  $f = 0.12 \text{ mm/rev}$  and  $a_p = 0.25 \text{ mm}$ , Figure 4-38(c), however they were similar in size to the primary serrations detected at  $f = 0.25 \text{ mm/rev}$  and  $a_p = 0.12 \text{ mm}$ , Figure 4-38(d). Furthermore, the evidence suggests that secondary serrations initiated from the propagation of micro-cracks nucleated on the primary serration surfaces, which were also acting as fracture-off points leading to their frequent failure during machining, Figure 4-38(c). These failed secondary serrations are similar in size to the minor pick-up deposits detected on the finished surfaces in the majority of low feed rate cuts, whilst the

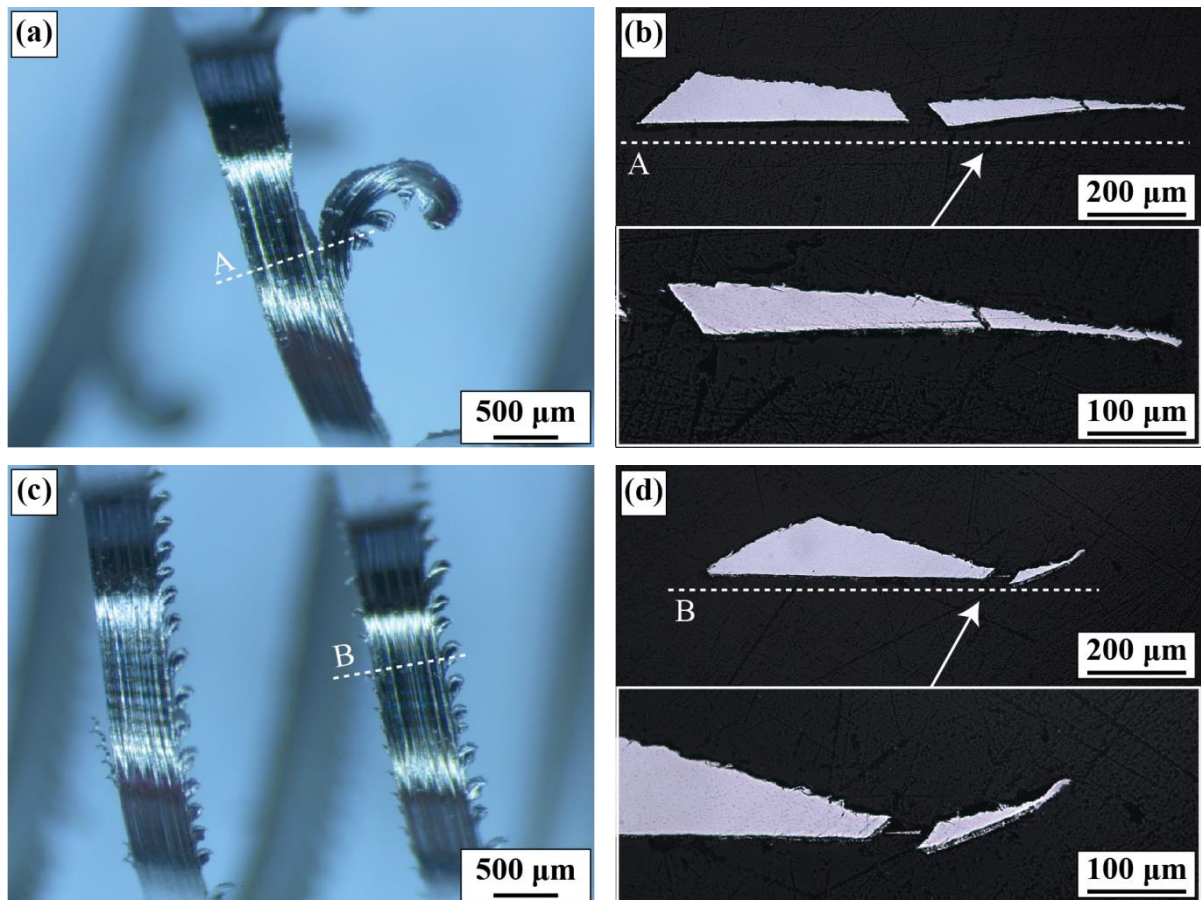
primary serrations formed at high  $f$  conditions and showed no signs of possible serraion failure, Figure 4-38(d).



**Figure 4-38: Effect of feed rate and depth of cut on FG RR1000 chip and serraion morphology at  $V_C = 30$  m/min;  $f = 0.12$  mm/rev and  $a_p = 0.25$  mm (a) Chip geometry, (c) Serrations,  $f = 0.25$  mm/rev  $a_p = 0.12$  mm (b) Chip geometry, (d) Serrations.**

At  $V_C = 50$  m/min, larger primary serrations were formed for both chip morphologies compared to  $V_C = 30$  m/min conditions, Figures 4-39(a,c), whilst Figures 4-39(b,d) revealed that low  $f$  and high  $a_p$  conditions produced wider chips with thinner cross-section profile compared to the compact cross-section profile of the chip produced at high  $f$  and low  $a_p$ . Figures 4-39(b,d) also shows that the secondary serrations at  $f = 0.12$  mm/rev and primary

serrations at  $f = 0.25$  mm/rev have similar cross-section profiles, while neither in this case primary serrations formed at high  $f$  that show evidence of fracturing-off.



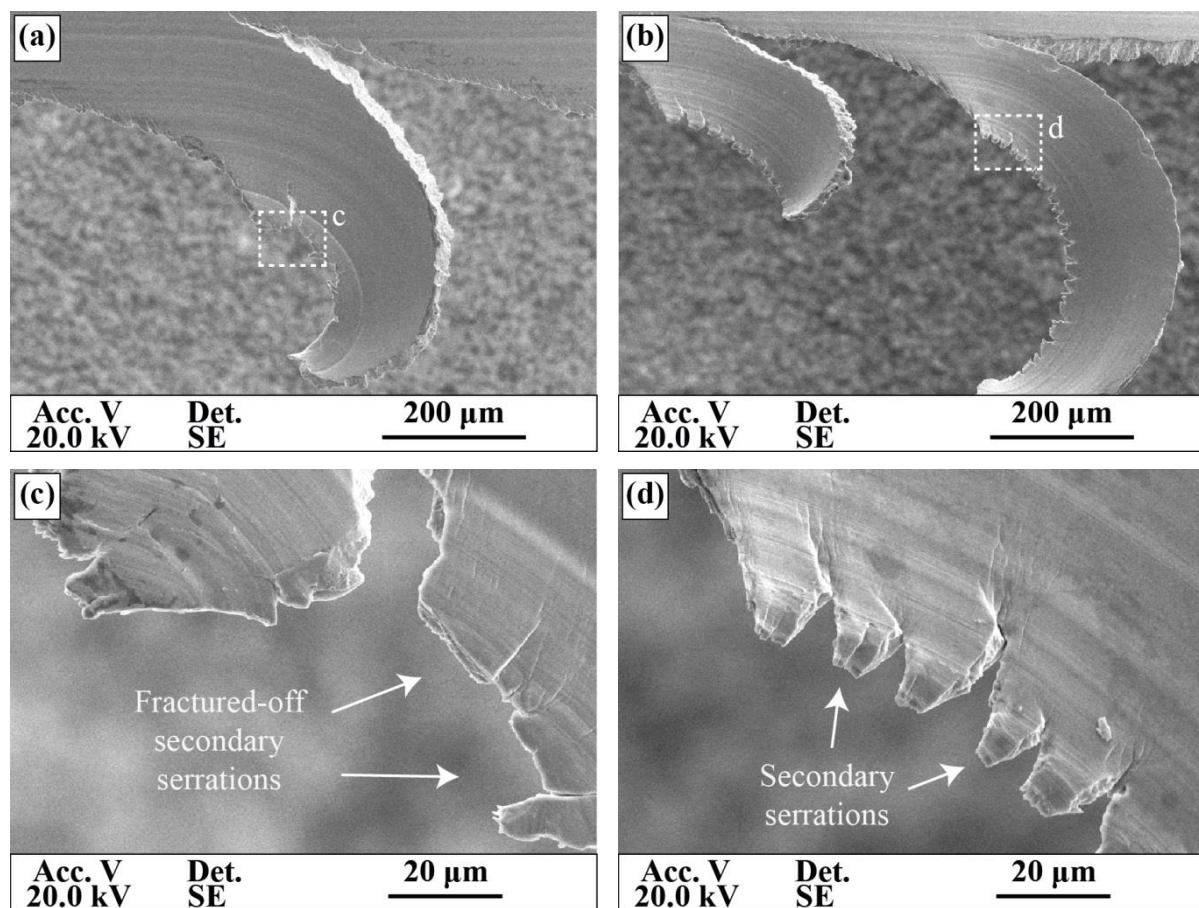
**Figure 4-39: Chip formation at  $V_C = 50$  m/min under LP cooling conditions;  $f = 0.12$  mm/rev and  $a_p = 0.25$  mm (a) Chip morphology and (b) Chip cross-section,  $f = 0.25$  mm/rev and  $a_p = 0.12$  mm (c) Chip morphology and (d) Chip cross-section.**

Figure 4-40 shows formation of primary hook shape serrations for both feed rate conditions at  $V_C = 70$  m/min, with  $f = 0.12$  mm/rev resulting in smaller serrations compared to  $V_C = 50$  m/min, Figure 4-40(a), and  $f = 0.25$  mm/rev resulting in non-uniform serrations sizes which appear to have propagated to identical thicknesses, Figure 4-40(b). Similar to the other assessed  $V_C$  conditions, Figure 4-40(c) revealed fracturing-off of the majority of secondary serrations machined at low  $f$ , whilst secondary serrations were formed at high  $f$

conditions, Figure 4-40(d), though in this case no evidence were observed suggesting possible serration failure tendency.

The chip formation data collected by 3D scanning confirm the optical inspection observations, Table 4-6, with thicker chips and lower primary serration propagation thicknesses ( $h_s$ ) produced at  $f = 0.25$  mm/rev, compared to all corresponding  $V_C$  and  $f = 0.12$  mm/rev conditions. Furthermore, chip compression ratio (CCR) decreased with increasing  $V_C$ , except for  $f = 0.25$  mm and  $V_C = 70$  m/min that resulted in CCR as the  $V_C = 50$  m/min conditions. These conditions also resulted in similar  $h_s$  values, which were found approximately 10  $\mu\text{m}$  higher than the  $h_s$  produced at  $V_C = 30$  m/min, though serration spacing ( $d_s$ ) more than doubled with increasing  $V_C$ . For  $f = 0.12$  mm/rev and  $a_p = 0.25$  mm,  $h_s$  and  $d_s$  increased when increasing  $V_C$  from 30 to 50 m/min, though both values decreased at  $V_C = 70$  m/min, compared to those achieved at  $V_C = 50$  m/min, validating the optical observations concerned with the serration size variation at these conditions.

Further observations in FG RR1000 machining include the variation in rake face wear mechanism at different machining conditions shown in Figure 4-41. Similar to the minimum cooling conditions, at  $f = 0.12$  mm/rev and  $a_p = 0.25$  mm adhered material was detected at  $V_C = 30$  m/min, Figure 4-41(a), whilst increasing  $V_C$  promoted development of crater wear on the tool's rake face with the most severe crater formed at high  $V_C$ , Figures 4-41(b-c). Furthermore, the latter conditions also resulted in oxidation forming on the tool rake faces and similar to crater wear its presence was more severe at  $V_C = 70$  m/min. Figures 4-41(d-f) however show that independently of  $V_C$  and corresponding  $Q$ ,  $f = 0.25$  mm and  $a_p = 0.12$  mm conditions resulted in the formation of thin adhered material layer only on the tool rake faces.



**Figure 4-40: Serration morphology at  $V_C = 70$  m/min under LP cooling conditions;  $f = 0.12$  mm/rev and  $a_p = 0.25$  mm (a) Primary serrations and (c) Secondary serrations,  $f = 0.25$  and mm/rev  $a_p = 0.12$  mm (b) Primary serrations and (d) Secondary serrations.**

**Table 4-6: FG RR1000 chip formation data for LP cooling conditions.**

$a_p = 0.25$ mm $f = 0.12$ mm/rev					
	$h_{max\_c}$ ( $\mu\text{m}$ )	$\epsilon$ ( $z = .95$ )	CCR	$h_s$ ( $\mu\text{m}$ )	$d_s$ ( $\mu\text{m}$ )
$V_C = 30$ m/min	122.3	$\pm 0.9$	1.95	40.3	539
$V_C = 50$ m/min	94.9	$\pm 0.7$	1.50	47.5	1726
$V_C = 70$ m/min	73.3	$\pm 1.0$	1.17	41.6	755
$a_p = 0.12$ mm $f = 0.25$ mm/rev					
	$h_{max\_c}$ ( $\mu\text{m}$ )	$\epsilon$ ( $z = .95$ )	CCR	$h_s$ ( $\mu\text{m}$ )	$d_s$ ( $\mu\text{m}$ )
$V_C = 30$ m/min	147.4	$\pm 1.6$	1.77	16.3	122
$V_C = 50$ m/min	119.9	$\pm 1.3$	1.44	27.1	202
$V_C = 70$ m/min	124.2	$\pm 0.8$	1.49	27.5	518

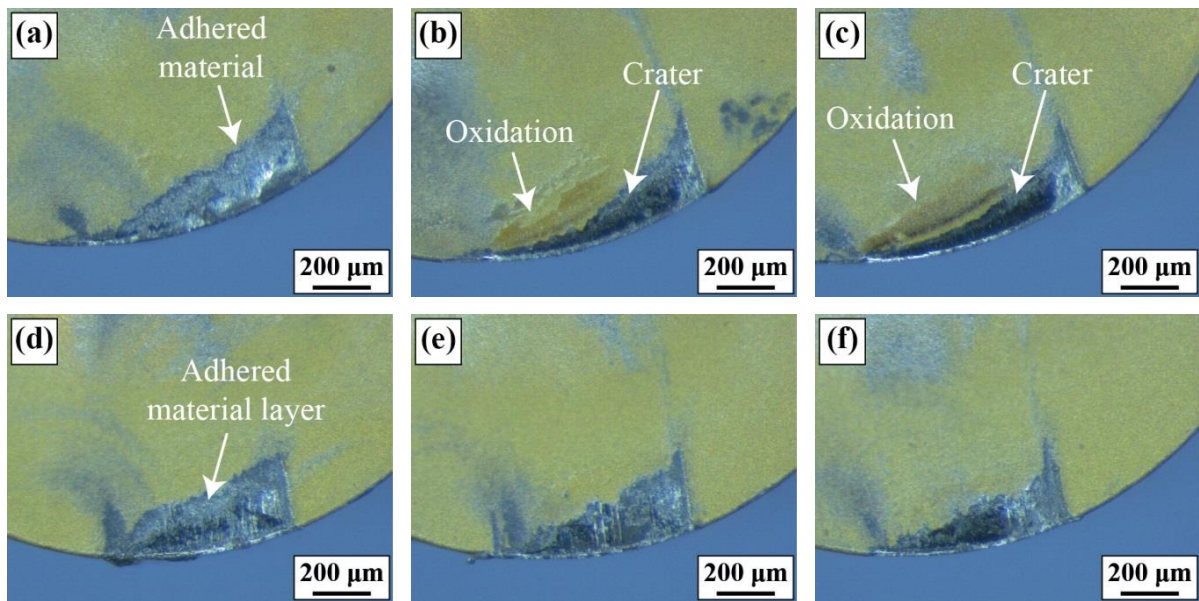


**Figure 4-41: Tool rake face wear mechanisms when machining FG RR1000 under LP cooling conditions;  $f = 0.12 \text{ mm/rev}$  and  $a_p = 0.25 \text{ mm}$  (a)  $V_C = 30 \text{ m/min}$ , (b)  $V_C = 50 \text{ m/min}$ , (c)  $V_C = 70 \text{ m/min}$ ,  $f = 0.25 \text{ mm/rev}$  and  $a_p = 0.12 \text{ mm}$  (d)  $V_C = 30 \text{ m/min}$ , (e)  $V_C = 50 \text{ m/min}$ , (f)  $V_C = 70 \text{ m/min}$ .**

Figure 4-42 shows that machining CG RR1000 and Alloy 718 resulted in similar primary serration geometries at corresponding machining conditions, even though CG RR1000 serrations appear larger than those when turning Alloy 718. Furthermore, cracks were formed on the surface of all CG RR1000 primary serrations, resulting in formation of secondary serrations at  $V_C \geq 50 \text{ m/min}$ , Figures 4-42(c,e), which at  $V_C = 70 \text{ m/min}$  also show the tendency to fracture-off. These failed secondary serrations appear similar in size to the Type 2 pick-ups detected on the corresponding machined surface. When machining Alloy 718, the serrations formed at  $V_C = 30 \text{ m/min}$  appear irregular, initially propagating to a constant thickness in the feed direction and then following a path opposing the chip flow, Figure 4-42(d). Figures 4-42(e-f) show that the rest of Alloy 718 chip serrations, whilst slight increase in their size was observed with increasing  $V_C$ .

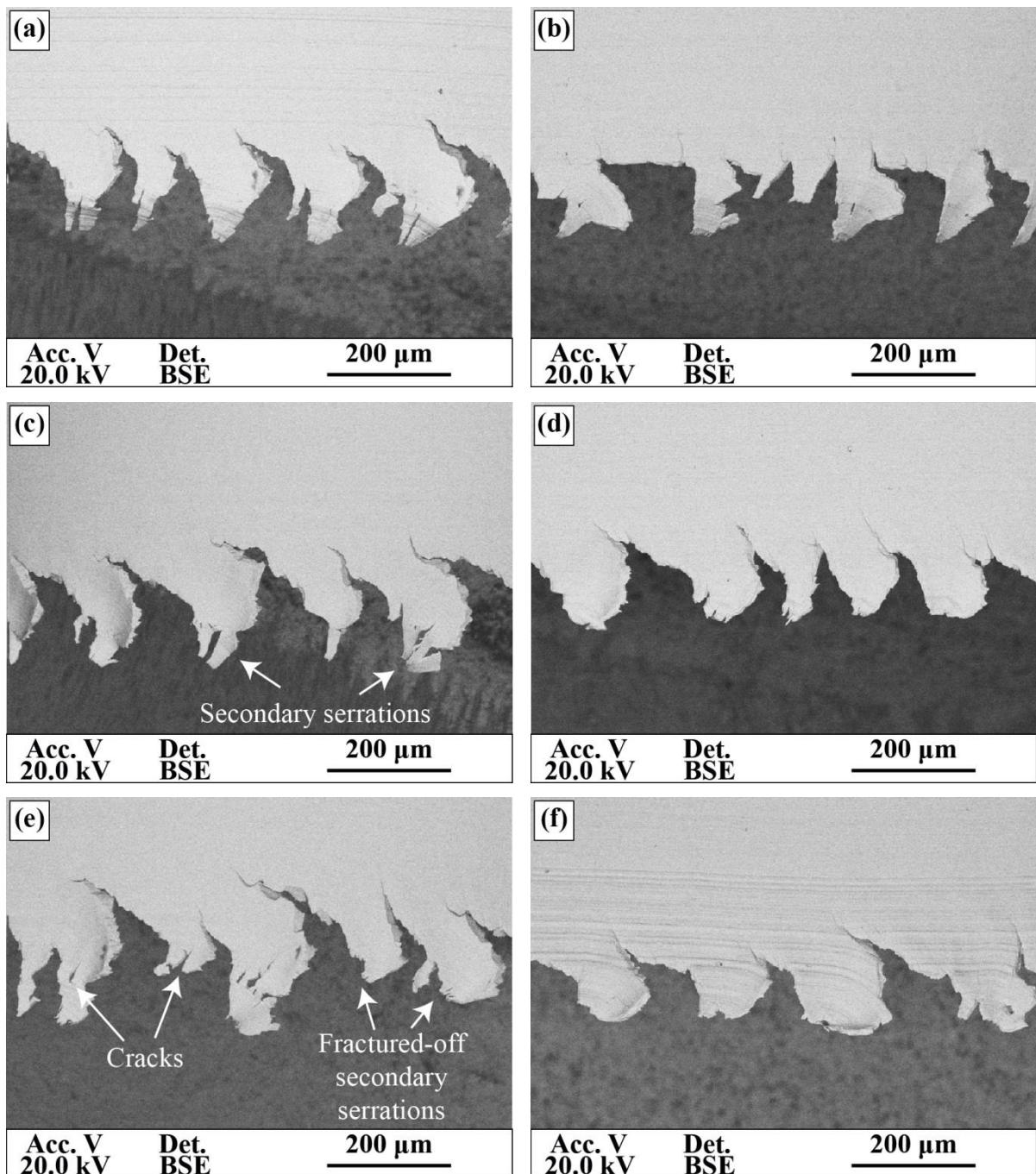


**Figure 4-42: Serration morphology when machining CG RR1000 and Alloy 718 under LP cooling conditions;  $V_c = 30 \text{ m/min}$  (a) CG RR1000 and (b) Alloy 718,  $V_c = 50 \text{ m/min}$  (c) CG RR1000 and (d) Alloy 718,  $V_c = 70 \text{ m/min}$  (e) CG RR1000 and (f) Alloy 718.**

The chip formation data shown in Tables 4-7 and 4-8 confirm the findings for CG RR1000 and Alloy 718 respectively, with the higher maximum serration thickness ( $h_s$ ) and higher serration spacing ( $d_s$ ) values produced when machining CG RR1000 explaining the larger serrations compared to those when machining Alloy 718. Furthermore, cut chip thickness ( $h_{max\_c}$ ) decreased with increasing  $V_C$  for both materials, though Alloy 718 produced thicker chips resulting in higher CCR values compared to CG RR1000 (and FG RR1000) at all corresponding cutting conditions.

**Table 4-7: CG RR1000 chip formation data for LP cooling conditions.**

$a_p = 0.25 \text{ mm } f = 0.12 \text{ mm/rev}$					
	$h_{max\_c} (\mu\text{m})$	$\epsilon (z = .95)$	CCR	$h_s (\mu\text{m})$	$d_s (\mu\text{m})$
$V_C = 30 \text{ m/min}$	124.1	$\pm 1.2$	1.98	22.4	184
$V_C = 50 \text{ m/min}$	100.1	$\pm 0.4$	1.61	22.1	251
$V_C = 70 \text{ m/min}$	85.2	$\pm 0.6$	1.36	28.5	259

**Table 4-8: Alloy 718 chip formation data for LP cooling conditions.**

$a_p = 0.25 \text{ mm } f = 0.12 \text{ mm/rev}$					
	$h_{max\_c} (\mu\text{m})$	$\epsilon (z = .95)$	CCR	$h_s (\mu\text{m})$	$d_s (\mu\text{m})$
$V_C = 30 \text{ m/min}$	132.4	$\pm 1.6$	2.11	16.1	132
$V_C = 50 \text{ m/min}$	124.3	$\pm 1.1$	1.98	16.5	141
$V_C = 70 \text{ m/min}$	117.8	$\pm 0.9$	1.87	16.4	168

#### 4.2.3.3 Cutting Forces

Figure 4-43 shows that the FG RR1000 machining forces recorded at low pressure cooling conditions varied according to the trend discussed in minimum cooling experiments, with cutting and push-off forces reducing when increasing  $V_C$  from 30 to 50 m/min and then both values increasing again at  $V_C = 70 \text{ m/min}$ . Feed force was unaffected by the variation in  $V_C$ .

and  $f$ , though it reduced when decreasing  $a_p$ . Overall higher machining loads were recorded when machining at  $a_p = 0.25$  mm and  $f = 0.12$  mm/rev, compared to machining at  $a_p = 0.12$  mm and  $f = 0.25$  mm/rev, even though at corresponding  $V_C$  values material removal rates were identical for both parameter combinations.

This phenomenon is also reflected in the specific cutting loads acting at the tool's edge, Figure 4-44, with all FG RR1000 experiments run at  $a_p = 0.25$  mm and  $f = 0.12$  mm/rev resulting in higher values than those found for experiments run at  $a_p = 0.12$  mm and  $f = 0.25$  mm/rev. Furthermore, increasing  $V_C$  resulted in higher specific cutting loads for both parameter combinations and amplified the performance difference between the two conditions. For example, at  $V_C = 30$  m/min the difference in the specific cutting load values achieved by the two parameters combinations was only 10%, compared to the 45% difference at  $V_C = 70$  m/min.

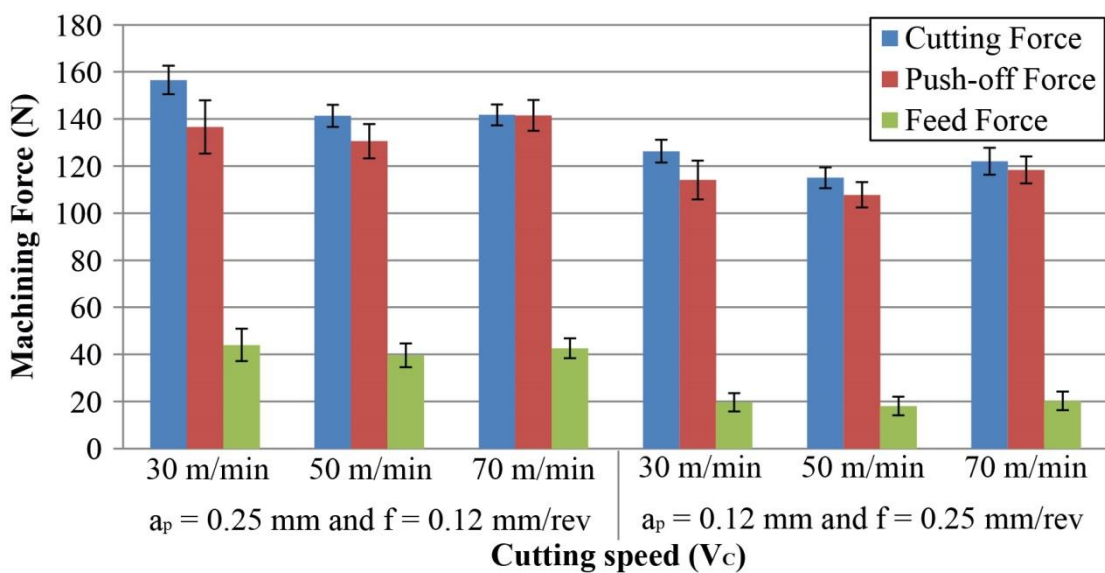


**Figure 4-43: Effect of uncut chip geometry on FG RR1000 machining forces under LP cooling conditions. (Error bars show the standard deviation)**

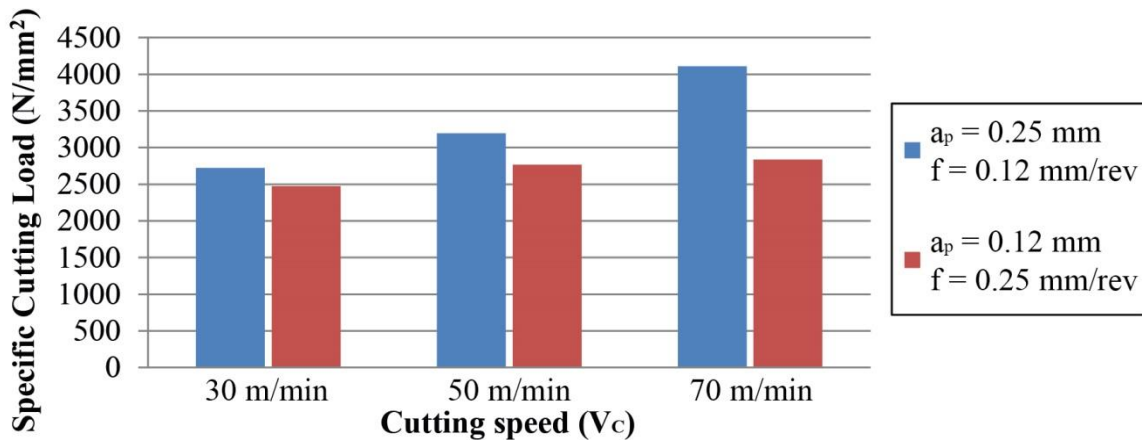


**Figure 4-44: FG RR1000 specific cutting load at LP cooling conditions.**

When machining CG RR1000 and Alloy 718, cutting and push-off forces reduced with increasing  $V_c$ , while feed force appears unaffected by the variation in  $V_c$  and workpiece material, Figure 4-45. Finally, Alloy 718 produced the lowest specific cutting loads compared to the other alloys at all corresponding machining conditions, Figure 4-46, whilst these values were similar to those achieved when machining FG RR1000 at low  $a_p$  and high  $f$ .

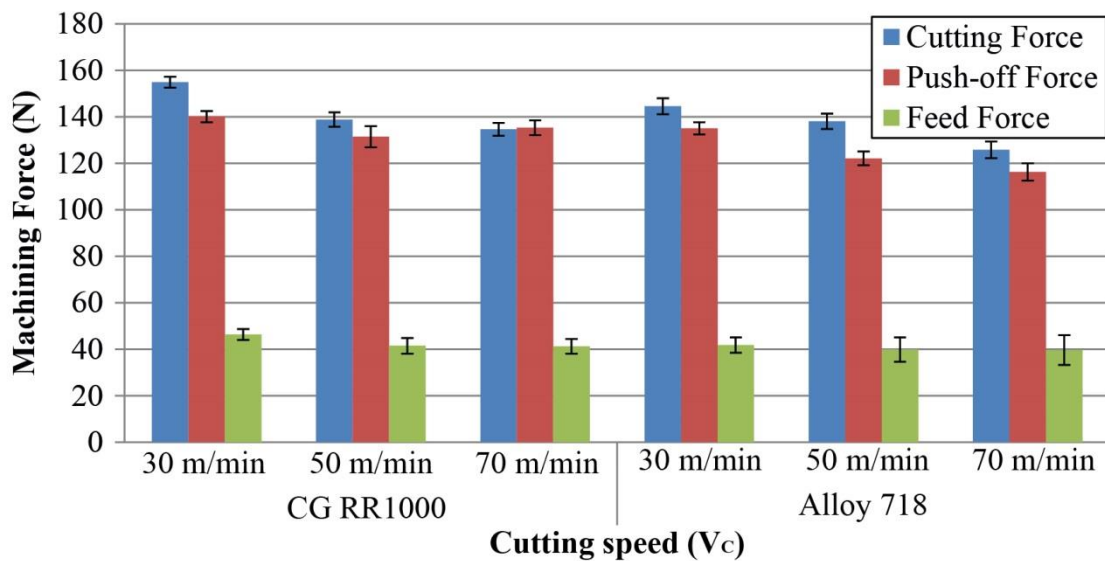


**Figure 4-45: CG RR1000 and Alloy 718 machining forces at  $a_p = 0.25 \text{ mm}$  and  $f = 0.12 \text{ mm/rev}$  under LP cooling conditions. (Error bars show the standard deviation)**

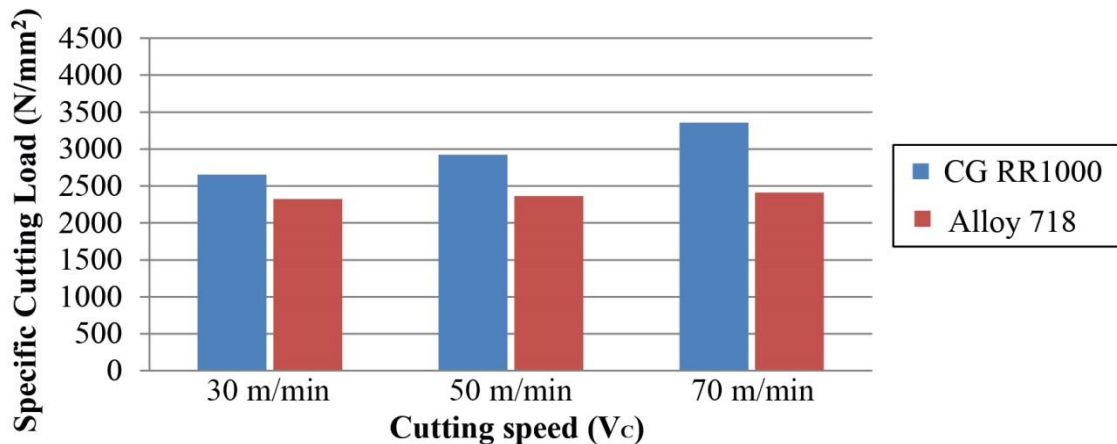


**Figure 4-46: CG RR1000 and Alloy 718 specific cutting load at  $a_p = 0.25$  mm and  $f = 0.12$  mm/rev under LP cooling conditions.**

#### 4.2.3.4 Effect of Cooling Failure

During the execution of these experiments a number of trials resulted in chip entrapment around the cutting tool, forming a phenomenon known as chip nesting, Figure 4-47(a). Da Silva et al. (2013) reported that this phenomenon is common in operations that produce long continuous ribbon chips, resulting in chip evacuation issues and cutting tool failure during production. Chip nesting has also been reported in RR1000 production line, whilst it was often associated with the occurrence of severe pick-up deposits. This was confirmed by the findings shown in Figures 4-47(b), which demonstrate the occurrence of frequent and severe pick-up deposits when machining FG RR1000 at  $V_c = 50$  m/min and  $a_p = 0.25$  mm under minimum cooling conditions while chip nesting was present. Pick-up occurred due to frequent chip serration failure at these conditions, Figures 4-47(c-d), a phenomenon that was not reported at the corresponding experiment presented in section 4.1.2 which resulted in pick-up free surface. However, chip serration failure when using these exact machining parameters was reported in dry turning (see section 4.1.1). This combined with the findings by Dahlman (2002) who reported increase in cutting temperature and reduction in tool life

due to chip interference with the coolant flow, indicates that chip entanglement blocked coolant supply at the cutting zone, and created machining conditions comparable to those reported in the dry experiments.

[Note: The experiments that produced chip nesting were repeated to ensure validity of the reported data.]

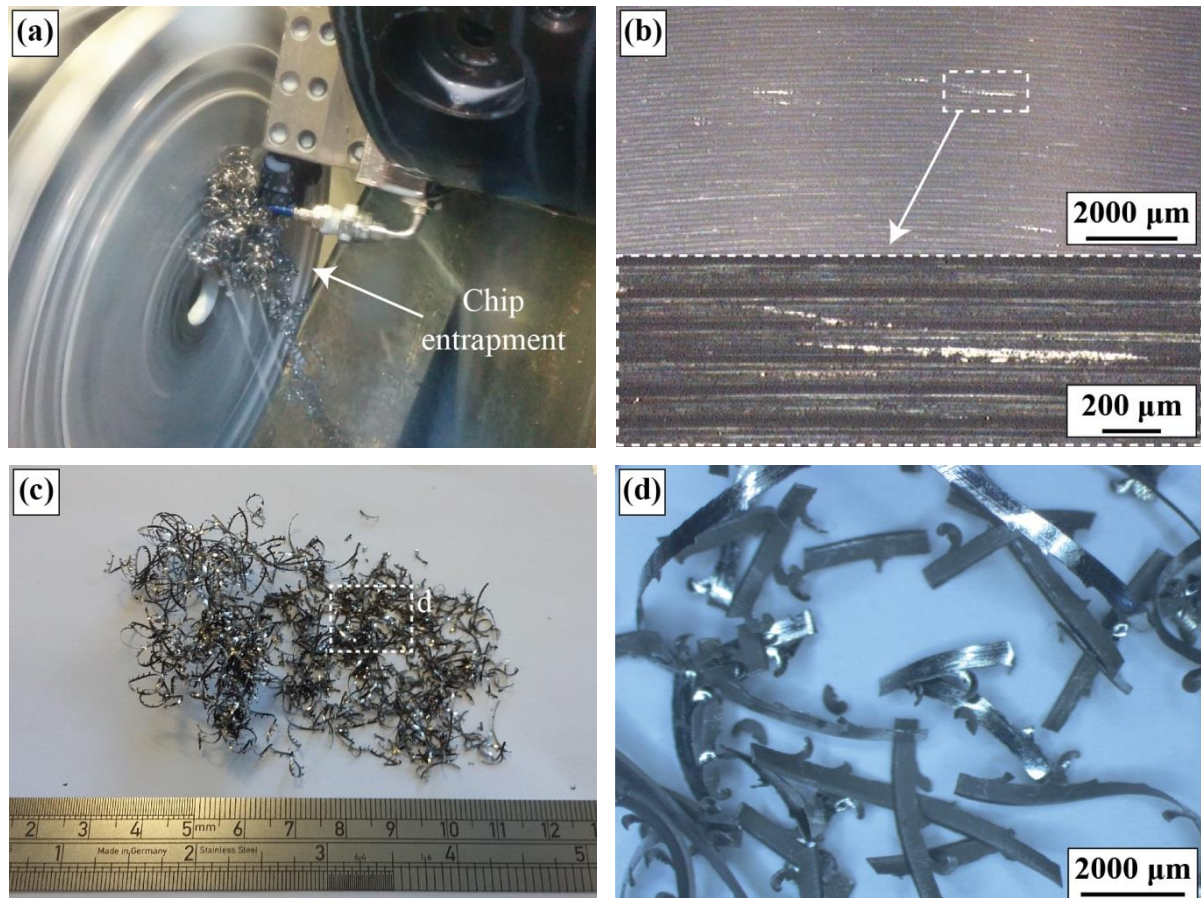


**Figure 4-47: Effect of chip entrapment during machining; (a) Chip nesting, (b) Surface finish, (c-d) Chip formation and serration failure.**

#### 4.2.3.5 Discussion - Cooled Trials (Phase 2)

The results presented show a clear link between cooling conditions and the likelihood of severe pick-up occurrence on FG RR1000 finish turned surfaces. Similar to the dry experiments, parent material deposits originated from smearing of fractured serrations formed at the thin chip trailing edges, though pick-up damage severity in these experiments was significantly reduced compared to the corresponding dry machined surfaces, in agreement with the findings in literature, Arunachalam et al. (2004b) and Zhou et al. (2012). Machining at  $V_C = 70$  m/min under minimum cooling were the only conditions favouring failure of primary serrations and thus resulting in severe major pick-up deposits, Figure 4-29, while at lower  $V_C$  only sporadic Type 1 and Type 2 pick-ups were observed due to deposition of secondary serrations. These minor pick-ups were also detected when machining under improved LP cooling conditions (i.e. higher pressure and flow rate) and corresponding cutting parameters, with no evidence of severe pick-up presence detected at  $V_C = 70$  m/min. Finally, machining at higher feed rate (i.e.  $f = 0.25$  mm/rev) under the effect of the latter cooling strategy resulted in pick-up free surfaces for all machining parameters, similar to the Inconel 718 findings by Zhou et al. (2012).

Overall, cooled conditions appear to have reduced pick-up occurrence by limiting the effect of machining parameters on serration failure mechanism that led to severe pick-ups in dry machining experiments, Figure 4-48. The results suggests that  $V_C$  was the dominant factor controlling serration formation at fixed  $f$ , whilst parameters related to lower cutting temperatures, i.e. low  $V_C$  and improved cooling performance, enhance the chip's ability to support machining strains at corresponding conditions and restrict the serration failure leading to improved surface finish. Hotter conditions generated due to the increase in material

removal rate or under dry conditions reduced the amount of work required to initiate fracture leading to higher levels of serration failure. This explains the frequent FG RR1000 primary and secondary serration failure of chips machined dry at  $V_C \leq 50$  m/min and  $f = 0.12$  mm/rev compared to the limited secondary serration failure only at corresponding cooled conditions. However, Machado and Wallbank (1997) found that increasing  $V_C$  limits the benefits of minimum coolant application, which aligns with the primary serration failure reoccurrence at  $V_C = 70$  m/min under minimum conditions. Whilst the phenomenon's absence at  $V_C = 70$  m/min and LP cooling conditions, indicates that improving the cooling performance counteracts the effect of increasing  $V_C$  by shifting the machining window away from catastrophic ductility conditions that lead to severe pick-ups. This cooling driven shift in machining conditions was also outlined by the fact the large hook shape primary serrations formed due to high  $d_s$  and  $h_s$  values observed at  $V_C = 30$  m/min for minimum cooling were then detected at  $V_C = 50$  m/min when machining under LP cooling conditions.

Figure 4-49 shows that increasing  $V_C$  reduced CCR independently of the cooling strategy due its effect on machining shear angle ( $\phi$ ) and  $h_{max\_c}$  as discussed by Trent and Wright (2000), with chips deformed close to the minimum theoretical value of  $CCR = 1$  when machining at  $V_C \geq 50$  m/min under dry and minimum cooling conditions. According to Atkins (2003), this phenomenon occurs when  $\phi$  reaches its saturation level for which chips deform to their absolute minimum cut thickness, as the relationship  $h_{max\_c} \geq h_{max\_u}$  is valid for all cutting conditions. Therefore, the fact that under improved LP cooling conditions  $\phi$  appears to have reached its maximum value only at  $V_C = 70$  min (i.e.  $CCR \approx 1$ ), combined with the fact that this cooling strategy produced overall thicker FG RR1000 chips compared to corresponding dry and minimum cooling conditions, Figure 4-49, provides further supporting evidence that 1. cooling improved overall chip deformation tolerance and 2.

improving cooling performance (i.e. increasing coolant pressure and flow rate) counteracts the effect of  $V_C$  on machining conditions. The fact that chips produced at  $V_C = 70$  m/min were sheared at saturated  $\phi$  means that while  $h_{max\_c}$  was unchanged, increasing  $V_C$  increased chip strain, thus requiring more work for chip deformation, which explains the increase in machining loads observed at these conditions compared to  $V_C = 50$  m/min.

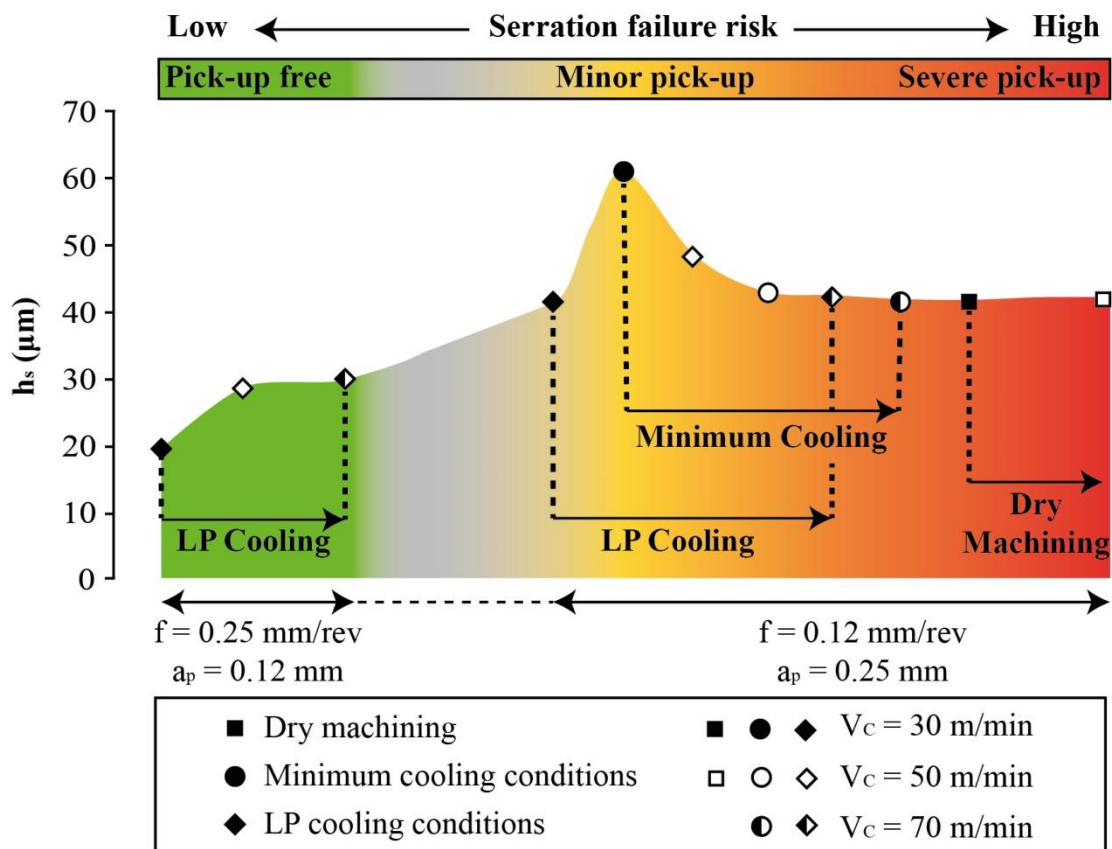


**Figure 4-48: FG RR1000 pick-up severity relationship to serration formation**

**mechanism at corresponding machining and cooling conditions.**

Furthermore, the lower CCR reduction when increasing  $V_C$  from 30 to 50 m/min at  $a_p = 0.25$  under LP cooling conditions, compared to the minimum cooling conditions, validates that improving cooling strategy performance is key in enhancing ductility in FG RR1000 chips, which also explains the observed improved control over serration failure and pick-up presence. When machining the more ductile CG RR1000 and Alloy 718, cooling within the

experimental range used appears to have less significant effect on chip formation, with chips deforming to almost identical CCR values under both dry and cooled conditions, whilst similar chip serration morphology was observed for both alloys. However, LP cooling conditions reduced CG RR1000 and Alloy 718  $h_s$  values by 10  $\mu\text{m}$  resulting in smaller chip serrations compared to corresponding dry conditions (i.e.  $f = 0.12 \text{ mm/rev}$ ,  $a_p = 0.25 \text{ mm}$  and  $V_C \leq 50 \text{ m/min}$ ), which confirms the FG RR1000 findings indicating improved chip plasticity tolerance at cooler conditions. At  $V_C = 70 \text{ m/min}$ , Alloy 718  $h_s$  value remained unaffected compared to CG RR1000 serrations that increased in size by propagating to  $h_s = 28.5 \mu\text{m}$  while forming secondary serrations, proving once more that Alloy 718 exhibits higher ductility than both RR1000 variants at corresponding machining conditions. The overall higher stain and possibly higher heat loads during machining indicated by the CG RR1000 higher specific loads compared to Alloy 718, Figure 4-46, explain the inferior deformation performance of CG RR1000 at these high plasticity conditions. Finally, the fact that CG RR1000 machined cooled at  $V_C = 70 \text{ m/min}$  produce identical primary and secondary serrations to those formed dry at  $V_C = 30 \text{ m/min}$ , whilst both cases resulted in secondary serraion failure and pick-up deposition, confirms the theory developed so far, that cooler conditions counteract the effect of increasing  $V_C$  on machining temperatures (and thus the chip's plasticity performance), thus shifting the machining window away from catastrophic ductility conditions.

Machining FG RR1000 at  $f = 0.25 \text{ mm/rev}$  and  $a_p = 0.12 \text{ mm}$  resulted in thicker chips with smaller and more frequent serrations, compared to  $f = 0.12 \text{ mm/rev}$  and  $a_p = 0.25 \text{ mm}$  conditions and corresponding material removal rates. Further observations at  $f = 0.25 \text{ mm/rev}$  and  $a_p = 0.12 \text{ mm}$  like 1. the serraion propagation to lower  $h_s$  values, 2. the lower specific cutting loads and 3. the lack of heat activated oxidation on the tools, compared to  $f = 0.12$

mm/rev and  $a_p = 0.25$  mm at corresponding  $V_C$  conditions, indicate that the chips machined at low  $f$  were subjected to higher strains and higher heat loads. Sharman et al. (2015) linked the thinner chip profiles to higher surface residual stresses, suggesting that the increase in the amount of chip material being machined below the tool's cutting edge rounding increases the ploughing energy of the cut, resulting in higher triaxiality and heat loads at the chip's trailing edge. El-Wardany and Elbestawi (1998) reported that these conditions increased serration size due to higher compressive stresses acting at the chip's edge, which taken in combination with the FG RR1000 experimental results indicate that in addition to the cooling process, the uncut chip geometry affects chip's trailing edge tolerance to damage and the amount of plastic deformation at the chip edge. Thus the lower amount of plastic deformation at the chip's trailing edge when machining at higher  $f$  resulted in serration formation with limited likelihood of failure, Figure 4-48, explaining the pick-up free surfaces at corresponding conditions.

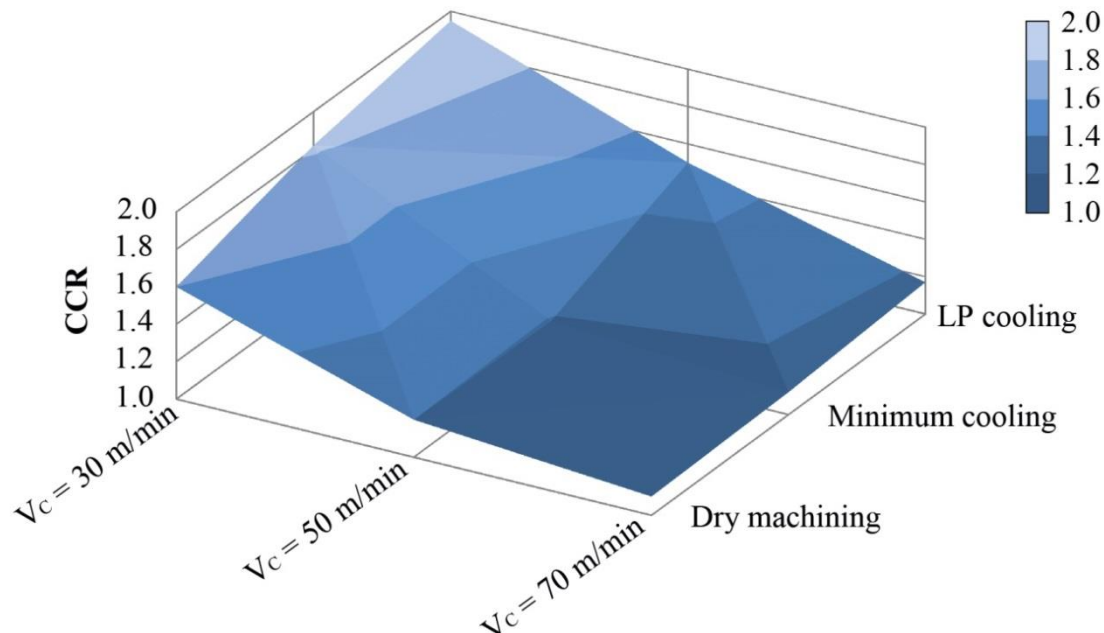


**Figure 4-49: Effect of cooling strategy and cutting speed on FG RR1000 chip**

**deformation at  $f = 0.12$  mm/rev and  $a_p = 0.25$  mm.**

Finally, the experiments resulting in pick-ups only at the first half of the cut (i.e. FG RR1000 minimum cooling at  $V_C = 70$  m/min and  $a_p = 0.13$  mm, CG RR1000 LP cooling at  $V_C = 70$  m/min and  $a_p = 0.25$  mm) indicate that even when conditions favour serration failure their deposition purely depends on the entrapment of these serrations between the tool and workpiece interface, explaining the circumstantial pick-up occurrence in RR1000 production.

Summarising the findings, it was shown that cooling increased the chip's tolerance to deformation, improving its ability to support machining strains and thus limiting the serration failure compared to dry machining. The evidence suggested that improving the cooling strategy performance (i.e. by increasing pressure and flow rate) can enhance the control over chip serration formation and failure at higher strain and heat conditions (i.e. high  $V_C$ ), suppressing the likelihood of parent material deposition without compromising the surface finish. In the case that surface roughness is not a production requirement, using higher feed rate resulted in smaller chip serrations due to lower machining strains introduced to the chip trailing edge, also explaining the lack of serration failure and pick-up deposition at these conditions.

### 4.3 COOLING PERFORMANCE INVESTIGATION TRIALS

#### 4.3.1 Cooling Strategy Performance Assessment Trials (Phase 3)

##### 4.3.1.1 Surface Integrity

The experimental trials conducted in Phase 3 resulted in pick-up free surfaces for all machining conditions, except for sporadic Type 1 and Type 2 pick-ups detected when turning FG RR1000 at  $V_C = 70$  m/min under rake face cooling only for both low and high pressure conditions, Figures 4-50(a-b). Surface roughness  $R_a$  and subsurface deformation depth were both unaffected by the variation in cutting parameters and cooling conditions, with  $R_a$  ranging from 0.29-0.33  $\mu\text{m}$  and subsurface distortion never exceeding the 1.5  $\mu\text{m}$  in depth for all samples, Figures 4-50(c-d).

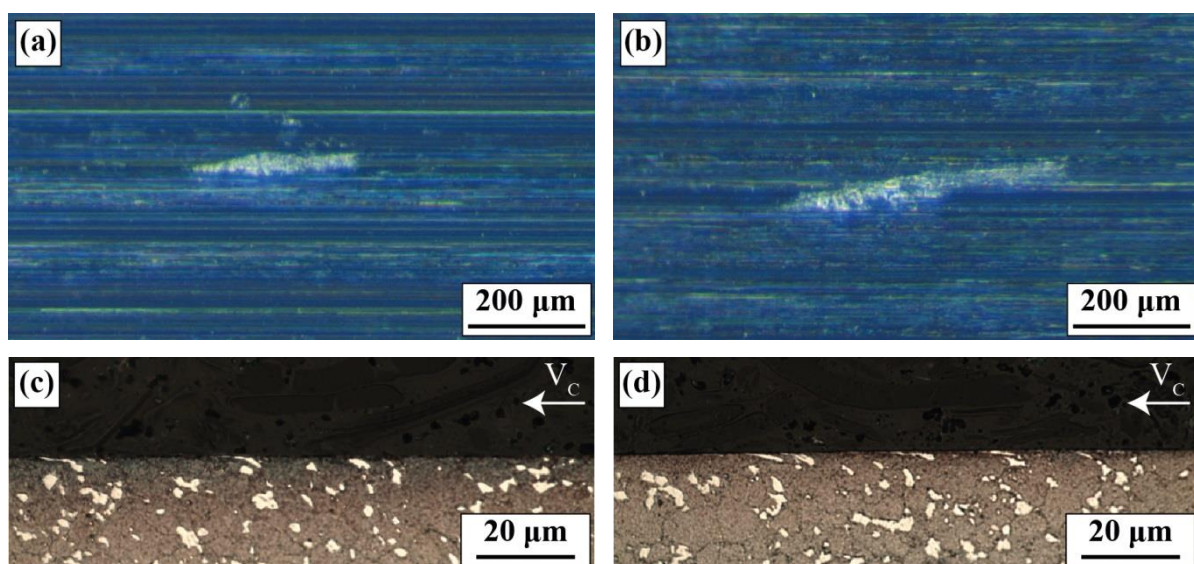
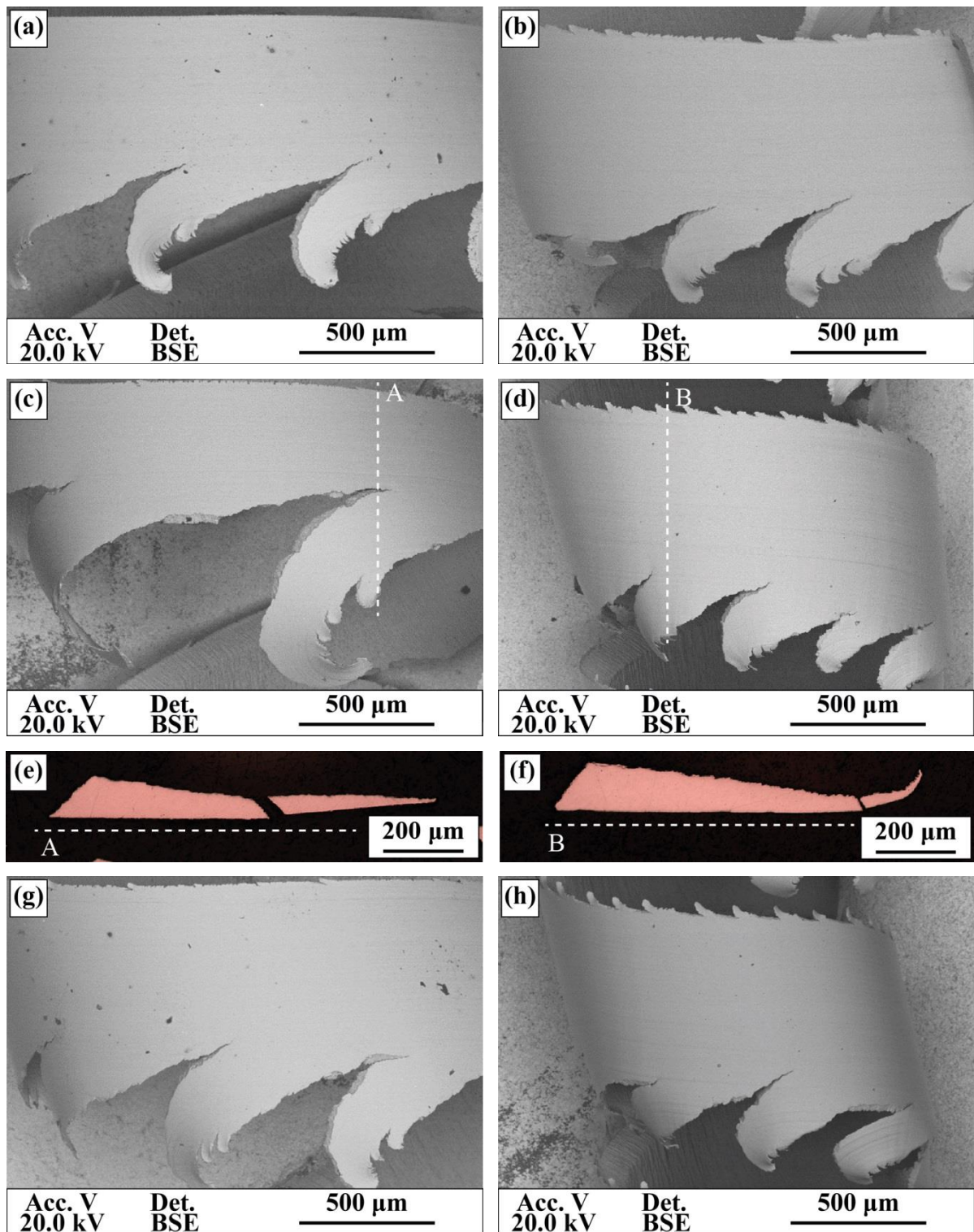


**Figure 4-50: FG RR1000 surface finish and subsurface deformation at  $V_C = 70$  m/min;**  
**Pick-up (a) Rake face cooling at  $P = 12$  bar and  $\lambda = 6.5$  l/min, (b) Rake face cooling at  $P = 70$  bar and  $\lambda = 6.5$  l/min, Subsurface deformation (c) Rake face cooling at  $P = 12$  bar and  $\lambda = 6.5$  l/min, (d) Rake and flank cooling at  $P = 70$  bar and  $\lambda = 9.1$  l/min.**

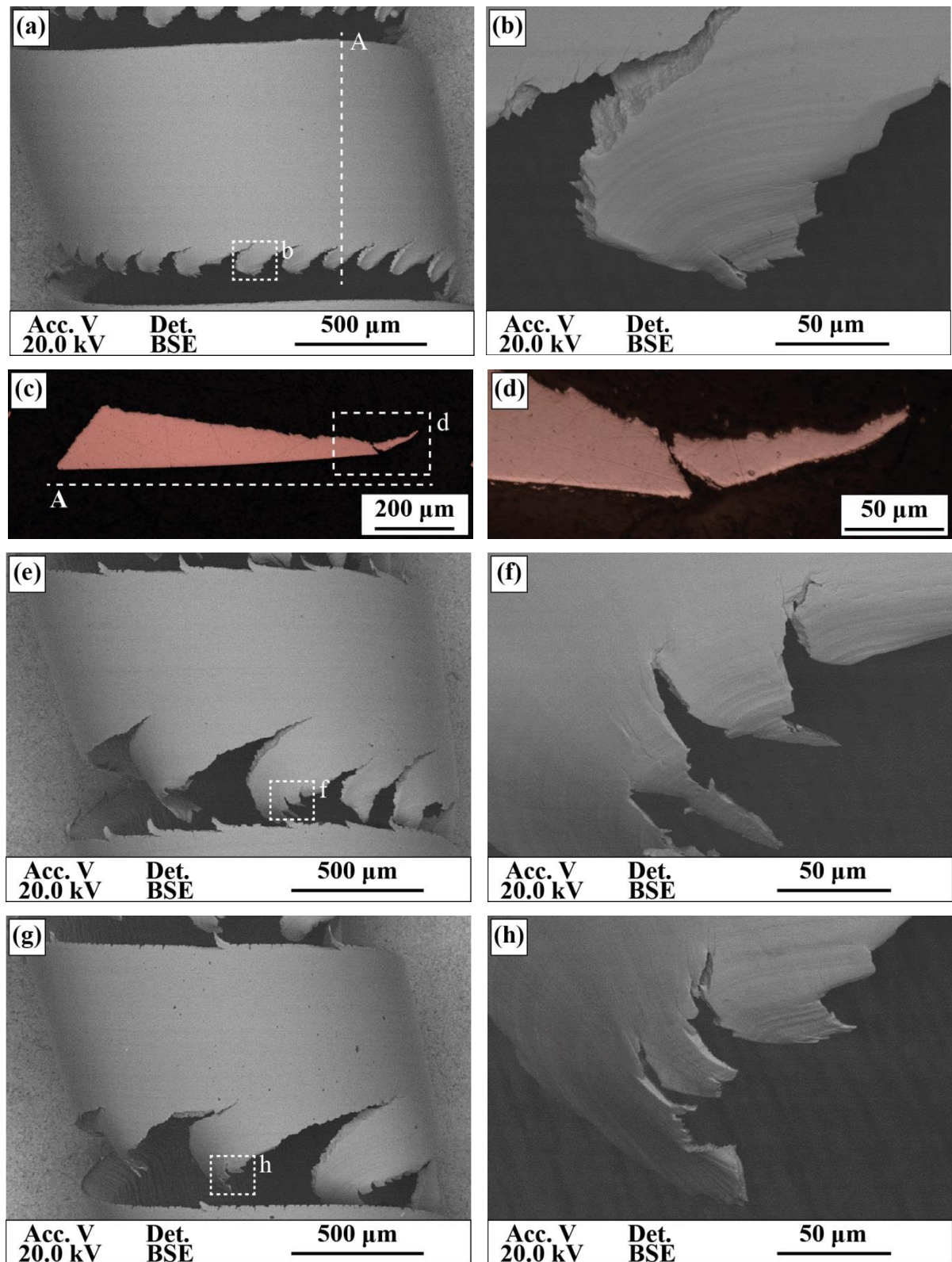
#### 4.3.1.2 Chip Geometry

Figure 4-51 shows the effect of coolant pressure on chip and serration morphology at fixed flow rate ( $\lambda = 6.5 \text{ l/min}$ ) when cooling the tool's rake face only. Similar to the Phase 2b experiments conducted at corresponding machining parameter combinations, increasing  $V_C$  from 30 to 50 m/min at low pressure conditions (i.e.  $P = 12 \text{ bar}$ ) increased the size of primary and secondary serrations, Figures 4-51(a,c), whilst further increase in cutting speed (i.e.  $V_C = 70 \text{ m/min}$ ) reduced the serration size compared to the  $V_C = 50 \text{ m/min}$  conditions, Figure 4-51(g). At high pressure cooling conditions (i.e.  $P = 70 \text{ bar}$ ) no variation in the serration size and morphology was observed with increasing  $V_C$ , Figures 4-51(b,d,h), whilst primary serrations appear similar to those observed at low  $P$  and low  $V_C$  conditions. Furthermore, the cross-sections of chips machined at  $V_C = 50 \text{ m/min}$  show that the larger primary serrations formed at low  $P$  conditions were caused by the serration propagation to higher thickness, Figure 4-51(e), compared to the lower serration thickness achieved at high  $P$  conditions resulting in smaller primary serrations, Figure 4-51(f); even though maximum chip thicknesses appears similar for both cooling conditions.

Furthermore, high pressure coolant application on both the tool's rake and flank faces at  $V_C = 30 \text{ m/min}$  produced the smallest and more frequent primary serrations of these experiments, Figure 4-52(a), due to propagating to lower thicknesses compared serrations observed when machining under different cooling conditions, Figures 4-52(c-d), whilst no secondary serrations were formed at these conditions, Figure 4-52(b). Further increase in  $V_C$  (i.e.  $\geq 50 \text{ m/min}$ ) produced similar primary and secondary serrations to those observed at the corresponding high pressure flank face cooling experiments, showing no failure tendency.



**Figure 4-51: FG RR1000 chip formation for low and high pressure rake cooling at  $\lambda = 6.5 \text{ l/min}$ ;  $V_C = 30 \text{ m/min}$  (a)  $P = 12 \text{ bar}$  and (b)  $P = 70 \text{ bar}$ ,  $V_C = 50 \text{ m/min}$  (c,e)  $P = 12 \text{ bar}$  and (d,f)  $P = 70 \text{ bar}$ ,  $V_C = 70 \text{ m/min}$  (g)  $P = 12 \text{ bar}$  and (h)  $P = 70 \text{ bar}$ .**



**Figure 4-52: FG RR1000 chip and serration formation under high pressure rake and flank cooling; (a-d)  $V_C = 30 \text{ m/min}$ . (e-f)  $V_C = 50 \text{ m/min}$ , (g-h)  $V_C = 70 \text{ m/min}$ .**

The chip formation data collected by 3D scanning confirm the optical inspection observations, Table 4-9, with  $h_{max\_c}$  decreasing at higher  $V_C$ , whilst chips were deformed to almost identical CCR values at corresponding  $V_C$  conditions independently of the assessed cooling strategies. Machining under rake cooling at 12 bar pressure resulted in the increase of  $h_s$  and  $d_s$  when increasing  $V_C$  from 30 to 50 m/min, whilst both values decreased at  $V_C = 70$  m/min compared to those achieved at  $V_C = 50$  m/min, confirming the optical observations suggesting identical variation trend in serration size as the Phase 2b LP cooling experiments. At high pressure rake cooling,  $h_s$  decreased approximately 5  $\mu\text{m}$  for every gradual increase in  $V_C$ , while similar  $d_s$  values were produced at all machining parameter combinations, explaining the similar serration size observed at these conditions. Finally, machining at  $V_C = 30$  m/min under rake and flank high pressure cooling resulted in half the  $h_s$  value compared to serrations produced at corresponding  $V_C$  and the other assessed cooling strategies, whilst increasing  $V_C \geq 50$  m/min resulted in similar  $h_s$  and  $d_s$  values as the corresponding high pressure rake cooling conditions.

Further observations in these experiments include the variation in rake face wear mechanism at different cooling conditions, Figure 4-53. Similar to previous low pressure cooling experiments, thin adhered material layer was detected at  $V_C = 30$  m/min, while increasing  $V_C$  promoted development of crater wear on the tool's rake face with the most severe crater formed at  $V_C = 70$  m/min. However, increasing cooling pressure eliminated crater wear formation and resulted only in adhered layer formation for the full range of assessed  $V_C$ , whilst the jet flow from flank cooling appears to enhance the mechanical wedge of high pressure coolant on chips, limiting the chip/tool interface area compared to the other assessed cooling strategies at corresponding  $V_C$  conditions. Furthermore, the rake and flank high pressure cooling produced no oxidation on the tool rake faces, compared to the

phenomenon occurring at  $V_C = 70$  m/min and rake only high pressure cooling, as well as when machining at  $V_C \geq 50$  m/min under low pressure rake cooling conditions. Figure 4-54 shows that this oxidation layer (Specimen 1) consists of elements (i.e. in oxide form, which explains the high oxygen content) found in the water/coolant solution used for these experiments (see Appendix 3). Finally, that lack of oxygen (O) and aluminium (Al) from the spectrum analysis of the tool's worn rake face area (Spectrum 3), compared to the tool's coating spectrum analysis (Spectrum 2), confirms the formation of crater wear that penetrated below the coating's thermal barrier (i.e.  $\text{Al}_2\text{O}_3$ ) reaching the final coating layer of Ti(C,N).

**Table 4-9: Effect of cooling performance on FG RR1000 chip formation data.**

<b>Rake cooling at 12 bar</b>					
	<b><math>h_{max\_c}</math> (μm)</b>	<b><math>\epsilon</math> (z = .95)</b>	<b>CCR</b>	<b><math>h_s</math> (μm)</b>	<b><math>d_s</math> (μm)</b>
<b><math>V_C = 30</math> m/min</b>	121.7	$\pm 1.2$	1.94	41.7	530
<b><math>V_C = 50</math> m/min</b>	91.4	$\pm 0.7$	1.45	48.2	1027
<b><math>V_C = 70</math> m/min</b>	78.5	$\pm 1.7$	1.25	42.4	915
<b>Rake cooling at 70 bar</b>					
	<b><math>h_{max\_c}</math> (μm)</b>	<b><math>\epsilon</math> (z = .95)</b>	<b>CCR</b>	<b><math>h_s</math> (μm)</b>	<b><math>d_s</math> (μm)</b>
<b><math>V_C = 30</math> m/min</b>	121.8	$\pm 1.9$	1.94	41.6	550
<b><math>V_C = 50</math> m/min</b>	91.2	$\pm 1.3$	1.45	37.1	417
<b><math>V_C = 70</math> m/min</b>	76.3	$\pm 1.5$	1.21	31.6	442
<b>Rake and flank cooling at 70 bar</b>					
	<b><math>h_{max\_c}</math> (μm)</b>	<b><math>\epsilon</math> (z = .95)</b>	<b>CCR</b>	<b><math>h_s</math> (μm)</b>	<b><math>d_s</math> (μm)</b>
<b><math>V_C = 30</math> m/min</b>	118.3	$\pm 1.3$	1.88	19.5	161
<b><math>V_C = 50</math> m/min</b>	89.5	$\pm 1.3$	1.42	35.6	452
<b><math>V_C = 70</math> m/min</b>	78.2	$\pm 0.9$	1.24	32.1	485

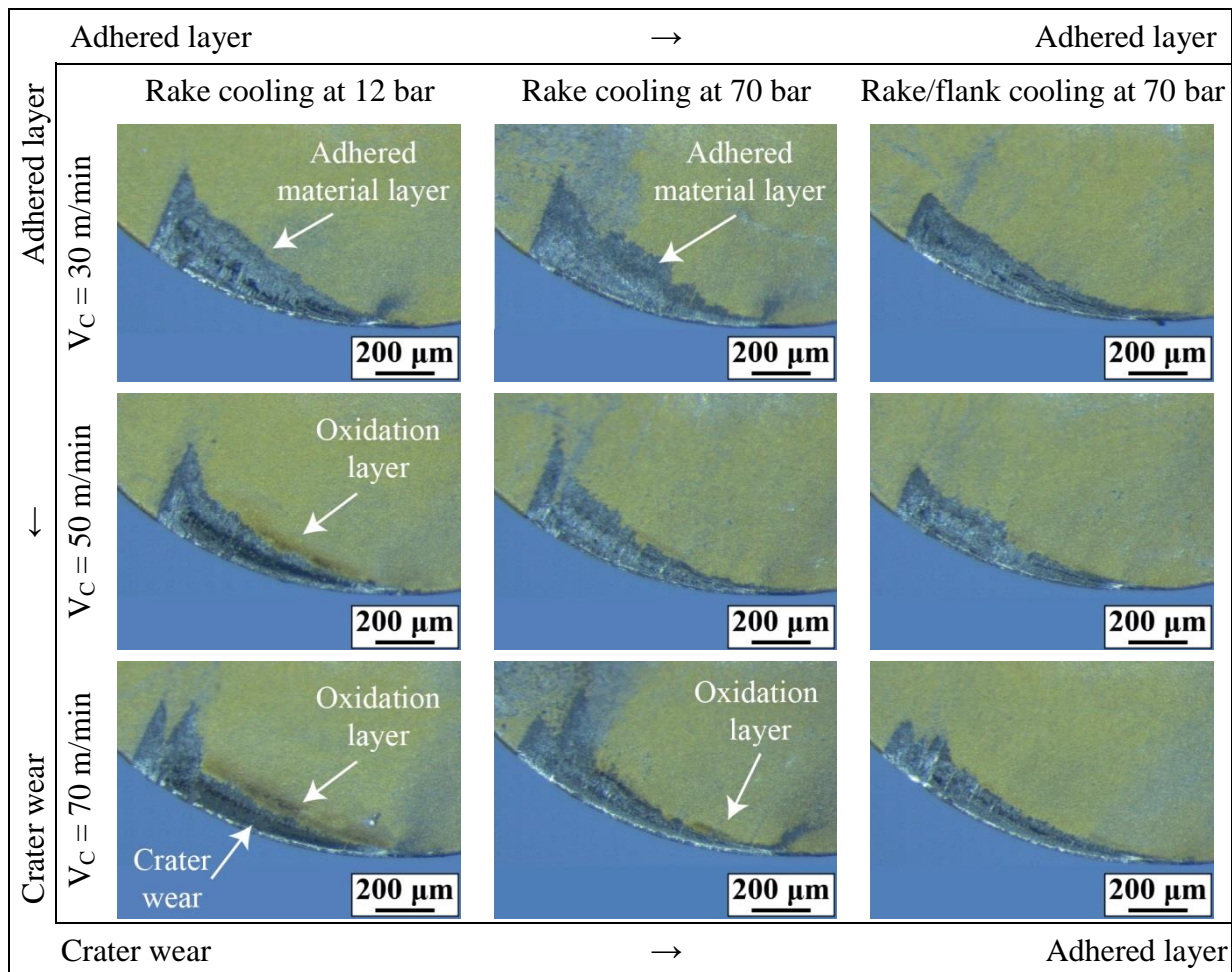


**Figure 4-53: Effect of cooling strategy performance on tool rake face wear mechanisms when machining FG RR1000.**

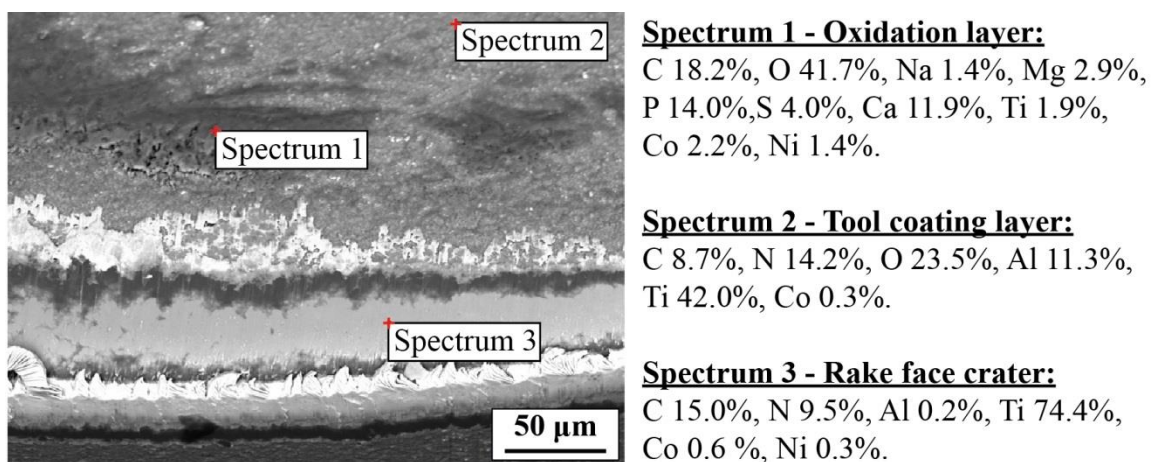


**Figure 4-54: Spectroscopy analysis in weight% of worn tool used when machining FG RR1000 at  $V_C = 70 \text{ m/min}$  under low pressure rake cooling conditions.**

#### 4.3.1.3 Low pressure rake and flank cooling case study

Applying low pressure coolant (i.e.  $P = 1.2 \text{ MPa}$ ) on the tool's rake and flank faces (i.e.  $\lambda = 6.5 + 6.5 \text{ l/min}$ ) when machining FG RR1000 at  $V_C = 30 \text{ m/min}$ ,  $a_p = 0.24 \text{ mm}$  and  $f = 0.12 \text{ mm/rev}$  resulted in similar chip formation and tool rake wear (without oxidation) as those for low  $P$  rake-only cooling and corresponding machining parameters, Figure 4-55(a-b). However, in this case coolant oxidation residue was observed on the tool's flank face, Figure 4-55(c), a phenomenon that was not detected for the tool used in high  $P$  rake and flank cooling process, Figure 4-55(d), which resulted in primary serration size reduction.

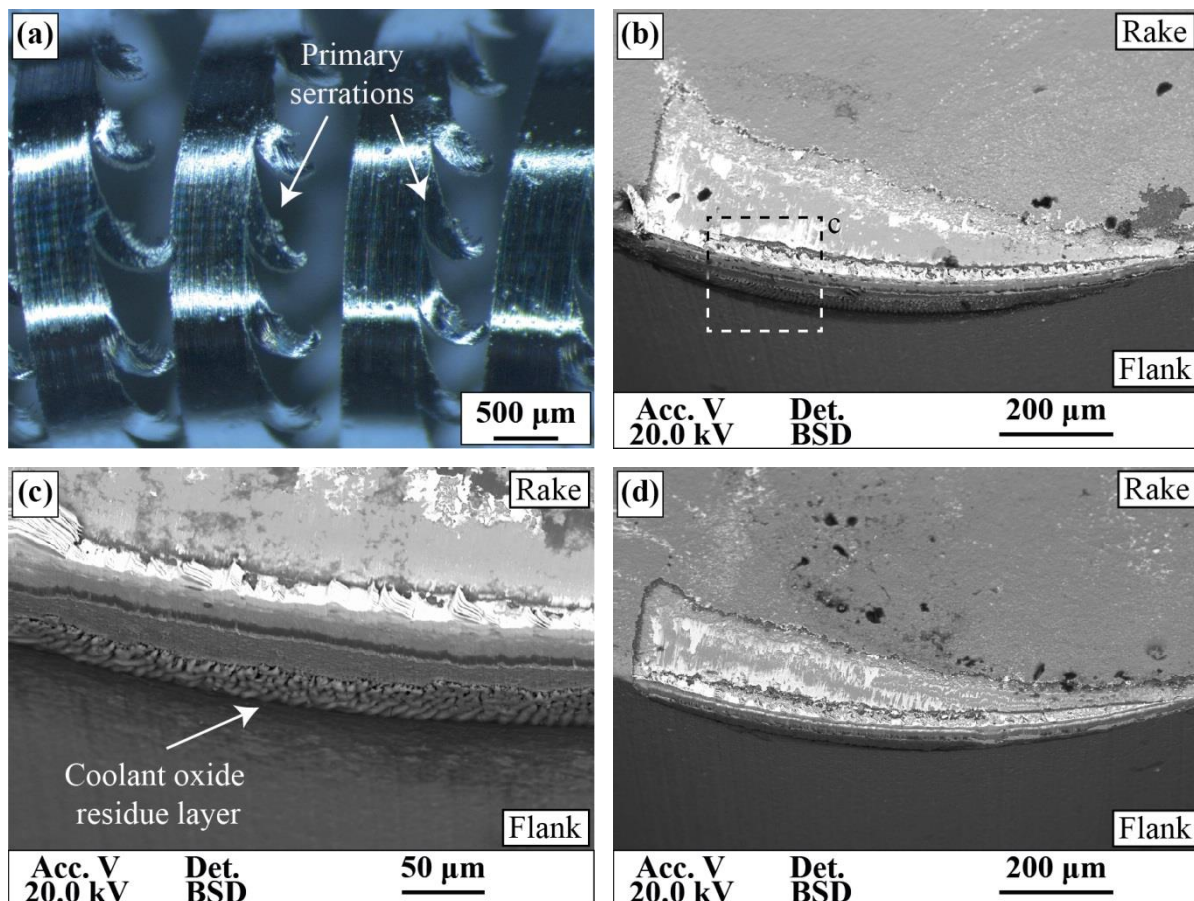


**Figure 4-55: Observations when machining under rake and flank cooling at  $V_C = 30 \text{ m/min}$ ; Worn tool (a-b)  $P = 12 \text{ bar}$  and (c)  $P = 70 \text{ bar}$ , (d) Chip formation at  $P = 12 \text{ bar}$ .**

#### 4.3.1.4 Cutting Forces

Table 4-10 shows that varying the cooling strategy when machining FG RR1000 resulted in similar machining forces at corresponding machining parameter combinations, whilst their values varied according to the trend discussed in previous experiments. Both cutting ( $F_C$ ) and push-off ( $F_P$ ) forces reduced when increasing  $V_C$  from 30 to 50 m/min and then both values increased again at  $V_C = 70$  m/min, while feed force ( $F_F$ ) was unaffected by the variation in  $V_C$ . Furthermore, the specific cutting loads acting at the tool's edge increased with increasing  $V_C$ , whilst they were found similar for corresponding machining conditions.

**Table 4-10: Effect of cooling performance on FG RR1000 machining loads.**

<b>Rake cooling at 12 bar</b>				
	$F_C$ (N)	$F_P$ (N)	$F_F$ (N)	Specific cutting load (N/mm <sup>2</sup> )
<b><math>V_C = 30</math> m/min</b>	$155.6 \pm 6.1$	$134.8 \pm 7.2$	$42.8 \pm 2.3$	2719.5
<b><math>V_C = 50</math> m/min</b>	$145.7 \pm 4.7$	$121.3 \pm 6.3$	$39.8 \pm 0.9$	3407.0
<b><math>V_C = 70</math> m/min</b>	$149.6 \pm 4.4$	$128.2 \pm 5.4$	$41.7 \pm 1.9$	4057.9
<b>Rake cooling at 70 bar</b>				
	$F_C$ (N)	$F_P$ (N)	$F_F$ (N)	Specific cutting load (N/mm <sup>2</sup> )
<b><math>V_C = 30</math> m/min</b>	$159.6 \pm 3.1$	$118.7 \pm 3.8$	$41.8 \pm 1.2$	2789.4
<b><math>V_C = 50</math> m/min</b>	$150.1 \pm 6.3$	$115.3 \pm 3.0$	$41.9 \pm 1.3$	3509.8
<b><math>V_C = 70</math> m/min</b>	$157.6 \pm 7.4$	$125.1 \pm 6.1$	$43.8 \pm 1.8$	4416.2
<b>Rake and flank cooling at 70 bar</b>				
	$F_C$ (N)	$F_P$ (N)	$F_F$ (N)	Specific cutting load (N/mm <sup>2</sup> )
<b><math>V_C = 30</math> m/min</b>	$169.5 \pm 3.3$	$121.4 \pm 3.1$	$40.7 \pm 1.0$	3056.9
<b><math>V_C = 50</math> m/min</b>	$152.9 \pm 4.2$	$114.2 \pm 2.0$	$39.6 \pm 0.7$	3650.8
<b><math>V_C = 70</math> m/min</b>	$152.9 \pm 6.1$	$141.8 \pm 2.1$	$41.8 \pm 1.2$	4180.8

#### *4.3.1.5 Discussion - Cooling Strategy Performance Assessment Trials (Phase 3)*

The presented results show a direct link between the FG RR1000 serration formation and the cooling strategy variables (i.e. coolant pressure ( $P$ ), coolant flow rate ( $\lambda$ ) and cooling position) identified in literature as key for controlling key machining heat loads, Huda et al. (2002), Dahlman (2002) Sørby and Tønnessen (2006) and Klocke et al. (2011). The identical chip formation characteristics, i.e. CCR and serration morphology, produced under rake cooling conditions at  $P = 12$  bar and  $\lambda = 6.5$  l/min and those observed in Phase 2b machined under  $P = 12$  bar and  $\lambda = 1.9$  l/min at corresponding machining parameters, indicate that increasing flow rate beyond a specific value appears to have negligible effect on the machining conditions controlling chip deformation and serration formation. This aligns with the observations by Klocke et al. (2011) who found that there is a limit in cutting temperature reduction achieved by a specific cooling strategy, and thus when that limit is achieved further increase in flow rate and/or cooling pressure only yields a constant outcome.

However, Wertheim et al. (1992) proved that delivering low coolant volume closer to the cutting edge outperformed flood cooling in terms of tool wear, indicating that the cooling effect on machining temperature reduction is greater when coolant penetrates deeper in the cutting zone. Nandy et al. (2009) also demonstrated that increasing rake cooling pressure generates a mechanical wedge in the chip/tool interface, enabling deeper coolant penetration into the cutting zone that resulted in accelerated heat dissipation and reduced crater wear. When machining at  $P = 70$  bar and  $\lambda = 6.5$  l/min crater wear was eliminated, while FG RR1000 serration morphology was identical for all parameter combinations and similar to those observed at  $V_C = 30$  m/min and low  $P$  conditions. Their similar serration spacing ( $d_s$ ) values when varying  $V_C$  indicates that at these conditions serration depth ( $h_s$ ) was defined by

the serration occurrence rate, explaining the fact that the thinner chips formed at higher  $V_C$  produced lower  $h_s$  values. Correlating these findings to those by Wertheim et al. (1992) and Nandy et al. (2009), indicate that the FG RR1000 chip trailing edges exhibited enhanced resilience to deformation at  $P = 70$  bar and  $\lambda = 6.5$  l/min compared to the low P cooling, probably due to the cooler high P conditions resulting in similar chip edge plasticity performance for the full range of assessed cutting speeds, even though chip strain increased with increasing  $V_C$ . Furthermore, the oxide residue layer detected on the tool rake faces shows that, for specific conditions, the coolant solution targeting the cutting zone was evaporating during cutting. Kaminski and Alvelid (2000) found that this phenomenon occurred at low pressure conditions when turning steel, with the layer of steam covering the chip/tool interface preventing heat dissipation and limiting cooling performance, whilst increasing pressure eliminated this phenomenon resulting in at least 30% reduction in machining temperatures. Su et al. (2016) explained that this formation of high pressure steam layer, known as Leidenfrost phenomenon, can only be penetrated by high momentum coolant flow during machining, explaining the more efficient heat removal process and low cutting temperatures at high pressure cooling conditions. The findings indicating extensive presence of this phenomenon at low P and  $V_C \geq 50$  m/min, compared its limited presence at high P and  $V_C = 70$  m/min, support further the serration formation findings suggesting that high P coolant resulted in cooler conditions than low P coolant and corresponding machining parameters.

Machining at  $V_C = 30$  m/min under high pressure rake and flank cooling resulted only in small primary serrations that penetrated to  $h_s \approx 20$   $\mu\text{m}$  compared to the rake-only cooling strategies and corresponding machining parameters that produced more than double  $h_s$  values, whilst the identical CCR and similar specific cutting loads suggest that chips were subjected

to comparable strains and similar strain rates independently of the cooling strategy. Sharman et al. (2008) proved that cooling the flank when machining Inconel 718 at  $V_C = 40$  m/min resulted in compressive surface residual stresses compared to the tensile stresses in rake-only cooling, suggesting that lower cutting temperatures were developed when cooling the tool's flank face. Su et al. (2016) also found that flank cooling reduced the tool/workpiece interface temperatures resulting in lower flank wear rates compared to the conventional rake cooling strategy. Combined these findings suggest that the small FG RR1000 primary serrations observed when cooling both tool faces were formed due to improved chip plasticity tolerance at the thin trailing edge, possibly caused by the accelerated heat removal rate and lower machining temperatures developed at these conditions. Furthermore, the coolant oxidation layer formed only at the tool's flank face used at  $V_C = 30$  m/min under low pressure rake and flank cooling, is indicative of 1. the high heat loads in the flank face that are not addressed with rake-only cooling strategies and 2. the fact that the unobstructed path of underjet flow allows coolant penetration closer to the cutting zone where temperatures are higher, supporting further the statement that combining flank and rake cooling accelerates heat dissipation. However, only the high P rake and flank cooling resulted in lower  $h_s$  values for which the Leidenfrost phenomenon was not observed, as its occurrence on the flank face at low P appears to have prevented sufficient reduction in cutting temperatures that at high P conditions improved chip edge plasticity tolerance.

Finally, further increase in  $V_C$  (i.e.  $\geq 50$  m/min) under the high P overjet and underjet application resulted in identical chip deformation and serration formation as the high P rake-only cooling conditions, indicating two possible scenarios: 1. Even if the combination of rake and flank cooling resulted in similar chip plasticity tolerance performance enhancement as that observed for  $V_C = 30$  m/min, this improvement is not sufficient to overcome the higher

chip strains introduced due increase in  $V_C$  and/or 2. Similar to the findings by Ezugwu and Bonney (2004) and Klocke et al. (2011) who observed the improved cooling performance is less effective on tool wear reduction and cutting temperature reduction, respectively, when increasing  $V_C$ , even though it always outperformed more conventional cooling strategies, it's possible that the combination of rake and flank cooling at  $V_C \geq 50$  m/min is less effective on heat dissipation and temperature reduction (and thus on chip plasticity performance improvement) resulting in comparable performance to high P rake-only cooling. However, it's possible that both scenarios are valid as the lack of pick-up deposition and coolant oxidation residue on tools at these conditions suggests overall superior cooling performance for flank and rake cooling at all corresponding machining parameters.

Summarising the findings, it was shown that maximising cooling strategy performance potential by applying high pressure cooling, which allows deeper penetration of the coolant to the cutting zone, and by cooling both tool faces involved in chip and surface formation, enhanced the thin trailing edge plasticity tolerance due to reducing the cutting temperatures. Combined with the lower strain and heat loads at lower cutting speed conditions, only small primary serrations were formed at these conditions with no tendency for failure; minimising the likelihood of pick-up deposition on the finished surfaces. Increasing  $V_C$  or reducing the cooling performance resulted in the increase chip strain and heat loads, while reducing chips deformation tolerance respectively; forming serrations with increasing risk of failure and higher deposition likelihood.

## 4.4 CHIP FORMATION TRIALS

### 4.4.1 Chip Formation - Dry Trials (Phase 4)

#### 4.4.1.1 Surface Integrity

Figure 4-56(a) shows the surface finish and pick-up deposition when dry machining FG RR1000 at  $V_C = 50$  m/min,  $a_p = 0.24$  mm and  $r_n = 1.5$  mm, with the full surface length produced in a single experimental run, while using the same tool to complete the sequence of three trials investigating the performance of  $f = 0.12$ ,  $0.18$  and  $0.24$  mm/rev, respectively, in this specific order. Machining at  $f = 0.12$  mm/rev produced the most severe pick-up damage, with all three pick-up types covering most of the dry turned surface, Figure 4-56(b), whilst the extensive presence of these protrusions resulted in the high average surface roughness  $R_a = 1.94 \mu\text{m}$ . Increasing  $f$  to  $0.18$  mm/rev reduced pick-up damage severity, with frequent occurrence Type 1 smearing residue and sporadic Type 3 major pick-ups only, Figure 4-56(c), resulting in  $R_a = 1.04 \mu\text{m}$ . Finally, further increase in  $f$  to  $0.24$  mm/rev resulted in pick-up free surface for the majority of the cut length with the exception of minor sporadic Type 2 pick-ups, Figure 4-56(d). Surface roughness  $R_a$  values at these conditions averaged at  $1.12 \mu\text{m}$ , though it should be noted that with the completion of the trial stage average flank wear was found to be  $0.46 \mu\text{m}$  which is more than double the acceptable production standard for FG RR1000 components.

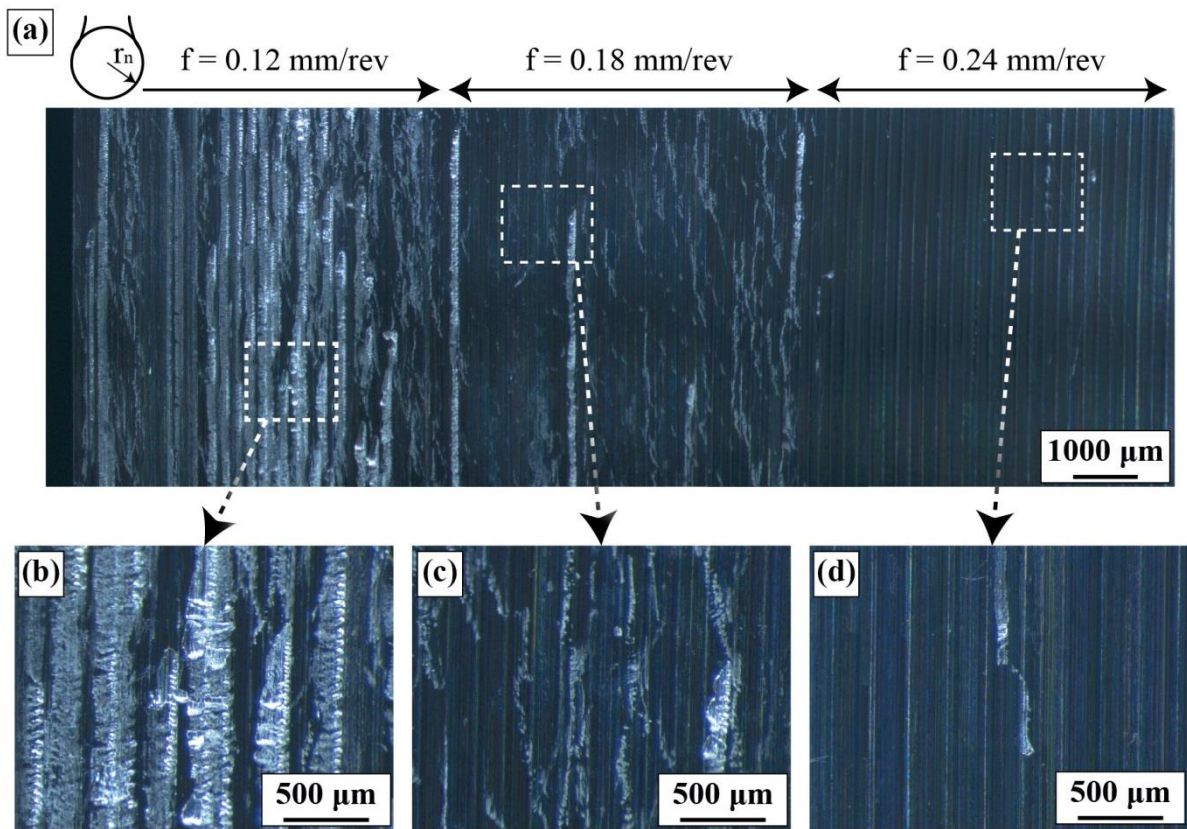


**Figure 4-56: Effect of feed rate on surface finish and pick-up deposition when dry machining FG RR1000 at  $V_C = 50 \text{ m/min}$ ,  $a_p = 0.24 \text{ mm}$  and  $r_n = 1.5 \text{ mm}$ ; (a) Full cutting length, Pick-up (b)  $f = 0.12 \text{ mm/rev}$ , (c)  $f = 0.18 \text{ mm/rev}$  and (d)  $f = 0.24 \text{ mm/rev}$ .**

#### 4.4.1.2 Chip Geometry

Primary and secondary serrations were detected on the trailing edges of FG RR1000 chips machined dry at  $V_C = 50 \text{ m/min}$ ,  $a_p = 0.24 \text{ mm}$ ,  $f = 0.12 \text{ mm/rev}$  and  $r_e = 35 \mu\text{m}$  for both tool radii ( $r_n$ ) of 1.5 mm and 3.0 mm. Higher  $r_n$  resulted in larger primary serrations, Figures 4-57(a-b), and both thinner and wider chip cross-section profiles compared to the thicker chip cross-sections produced at  $r_n = 1.5 \text{ mm}$  and corresponding machining parameters, Figures 4-57(c-d). However, machining with  $r_n = 3.0 \text{ mm}$  and sharper edge rounding (i.e.  $r_e = 15 \mu\text{m}$ ) produced primary serrations only, which were smaller and more frequent compared to those

formed when using tools with  $r_e = 35 \mu\text{m}$ , Figures 4-57(e-f), whilst they appear to have propagated to lower thicknesses than those at corresponding conditions, Figures 4-57 (g-h).

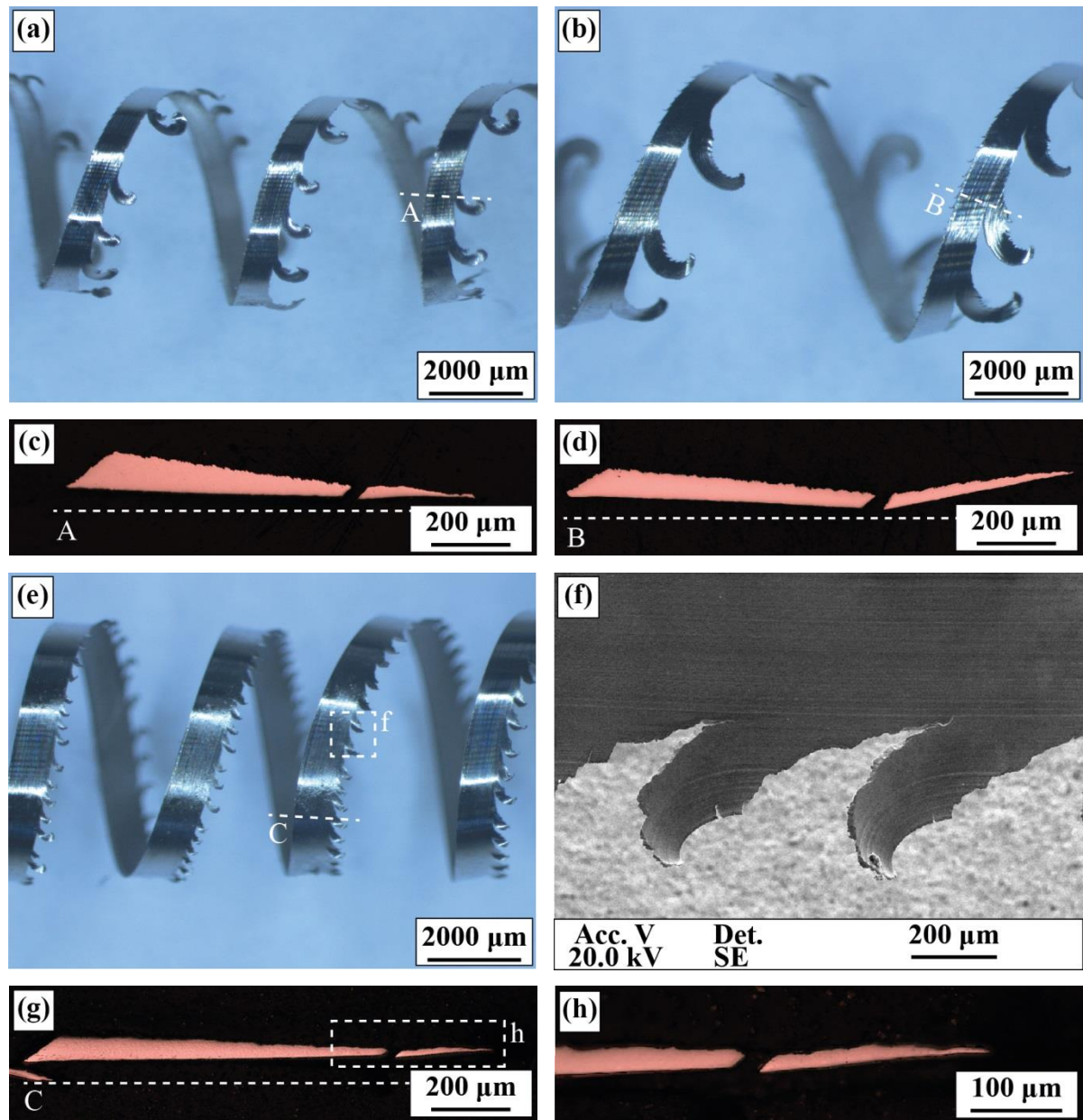


**Figure 4-57: Effect of tool radius and tool edge rounding on chip and serration**

formation when dry turning FG RR1000 at  $V_C = 50 \text{ m/min}$ ,  $a_p = 0.24 \text{ mm}$  and  $f = 0.12 \text{ mm/rev}$ ; (a,c)  $r_n = 1.5 \text{ mm}$  and  $r_e = 35 \mu\text{m}$ , (b,d)  $r_n = 3.0 \text{ mm}$  and  $r_e = 35 \mu\text{m}$ , (e-h)  $r_n = 3.0 \text{ mm}$  and  $r_e = 15 \mu\text{m}$ .

Figures 4-58(a-d) shows that increasing  $f$  when using tools with  $r_n = 1.5$  mm and  $r_e = 35 \mu\text{m}$  resulted in smaller primary serrations and thicker chip cross-sections than the corresponding  $f = 0.12 \text{ mm/rev}$  conditions. However, at  $f = 0.24 \text{ mm/rev}$  hook shaped primary serrations and secondary serrations were observed, Figure 4-58(e), while  $f = 0.36 \text{ mm/rev}$  resulted in primary serrations only that appear to have propagated to lower thickness than those for  $f = 0.24 \text{ mm/rev}$ , Figure 4-58(f).

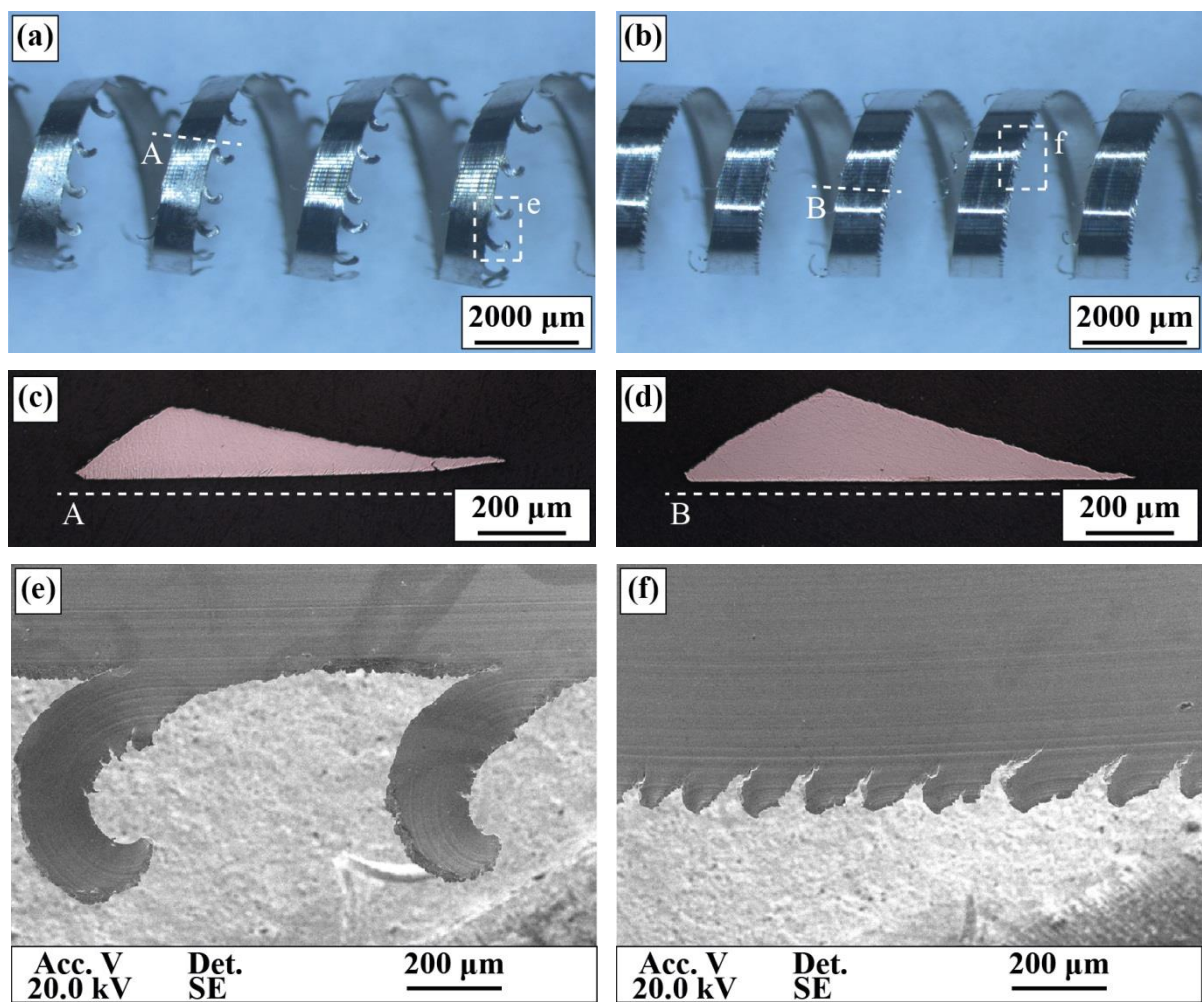


**Figure 4-58: Effect of feed rate on chip formation when dry turning FG RR1000 at  $V_C = 50 \text{ m/min}$ ,  $a_p = 0.24 \text{ mm}$ ,  $r_n = 1.5 \text{ mm}$  and  $r_e = 35 \mu\text{m}$ ;  $f = 0.24 \text{ mm/rev}$  (a) Chip morphology, (c) Chip cross-section and (e) Serrations,  $f = 0.36 \text{ mm/rev}$  (b) Chip morphology, (d) Chip cross-section and (f) Serrations.**

Similar was the effect when increasing  $f$  to 0.24 mm/rev for tools with  $r_n = 3.0$  mm and both  $r_e = 35 \mu\text{m}$  or  $r_e = 15 \mu\text{m}$ , with smaller serrations forming compared to the corresponding  $f = 0.12$  mm/rev conditions, whilst  $r_e = 35 \mu\text{m}$  produced both primary and secondary serrations, Figure 4-59(a), compared to  $r_e = 15 \mu\text{m}$  that resulted in smaller primary serrations only, Figure 4-59(b). However, further increase in  $f$  (i.e. 0.36 mm/rev) only affected the primary serrations formed at  $r_e = 15 \mu\text{m}$ , with  $r_e = 35 \mu\text{m}$  resulting in identical serraion morphology as the  $f = 0.24$  mm/rev conditions, Figures 4-59(c-d).

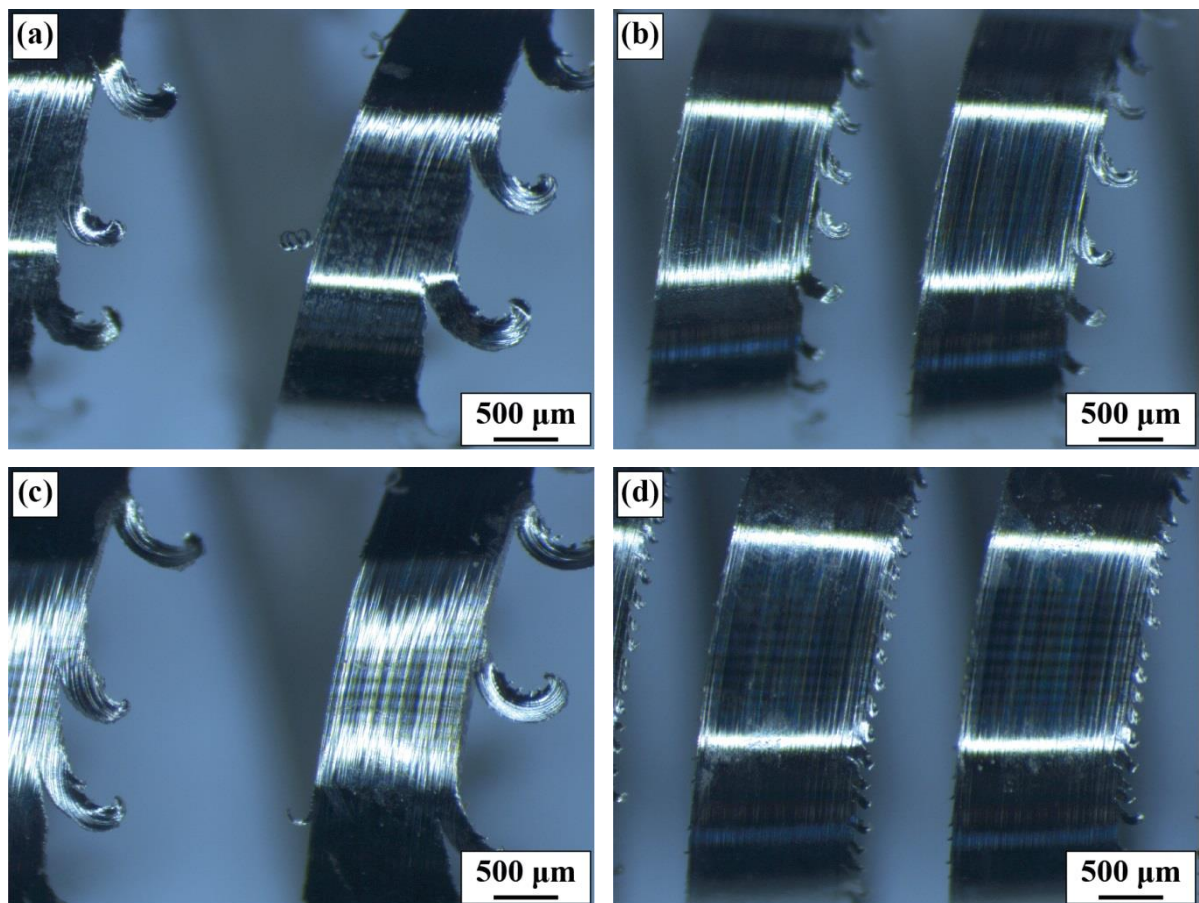


**Figure 4-59: Effect of feed rate and tool edge rounding on chip formation when dry turning FG RR1000 at  $V_C = 50$  m/min,  $a_p = 0.24$  mm and  $r_n = 3.0$  mm;  $f = 0.24$  mm/rev  
(a)  $r_e = 35 \mu\text{m}$  and (b)  $r_e = 15 \mu\text{m}$ ,  $f = 0.36$  mm/rev (c)  $r_e = 35 \mu\text{m}$  and (d)  $r_e = 15 \mu\text{m}$ .**

The chip formation data collected by 3D scanning, Table 4-11, show that increasing feed rate produced overall thicker chips, with increasing  $r_n$  resulting in lower  $h_{max\_c}$  values for corresponding  $f$  conditions and machining with sharper edge rounding producing thicker chips than the blunter edge  $r_n = 3.0$  mm tools. CCR values appear unaffected by the increase in  $f$  except for the combination of  $f = 0.36$  mm/rev and  $r_e = 35 \mu\text{m}$  that reduced CCR for both tool radii, whilst this effect was greater for high  $r_n$  conditions. Furthermore, increasing  $f$  reduced both the  $h_s$  and  $d_s$  values when using tools with  $r_n = 1.5$  mm and  $r_e = 35 \mu\text{m}$  or  $r_n = 3.0$  mm  $r_e = 15 \mu\text{m}$ , explaining the observed reduction in serration size at these parameters, however the sharp edge tool resulted in at least half  $h_s$  values for all corresponding conditions. For  $r_n = 3.0$  mm and  $r_e = 35 \mu\text{m}$ , increasing  $f$  only reduced  $d_s$  values with similar  $h_s$  found for all assessed feed rate conditions.

**Table 4-11: FG RR1000 chip formation data at variable feed rate, tool radius and tool edge rounding for fixed  $V_C = 50$  m/min and  $a_p = 0.24$  mm.**

$r_n = 1.5 \text{ mm } r_e = 35 \mu\text{m}$					
	$h_{max\_c} (\mu\text{m})$	$\varepsilon (z=.95)$	CCR	$h_s (\mu\text{m})$	$d_s (\mu\text{m})$
<b><math>f = 0.12 \text{ mm/rev}</math></b>	84.5	$\pm 0.9$	1.37	41.4	1097
<b><math>f = 0.24 \text{ mm/rev}</math></b>	155.0	$\pm 1.1$	1.34	34.2	804
<b><math>f = 0.36 \text{ mm/rev}</math></b>	197.0	$\pm 3.3$	1.22	18.9	143
$r_n = 3.0 \text{ mm } r_e = 35 \mu\text{m}$					
	$h_{max\_c} (\mu\text{m})$	$\varepsilon (z=.95)$	CCR	$h_s (\mu\text{m})$	$d_s (\mu\text{m})$
<b><math>f = 0.12 \text{ mm/rev}</math></b>	57.8	$\pm 0.9$	1.29	40.9	2530
<b><math>f = 0.24 \text{ mm/rev}</math></b>	110.5	$\pm 1.8$	1.29	41.7	1120
<b><math>f = 0.36 \text{ mm/rev}</math></b>	121.9	$\pm 1.4$	1.00	37.4	894
$r_n = 3.0 \text{ mm } r_e = 15 \mu\text{m}$					
	$h_{max\_c} (\mu\text{m})$	$\varepsilon (z=.95)$	CCR	$h_s (\mu\text{m})$	$d_s (\mu\text{m})$
<b><math>f = 0.12 \text{ mm/rev}</math></b>	61.6	$\pm 0.6$	1.37	20.7	499
<b><math>f = 0.24 \text{ mm/rev}</math></b>	115.3	$\pm 1.3$	1.35	16.1	475
<b><math>f = 0.36 \text{ mm/rev}</math></b>	167.0	$\pm 1.0$	1.37	7.2	210

Figure 4-60(a) shows that similar chip morphology and primary serration formation were produced when using the 1105 high temperature resistant coating grade to machine FG RR1000 at  $V_C = 50$  m/min,  $a_p = 0.24$  mm,  $f = 0.12$  mm/rev,  $r_n = 3.0$  mm and  $r_e = 15 \mu\text{m}$  to those observed when using S05F grade at corresponding conditions. Reducing  $a_p$  to 0.12 mm at corresponding parameters, resulted in smaller and more frequent primary serrations, Figure 4-60(b), while neither case formed secondary serrations.

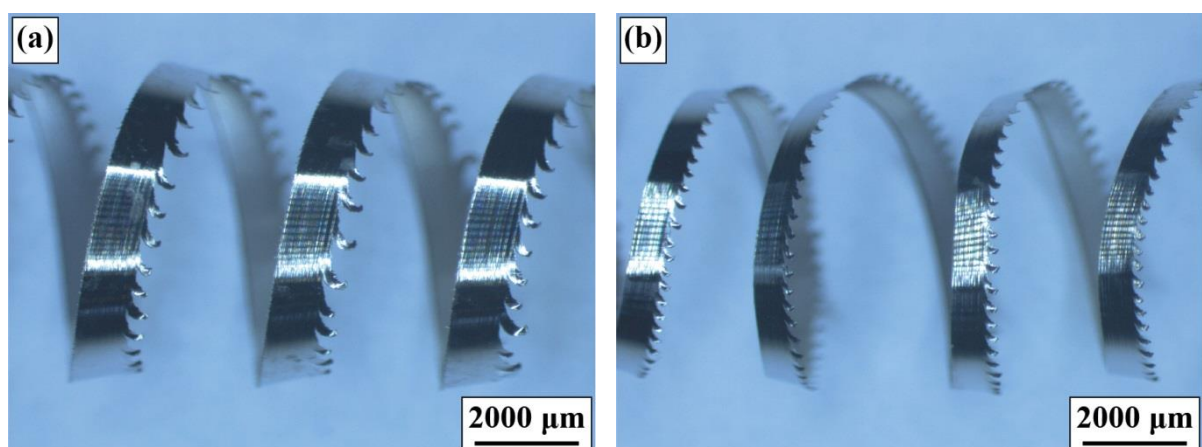


**Figure 4-60: Chip and serraion morphology when machining FG RR1000 at  $V_c = 50$  m/min,  $f = 0.12$  mm/rev,  $r_n = 3.0$  mm and  $r_e = 15 \mu\text{m}$  with 1105 coating grade; (a)  $a_p = 0.24$  mm, (b)  $a_p = 0.12$  mm.**

Machining with uncoated tool at  $V_C = 50$  m/min,  $a_p = 0.12$  mm,  $f = 0.12$  mm/rev,  $r_n = 3.0$  mm and  $r_e = 15 \mu\text{m}$  produced continuous helical chip, compared to the continuous ribbon shaped chips observed so far, Figure 4-61(a), whilst the serrations formed at the chip's edge were significantly smaller than any of the primary serrations observed when machining with coated tools at any of the assessed conditions, Figure 4-61(c). Reducing  $V_C$  to 30 m/min produced continuous ribbon chip and reduced primary serraion size even further, Figure 4-61(b), due to frequent minor cracking of the thin trailing edge, Figure 4-61(d). Figures 4-

61(e-f) also indicate that reducing  $V_C$  from 50 to 30 m/min at these conditions almost doubled the maximum chip thickness.

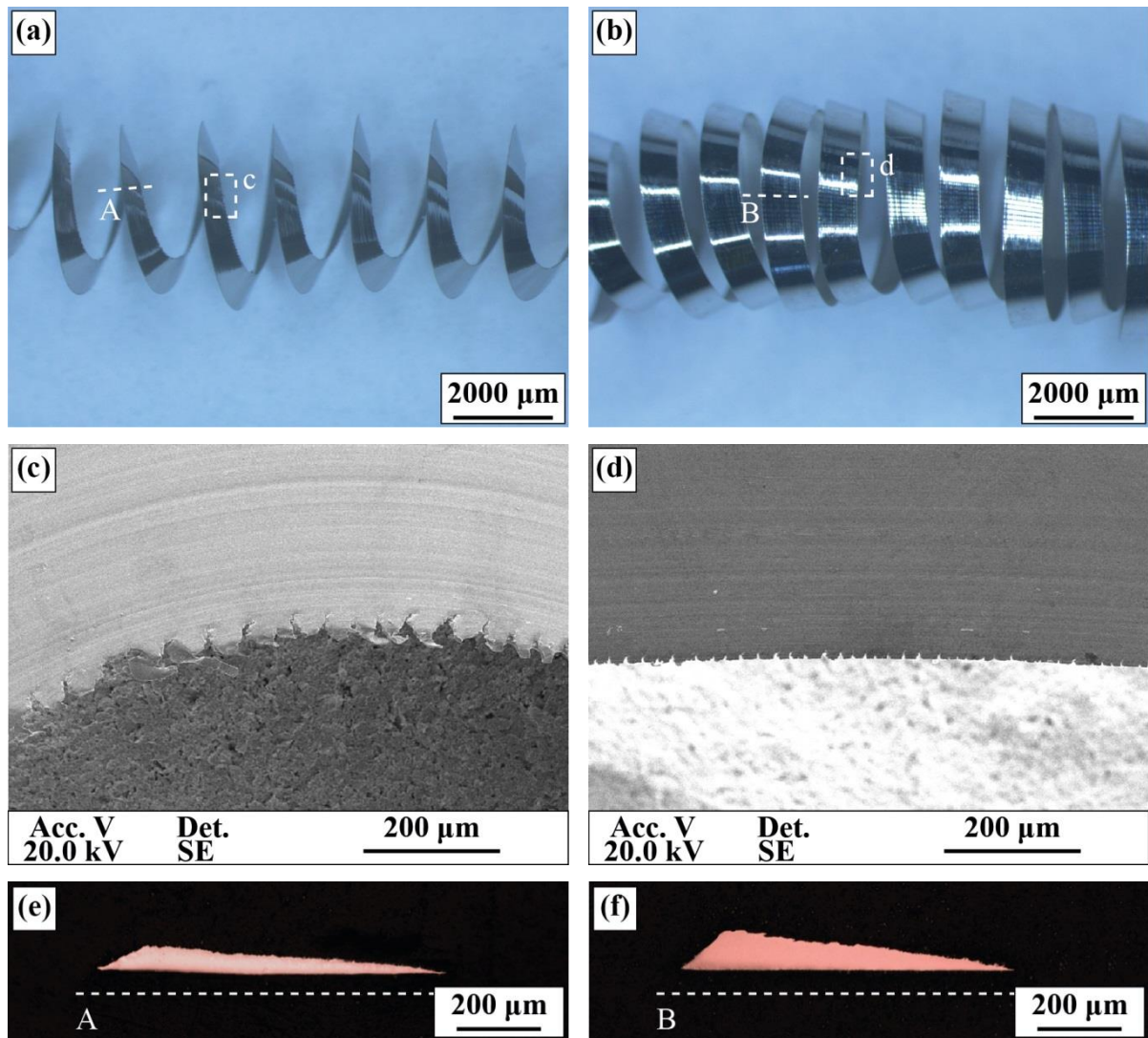


**Figure 4-61: Chip and serration morphology when machining FG RR1000 at  $a_p = 0.12$  mm,  $f = 0.12$  mm/rev,  $r_n = 3.0$  mm and  $r_e = 15$   $\mu\text{m}$  with uncoated tool;  $V_C = 50$  m/min (a) Chip morphology, (c) Serrations and (e) Chip cross-section,  $V_C = 30$  m/min (b) Chip morphology, (d) Serrations and (f) Chip cross-section.**

The chip formation data collected by 3D scanning confirm the findings in Figure 4-60, Table 4-12, with the 1105 coating grade tool resulting in similar  $h_s$  and  $d_s$  values as the corresponding S05F tool, even though thicker chips and higher CCR were found at these

conditions. Decreasing  $a_p$  reduced the serration spacing, whilst CCR and  $h_s$  were identical to the high  $a_p$  conditions. Using uncoated tools at  $V_C = 50$  m/min,  $a_p = 0.12$  mm,  $f = 0.12$  mm/rev,  $r_n = 3.0$  mm and  $r_e = 15 \mu\text{m}$  increased  $h_{\max,c}$  and reduced the  $h_s$  and  $d_s$  values compared to corresponding coated tools conditions, whilst reducing  $V_C$  to 30 m/min increased further  $h_{\max,c}$ .

**Table 4-12: FG RR1000 chip formation data when using different tool grades.**

<b>1105 grade (<math>r_n = 3.0</math> mm and <math>r_e = 15 \mu\text{m}</math>)</b>					
	$h_{\max,c} (\mu\text{m})$	$\epsilon (z = .95)$	CCR	$h_s (\mu\text{m})$	$d_s (\mu\text{m})$
$V_C = 50$ m/min $a_p = 0.24$ mm	66.8	$\pm 0.8$	1.49	18.3	654
$V_C = 50$ m/min $a_p = 0.12$ mm	47.4	$\pm 0.8$	1.51	17.1	341
<b>Uncoated tool (<math>r_n = 3.0</math> mm and <math>r_e = 15 \mu\text{m}</math>)</b>					
	$h_{\max,c} (\mu\text{m})$	$\epsilon (z = .95)$	CCR	$h_s (\mu\text{m})$	$d_s (\mu\text{m})$
$V_C = 30$ m/min $a_p = 0.12$ mm	86.2	$\pm 0.6$	2.75	-	-
$V_C = 50$ m/min $a_p = 0.12$ mm	54.0	$\pm 0.5$	1.72	6.7	62

Figure 4-62 shows that machining FG RR1000 with S05F coated tools at  $V_C = 30$  m/min,  $f = 0.12$  mm/rev,  $r_n = 3.0$  mm and  $r_e = 15 \mu\text{m}$  resulted in continuous ribbon chips with only primary serrations forming at the chip's thin edge, which appear smaller than those formed at corresponding  $V_C = 50$  m/min conditions. Increasing  $a_p$  at these conditions formed larger hook shape serrations which exhibited tendency for fracturing-off during machining, Figures 4-62(b). This phenomenon was also observed for the irregular shaped serrations formed at both  $a_p$  cases and  $f = 0.24$  mm/rev conditions, Figure 4-63(a-b). Figures 4-63(c-d) demonstrate that elongated ribbon shape serrations were formed at these conditions, which when fractured result in large sections of the thin edge showing no evidence of serration formation; similar to dry turning Inconel at  $f = 0.12$  mm/rev in Phase 1 experiments. Finally,

further increase in  $f$  (i.e. 0.36 mm/rev) reduced the serration size for both  $a_p$  conditions, whilst eliminating their failure tendency, Figure 4-63(e-f).

The chip formation data collected by 3D scanning for  $V_C = 30$  m/min, Table 4-12, show that lower  $h_s$  and  $d_s$  values were produced at  $a_p = 0.12$  mm and  $f = 0.12$  mm/rev compared to the corresponding  $a_p = 0.24$  mm conditions. Similar to the trend outlined in  $V_C = 50$  m/min, increasing  $f$  reduced  $h_s$  and  $d_s$  values for both  $a_p$  conditions and resulted in identical values at  $f = 0.36$  mm/rev. Finally, machining at higher  $f$  resulted overall in thicker chips, however, CCR at  $a_p = 0.24$  mm reduced with increasing  $f$  from 0.12 to 0.14 mm/rev compared to the similar CCR values achieved  $a_p = 0.12$  mm for all  $f$  conditions.

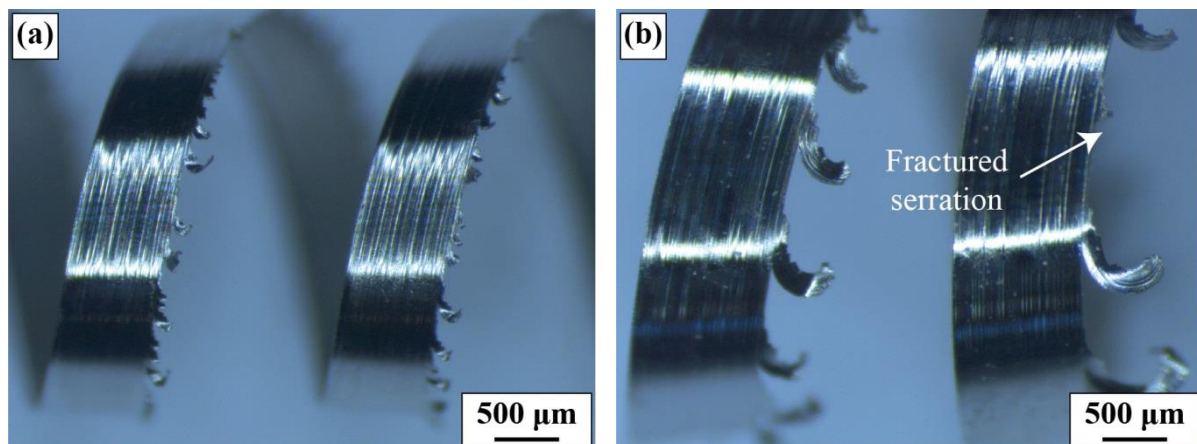


**Figure 4-62: Effect of depth of cut on FG RR1000 chips machined dry with S05F coated tools at  $V_C = 30$  m/min,  $f = 0.12$  mm/rev,  $r_n = 3.0$  mm and  $r_e = 15$   $\mu\text{m}$ ; (a)  $a_p = 0.12$  mm, (b)  $a_p = 0.24$  mm.**

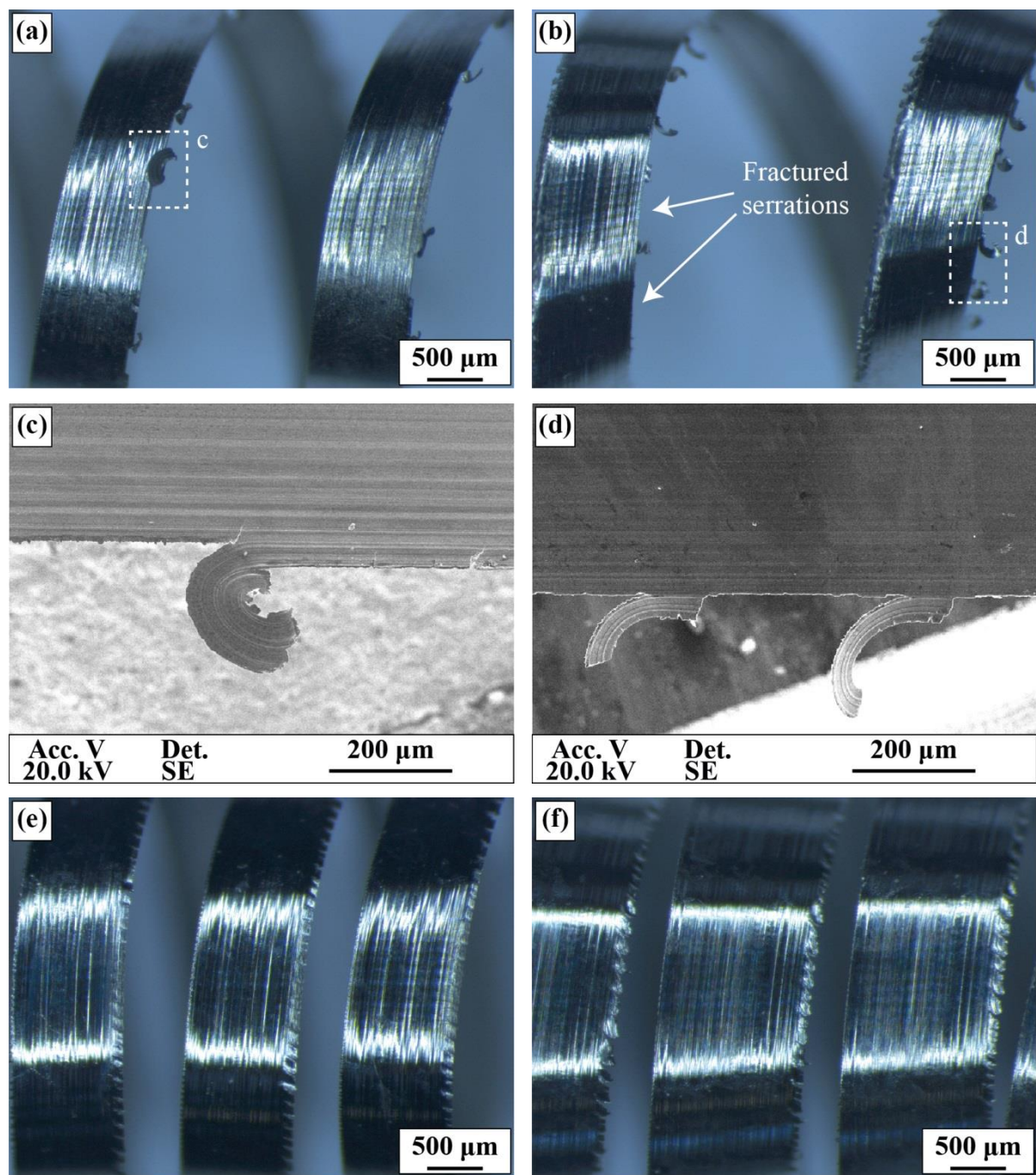


**Figure 4-63: Effect of depth of cut and feed rate on FG RR1000 chips machined dry with S05F coated tools at  $V_C = 30 \text{ m/min}$ ,  $r_n = 3.0 \text{ mm}$  and  $r_e = 15 \mu\text{m}$ ;  $f = 0.24 \text{ mm/rev}$**

**(a,c)**  $a_p = 0.12 \text{ mm}$  and **(b,d)**  $a_p = 0.24 \text{ mm}$ ,  $f = 0.36 \text{ mm/rev}$  **(e)**  $a_p = 0.12 \text{ mm}$  and **(f)**  $a_p = 0.24 \text{ mm}$ .

**Table 4-13: FG RR1000 chip formation data at variable feed rate and depth of cut for fixed  $V_C = 30 \text{ m/min}$ ,  $r_n = 3.0 \text{ mm}$  and  $r_e = 15 \mu\text{m}$ .**

$a_p = 0.12 \text{ mm}$					
	$h_{max\_c} (\mu\text{m})$	$\epsilon (z=.95)$	CCR	$h_s (\mu\text{m})$	$d_s (\mu\text{m})$
<b><math>f = 0.12 \text{ mm/rev}</math></b>	63.4	$\pm 1.1$	2.02	14.0	329
<b><math>f = 0.24 \text{ mm/rev}</math></b>	120.1	$\pm 1.0$	2.06	9.4	-*
<b><math>f = 0.36 \text{ mm/rev}</math></b>	158.0	$\pm 2.5$	1.97	5.9	128
$a_p = 0.24 \text{ mm}$					
	$h_{max\_c} (\mu\text{m})$	$\epsilon (z=.95)$	CCR	$h_s (\mu\text{m})$	$d_s (\mu\text{m})$
<b><math>f = 0.12 \text{ mm/rev}</math></b>	85.9	$\pm 0.5$	1.91	21.1	764
<b><math>f = 0.24 \text{ mm/rev}</math></b>	144.4	$\pm 0.8$	1.69	6.7	324
<b><math>f = 0.36 \text{ mm/rev}</math></b>	204.3	$\pm 1.6$	1.68	6.6	120

\* Not possible to calculate due to the phenomenon shown in Figures 4-63(a,c).

#### 4.4.1.3 Cutting Forces

Table 4-14 shows that increasing  $f$  when turning FG RR1000 at  $V_C = 50 \text{ m/min}$  and  $a_p = 0.24 \text{ mm}$  increased machining forces for all conditions, whilst both low  $r_n$  and low  $r_e$  resulted in lower  $F_C$  and  $F_P$  values, and also lower specific cutting loads than corresponding high  $r_n$  and/or high  $r_e$  conditions. In addition, increasing  $f$  overall reduced specific cutting loads, except at  $f = 0.36 \text{ mm/rev}$  and  $r_e = 35 \mu\text{m}$ , which for  $r_n = 1.5 \text{ mm}$  resulted in similar specific cutting loads as the  $f = 0.24 \text{ mm/rev}$  conditions, and for  $r_n = 3.0$  resulted in higher specific cutting loads than the  $f = 0.24 \text{ mm/rev}$  conditions. Taken in combination with the

Table 4-15 shows that increasing  $f$  at  $V_C = 30 \text{ m/min}$  resulted in similar  $F_C$  and  $F_P$  increase trend as the  $V_C = 50 \text{ m/min}$  conditions, though low  $V_C$  resulted in overall higher force values. Finally, low  $V_C$  resulted in lower specific cutting loads than the corresponding  $V_C = 50 \text{ m/min}$ , which also reduced with increasing  $f$ , whilst varying  $a_p$  appears to be less significant on these values especially at higher  $f$ .

**Table 4-14: Effect of feed rate, tool radius and tool edge rounding on FG RR1000 machining loads at fixed  $V_C = 50$  m/min and  $a_p = 0.24$  mm.**

$r_n = 1.5 \text{ mm } r_e = 35 \mu\text{m}$				
	$F_C$ (N)	$F_P$ (N)	$F_F$ (N)	Specific cutting load (N/mm <sup>2</sup> )
<b>f = 0.12 mm/rev</b>	133.8 ± 1.6	136.9 ± 3.1	43.7 ± 1.2	3447.1
<b>f = 0.24 mm/rev</b>	224.6 ± 3.1	169.9 ± 7.2	47.2 ± 2.5	2961.3
<b>f = 0.36 mm/rev</b>	311.2 ± 5.4	205.9 ± 6.1	47.8 ± 2.4	3049.6
$r_n = 3.0 \text{ mm } r_e = 35 \mu\text{m}$				
	$F_C$ (N)	$F_P$ (N)	$F_F$ (N)	Specific cutting load (N/mm <sup>2</sup> )
<b>f = 0.12 mm/rev</b>	165.2 ± 2.5	182.0 ± 4.6	43.4 ± 1.7	4491.4
<b>f = 0.24 mm/rev</b>	267.2 ± 4.1	231.8 ± 6.4	53.4 ± 2.3	3640.2
<b>f = 0.36 mm/rev</b>	356.5 ± 7.9	260.8 ± 4.6	57.5 ± 4.6	4210.8
$r_n = 3.0 \text{ mm } r_e = 15 \mu\text{m}$				
	$F_C$ (N)	$F_P$ (N)	$F_F$ (N)	Specific cutting load (N/mm <sup>2</sup> )
<b>f = 0.12 mm/rev</b>	146.1 ± 2.1	149.8 ± 3.5	36.6 ± 1.3	3740.2
<b>f = 0.24 mm/rev</b>	239.1 ± 2.6	184.7 ± 5.0	43.2 ± 1.8	3112.6
<b>f = 0.36 mm/rev</b>	324.4 ± 4.5	205.5 ± 7.9	45.9 ± 3.0	2796.8

**Table 4-15: Effect of feed rate and depth of cut on FG RR1000 machining loads at fixed  $V_C = 30$  m/min,  $r_n = 3.0$  mm and  $r_e = 15 \mu\text{m}$ .**

$a_p = 0.12 \text{ mm}$				
	$F_C$ (N)	$F_P$ (N)	$F_F$ (N)	Specific cutting load (N/mm <sup>2</sup> )
<b>f = 0.12 mm/rev</b>	103.0 ± 2.1	106.0 ± 3.8	16.9 ± 1.3	3567.7
<b>f = 0.24 mm/rev</b>	157.4 ± 2.3	136.1 ± 3.9	23.1 ± 1.5	2704.6
<b>f = 0.36 mm/rev</b>	197.1 ± 2.8	147.9 ± 4.6	23.6 ± 1.8	2416.6
$a_p = 0.24 \text{ mm}$				
	$F_C$ (N)	$F_P$ (N)	$F_F$ (N)	Specific cutting load (N/mm <sup>2</sup> )
<b>f = 0.12 mm/rev</b>	164.3 ± 1.8	160.4 ± 3.3	38.5 ± 1.3	3016.9
<b>f = 0.24 mm/rev</b>	254.1 ± 3.5	197.7 ± 6.0	45.2 ± 2.4	2642.4
<b>f = 0.36 mm/rev</b>	331.8 ± 3.6	194.1 ± 5.6	46.9 ± 2.0	2332.8

#### *4.4.1.4 Discussion – Chip Formations Trials (Phase 4)*

The presented results show a direct link between  $h_{max\_c}$  and FG RR1000 serration size at fixed  $a_p$ , as increasing  $f$  resulted in thicker chips with smaller serrations for all assessed conditions. At  $V_C = 50$  m/min and  $a_p = 0.24$  mm, higher  $f$  combined with  $r_n = 1.5$  mm and  $r_e = 35 \mu\text{m}$  resulted in lower  $h_s$  values, whilst  $f = 0.36$  mm/rev produced small primary serration only; indicating that these conditions reduced the plastic deformation at the chip's trailing edge. These observations align with the findings by Kishawy and Elbestawi (1999) who reported that increasing  $f$  when turning steel resulted in smaller serrations, due to less chip material being machined at the tool's edge rounding where localised deformation is higher. Therefore, the lower triaxiality at the chip's thin trailing edge when increasing  $f$  explains both the reduction in chip serraton and serraton failure at corresponding conditions, which also led to less severe pick-ups, Figure 4-56. Furthermore, it is important to note that even when machining with worn tool (of  $r_n = 1.5$  mm) under dry conditions, high  $f$  produced sporadic minor pick-ups only with the majority of the surface area being pick-up free, compared to complete surface coverage with pick-ups at low  $f$  and new tool. The phenomenon suggests that low  $f$  conditions promoted severe serraton fracture, compared to the combination of higher  $f$  and worn tool conditions, indicating the extent of feed rate effect on the amount of strain at the chip's trailing edge.

The effect of higher  $f$  values on chip's edge deformation was less significant when machining with  $r_n = 3.0$  mm, as higher  $h_s$  values and larger primary serrations were formed compared to corresponding  $r_n = 1.5$  mm conditions. Sharman et al. (2015) reported higher strain at the chip's thin trailing edge when machining under chip thinning conditions, whilst Chou and Song (2004) found that higher  $r_n$  increases the cut's ploughing energy subjecting

both the chip and surface at higher strain and heat loads. Observations like 1. the overall higher specific cutting loads at  $r_n = 3.0$  mm compared to  $r_n = 1.5$  mm and 2. the increase in specific cutting loads for  $f = 0.36$  mm/rev compared to  $f = 0.24$  mm/rev at these conditions, align with the literature findings showing that increasing  $r_n$  counteracted the effect of higher  $f$  on reducing chip deformation, especially at its thin edge. Furthermore, these higher chip plastic deformation conditions also resulted in CCR reduction at  $f = 0.36$  mm/rev and  $r_n = 3.0$  mm compared to the other  $f$  and/or lower  $r_n$  conditions, indicating that the chip's plasticity tolerance was limited possibly due to increase in the chip's formation heat loads, similar to the observations by Chou and Song (2004).

In comparison, using tools with  $r_n = 3.0$  mm and sharper edge (i.e.  $r_e = 15 \mu\text{m}$ ) resulted only in primary serrations for all assessed conditions, with  $h_s$  reducing at higher  $f$  and serrations penetrating to less than half the  $h_s$  values compared to those for corresponding  $r_e = 35 \mu\text{m}$  conditions. These observations indicate reduction in localised deformation at the chip's thin edge when machining with sharper tools, which aligns with the findings by Bitans and Brown (1965) who demonstrated that lower  $r_e$  decreased chip deformation at the cutting edge, resulting also in shallower sub-surface distortion, due to less severe ploughing effect of the tool's edge geometry compared to blunter tools. Furthermore, Thiele et al. (2016) showed that using sharper tool edge rounding produced shallower sub-surface distortion and lower surface tensile residual stresses compared to using tools with larger  $r_e$ , which combined with the observations by Hughes et al. (2004) who observed improved tool life when using sharper tools for finish turning Ti6Al4V compared to blunter tools, suggest that using sharper tools favour reduction in mechanical and heat related plastic deformation of the chips, surfaces and tools. Therefore, the findings by Thiele et al. (2016) and Hughes et al. (2004) as well as the less severe chip serraion explain the lower mechanical loads and reduction in specific cutting

loads when machining with sharper tools, as they are all indicative of lower machining strains at these conditions. Whilst the higher CCR values achieved compared to corresponding  $r_e = 35 \mu\text{m}$  suggest that the overall chip plasticity was also improved, possibly due to lower chip formation heat loads associated with the lower amount of work required to deform the FG RR1000 chips at these conditions.

Substituting S05F tools (i.e. TiN/Al<sub>2</sub>O<sub>3</sub>/TiCN) with 1105 grade tools (i.e. TiAlN coated carbide) at  $V_C = 50 \text{ m/min}$   $r_n = 3.0 \text{ mm}$  and  $r_e = 15 \mu\text{m}$  resulted in higher CCR, indicating that although uncut chip geometry was identical for both cases, and thus shearing strain should have been identical, the machining conditions resulted in different strain rates. Ostafiev et al. (1999) found that the tool material thermal conductivity and tool coating grade affect the cut's heat flux as they control the heat diffusion rate through the tool's body. Chinchanikar and Choudhury (2014) also demonstrated that the coating's insulating performance controls the amount of heat reflected back to the cutting zone, and thus the maximum cutting temperature, with TiAlN coating resulting in lower cutting temperatures compared to the superior thermal barrier multilayer coating TiCN/Al<sub>2</sub>O<sub>3</sub>/TiN. Taken in combination, it is suggested that lower chip heat loads were developed when machining with the 1105 grade tools compared to S05F tools, which could explain the superior plasticity tolerance demonstrated by the chips machined at these conditions. Sharman et al. (2006) used the same concept to explain the lower residual tensile stresses found when machining Inconel 718 with uncoated tools compared to using coated tools. The authors suggested that the lack of thermal barrier protecting the tool enhanced the heat dissipation rate through the tool's body leading to lower machining temperatures. This also suggests that using uncoated tools reduce the heat loads concentrated in the chips, explaining the thicker chips produced with uncoated tools compared to  $V_C = 50 \text{ m/min}$ ,  $a_p = 0.12 \text{ mm}$ ,  $f = 0.12 \text{ mm/rev}$ ,  $r_n = 3.0 \text{ mm}$ ,  $r_e = 15 \mu\text{m}$  and

coated tool conditions, which is indicative of overall improved chip plasticity tolerance at these conditions. The phenomenon also affected plasticity at the chips thin trailing edge, resulting in smaller and shallower serrations. Minimizing strain and heat loads by decreasing  $V_C$  when using uncoated tools, resulted in even higher CCR and minimal chip serraion, verifying the suggested theory that both serraion formation and failure are affected by the amount of strain at the cutting edge as well as the ability of the chip to support the strains, depending on the heat conditions.

Finally, reducing  $V_C$  when using coated sharp S05F tools had similar but less significant effect to that observed at corresponding uncoated tool conditions, with higher CCR produced due to the decrease in shear angle compared to  $V_C = 50$  m/min, as explained by Trent and Wright (2000), whilst chip serraion size and  $h_s$  reduced due to the reduction in strains at these conditions (also indicative by the lower specific cutting loads compared to those for  $V_C = 50$  m/min). However, also interesting is the fact that combining the effect of higher  $f$  and sharper tools resulted in similar serraion formation and failure trend mechanisms for FG RR1000 chips as those observed for more ductile Alloy 718 chips machined at  $f = 0.12$  mm/rev and  $r_e = 35 \mu\text{m}$  in Phase 1 of the experiments, see Figures 4-14 and 4-63(a-d). The phenomenon confirms that at lower strain conditions the less ductile alloy had similar plasticity performance to that of more ductile alloy undergoing higher stain, validating the role of mechanical properties, and especially that of workpiece ductility, on serraion formation.

Summarising the findings, it is evident that conditions reducing the amount of material machined below the tool's edge rounding at the chips trailing edge, like the higher  $f$ , lower  $r_n$  and sharper tools, reduced localised triaxiality leading to less severe chip serraion, limiting the likelihood for serraion detachment and thus resulting in minimal pick-up deposition at

corresponding conditions. They also appear to create conditions that affect material flow, improving the overall chip plasticity, leading to higher CCR values and lower machining strains. However, the benefits of using shaper tools require further investigation as it has been demonstrated in the past that sharp tool edges can be compromised under high machining forces and temperature conditions when machining high strength materials, Bitans and Brown (1965). Finally, similar to the cooling experiments in Phase 2-3, it was found that machining with uncoated tools affected the cut's heat flux balance, with the lower chip formation heat loads at these conditions enhancing the plasticity performance of the chip and resulting in higher CCR and lower chip serration.

## 5 SUMMARY DISCUSSION

A series of experiments were conducted in order to identify the origin, formation and deposition mechanism of pick-up, whilst investigating the effect of workpiece microstructure, machining parameters and cooling strategy on chip formation and pick-up severity. A novel methodology was developed to extract chip formation data from the collected chip samples, which when correlated to the recorded machining load data as well as the chip, surface and worn tool optical analysis data proved that pick-up is a chip formation related defect.

Pick-up deposits on finish turned surfaces originated from the ductile failure of serrations forming on the chip trailing edges, which were deposited due to their entrapment between the tool and workpiece interface during machining. These serrations form when the chip material damage strain threshold is exceeded, whilst high triaxiality conditions at the chip edge promote the serration failure and increase in pick-up severity. Chip thinning parameters were found to increase localised chip deformation, for example the low feed rate values enforced in FG RR1000 production line due to the low surface roughness Ra standard, which combined with FG RR1000's low ductility, compared to other superalloys, explains the concurrent emergence of serrations and higher levels of pick-up deposits with the introduction of this alloy in production and its so-called 'sensitivity' to pick-up. The more ductile CG RR1000 and Alloy 718 demonstrated higher plasticity tolerance than FG RR1000 resulting in smaller serrations and lower pick-up severity for the majority of corresponding assessed machining parameters. On a side note, it is of great interest the fact that thin chips observed in literature for orthogonal turning resulted in similar edge serrations as the cold

rolled thin material strips, Figure 5-1(a-b), proving that the ductile nature of edge fracture due to localised deformation applies in range of material deformation operations.

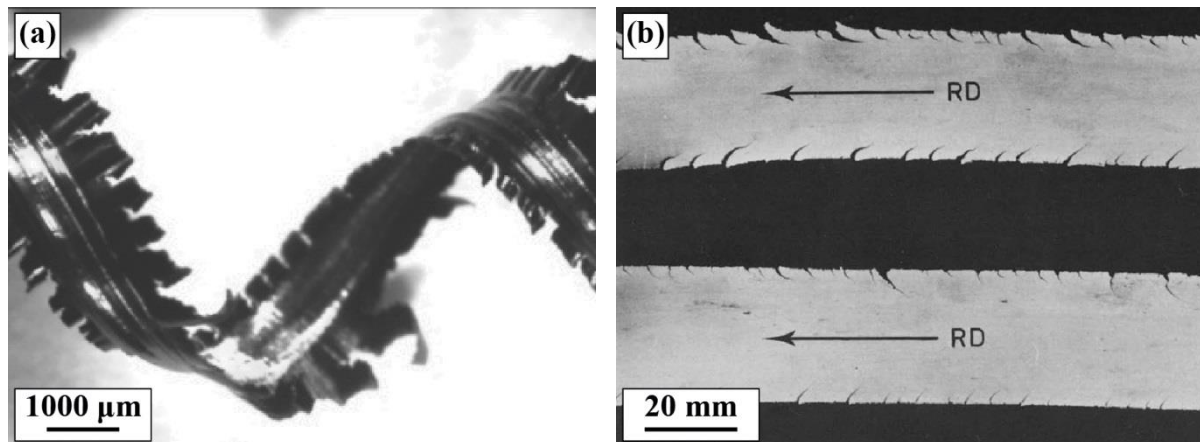


**Figure 5-1: (a) Chip formation in orthogonal turning, Salem et al. (2012); (b) Cold rolled material strips, Dodd and Boddington (1980).**

These experiments have also demonstrated that parameters increasing heat loads during machining limit the chip plasticity tolerance in the materials analysed (i.e. higher depth of cut and higher cutting speed), and when combined to higher chip strain conditions (i.e. at high cutting speed) they promoted both serration failure and more severe pick-up. Applying coolant during machining reduced the chip heat loads and improved the chip deformation tolerance, also affecting the serration formation mechanism and limiting serration fracture, Figure 5-2. This explains the reduction in pick-up occurrence and improvement in surface finish under cooled conditions observed both in these experiments and in literature; verifying the project's hypothesis that this defect is related to the chip formation conditions and not to the surface state conditions as suggested in literature. It was also demonstrated that improved cooling performance increased further the chip deformation tolerance, especially at its thin trailing edge, indicating that these conditions alter the cut's heat flux balance due to enhancing the heat dissipation and reducing the chip formation heat loads. Therefore, when

machining FG RR1000 at low feed rate targeting low surface roughness Ra values, the combination of  $V_C = 30$  m/min and high pressure rake and flank face cooling is recommended, Table 5-1, for minimum likelihood of serration failure and minimum risk for pick-up occurrence, Figure 5-2. If higher  $V_C$  was to be used in production, high pressure rake and flank face cooling remains the recommended cooling strategy, even though increasing  $V_C$  was found to reduce its effect on chip deformation, which increases the likelihood of pick-up.

In the case the strict surface roughness Ra standards were to be relaxed in FG RR1000 production (i.e. currently Rolls-Royce plc considers increasing the limit of Ra value from 0.8 to 1.2  $\mu\text{m}$ ) then increasing feed rate is recommended, Table 5-2. Higher  $f$  was found to produce thicker chips that resulted only in small primary serrations, due to limiting the localised deformation at the chip's thin edge. The enhanced control over serration formation and the limited serration failure likelihood at these conditions, without the requirement of sophisticated cooling strategies, allow for even higher cutting speeds to be used (i.e.  $V_C \geq 50$  m/min) with limited increase in pick-up occurrence risk. Furthermore, the recommended combination of  $f = 0.25$  mm/rev and  $a_p = 0.12$  mm achieves identical material removal rate to parameters used in production at corresponding  $V_C$ , while also resulting in lower machining forces and lower specific cutting loads. In terms of tool radius, using lower  $r_n$  is recommended where possible, as increasing  $r_n$  was found to have the opposite effect to high  $f$ , due to producing thinner chips with higher localised deformation at their thin edge, whilst resulting in higher ploughing energy.

Other conditions enhancing control over serration formation and failure were: 1. the use of tools with sharper edge, as the lower cutting edge rounding was found to reduce localised chip plasticity at the thin edge compared to standard tools and 2. the use of different coating grade or even uncoated tools, which were found to alter heat flux affecting chip deformation

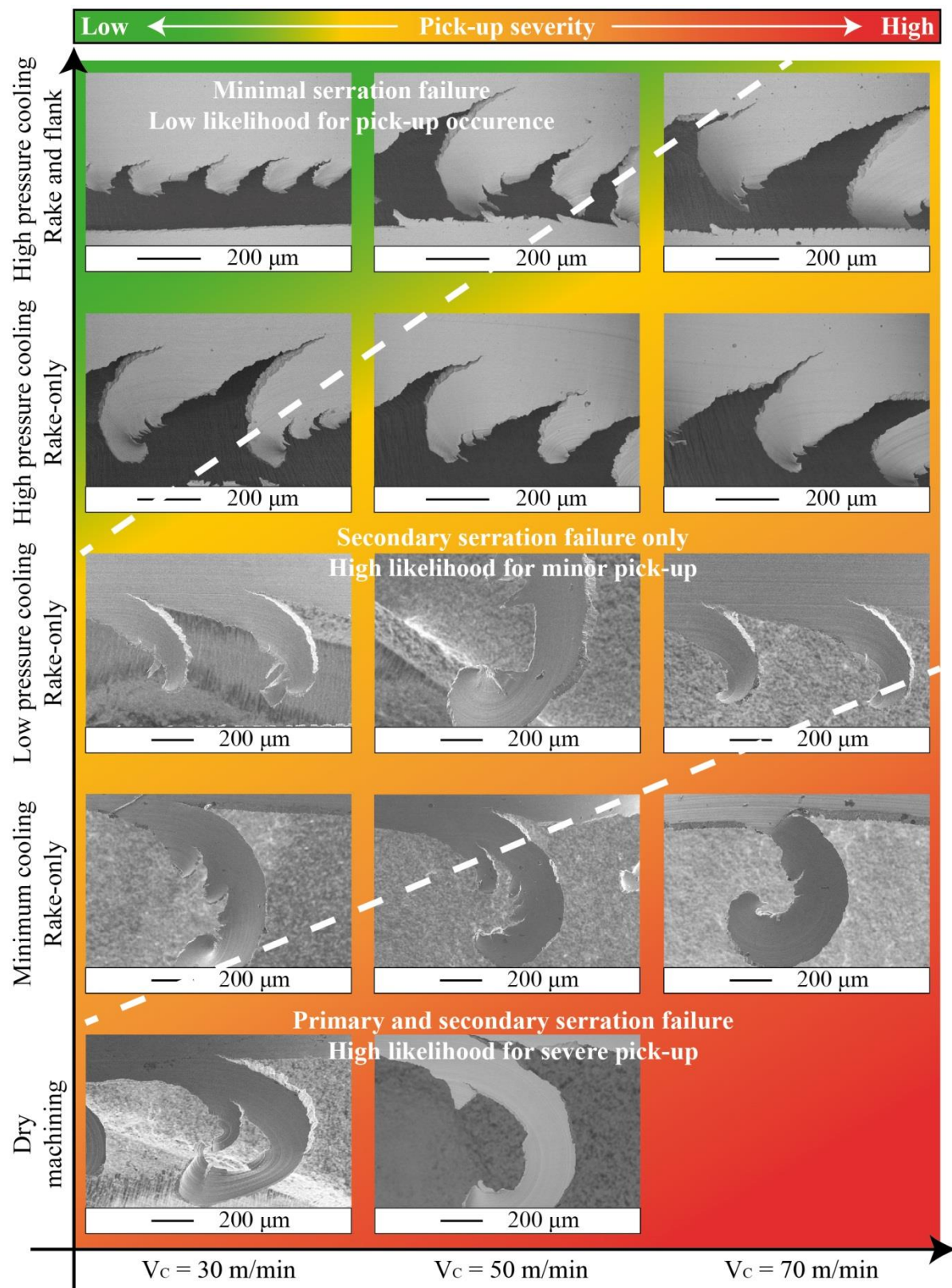


**Figure 5-2: Effect of cooling strategy and cutting speed on FG RR1000 chip serrations produced at  $a_p = 0.25 \text{ mm}$ ,  $f = 0.12 \text{ mm/rev}$ ,  $r_n = 1.5 \text{ mm}$  and  $r_e = 35 \mu\text{m}$ .**

and serration formation. Therefore, both conditions validate the previous concepts stating that the parameters limiting localised deformation and those enhancing chip plasticity tolerance, through improved heat dissipation and lower heat loads, enhance the control over FG RR1000 serration formation and failure. However, neither is recommended to be used in production at this stage as they are known to have inferior tool wear resistance than the current tool option, which is critical for fulfilling the sub-surface integrity production standards.

**Table 5-1: Recommended machining parameters for pick-up free surfaces and surface roughness  $R_a \leq 0.8 \mu\text{m}$ .**

Machining Parameters	Recommended Values
Cutting speed, $V_C$	30-50 m/min
Depth of cut, $a_p$	0.25 mm
Feed rate, $f$	0.12 mm/rev
Tool radius, $r_n$	1.5 mm or lower
Tool edge rounding, $r_e$	35 $\mu\text{m}$
Tool grade	S05F coated carbide
Cooling strategy	High pressure rake and flank cooling

**Table 5-2: Recommended machining parameters for pick-up free surfaces and surface roughness  $R_a \leq 1.2 \mu\text{m}$ .**

Machining Parameters	Recommended Values
Cutting speed, $V_C$	50-70 m/min
Depth of cut, $a_p$	0.12 mm
Feed rate, $f$	0.25 mm/rev
Tool radius, $r_n$	1.5 mm or lower
Tool edge rounding, $r_e$	35 $\mu\text{m}$
Tool grade	S05F coated carbide
Cooling strategy	Low pressure rake cooling or better

## 6 CONCLUSIONS

The origin of surface pick-up during finish turning operations of the advanced powder metallurgy superalloy RR1000 has been investigated and the following conclusions can be drawn:

- Serrations form at the chip's thin trailing edge when the material damage strain threshold is exceeded leading to fracture, serration formation and often to serration failure.
- The formation and fracturing-off of serrations, due to the ductile failure of the chip, promoted their entrapment between the tool and workpiece interface, leading to their smearing and deposition on to the machined surfaces in the form of pick-ups.
- The reduced ductility performance of FG RR1000 combined with the suggested higher strain and heat loads in this alloy variant machining, resulted in the extended failure and deposition of the primary and secondary chip serrations causing more severe surface damage compared to that caused when machining the more ductile CG RR1000 at corresponding conditions.
- The strict requirement for very low surface roughness values, dictating the use of low feed rates, results in production of very thin chips, which are conditions leading to higher localised deformation at the chips trailing edge, causing the formation and fracture of serrations that lead to pick-up.
- Increasing  $V_C$  and  $a_p$  under dry conditions resulted in the increase of pick-up severity for both FG and CG RR1000.

- Machining Alloy 718 under dry conditions resulted in more severe pick-up at low  $V_C$ , demonstrating that the relationship between chip ductility conditions and pick-up damage is more complex than the linear relationship shown when machining RR1000, with the serration fracturing-off tendency depending on whether the ductility conditions at the chip's edge favour the serration propagation to failure independently of their propagation thickness.
- Maximum pick-up surface coverage under dry conditions occurred in FG RR10000 machining at high Q that corresponded to maximum serration of the chip's trailing edge and frequent serration fracture. Minimum damage was detected when machining CG RR1000 at low Q that corresponded to minimum serration size and the formation of primary serrations only.
- Understanding the role of microstructure and machining parameters on the chip formation mechanism and thus presence of pick-up is vital for the production optimisation of RR1000 components.
- Coolant application reduced pick-up occurrence and severity due to enhancing the chip's ability to support machining strains at corresponding conditions and thus restricting the serration failure leading to improved surface finish.
- At fixed f and cooling conditions,  $V_C$  was the parameter with most significant effect on FG RR1000 serration formation due to its influence on chip formation strain and heat loads.
- Improving cooling performance counteracts the effect of increasing  $V_C$  by shifting the machining window away from catastrophic ductility conditions that lead to severe pick-ups. It was also found to improve ductility in FG RR1000 chips, which also explains the observed improved control over serration failure and pick-up presence.

- The failure of coolant supply, due to the chip interaction with the jet flow, led to conditions similar to the dry machining experiments, favouring the serration detachment from the chip's edge and pick-up deposition.
- Increasing flow rate beyond a specific value appears to have negligible effect on the machining conditions controlling chip deformation and serration formation.
- High pressure coolant resulted in cooler conditions than corresponding low pressure coolant, resulting in lower the chip formation heat loads, which enhanced the plasticity tolerance at the thin edge of FG RRR1000 chips.
- High pressure coolant supply combined with cooling both the rake and flank tool faces appears to have produced the cooler condition compared to the other assessed cooling strategies, resulting in minimal the likelihood of serration detachment and pick-up deposition.
- Similar to the effect of cooling, it was found that machining with uncoated tools affected the cut's heat flux balance, with the lower chip formation heat loads at these conditions enhancing the plasticity performance of the chip, thus resulting in higher CCR and lower chip serration.
- Uncut chip geometry was also found to affect the chip's trailing edge tolerance to damage as well as the amount of plastic deformation at the chip edge, with the thicker chips produced at high  $f$  and/or low  $r_n$  resulting in lower localised deformation at the chip's trailing edge, limiting chip serration and reducing the likelihood of pick-up deposition.
- Machining with sharper tools was found to reduce localised plastic deformation leading to less severe FG RR1000 chip serration and reducing the likelihood for serration detachment.

## 7 RECOMMENDED FURTHER WORK

The industrial optimisation focus of the project as well as the practical approach taken in order to identify the origin and deposition of pick-up on finish turned surfaces has successfully identified trends in machining conditions favouring the occurrence of the defect. It has also enabled the reduction of pick-up in production by assessing and validating cutting strategies, which enhanced chip and serration control. However, the limitations in this approach have created a number of paths for future work, presented below, that would enhance the understanding of chip formation when machining the low ductility, high strength FG RR1000 or other similar superalloys:

- This study has reached the conclusion that serrations are formed at the thin trailing edge of chips when the material's damage threshold is exceeded, though the lack of material flow data restricts the ability to pinpoint the conditions at which serration formation will initiate. It is proposed that this data pool is created and a model is developed to predict the FG RR1000 chip flow behaviour without the requirement for experimental trials.
- It has also been observed that serrations transform by varying their size, spacing and penetration depth or even by creating secondary serrations at the edges of primary serrations. In addition, serration detachment is also believed to be part of this transformation mechanism, as in occasion serrations demonstrated tendency for breaking-off of the chip's edge instead of transforming. The different assessed materials exhibited different response to this transformation mechanism at

corresponding machining parameters, verifying that material properties are key in serration formation. Therefore, developing a model that simulates and predicts the specific chip flow conditions favouring serration detachment instead of serration transformation are critical for identifying sweet spots in the machining operation window for which the serration formation is stable and pick-up likelihood is limited. This is essential when specific production requirements limit the selection of machining parameters that could eliminate the serration occurrence.

- Furthermore, the experiments revealed that varying cooling performance affects serration formation, whilst the effect of a specific cooling strategy was found to be different on chip flow and serration formation when machining a range of superalloys. It is of great interest to develop a chip formation model simulating the effect of cutting heat flux on material flow response during machining, especially with cooling process being integral in modern finish production operations. The data presented in this project could be used to validate the accuracy of such FG RR1000 model, which could then be used to rectify between the possible suggested effects of cooling on FG RR1000 serration formation, for example the effect of underjet at  $V_C \geq 50$  m/min etc.
- Based on the literature observations by Bresseler et al. (1997) and Pawade et al. (2007), it was found that high speed finish turning of steels and superalloys, respectively, resulted in the occurrence of the surface defect known as sideflow, whilst at lower cutting speeds and corresponding parameters material deposits were also detected on the finished surfaces. Taken in combination with the findings by El-Wardany and Elbestawi (1998) who linked sideflow to chip material that remained uncut on the surface forming serrations at the chip's edge when hard turning steel, whilst in this study pick-ups were linked to the detachment of serrations forming at

the chip's thin trailing edge during machining at low to intermediate cutting speeds, there is a growing belief that pick-up and sideflow are linked mechanisms. It appears that pick-ups occur at lower cutting speeds, when conditions allow serration formation and then fracture, whilst at higher cutting speeds the transformation into sideflow means that serrations remain uncut on the surface as they are squeezed between the tool and workpiece interface. It is suggested to investigate further this theory as apart from the academic value in proving the probable link between the origins of these two defects, it is possible that the future plans to move FG RR1000 production to a high speed machining strategy would be affected by the occurrence of sideflow.

- Although tool wear has not been part of the scope in this study, findings in literature suggest that worn tools result more severe pick-ups, Axinte et al. (2006), as tool wear was proven to increase machining strains and heat loads, Sharman et al. (2006), which are conditions found to promote chip serration and serration detachment. A study on the effect of tool wear on pick-up severity is recommended, focusing however on the observations that suggested limited effect of tool wear on pick-up when machining at high feed rates.
- Furthermore, if higher feed rates were to be used in FG RR1000 production a machinability study should be performed, investigating the effect of feed rate on subsurface integrity as the only condition found to increase RR1000 subsurface plastic distortion in these experiments was the increase in feed rate.
- Improving cooling performance was proven to enhance the chip's plasticity, though it was also demonstrated that depending on the cooling strategy there are limitations in their effectiveness. Therefore, it is suggested to assess the performance of novel cooling solutions on serration formation, like cryogenic cooling.

- For the Phase 1 experiments the dry cuts were performed in a face turning configuration, while in Phase 4 experiments the dry cuts were performed in the outer diameter (OD) turning configuration, with the only parameter combination used in both phases, i.e.  $V_C = 50$  m/min,  $a_p = 0.25\text{-}0.24$  mm,  $f = 0.12$  mm/rev,  $r_n = 1.5$ mm and  $r_e = 35\mu\text{m}$ , resulting in higher CCR values and lower machining loads for the OD configuration compared to the corresponding facing operation. FG RR1000 rotative component features require hybrid turning operations with the tool-workpiece configuration transforming from facing to OD during the cut's progression, whilst these operations are performed in a vast range of workpiece diameters. For the purposes of this study, it was assumed that both turning operation configurations were compatible, however, it appears that FG RR1000 machining conditions may vary depending on the workpiece geometry even for almost identical uncut chip geometry and material removal rate. Taking into considerations the findings by Campocasso et al. (2013) who found that tuning at different workpiece diameters under identical machining parameters resulted in different machining loads, suggesting variation in the machining conditions; it is critical to investigate further any possible effects of workpiece configuration on chip formation mechanics.

## REFERENCES

- Abukhshim, N. A., Mativenga, P. T., & Sheikh, M. A. (2006). Heat generation and temperature prediction in metal cutting: A review and implications for high speed machining. *International Journal of Machine Tools and Manufacture*, 46(7–8), 782–800.
- Ardi, D. T., Li, Y. G., Chan, K. H. K., Blunt, L., & Bache, M. R. (2014). The effects of machined topography on fatigue life of a nickel based superalloy. *Procedia CIRP*, 13, 19–24.
- Arrazola, P. J., Garay, A., Iriarte, L. M., Armendia, M., Marya, S., & Le Maître, F. (2009). Machinability of titanium alloys (Ti6Al4V and Ti555.3). *Journal of Materials Processing Technology*, 209(5), 2223–2230.
- Arunachalam, R. M., & Mannan, M. A. (2003). Surface Finish and Residual Stresses in Facing of Age Hardened Inconel 718. In *Materials Science Forum* (Vol. 437–438, pp. 503–506).
- Arunachalam, R. M., Mannan, M. A., & Spowage, A. C. (2004a). Residual stress and surface roughness when facing age hardened Inconel 718 with CBN and ceramic cutting tools. *International Journal of Machine Tools and Manufacture*, 44(9), 879–887.
- Arunachalam, R. M., Mannan, M. A., & Spowage, A. C. (2004b). Surface integrity when machining age hardened Inconel 718 with coated carbide cutting tools. *International Journal of Machine Tools and Manufacture*, 44(14), 1481–1491.

- Asai, S., & Kobayashi, A. (1990). Observations of chip producing behaviour in machining and study on generating mechanism. *Precision Engineering*, 137–143.
- ASTM International. (2013). *ASTM E112 - 13 Standard Test Methods for Determining Average Grain Size*. West Conshohocken.
- Atkins, A. G. (2003). Modelling metal cutting using modern ductile fracture mechanics: Quantitative explanations for some longstanding problems. *International Journal of Mechanical Sciences*, 45(2), 373–396.
- Axinte, D. A., Andrews, P., Li, W., Gindy, N., & Withers, P. J. (2006). Turning of advanced Ni based alloys obtained via powder metallurgy route. *CIRP Annals - Manufacturing Technology*, 55(1), 117–120.
- Bailey, J. A. (1977). Surface Damage During Machining of Solution Treated and Aged 18% Nickel Maraging Steel Part 2 - Lubricated Conditions. *Wear*, 44, 371–376.
- Banik, A., Green, K. A., Hardy, M. C., Mourer, D. P., & Reay, T. (2004). Low cost powder metal turbine components. *Superalloys 2004 (Tenth International Symposium)*, 571–576.
- Barry, J., & Byrne, G. (2002). The Mechanisms of Chip Formation in Machining Hardened Steels. *Journal of Manufacturing Science and Engineering*, 124(3), 528.
- Basaran, M. (2011). *PhD Thesis: Stress state dependent damage modeling with a focus on the lode angle influence*. Aachen: Shaker.
- Bhatt, A., Attia, H., Vargas, R., & Thomson, V. (2010). Wear mechanisms of WC coated and uncoated tools in finish turning of Inconel 718. *Tribology International*, 43(5–6), 1113–

1121.

Bitans, K., & Brown, R. H. (1965). An investigation of the deformation in orthogonal cutting.

*International Journal of Machine Tool Design and Research*, 5(3), 155-165.

Bresseler, B., El-Wardany, T. I., & Elbestawi, M. A. (1997). Material Side Flow in High Speed Finish Boring of Case Hardened Steel. In *1st French and German Conference on High Speed Machining* (pp. 196–206).

Bushlya, V., Schultheiss, F., Gutnichenko, O., Zhou, J. M., & Ståhl, J.-E. (2015). On the Analytical Representation of Chip Area and Tool Geometry when Oblique Turning with Round Tools. Part 1: Chip Area Parameters under Variation of Side and Back Rake Angle. *Procedia CIRP*, 31, 417–422.

Bushlya, V., Zhou, J. M., Lenrick, F., Avdovic, P., & Ståhl, J. E. (2011). Characterization of white layer generated when turning aged inconel 718. *Procedia Engineering*, 19, 60–66.

Campocasso, S., Costes, J. P., Fromentin, G., Bissey-Breton, S., & Poulachon, G. (2013). Improvement of cutting forces modeling based on oriented cutting tests. *Procedia CIRP*, 8, 206–211.

Cantero, J. L., Díaz-Álvarez, J., Miguélez, M. H., & Marín, N. C. (2013). Analysis of tool wear patterns in finishing turning of Inconel 718. *Wear*, 297(1–2), 885–894.

Chandrasekaran, H., & Johansson, J. O. (1994). Chip Flow and Notch Wear Mechanisms during the Machining of High Austenitic Stainless Steels. *CIRP Annals - Manufacturing Technology*, 43(1), 101–105.

- Chen, L., El-Wardany, T. I., Nasr, M., & Elbestawi, M. A. (2006). Effects of edge preparation and feed when hard turning a hot work die steel with polycrystalline cubic boron nitride tools. *CIRP Annals - Manufacturing Technology*, 55(1), 89–92.
- Childs, T., Maekawa, K., Obikawa, T., & Yamane, Y. (2000). *Metal Machining Theory and Applications* (1st ed.). London: Arnold Publishers.
- Chinchanikar, S., & Choudhury, S. K. (2014). Evaluation of Chip-tool Interface Temperature: Effect of Tool Coating and Cutting Parameters during Turning Hardened AISI 4340 Steel. *Procedia Materials Science*, 6(Icmpc), 996–1005.
- Chou, Y. K., & Song, H. (2004). Tool nose radius effects on finish hard turning. *Journal of Materials Processing Technology*, 148(2), 259–268.
- Crawforth, P., Taylor, C. M., & Turner, S. (2016). The Influence of Alloy Chemistry on the Cutting Performance and Deformation Kinetics of Titanium Alloys during Turning. *Procedia CIRP*, 45, 151–154.
- Da Silva, R. B., MacHado, Á. R., Ezugwu, E. O., Bonney, J., & Sales, W. F. (2013). Tool life and wear mechanisms in high speed machining of Ti-6Al-4V alloy with PCD tools under various coolant pressures. *Journal of Materials Processing Technology*, 213(8), 1459–1464.
- Dahlman, P. (2002). A comparison of temperature reduction in high-pressure jet-assisted turning using high pressure versus high flowrate. *Proceedings of the Institution of Mechanical Engineers -- Part B -- Engineering Manufacture (Professional Engineering Publishing)*, 216(4), 467-473.
- Daymi, A., Boujelbene, M., Salem, S. Ben, Hadj Sassi, B., Torbaty, S., & Sassi, B. H. (2009).

- Effect of the cutting speed on the chip morphology and the cutting forces. *International Scientific Journal*, 1(2), 77–83.
- Dearnley, P. A., & Trent, E. M. (1982). Wear mechanisms of coated carbide tools. *Metals Technology*, 9(1), 60–75.
- Denguir, L., Outeiro, J., Fromentin, G., Vignal, V., & Besnard, R. (2014). Influence of cutting process mechanics on surface integrity and electrochemical behavior of OFHC copper. *Procedia CIRP*, 13, 186–191.
- Desaigues, J. E., Lescalier, C., Bomont-Arzur, A., Dudzinski, D., & Bomont, O. (2016). Experimental study of Built-Up Layer formation during machining of high strength free-cutting steel. *Journal of Materials Processing Technology*, 236, 204–215.
- Devillez, A., Schneider, F., Dominiak, S., Dudzinski, D., & Larrouquere, D. (2007). Cutting forces and wear in dry machining of Inconel 718 with coated carbide tools. *Wear*, 262, 931–942.
- Dhar, N. R., & Kamruzzaman, M. (2007). Cutting temperature, tool wear, surface roughness and dimensional deviation in turning AISI-4037 steel under cryogenic condition. *International Journal of Machine Tools and Manufacture*, 47(5 SPEC. ISS.), 754–759.
- Diniz, A. E., & Micaroni, R. (2007). Influence of the direction and flow rate of the cutting fluid on tool life in turning process of AISI 1045 steel. *International Journal of Machine Tools and Manufacture*, 47(2), 247–254.
- Dodd, B., & Boddington, P. (1980). The causes of edge cracking in cold rolling. *Journal of Mechanical Working Technology*, 3, 239–252.

- Dolinšek, S., Ekinović, S., & Kopač, J. (2004). A contribution to the understanding of chip formation mechanism in high-speed cutting of hardened steel. *Journal of Materials Processing Technology*, 157–158(SPEC. ISS.), 485–490.
- Donachie, M. J., & Donachie, S. J. (2002). *Superalloys : a technical guide* (2nd ed.). ASM International.
- El-Wardany, T. I., & Elbestawi, M. A. (1998). Phenomenological Analysis of Material Side Flow in Hard Turning: Causes, Modeling, and Elimination. *Machining Science and Technology*, 2(2), 239–251.
- El-Wardany, T. I., Kishawy, H. A., & Elbestawi, M. A. (2000a). Surface Integrity of Die Material in High Speed Hard Machining, Part 1: Micrographical Analysis. *Journal of Manufacturing Science and Engineering*, 122(November), 620–631.
- El-Wardany, T. I., Kishawy, H. A., & Elbestawi, M. A. (2000b). Surface Integrity of Die Material in High Speed Hard Machining, Part 2: Microhardness Variations and Residual Stresses. *Journal of Manufacturing Science and Engineering*, 122(November), 632–641.
- El-Wardany, T. I., Mohammed, E., & Elbestawi, M. A. (1996). Cutting Temperature of Ceramic Tools in High Speed Machining of Difficult-to-Cut Materials. *International Journal of Machine Tools and Manufacture*, 36(5), 611–634.
- Ezugwu, E. O., & Bonney, J. (2004). Effect of high-pressure coolant supply when machining nickel-base, Inconel 718, alloy with coated carbide tools. *Journal of Materials Processing Technology*, 153–154(1–3), 1045–1050.
- Ezugwu, E. O., & Tang, S. H. (1995). Surface abuse when machining cast iron (G-17) and nickel-base superalloy (Inconel 718) with ceramic tools. *Journal of Materials Processing Technology*, 53(1–3), 1045–1050.

- Processing Tech.*, 55(2), 63–69.
- Ezugwu, E. O., Wang, Z. M., & Machado, A. R. (1999). The machinability of nickel-based alloys: a review. *Journal of Materials Processing Technology*, 86(1), 1–16.
- Ezugwu, E. O., Wang, Z. M., & Okeke, C. I. (1999). Tool Life and Surface Integrity When Machining Inconel 718 With PVD- and CVD-Coated Tools. *Tribology Transactions*, 42(2), 353–360.
- Gatto, A., & Iuliano, L. (1994). Chip Formation Analysis in High Speed Machining of a Nickel Base Superalloy with Silicon Carbide Whisker-Reinforced Alumina. *International Journal of Machine Tools & Manufacture*, 34(8), 1147–1161.
- Grzesik, W. (1998). The role of coatings in controlling the cutting process when turning with coated indexable inserts. *Journal of Materials Processing Technology*, 79(1–3), 133–143.
- Guédou, J.-Y., Augustins-Lecallier, I., Nazé, L., Caron, P., & Locq, D. (2008). Development of a new fatigue and creep resistant PM nickel-base superalloy for disk applications. *Superalloys 2008*, 21–30.
- Guo, Y. B., & Yen, D. W. (2004). A FEM study on mechanisms of discontinuous chip formation in hard machining. *Journal of Materials Processing Technology*, 155–156(1–3), 1350–1356.
- Hardy, M. C., Herbert, C. R. J., Kwong, J., Li, W., Axinte, D. A., Sharman, A. R. C., ... Withers, P. J. (2014). Characterising the integrity of machined surfaces in a powder nickel alloy used in aircraft engines. *Procedia CIRP*, 13, 411–416.

- Hardy, M. C., Zirbel, B., Shen, G., & Shankar, R. (2004). Developing damage tolerance and creep resistance in a high strength nickel alloy for disc applications. *Superalloys 2004*, 83–90.
- Hood, R., Morris, J., & Soo, S. L. (2016). Workpiece Surface Integrity when Milling Udiment 720 Superalloy. *Procedia CIRP*, 45, 283–286.
- Houghton plc. (2013). *Material Safety Data Sheet - Hocut 795BR (13086)*.
- Hua, J., & Shivpuri, R. (2005). A Cobalt Diffusion Based Model for Predicting Crater Wear of Carbide Tools in Machining Titanium Alloys. *Journal of Engineering Materials and Technology*, 127(1), 136–144.
- Huang, Y., & Liang, S. Y. (2003). Cutting forces modeling considering the effect of tool thermal property — application to CBN hard turning. *International Journal of Machine Tools & Manufacture*, 43, 307–315.
- Huang, Y., & Liang, S. Y. (2005). Effect of Cutting Conditions on Tool Performance in CBN Hard Turning. *Journal of Manufacturing Processes*, 7(1), 10–16.
- Huda, M. Al, Yamada, K., Hosokawa, A., & Ueda, T. (2002). Investigation of Temperature at Tool-Chip Interface in Turning Using Two-Color Pyrometer. *Journal of Manufacturing Science and Engineering*, 124(2), 200.
- Hughes, J. I., Sharman, A. R. C., & Ridgway, K. (2004). The effect of tool edge preparation on tool life and workpiece surface integrity. *Proceedings of the Institution of Mechanical Engineers, Part B: Journal of Engineering Manufacture*, 218(9), 1113–1123.

- Jackson, M. P., & Reed, R. C. (1999). Heat treatment of UDIMET 720Li: the effect of microstructure on properties. *Materials Science and Engineering A* 259, 259, 85–97.
- Joshi, S., Tewari, A., & Joshi, S. (2013). Influence of Preheating on Chip Segmentation and Microstructure in Orthogonal Machining of Ti6Al4V. *Journal of Manufacturing Science and Engineering*, 135(6), 1-11.
- Kaminski, J., & Alvelid, B. (2000). Temperature reduction in the cutting zone in water-jet assisted turning. *Journal of Materials Processing Technology*, 106(1–3), 68–73.
- Kappmeyer, G., Hubig, C., Hardy, M., Witty, M., & Busch, M. (2012). Modern machining of advanced aerospace alloys-Enabler for quality and performance. *Procedia CIRP*, 1(1), 28–43.
- Kishawy, H. A. (1998). *PhD thesis: Chip Formation and Surface Integrity in High Speed Machining of Hardened Steel.pdf*. McMaster University.
- Kishawy, H. A., & Elbestawi, M. A. (1999). Effects of process parameters on material side flow during hard turning. *International Journal of Machine Tools and Manufacture*, 39(7), 1017–1030.
- Kishawy, H. A., & Elbestawi, M. A. (2001). Tool wear and surface integrity during high-speed turning of hardened steel with polycrystalline cubic boron nitride tools. *Proceedings of the Institution of Mechanical Engineers, Part B: Journal of Engineering Manufacture*, 215, 755–767.
- Kishawy, H. A., Haglund, A., & Balazinski, M. (2006). Modelling of Material Side Flow in Hard Turning. *CIRP Annals - Manufacturing Technology*, 55(1), 85–88.

- Kitagawa, T., Kubo, A., & Maekawa, K. (1997). Temperature and wear of cutting tools in high-speed machining of Inconel 718 and Ti6Al6V2Sn. *Wear*, 202(2), 142–148.
- Klocke, F., Sangermann, H., Krämer, A., & Lung, D. (2011). Influence of a high-pressure lubricoolant supply on thermo-mechanical tool load and tool wear behaviour in the turning of aerospace materials. *Proceedings of the Institution of Mechanical Engineers, Part B: Journal of Engineering Manufacture*, 225(1), 52–61.
- Komanduri, R. (1971). Some Aspects of Machining With Negative Rake Tools Simulating Grinding. *International Journal of Machine Tool Design and Research*, 11, 223–233.
- Komanduri, R. (1982). Some clarifications on the mechanics when machining titanium alloys of chip formation. *Wear*, 76, 15–34.
- Komanduri, R., & Schroeder, T. A. (1986). On Shear Instability in Machining a Nickel-Iron Base Superalloy. *Journal of Engineering for Industry*, 108(2), 93–100.
- Komanduri, R., & Von Turkovich, B. F. (1981). New observations on the mechanism when machining titanium alloys of chip formation. *Wear*, 69(2), 179–188.
- König, W., Berktold, A., & Koch, K. F. (1993). Turning versus Grinding - A Comparison of Surface Integrity Aspects and Attainable Accuracies. *CIRP Annals - Manufacturing Technology*, 42(1), 39–43.
- Kumar, S. A., Rahman, M., & Ng, S. L. (2002). Effect of high-pressure coolant on machining performance. *International Journal of Advanced Manufacturing Technology*, 20(2), 83–91.
- Li, L., Li, B., Li, X., & Enhmann, K. F. (2014). Experimental Investigation of Hard Turning

Mechanisms by PCBN Tooling Embedded Micro Thin Film Thermocouples. *Proceedings of the ASME 2012 International Manufacturing Science and Engineering Conference*, 1–10.

Li, W., Withers, P. J., Axinte, D., Preuss, M., & Andrews, P. (2009). Residual stresses in face finish turning of high strength nickel-based superalloy. *Journal of Materials Processing Technology*, 209(10), 4896–4902.

Li, X. (1995). Study of the jet-flow rate of cooling in machining Part 2. Simulation study. *Journal of Materials Processing Tech.*, 62, 157–165.

Liao, Y. S., & Shiue, R. H. (1996). Carbide tool wear mechanism in turning of Inconel 718 superalloy. *Wear*, 193(1), 16–24.

Mair, W. A., & Birdsall, D. L. (1998). *Aircraft performance*. Cambridge University Press.

Matsumoto, Y., Hashimoto, F., Lahoti, G., & Company, T. T. (1999). Surface Integrity Generated by Precision Hard Turning. *CIRP Annals - Manufacturing Technology*, 48(1), 59–62.

May, J. R., Hardy, M. C., Bache, M. R., & Kaylor, D. D. (2011). Microstructure and Mechanical Properties of an Advanced Nickel-Based Superalloy in the as-HIP Form. *Advanced Materials Research*, 278, 265–270.

Merchant, M. E. (1945). Mechanics of the Metal Cutting Process. I. Orthogonal Cutting and a Type 2 Chip. *Journal of Applied Physics*, 16(5), 267–275.

Mitchell, R. J., Hardy, M. C., Preuss, M., & Tin, S. (2004). Development of  $\gamma'$  Morphology in P/M Rotor Disc Alloys During Heat Treatment. *Superalloys 2004 (Tenth*

- International Symposium), 361–370.*
- Mitchell, R. J., Lemsky, J. A., Ramanathan, R., Li, H. Y., Perkins, K. M., & Connor, L. D. (2008). Process Development & Microstructure & Mechanical Property Evaluation of a Dual Microstructure Heat Treated Advanced Nickel Disc Alloy. *Superalloys 2008*, 347–356.
- Nakayama, K., Arai, M., & Kanda, T. (1988). Machining Characteristics of Hard Materials. *CIRP Annals - Manufacturing Technology*, 37(1), 89–92.
- Nandy, A. K., Gowrishankar, M. C., & Paul, S. (2009). Some studies on high-pressure cooling in turning of Ti-6Al-4V. *International Journal of Machine Tools and Manufacture*, 49(2), 182–198.
- National Academy of Sciences. (2006). *A Review of United States Air Force and Department of Defense Aerospace Propulsion Needs Committee*.
- Nedic, B. P., & Eric, M. D. (2014). Cutting Temperature Measurement and Material Machinability. *Thermal Science*, 18, 259–268.
- Ng, E.-G., & Aspinwall, D. K. (2002). The Effect of Workpiece Hardness and Cutting Speed on the Machinability of AISI H13 Hot Work Die Steel When Using PCBN Tooling. *Journal of Manufacturing Science and Engineering*, 124(3), 588.
- Obikawa, T., Sasahara, H., Shirakashi, T., & Usui, E. (1997). Application of Computational Machining Method to Discontinuous Chip Formation. *Journal of Manufacturing Science and Engineering*, 119(4B), 667.
- Okushima, K., & Hitomi, K. (1961). An Analysis of the Mechanism of Orthogonal Cutting

- and Its Application to Discontinuous Chip Formation. *Journal of Engineering for Industry*, 83(4), 545–555.
- Olovsjo, S., & Nyborg, L. (2012). Influence of microstructure on wear behaviour of uncoated WC tools in turning of Alloy 718 and Waspaloy. *Wear*, 282–283, 12–21.
- Olovsjö, S., Wretland, A., & Sjöberg, G. (2010a). The effect of grain size and hardness of Waspaloy on the wear of cemented carbide tools. *International Journal of Advanced Manufacturing Technology*, 50(9–12), 907–915.
- Olovsjö, S., Wretland, A., & Sjöberg, G. (2010b). The effect of grain size and hardness of wrought Alloy 718 on the wear of cemented carbide tools. *Wear*, 268(9–10), 1045–1052.
- Ostafiev, V., Kharkevich, A., Weinert, K., & Ostafiev, S. (1999). Tool Heat Transfer in Orthogonal Metal Cutting. *Journal of Manufacturing Science and Engineering*, 121(4), 541–549.
- Ozel, T., Llanos, I., Soriano, J., & Arrazola, P.-J. (2011). 3D Finite Element Modelling of Chip Formation Process for Machining Inconel 718: Comparison of Fe Software Predictions. *Machining Science and Technology*, 15(1), 21–46.
- Palanisamy, S., McDonald, S. D., & Dargusch, M. S. (2009). Effects of coolant pressure on chip formation while turning Ti6Al4V alloy. *International Journal of Machine Tools and Manufacture*, 49(9), 739–743.
- Pawade, R. S., Joshi, S. S., & Brahmkar, P. K. (2008). Effect of machining parameters and cutting edge geometry on surface integrity of high-speed turned Inconel 718. *International Journal of Machine Tools and Manufacture*, 48(1), 15–28.

- Pawade, R. S., Joshi, S. S., Brahmankar, P. K., & Rahman, M. (2007). An investigation of cutting forces and surface damage in high-speed turning of Inconel 718. *Journal of Materials Processing Technology*, 192–193, 139–146.
- Poulachon, G., & Moisan, A. L. (2000). Hard Turning: Chip Formation Mechanisms and Metallurgical Aspects. *Journal of Manufacturing Science and Engineering*, 122(3), 406.
- Preuss, M., da Fonseca, J. Q., Grant, B., Knoche, E., Moat, R., & Daymond, M. (2008). The effect of y' particle size on the deformation mechanism in an advanced polycrystalline nickel-base superalloy. *Superalloys 2008: 11th International Symposium on Superalloys*, (10), 405–414.
- Qiu, C. (2010). *PhD Thesis: Net-shape hot isostatic pressing of a nickel-based powder superalloy*. The University of Birmingham.
- Reed, R. C. (Roger C. (2006). *The superalloys : fundamentals and applications*. Cambridge University Press.
- Sadat, A. B., & Reddy, M. Y. (1992). Surface integrity of inconel-718 nickel-base superalloy using controlled and natural contact length tools. part I: Lubricated. *Experimental Mechanics*, 32(3), 282–288.
- Salem, S. Ben, Bayraktar, E., Boujelbene, M., & Katundi, D. (2012). Effect of cutting parameters on chip formation in orthogonal cutting. *Journal of Achievements in Materials and Manufacturing Engineering*, 50(1), 7–17.
- Sanchez, L. E. d. A., Palma, G. L., Marinescu, I., Modolo, D. L., Nalon, L. J., & Santos, A. E. (2012). Effect of different methods of cutting fluid application on turning of a difficult-to-machine steel (SAE EV-8). *Proceedings of the Institution of Mechanical*

- Engineers, Part B: Journal of Engineering Manufacture*, 227(2), 220–234.
- Schulz, H., & Moriwaki, T. (1992). High-speed Machining. *CIRP Annals - Manufacturing Technology*, 41(2), 637–643.
- Sharman, A. R. C., Amarasinghe, A., & Ridgway, K. (2008). Tool life and surface integrity aspects when drilling and hole making in Inconel 718. *Journal of Materials Processing Technology*, 200(1–3), 424–432.
- Sharman, A. R. C., Aspinwall, D. K., Dewes, R. C., Clifton, D., & Bowen, P. (2001). The effects of machined workpiece surface integrity on the fatigue life of  $\gamma$ -titanium aluminide. *International Journal of Machine Tools and Manufacture*, 41(11), 1681–1685.
- Sharman, A. R. C., Dewes, R. C., & Aspinwall, D. K. (2001). Tool life when high speed ball nose end milling Inconel 718 TM. *Journal of Materials Processing Technology*, 118, 0–6.
- Sharman, A. R. C., Hughes, J. I., & Ridgway, K. (2006). An analysis of the residual stresses generated in Inconel 718<sup>TM</sup> when turning. *Journal of Materials Processing Technology*, 173(3), 359–367.
- Sharman, A. R. C., Hughes, J. I., & Ridgway, K. (2008). Surface integrity and tool life when turning Inconel 718 using ultra-high pressure and flood coolant systems. *Proceedings of the Institution of Mechanical Engineers, Part B: Journal of Engineering Manufacture*, 222(6), 653–664.
- Sharman, A. R. C., Hughes, J. I., & Ridgway, K. (2015). The effect of tool nose radius on surface integrity and residual stresses when turning Inconel 718. *Journal of Materials*

- Processing Technology*, 216, 123–132.
- Shaw, M. ., & Vyas, A. (1998). The Mechanism of Chip Formation with Hard Turning Steel. *CIRP Annals - Manufacturing Technology*, 47(1), 77–82.
- Shaw, M. C., & Vyas, A. (1993). Chip Formation in the Machining of Hardened Steel. *CIRP Annals - Manufacturing Technology*, 42(1), 29–33.
- Sima, M., & Öznel, T. (2010). Modified material constitutive models for serrated chip formation simulations and experimental validation in machining of titanium alloy Ti-6Al-4V. *International Journal of Machine Tools and Manufacture*, 50(11), 943–960.
- Smart, E. F., & Trent, E. M. (1975a). Coolants and Cutting Tool Temperatures. In *Proceedings of the Fifteenth International Machine Tool Design and Research Conference* (pp. 187–195). London: Macmillan Education UK.
- Smart, E. F., & Trent, E. M. (1975b). Temperature distribution in tools used for cutting iron, titanium and nickel. *International Journal of Production Research*, 13(3), 265–290.
- Soo, S. L., Hood, R., Aspinwall, D. K., Voice, W. E., & Sage, C. (2011). Machinability and surface integrity of RR1000 nickel based superalloy. *CIRP Annals - Manufacturing Technology*, 60(1), 89–92.
- Sørby, K., & Tønnessen, K. (2006). High-pressure cooling of face-grooving operations in Ti6Al4V. *Proceedings of the Institution of Mechanical Engineers, Part B: Journal of Engineering Manufacture*, 220(10), 1621–1627.
- Steglich, D., Wafai, H., & Brocks, W. (2010). Anisotropic Deformation and Damage in Aluminium 2198 T8 Sheets. *International Journal of Damage Mechanics*, 19(2), 131–

152.

- Su, G. S., Guo, Y. K., Song, X. L., & Tao, H. (2016). Effects of high-pressure cutting fluid with different jetting paths on tool wear in cutting compacted graphite iron. *Tribology International*, 103, 289–297.
- Thakur, A., Mohanty, A., Gangopadhyay, S., & Maity, K. P. (2014). Tool Wear and Chip Characteristics during Dry Turning of Inconel 825. *Procedia Materials Science*, 5, 2169–2177.
- Thakur, D. G., Ramamoorthy, B., & Vijayaraghavan, L. (2009). Study on the machinability characteristics of superalloy Inconel 718 during high speed turning. *Materials and Design*, 30(5), 1718–1725.
- Thiele, J. D., & Melkote, S. N. (1999). Effect of cutting edge geometry and workpiece hardness on surface generation in the finish hard turning of AISI 52100 steel. *Journal of Materials Processing Technology*, 94(2), 216–226.
- Thiele, J. D., Melkote, S. N., Peascoe, R. A., & Watkins, T. R. (2016). Effect of Cutting-Edge Geometry and Workpiece Hardness on Surface Residual Stresses in Finish Hard Turning of AISI 52100 Steel. *Journal of Manufacturing Science and Engineering*, 122(November 2000), 642–649.
- Thomas, T. R. (1981). Characterization of surface roughness. *Precision Engineering*, 3(2), 97–104.
- Trent, E. M., & Wright, P. K. (2000). *Metal Cutting*. Vasa (4th ed.). Butterworth-Heinemann.
- Vyas, A., & Shaw, M. C. (1999). Mechanics of saw-tooth chip formation in metal cutting.

- Journal of Manufacturing Science and Engineering, Transactions of the ASME, 121(2).*
- Wertheim, R., Rotberg, J., & Ber, A. (1992). Influence of High-pressure Flushing through the Rake Face of the Cutting Tool. *CIRP Annals - Manufacturing Technology, 41(1)*, 101–106.
- Wright, P. K., & Chow, J. G. (1982). Deformation Characteristics of Nickel Alloys During Machining. *Journal of Engineering Materials and Technology, 104*, 85–93.
- Xue, C., & Chen, W. (2011). Adhering layer formation and its effect on the wear of coated carbide tools during turning of a nickel-based alloy. *Wear, 270(11–12)*, 895–902.
- Zhou, J. M., Bushlya, V., & Stahl, J. E. (2012). An investigation of surface damage in the high speed turning of Inconel 718 with use of whisker reinforced ceramic tools. *Journal of Materials Processing Technology, 212(2)*, 372–384.

# APPENDICES

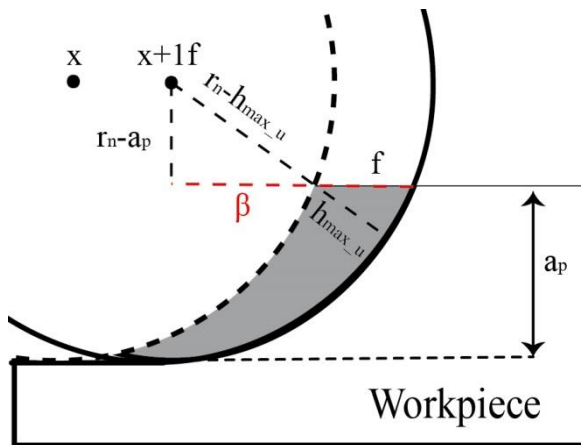
## APPENDIX 1

- Formula derivations for uncut chip geometry dimensions used in chip formation data analysis:

---

### Maximum uncut chip thickness formula derivation, $h_{\max\_u}$

---



$$h_{\max\_u} = r_n - \sqrt{(r_n - a_p)^2 + (\beta - f)^2}$$

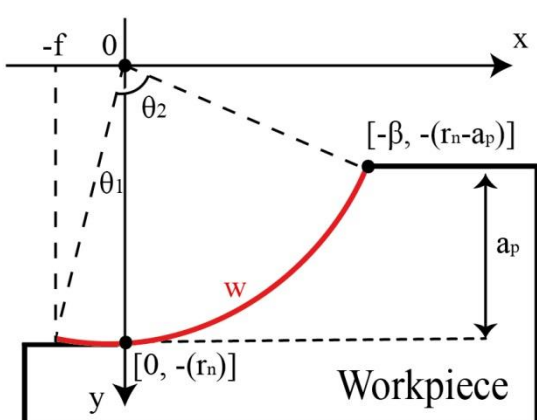
for

$$\beta = \sqrt{2 * r_n * a_p - a_p^2}$$

---

### Calculated chip width formula derivation, w

---



$$w = \theta_w * r_n$$

for

$$\theta_w = \theta_2 - \theta_1$$

$$\theta_2 = \tan^{-1}\left(\frac{\sqrt{\beta}}{r_n - a_p}\right)$$

$$\theta_1 = \frac{\pi}{2} - \cos^{-1}\left(\frac{-f}{2 * r_n}\right)$$

$(\theta_1$  by Denguir et al. (2014))

- Table of calculated uncut values used in chip formation data analysis:

<b>r<sub>n</sub> (mm)</b>	<b>a<sub>p</sub> (mm)</b>	<b>f (mm/rev)</b>	<b>h<sub>max_u</sub> (mm)</b>	<b>w (mm)</b>
1.5	0.25	0.12	0.06285	0.93854
1.5	0.13	0.12	0.04473	0.68911
1.5	0.12	0.25	0.07924	0.72922
1.5	0.24	0.12	0.06157	0.92029
1.5	0.24	0.24	0.11546	0.98034
1.5	0.24	0.36	0.16074	1.04070
3.0	0.24	0.12	0.04497	1.26815
3.0	0.24	0.24	0.08568	1.32818
3.0	0.24	0.36	0.12197	1.38826
3.0	0.12	0.12	0.03136	0.91139
3.0	0.12	0.24	0.05816	0.97141
3.0	0.12	0.36	0.08027	1.03149

## APPENDIX 2

Example of chip formation calculations according to the process described in section 3.3:

<b>CG RR1000, LP cooling (Phase 2b), V<sub>C</sub> = 50 m/min, a<sub>p</sub> = 0.25 mm f = 0.12 mm/rev</b>						
<b>3D scan values</b>	<b>Length AB</b>	<b>Angle A</b>	<b>Dataset</b>	<b>Length AB</b>	<b>Angle A</b>	<b>h<sub>max_u</sub> (μm)</b>
#1	149.1	42.1	#1	42.1	149.1	99.96
#2	148.4	42.6	#2	42.1	148.4	99.49
#3	147.3	41.9	#3	42.1	147.3	98.75
#4	148.7	42.8	#4	42.1	148.7	99.69
#5	147.5	43.1	#5	42.1	147.5	98.89
			#6	42.6	149.1	100.92
			#7	42.6	148.4	100.45
			#8	42.6	147.3	99.70
			#9	42.6	148.7	100.65
			#10	42.6	147.5	99.84
			#11	41.9	149.1	99.57
			#12	41.9	148.4	99.11
			#13	41.9	147.3	98.37
			#14	41.9	148.7	99.31
			#15	41.9	147.5	98.51
			#16	42.8	149.1	101.30
			#17	42.8	148.4	100.83
			#18	42.8	147.3	100.08
			#19	42.8	148.7	101.03
			#20	42.8	147.5	100.22
<b>Statistical Analysis</b>		<b>Value</b>	#21	43.1	149.1	101.88
Mean (μm)		100.12	#22	43.1	148.4	101.40
Sample size		25	#23	43.1	147.3	100.65
Confidence coefficient		1.96	#24	43.1	148.7	101.60
Margin of error (μm)		3.863	#25	43.1	147.5	100.78

## APPENDIX 3

Houghton Hocut 795BR (13086) composition and information on ingredients list, Houghton plc (2013):

<b>Chemical</b>	<b>Formula</b>	<b>Weight %</b>
Distillates (petroleum), hydrotreated light naphthenic	Unspecified	25% - 50%
Neutralised Dicyclohexylamine	C <sub>12</sub> H <sub>23</sub> N	2.5% - 10%
Phosphoric acid, isotridecyl ester	C <sub>13</sub> H <sub>29</sub> O <sub>4</sub> P	2.5% - 10%
2-Aminoethanol	C <sub>2</sub> H <sub>7</sub> NO	1% - 2.5%
2-(2-Butoxyethoxy)ethanol	C <sub>8</sub> H <sub>18</sub> O <sub>3</sub>	1% - 2.5%
N,N'-Methylenebismorpholine	C <sub>9</sub> H <sub>18</sub> N <sub>2</sub> O <sub>2</sub>	1% - 2.5%
Neutralised 2-Aminoethanol	C <sub>2</sub> H <sub>7</sub> NO	1% - 2.5%
3-Iodo-2-propynylbutylcarbamate	C <sub>8</sub> H <sub>12</sub> INO <sub>2</sub>	0% - 1%